A high precision position sensitive detection technology for Micro-Electro-Mechanical Systems (MEMS) based on an optical resonant cavity

A DISSERTATION PRESENTED
BY
GINO PUTRINO BE(HONS), BSC
TO
THE DEPARTMENT OF ELECTRICAL AND ELECTRONIC ENGINEERING

IN PARTIAL FULFILLMENT OF THE REQUIREMENTS
FOR THE DEGREE OF
DOCTOR OF PHILOSOPHY
IN THE SUBJECT OF
ELECTRICAL AND ELECTRONIC ENGINEERING

THE UNIVERSITY OF WESTERN AUSTRALIA
PERTH, WESTERN AUSTRALIA
SEPTEMBER 2013

© *2013 - Gino Putrino*
All rights reserved.

A high precision position sensitive detection technology for Micro-Electro-Mechanical Systems (MEMS) based on an optical resonant cavity

Abstract

This thesis examines the light transmission through the optical microcavity created in a gap between a diffraction grating etched into a silicon photonic waveguide and a free-standing MEMS structure. The optical microcavities studied are very small - having typical dimensions 12 μm long, 4 μm wide and 2 μm high when designed for use with light at telecommunications wavelengths. The power transmitted through this cavity can be modulated by changing the height of the MEMS structure. Extremely small changes in the height of the microcavity result in very large changes in optical power, due to the optical resonance in the microcavity. The sensitivity of this effect was studied, and it was found that the potential deflection noise density (DND) with respect to the height change of the microcavity was in the range of a few fm/$\sqrt{\text{Hz}}$. This sensitivity is adequate for the detection of the movement of the MEMS structures due to thermo-mechanical noise, and such a measurement is presented. Experimentally, the DND for a silicon nitride cantilever was measured to within a single pm/$\sqrt{\text{Hz}}$, even though the optimisation of the measurement system was beyond the scope of this thesis.

Whilst the microcavity itself is tiny, its strong response to small changes in the position of the suspended MEMS has the potential for a large range of applications. One potential application may be found in the field of MEMS sensors. MEMS sensors are a new class of chemical/biological sensor based on using the movement of functionalized MEMS structures to detect specific chemical compounds. These sensors are extremely robust, and have been shown to be able to provide down to zeptogram (10^{-21}) sensitivity. Unfortunately, the wider adoption of MEMS sensors has been limited in part by the lack of a technology sufficient to the task of measuring the movement of the MEMS structures accurately and in great enough number to make the sensing practical outside of laboratory environments.

The optical microcavities studied, designed, fabricated and tested within the pages of this thesis performs extremely well and provides an approach for on-chip detection of MEMS structure height changes that is extendable to monitoring large arrays. Optic fiber fed MEMS sensors may be read-out using this technology, and could be used as part of a remotely operated

fiber sensing network. The gratings and silicon photonic waveguides are fabricated using CMOS compatible technologies. The MEMS structures tested were microcantilevers and microbridges, however the height measurement technique should be easily extended to other types of MEMS structures.

Contents

1 Introduction 1
- 1.1 Microelectromechanical Systems . . . 1
- 1.2 Silicon Photonics . . . 3
- 1.3 Thesis Overview . . . 3

2 MEMS Sensor Positioning Techniques 5
- 2.1 MEMS Sensor Operation Fundamentals . . . 5
- 2.2 MEMS Sensor Implementations . . . 10
- 2.3 Read-out methods . . . 13
- 2.4 Chapter Conclusions and Thesis Objectives . . . 24

3 Theory of Operation 25
- 3.1 Physical Description of Device . . . 25
- 3.2 Modeling methodology . . . 27
- 3.3 Diffraction Grating Couplers - Background Theory . . . 29
- 3.4 Calculation of maxima and minima . . . 31
- 3.5 FDTD simulations . . . 32
- 3.6 Theory and Simulation Conclusions . . . 45

4 Device Design and Fabrication 47
- 4.1 Photonic circuit . . . 47
- 4.2 MEMS Structures . . . 50
- 4.3 Fabricated Devices . . . 58
- 4.4 Device Design and Fabrication Conclusions . . . 63

5 Demonstration of Readout Technique 67
- 5.1 Reference Measurements . . . 67
- 5.2 Experimental Setup - Optical alignment and Coupling . . . 68
- 5.3 Grating Characterisation . . . 71
- 5.4 Microbridge . . . 71
- 5.5 Microcantilever . . . 76
- 5.6 Conclusion . . . 84

6 Sensitivity, Noise Analysis and Brownian Motion 87
6.1 Theoretical Sensitivity and Noise Analysis 87
6.2 Experimental Limits of Detection 93
6.3 Conclusion 99

7 Conclusions and Future Work 101
7.1 Conclusions 101
7.2 Future Work 104

Appendices 111

A Publications Arising From The PhD Program 113
A.1 Refereed Journal Articles 113
A.2 Patents 113
A.3 Refereed Conference Papers 114

B Awards Won During The PhD Program 115

C LETI Standard Process Capabilities 117
C.1 ePIXfab 117
C.2 LETI 117

D Sample FDTD Code 119

E Microfabrication Process Used To Create MEMS 123
E.1 Fabrication of MEMS 123

F Measurement methodology 129
F.1 Optical Profilometer 129
F.2 Vibrometer 130
F.3 Photodiodes 131
F.4 Transimpedance Amplifiers 131
F.5 Actuation 131
F.6 Time Domain Measurements 132
F.7 Frequency Domain Measurements 132

References 133

Listing of figures

1.1.1 MEMS market forecast by devices. Source: http://www.i-micronews.com/reports/Status-MEMS-Industry-2013/1/384/ 2

2.1.1 Example of the static mode operation of a MEMS cantilever protein sensor. (a) The micro-cantilever has been functionalized, but no detection event has yet occurred. The cantilever beam is flat, and the pre-detection surface stress of the beam is σ_1. In its normal state, the cantilever tip is a distance z above the substrate. (b) The protein has bonded to the functionalization layer, and the resulting surface stress, σ_2 has resulted in the elastic stretching of the surface, causing the cantilever beam to deform. As a result, the tip of the cantilever beam is now a distance of $z + \delta$ above the substrate. 6

2.1.2 Deflection at the tip of a 100 μm long Pd/SiN_x cantilever due to hydrogen absorption as predicted by Equation 2.3. The deflection due to hydrogen partial pressure in air is indicated. 7

2.2.1 Two early implementation of free-standing MEMS structures. Top: Schematic of the resonant gate transistor fabricated by Nathanson *et al.* [31], and Bottom: the pressure sensor etched from a single silicon wafer by Greenwood [32] . . . 10

2.2.2 An early implementation of a cantilever sensor array. Left: SEM image of the microcantilever sensor array prior to the deposition of sensor coatings [45], and Right: schematic view of the polymer coatings used for the eight cantilevers [46] 12

2.3.1 Schematics of external optical read-out techniques. Left: Fukuma's position sensitive detector technique [63], and Right: Thornton's external optical interferometer technique [64] 14

2.3.2 Various integrated micro-cavity read-out techniques. Left: Schematic of micro-harp technique. Optical power is fed to the differently functionalized micro-bridges, and an optical micro-cavity is formed between the substrate and the reflective microbridge [69]. Center: SEM of the Preussner *et al.* in plane micro-cavity. Light is fed along a silicon waveguide, and the etched DBR grating can be actuated to the left (c) or right (d) either shortening or lengthening the cavity [70]. Right: Eichenfield *et al.* zipper cavity. Mechanical motion of the zipper cavity nanobeams changes the transmitted optical intensity through the phase modulation of the internal cavity field [71] 15

2.3.3 Various integrated micro-disk read-out techniques. (i) Srinivasan *et al.* microdisk coupled to a nanocantilever [76]. (ii) Colourized SEM of the microdisk system fabricated by Gavartin *et al.* This system consists of a doubly clamped, high-stress Si_3N_4 nanomechanical beam (blue) coupled via the near-field to a silica microdisk resonator (red). Both the resonator and the pads holding the beam rest on silicon pedestals (green) [77]. (iii) Micro-disk technique demonstrated by Miao *et al.* [78]. 17

2.3.4 Schematics of two cantilever as waveguide techniques. Left: Zinoviev *et al.* system [80]. Right: Noh *et al.* differential output system [81]. 18

2.3.5 Implementation of miscellaneous optical readout techniques. Top: Photo and schematic of Carpenter *et al.* double Bragg grating technique [84]. Bottom Left: Iannuzzi fiber top cantilever [85]. Bottom Right: Schematic of Pham *et al.* grated waveguide evanescent field technique [86]. 20

2.3.6 Various electronic read-out systems: Top Left: Schematic of piezoresistance array technique [95]. Right: Schematic and SEM of Huang *et al.* magnetomotive technique [96]. Bottom Left: Knobel *et al.* single electron transistor [97]. The scale bar represents 1 μm 22

3.1.1 Isometric view of the proposed interrogating grating structure (not to scale). . . 26

3.1.2 Cross-section of the full device through A'A from Figure 3.1.1 27

3.2.1 Isometric diagram of the modeled diffraction grating implemented in SOI wafer (not to scale). The SOI wafer is made up of a 230 nm thick epitaxial silicon layer, 2 μm thick BOX layer, and silicon handle layer. It is proposed that the grating is etched into the epitaxial silicon and has a pitch of 610 nm, depth 50 nm, length 11.9 μm, and width 4μm. 28

3.3.1 Ray diagram of light travelling at an angle of incidence, θ_i from the normal, passing from one medium (with refractive index n_1) through a grating with pitch Λ into an second medium (refractive index n_2). The light is diffracted at the grating and the rays of power P_m radiating at angles θ_m for the orders $m = -1, 0, 1$ of diffraction are shown. 29

3.3.2 Slab waveguide grating structure on top of a high reflectivity substrate [117]. Light travelling in the waveguide in a guided mode (P_{in}) is coupled by the grating towards both the cover and the substrate. The light travelling towards the substrate passes through a low refractive index buffer which forms a highly reflective interface with the substrate. When this structure is well designed, the majority of light will reflect back from the substrate to join the light leaving the grating (P_{out}). Some light will be lost through the substrate, and, depending on the efficiency of the grating, a portion of light will continue to travel through the substrate. θ is the angle that the light leaves the grating. n_1, n_2, n_3, and n_4 are the refractive indices of the cover region, waveguide, low index buffer, and substrate respectively. Λ is the pitch of the grating, h is the thickness of the waveguide layer, and b is the thickness of the low index buffer layer. 30

3.5.1 Modeled results at $\lambda = 1550$ nm for a SOI waveguide 230 nm thick with a grating of pitch 610 nm, depth 50 nm, and length 11.9 μm. Calculated TE field distributions through section A'A in Figure 3.1.1 for the case where there is no cantilever. Blue represents positive intensity, red represents negative. 32

3.5.2 Modeled results of the loss parameter a for the wavelength range 1340-1830 nm. Shaded area represents the wavelength range of an erbium doped fiber amplifier. 33

3.5.3 Modeled results at $\lambda = 1550$ nm for a cantilever with a perfect reflector over a SOI waveguide 230 nm thick. The grating has pitch 630 nm and is 11.9 μm long. Calculated TE field distributions through section A'A in Figure 3.1.1 with a separation of 0.8 μm. This separation gives maximum transmitted power. (a) The TE field strength overlain over the structure. (b) Plot of the TE field intensity through sections B'B, C'C, and D'D, which represent points of interest before the grating, along the grating and after the grating respectively. 34

3.5.4 Modeled results at $\lambda = 1550$ nm for a cantilever with a perfect reflector over a SOI waveguide 230 nm thick. The grating has pitch 630 nm and is 11.9 μm long. TE field distribution with a separation 1.2 μm (minimum in transmitted power). (a) The TE field strength overlain over the structure. A significant portion of the energy is coupled into the substrate rather than the output waveguide. (b) Plot of the TE field intensity through sections B'B, C'C, and D'D, which represent points of interest before the grating, along the grating and after the grating respectively. 35

3.5.5 Modeled results at $\lambda = 1550$ nm for a cantilever with a perfect reflector over a SOI waveguide 230 nm thick. Power transmitted as a function of cantilever-grating separation for a diffraction grating of both 4 μm width and an infinite width (2D) approximation. 37

3.5.6 2D FDTD modeled results at λ = 1548, 1651, and 1702 nm for a cantilever with a perfect reflector over a SOI waveguide 230 nm thick. Power transmitted as a function of cantilever-grating separation for the various wavelengths. Inset shows the peak-to-peak period (Λ) for various wavelengths in the range 1300-1800 nm. 37

3.5.7 Schematic of a proposed system to address large arrays of microbridges. 39

3.5.8 2D FDTD modeled results at λ = 1550 nm for a cantilever with a perfect reflector over a SOI waveguide 230 nm thick. Power transmitted as a function of cantilever-grating separation for a diffraction grating of 4, 8, 12 and 16 μm length. 40

3.5.9 Modeled results at λ = 1550 nm for a cantilever with a dielectric mirror over a SOI waveguide 230 nm thick and 4 μm wide with a grating of pitch 610 nm, depth 50 nm, and length 11.9 μm. The mirrors simulated have a bottom surface reflectivity of 9%, 25%, 36%, and 51%. Power transmitted as a function of cantilever-grating separation is displayed. 41

3.5.10 Modeled results at $\lambda = 1550$ nm for a SOI waveguide 230 nm thick and 4 μm wide with a grating of pitch 610 nm, depth 50 nm, and length 11.9μm. Calculated TE field distributions through section A'A in Figure 3.1.1 for the case of a dielectric cantilever with $\varepsilon_r = 3.45$ (Corresponding to a reflectivity of 9% at each surface). (a) TE field when the grating-cantilever separation is 0.8 μm. This separation gives maximum transmitted power. (b) TE field when the grating-cantilever separation is 1.2 μm (minimum transmitted power). Note that in both cases, substantial optical power (around 5 dB) is lost through the cantilever due to its low reflectivity. 41

3.5.11 Schematic illustration of the cantilever/grating from Figure 3.1.1 in YZ cross-sectional view. a: Grating is too narrow – when the micro-cantilever is deflected, some light is not coupled back into the grating. b: Grating is too wide – when Gap1 » Gap2, multiple cavity resonances exist, broadening spectral width (axis is consistent with Figure 3.1.1). 42

3.5.12 Modeled results of the loss parameter a for the wavelength range 1340-1830 nm in both air and water. 44

3.5.13 Modeled results at λ = 1550 nm for a SOI waveguide 230 nm thick and 4 μm wide with a grating of pitch 610 nm, depth 50 nm, and length 11.9 μm. Calculated TE field distributions through section A'A in Figure 3.1.1 for the case without a cantilever. (a) TE field when the medium above the grating is air. (b) TE field when the medium above the grating is water. 44

3.5.14 Modeled results at λ = 1550 nm for a cantilever in air and water over a SOI waveguide 230 nm thick with an embedded grating. Power transmitted as a function of cantilever-grating separation is displayed. 45

4.1.1 LETI process flow. (i) Starting with an SOI wafer chosen with an epitaxial silicon thickness able to operate as a waveguide for infra-red light (220 nm), and a SiO_2 thickness (2 μm) chosen to support the operation of the Si waveguide and grating couplers, (ii) a 220 nm silicon etch is performed to remove the parts of the epitaxial silicon which are not going to be needed for the photonic circuit. This forms the waveguides and adiabatic tapers. (iii) Subsequently, a 70 nm silicon etch is performed to define the diffraction gratings. (iv) A layer of SiO_2 is deposited, and (v) is chemo-mechanically polished down to a height of 100 nm above the top of the epitaxial silicon. This step provides a flat planarized surface for the fabrication of the overlying MEMS structures. 48

4.1.2 Top schematic view of the photonic circuit used. When a suspended MEMS beam with a reflective under-surface (not shown) is fabricated above the interrogating grating, an optical microcavity will form, and the input laser signal, P_{in} will be modulated based on the movement of the MEMS beam, creating the output signal P_{out}. 49

4.1.3 Isometric diagram of the diffraction grating (not to scale). The grating is 12.6 μm long, 10 μm wide, with a thickness of 220 nm, and a pitch of 630 nm. The grating is a square wave grating, and so its ridges and grooves are both 315 nm. The grating depth is 70 nm. 49

4.1.4 Isometric diagram of an adiabatic taper (not to scale). This component 220 nm thick, starts with a width of 10 μm and shrinks to a width of 3 μm over a length of either 300 or 200 μm. 50

4.1.5 Isometric diagram of the 50-50 optical splitter (not to scale) 51

4.2.1 Reflectance of Aluminium, Silver and Gold evaporated in ultrahigh vacuum [133, 134] 52

4.2.2 Typical top hat anchor structure. 52

4.2.3 Impact of tensile stress on the theoretical resonant frequency of microbridges made from PECVD SiN_x with a thickness of 750 nm, and a length (width) of either 220 μm (20 μm) or 110 μm (10 μm). The resonant frequency and tensile stress of the beam fabricated in Section 4.3.1 is indicated by the dashed blue line. For this calculation a Young's modulus, E, of 150 GPa and a density, ρ, of 3184 kg/m^3 were assumed for the silicon nitride. 54

4.2.4 Isometric image of a Guckel Ring. 55

4.2.5 Electrostatic actuation of a cantilever modeled as two charged plates, one of which is movable on simple spring. At rest, the two plates are separated by distance d. When a voltage V is applied, the generated electrostatic force, F_e, draws the movable plate a distance Δx towards the fixed plate until F_e is balanced by the spring restoring force, F_r. If F_e large enough that it can overwhelm F_r, then snap down occurs. 58

4.3.1 Sample doubly clamped beam fabricated over a photonic circuit. (top) Colourized 3D optical profilometry image. (bottom) Plot of the measured beam profile of cross-section AA'. 60
4.3.2 Sample cantilever fabricated without actuation pads. (a) Colourized 3D optical profilometry image of cantilever, (b) Plot of the measured beam profile of cross-section AA'. Note that the anchor shows only as a shadow in the profilometry image as there is no metal on that part of the device, and the SiN_x does not provide enough of a reflection for the profilometer to map an image. 61
4.3.3 Sample released cantilever fabricated over a photonic circuit with actuation pads. (a) Colourized 3D Zygo optical profilometry image of cantilever, (b) Plot of the Dektak stylus profilometry measured beam profile of cross-section BB' for the unreleased device. (c) Plot of optical profilometry measured beam profile of cross-section CC' for the released device. 62
4.3.4 Anchor effect measurements. 3D Optical profilometry of released cantilever beam profiles for devices with (a) a triangular, and (b) a square top hat style anchor. 62
4.3.5 Anchor effect measurements. (a) Optical profilometry of released cantilever beam profiles for devices with a square, triangular and circular anchor (b) Vibrometer speed measurements for cantilevers with a triangular and circular anchor. 64
4.3.6 Guckel ring measurements. A buckled Guckel ring with initial pre-released outer radius of 90 μm (a)3D Optical profilometry of the ring (a) Profile of the middle crossbar. 65
4.3.7 Optical profilometry of a film of polyimide and gold deposited on a silicon substrate. 65

5.2.1 Typical CCD camera image used for the alignment of input/output fiber tips to diffraction input/output gratings on the microchip. 69
5.2.2 Photo of the laboratory experimental setup. Main image is a close up of an electrically actuated sample sitting on a chip carrier and fed light via optic fibers suspended in brass fibre chucks. The inset shows an image of the optical station which includes the translation stages used to align the fiber optics to the sample. 70
5.3.1 Optical spectrum of the normalised output from a sample chip when using the supercontinuum light source as an input. Inset shows the output of the supercontinuum light source. 72
5.4.1 Colourized SEM image of the fabricated microbridge. 73
5.4.2 Measured 1585 nm laser optical power and displacement for the actuated microbridge with respect to time. 74
5.4.3 Measured 1585 nm optical power transmitted through the device for several vibration cycles of the suspended microbridge compared to 2-D FDTD simulation results as a function of the gap. 75

5.4.4 Measured 1550- 1585-, and 1610 nm optical power transmitted through the device for several vibration cycles of the suspended microbridge. Error bars show the extent of measured variation. The inset shows the gap for peak optical transmission shifting as a function of laser wavelength. 75
5.4.5 Measured optical power transmitted through the device for an actuation frequency sweep from 288-294 kHz. 76
5.5.1 SEM image of a microcantilever. Note that the optical waveguide does not appear in an SEM image as it is below the SiO_2 planarization layer. The dashed line is drawn on the image to indicate the position of the optical waveguide. 77
5.5.2 Optical surface profile of the microcantilever to be analysed. 78
5.5.3 Measured cantilever peak-to-peak displacement amplitude as a function of sinusoidal wave actuation voltage at the microcantilever's resonant frequency. 78
5.5.4 Transmitted optical power from grating ($\lambda = 1585$ nm) when the microcantilever is actuated with a sinusoidal signal of various voltage amplitudes at the microcantilever's resonant frequency. 79
5.5.5 Measured and FDTD simulated optical output of the device for a 1550 nm laser vs cantilever-grating gap. 80
5.5.6 Measured optical output of the device vs cantilever-grating gap for 1585 and 1610 nm light. Differing y-axis scales are used here due to the experimental setup having different coupling efficiencies for the various laser wavelengths tested. . . 80
5.5.7 Locus of points obtained by comparing measured 1550- and 1585 nm wavelength output power for matching cantilever positions as the cantilever beam travels from through its movement range. Each arm of the spiral represents approximately an 800 nm segment of the distance the cantilever oscillates through (indicated by both arrows and colour shading). 81
5.5.8 Measured optical response of the readout technique when the microcantilever is subjected to a frequency sweep from 1 to 100 kHz using sine wave actuation with a peak to peak voltage of 10 mV. 82
5.5.9 Measured optical response when a 200 μm microcantilever is actuated by a 5 V step at time $t = 0$ 84

6.1.1 3-D FDTD simulation of power transmitted as a function of cantilever grating separation for a diffraction grating 4 μm in width. The shot noise limited DND, DND_{sn}, calculated from Equation 6.15 over this separation range is also shown. The region where DND values are less than 25 fm/$\sqrt{\text{Hz}}$ is shaded, showing the operating ranges where DND can be kept below this level. 91
6.1.2 Calculation of DND components as a function of input laser power, P_{in}. For a 100 μm long cantilever, thermal-mechanical noise dominates for input optical powers above 50 μW. For a 50 μm long cantilever thermal-mechanical noise dominates for input optical powers above 0.6 mW. 93

6.2.1 Measured power transmitted through (top) the microbridge and (bottom) the microcantilever. The slope used as $\delta P_{out}/\delta z$ in the MDD and DND calculations is indicated (106 nW/nm for the microbridge, 14 nW/nm for the micocantilever). (Replotted data was first presented in Figures 5.4.3 and 5.5.5) . . . 95
6.2.2 Modeled normalized modal shapes of the cantilever for the first two vibration modes (Normalization is to the end deflection for each mode). The highlighted area represents the region of the cantilever that the diffraction grating is measuring. The outer circumference of the top hat anchor starts at -50 μm and ends at +50 μm along the x-axis, which is the starting point of the suspended beam of the cantilever. 96
6.2.3 Transmitted power through a grating beneath a thermo-mechanically excited cantilever and measured by the spectrum analyzer using a reserve bandwidth of 1 kHz. 97
6.2.4 Predicted Brownian noise envelope compared to measured optical power modulation from read-out device. A measurement of the noise of the laser when coupled through the chip is also presented. 99

7.2.1 Scanning electron micrograph of a fabricated, compact 70×60 μm^2 WDM based on arrayed waveguide grating technology [160]. 104
7.2.2 Schematic diagram of an optical feedforward compensation system shown to lower RIN to -160 dB/Hz [153]. 105
7.2.3 Isometric view of a proposed multiple interrogating grating structure. 106
7.2.4 Isometric view of a possible AFM implementation. 109

B.0.1 Splash screen of two minute thesis animation. 116

E.1.1 MEMS process flow. A MEMS cantilever is built by depositing and patterning several layers of various thin films. This figure does not include the step for the deposition of the electrostatic pads and wiring. 124

F.1.1 3D optical surface profilometry image of various MEMS devices. Idiosyncrasies of the measurement tool can be seen: the embedded Si waveguide appears to be above the substrate surface, and a ”curtain” effect in the region beneath suspended structures is visible. 130

If nature can do it, then so can we.

Acknowledgments

I would like to express my very great appreciation to my three supervisors, Professor John Dell, Professor Adrian Keating, and Professor Mariusz Martyniuk, as well as the head of our group Professor Lorenzo Faraone. Without your guidance and support, this thesis would not exist.

I wish also to acknowledge the help provided by Dr Roger Jeffery, who supplied good conversation and an excellent low-noise transimpedance amplifier.

Assistance provided by the Centre for Microscopy, Characterisation and Analysis was greatly appreciated, especially Asst/Prof Alexandra Suvorova and Peter Duncan, whose assistance with the SEM systems was extremely helpful.

Special thanks must go to all the members of the Microelectronics Research Group, especially Sabine Betts, I don't know how the group would function without you.

Finally, I would like to acknowledge the Australian Government, and The University of Western Australia for the opportunity to undertake the PhD program.

There's plenty of room at the bottom

Richard Feynman

1

Introduction

In 1963, Frank Wanlass filed a patent for complementary metal-oxide-semiconductor (CMOS) technology and sparked a revolution [1]. Over the last 50 years, transistors based on CMOS technology have become one of the most successful devices ever invented. This technology is so useful that the typical adult living in a developed country carries over 40 million semiconductor transistors in their pocket, and the current generation of personal computers contain over two billion semiconductor transistors in their CPUs alone [2]. The sheer ubiquity of these devices is possible because the invention of CMOS was in a large part responsible for instigating several decades of transistor miniaturization, causing cleanroom processes and techniques such as photolithography, thin film deposition and wet/dry etching to be continuously improved and refined.

Although these tools and techniques were funded and developed for applications in microelectronics, in the past couple of decades, they have been adopted by other fields, one of which is the manufacturing of incredibly tiny, mechanical moving parts which are integrated with, and complement electronics circuits. This class of devices is referred to as microelectromechanical systems (MEMS).

1.1 Microelectromechanical Systems

MEMS are typically characterized by having moving parts, and being made up of components between 1 to 100 μm in size. Generally, MEMS are fabricated using thin film technology, and tend to have a very large surface area to volume ratio. Therefore at this size, forces that scale by volume, such as gravity and inertia, are dominated by forces that scale by area, such as

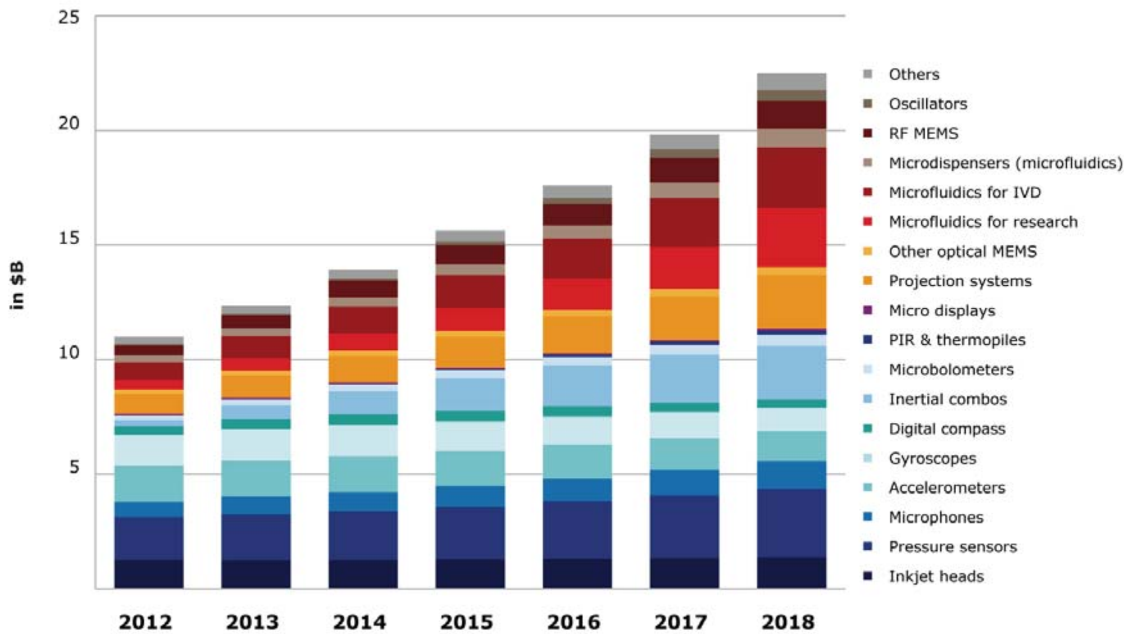

Figure 1.1.1: MEMS market forecast by devices. Source: http://www.i-micronews.com/reports/Status-MEMS-Industry-2013/1/384/

electrostatics or wetting.

Due to fatigue and creep issues, metals are generally not used as the structural material for the mechanical components of MEMS [3], although titanium substrates are being actively investigated [4, 5], and thermal management techniques have been successfully applied to overcome these issues in aluminium structures [6]. More typically, materials such as silicon (including both crystalline silicon and polysilicon), polymers, or ceramics such as silicon nitride and silicon carbide are used due to their more desirable mechanical properties. The resulting devices have been observed to be very robust, with lifetimes exceeding 100 billion switching cycles without failure and no significant degradation in performance [7].

1.1.1 MEMS Applications

The benefits of such small scale, robust devices are compelling, and so MEMS have been finding usefulness in many different applications. MEMS devices can generally be considered as belonging to one of three main classifications: sensors, actuators or structures. They have been used in many areas, including but not limited to: accelerometers in cars and portable electronics [8], lab-on-chip biological sensing [9], pressure sensors for applications in car tyres and blood [10, 11], and actuating mirror parts for pico projectors [12]. Based on current trends, the MEMS industry is expected to enjoy a compound annual growth rate (CAGR) of 13% over the next five years, becoming a $US22.5 billion market by 2018 (see Figure 1.1.1). The automotive tyre pressure monitoring system (TPMS) is perhaps the next major area which MEMS is set to have an impact worldwide [13].

Due to inherent similarities in the fabrication of MEMS and microelectronics, it is possible to retro-fit lower resolution microelectronics fabrication plants to produce MEMS. This has lowered the initial start-up costs for MEMS foundries, leading to a number of such foundries establishing a foothold over the last 10 years.

1.2 Silicon Photonics

A second field that has been burgeoning in recent decades is that of silicon photonics and micro-optics. The advent of the internet, and the public demand for high bandwidth content has led to a huge amount of activity researching high speed optical technologies required to support the fiber network. Additionally, the inexorable increase in CPU speeds for computing has led to companies such as Intel and IBM to overcome the data transmission bottlenecks limiting the next generations of computer processors [14, 15].

The intersection of these two fields - micro-optics and MEMS, has given rise to the new field of micro-opto-electro-mechanical systems (MOEMS). Applications of MOEMS include microbolometers, tunable VCSELs, and optical switches.

1.3 Thesis Overview

In this work a specific MOEMS device will be examined - more specifically, the behaviour of light travelling through a micro-optical cavity placed beneath a suspended MEMS structure will be investigated.

It will be found that amplitude modulation of light travelling through the microcavity is caused by movement of the MEMS structure, and provides an extremely sensitive measure of the position of that MEMS structure. Detecting the position of a MEMS structure with high sensitivity is a common problem for MEMS technology, and techniques to do this are necessary for applications ranging from chemical/biological sensing[16] to atomic force microscopy[17].

This thesis will be arranged as follows. Chapter 2 will provide an overview of the current state of the art MEMS sensor technologies that we are interested in, and provide some motivation for why new techniques are required to address the existing problems with the technology. Chapter 3 will describe the proposed solution to these issues, present a specific design for this solution, and perform extensive optical modeling of the design in order to determine whether it is appropriate technology for the task at hand. Chapter 4 will present a realization of the design using common silicon and MEMS fabrication technologies. A fabrication process will be designed and tuned to the task of making MEMS suitable to the needs of the experiments. Chapter 5 will describe the experimental measurement set-up, and present the measurement results obtained from operating the devices. Chapter 6 will analyse these results by first deriving calculations to determine the theoretical limits of detection of the device, and then applying these calculations to the measurements. Finally, Chapter 7 presents the conclusions that can be drawn from the analysis performed in this thesis, and sets out a listing of potential future work which would be of interest to pursue.

This work has been extremely successful, and has generated enough industry interest to fund the application of three international patents, which are currently in a status of pending [18–20]. A listing of publications arising from this thesis are provided in Appendix A.

Only he who can see the invisible can do the impossible.

Frank Gaines

2

MEMS Sensor Positioning Techniques

MEMS chemical and biological sensors have been recently shown to have the ability to measure mass with zepto-gram (10^{-21} g) sensitivity [21].

MEMS sensors are very robust, and generally do not respond to macroscopic, environmental vibrations. Due to their small size, many hundreds, if not thousands, of sensors can be placed on a single chip, providing the opportunity for improving detection statistics, thermal compensation and also the potential for multi-analyte testing - where different structures next to each other could be functionalized for different substances.

2.1 MEMS Sensor Operation Fundamentals

MEMS sensors are created by taking a MEMS structure - such as a cantilever or doubly clamped beam - coating it in an analyte which can preferentially bond to the substance that it is desirable to detect (this coating process is termed functionalization), and then watching that structure for a detection event. These sensors can be designed to operate in one of two main modes, designated in the literature as either static or dynamic mode.

2.1.1 Static Mode

If the substance being sensed bonds to a surface of a cantilever beam, the surface stresses occurring will cause that cantilever beam to bend. Monitoring the change of the cantilever position due to this bending gives an indication of whether a sensing event has occurred. In

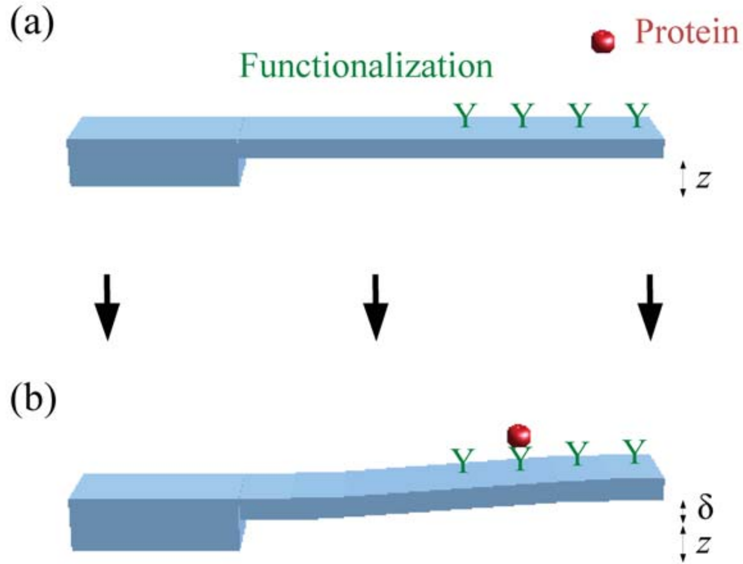

Figure 2.1.1: Example of the static mode operation of a MEMS cantilever protein sensor. (a) The micro-cantilever has been functionalized, but no detection event has yet occurred. The cantilever beam is flat, and the pre-detection surface stress of the beam is σ_1. In its normal state, the cantilever tip is a distance z above the substrate. (b) The protein has bonded to the functionalization layer, and the resulting surface stress, σ_2 has resulted in the elastic stretching of the surface, causing the cantilever beam to deform. As a result, the tip of the cantilever beam is now a distance of $z + \delta$ above the substrate.

aqueous environments, the bending due to surface stresses is approximately the same as bending in gaseous environments, so this technique can be used in both.

Static Mode Sensitivity

When changes to cantilever sensors interacting with their environment are primarily due to surface phenomena, the amount of bending due to surface stresses for a thin cantilever can be modeled by the Stoney equation [22]:

$$\frac{1}{R} = \frac{6(1 - \nu)}{Et^2}\sigma \tag{2.1}$$

where R is the radius of curvature of the cantilever, t is its thickness, σ is the differential surface stress (i.e. $\sigma_1 - \sigma_2$ where σ_1 and σ_2 are the surface stresses of the top and bottom layer respectively), ν is Poisson's ratio, and E is Young's modulus for the cantilever material.

The displacement of the tip of the cantilever, δ, is related to the radius of curvature, R, and length, L, of the cantilever by $1/R = 2\delta/L^2$. From this and the Stoney equation, the cantilever tip displacement as a function of the surface stress is:

$$\delta = \frac{3L^2(1 - \nu)}{Et^2}(\sigma_1 - \sigma_2) \tag{2.2}$$

Therefore to maximize sensitivity, this technique is best used with long, thin, and flexible (low Young's modulus and Poisson's ratio) cantilever beams.

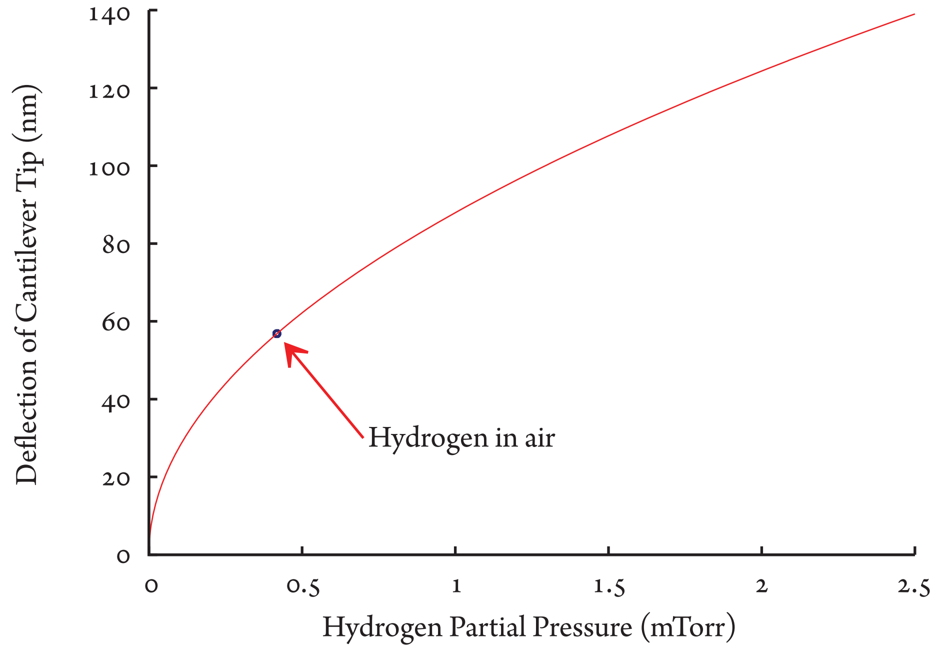

Figure 2.1.2: Deflection at the tip of a 100 μm long Pd/SiN$_x$ cantilever due to hydrogen absorption as predicted by Equation 2.3. The deflection due to hydrogen partial pressure in air is indicated.

Example: Palladium-coated Cantilever Sensor

Since palladium expands when absorbing hydrogen, an expression for the change in radius of curvature, R, of a cantilever coated on one side with palladium when exposed to hydrogen was derived by Okyama *et al.* [23]:

$$\frac{1}{R} = \frac{2\left(\Delta V/V_0\right) a_1 E_1}{K a_2^2 E_2} \sqrt{pH_2} \tag{2.3}$$

where pH_2 is the partial pressure of hydrogen in Torr, V_0 is the atomic volume of palladium, and ΔV is the characteristic volume change per hydrogen atom. The ratio $\Delta V/V_0$ in this situation is 0.19 [24]. The thicknesses of the palladium layer and the structural layer of the cantilever are a_1 and a_2, respectively. The Young's modulus of the palladium layer and the structural layer of the cantilever are E_1 and E_2 respectively. K is Sieverts's constant for the prediction of solubility of gases in metals [25]. For the case of hydrogen dissolving into palladium, $K = 49$ [23]. Note that Equation 2.3 is only a valid approximation for hydrogen partial pressures less than 30 Torr.

Figure 2.1.2 shows the deflection of a cantilever tip due to the absorption of hydrogen when we assume a 100 μm long, 750 nm thick silicon nitride cantilever (Young's modulus 150 GPa), coated with a 50 nm layer of palladium (Young's modulus 121 GPa [23]). It can be seen from this figure that the ability to sense nanometre deflections of the cantilever tip gives sub-mTorr sensitivity of the hydrogen partial pressure.

2.1.2 Dynamic Mode

All mechanical structures have a characteristic frequency that they prefer to vibrate at known as their resonant frequency, which is related to the mass, physical dimensions and other properties of that structure. For a MEMS sensor, when the substance being sensed bonds to the mechanical structure, the mass of the structure, and therefore the resonant frequency of the structure will change. This technique is best used with thick, rigid MEMS beams with high resonant frequencies. This technique is not particular effective in aqueous environments due to the damping that occurs, and so is best used in gas sensing applications.

Two other response parameters are also available for a micro-cantilever operating in dynamic mode - Q-factor and the amplitude of vibration [26]. In most cases, these parameters can be measured simultaneously with the frequency measurement.

Dynamic Mode Frequency Sensitivity

When the dimensions of a cantilever are known, its spring constant, k, can be calculated by [3]:

$$k = \frac{F}{\delta} = \frac{Ewt^3}{4L^3} \tag{2.4}$$

where E is the Young's modulus of the beam material, and w, t, and L are respectively the cantilever width, thickness and length. F is the force applied to the cantilever tip, and δ is the deflection from rest of the cantilever as defined in Figure 2.1.1.

The resonant frequency of the cantilever is [3]:

$$f_0 = \frac{1}{2\pi}\sqrt{\frac{k}{m_{eff}}} = \frac{1}{2\pi}\sqrt{\frac{Ewt^3}{4m_{eff}L^3}} \tag{2.5}$$

where m_{eff} is the effective mass of the cantilever beam. The effective mass of the cantilever is related to the mass of the cantilever, m_b by $m_{eff} = nm_b$, where n is a geometric parameter, equal to 0.24 for a cantilever beam of a rectangular cross-section [27].

MEMS sensors can be functionalized via a number of techniques, ranging from metal evaporation to dip pen nanolithography, depending on the functionalization coating required. The functional materials can be as simple as a palladium coating used for preferential absorption of hydrogen [28], or as complex as a specific peptide coating to adsorb a specific volatile organic compound for biological sensing [29].

If the cantilever is functionalized only in the region at the very tip, then adding a small mass m_d at the end of the cantilever will cause the total effective mass of the beam, m_t to become $m_t = m_{eff} + m_d$. In this case, the expression for the resonant frequency becomes:

$$f_0 = \frac{1}{2\pi}\sqrt{\frac{Ewt^3}{4m_tL^3}} = \frac{1}{2\pi}\sqrt{\frac{Ewt^3}{4L^3(m_d + 0.24wtL\rho)}} \tag{2.6}$$

where ρ is the density of the beam. The mass sensitivity, S_m, of such a device is defined by [3]:

$$S_m = \lim_{\Delta m \to 0} \frac{1}{f} \frac{\Delta f}{\Delta m} = \frac{1}{f} \frac{df}{dm} \tag{2.7}$$

For the case where the cantilever is functionalized only on the tip of the beam, S_m is defined by [3]:

$$S_m = \frac{-\xi}{2\rho(\xi t_d + 0.24t)} \tag{2.8}$$

where ξ is the fractional area coverage of the deposited mass, and t_d is the additional thickness of the deposited mass. Note the negative sign which indicates that the resonant frequency will decrease as mass is deposited.

When the cantilever is functionalized uniformly along the beam, S_m is given by [3]:

$$S_m = \frac{1}{\rho t} \tag{2.9}$$

Here the positive value of S_m indicates that as mass is deposited, the resonant frequency will increase. A useful figure of merit is the minimum detectable mass density (MDMD) which is defined by rearranging Equation 2.7 to:

$$MDMD = \Delta m_{min} = \frac{1}{S_m} \frac{\Delta f_{min}}{f} \tag{2.10}$$

where Δf_{min} is the minimum detectable frequency change by the readout system. A ratio for the minimum detectable frequency shift to operation frequency in modern electronics, $\Delta f_{min}/f$, is typically 2×10^{-7}.

Dynamic Mode Q-factor Sensitivity

The damping caused by the medium will effect the response of a cantilever around its resonance frequency. For systems with a large Reynolds number, and excitations that are much less than the cantilever length, it can be shown that the viscosity, η, of the medium that the cantilever is oscillating in can be given by [26]:

$$\eta = \frac{8k^2}{3\pi^2 R^4 n^2 \rho_f \omega^3 Q^2 (4 + 9/Q^2)} \tag{2.11}$$

where n and R are geometric factors which should be invariant for a given cantilever under any fluid and can be determined by fitting to the cantilever response data, ω is the frequency for maximum amplitude response of the cantilever, Q is the quality factor of the cantilever, k is the spring constant of the cantilever and ρ_f is the density of the fluid, and can be calculated by [26]:

$$\rho = \frac{3}{2\pi R^3} \left[\frac{4k}{\omega\,(4 + 9/Q^2)} - m_{eff} \right] \tag{2.12}$$

where m_{eff} is the effective mass of the cantilever.

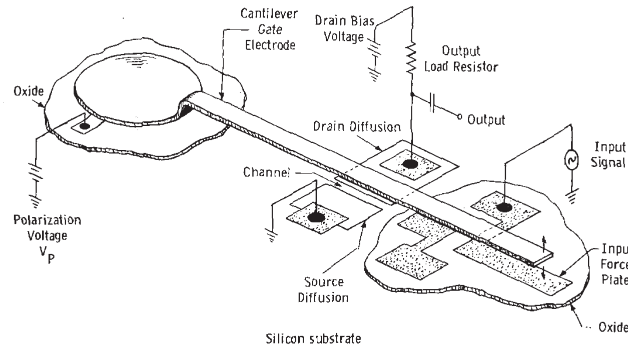

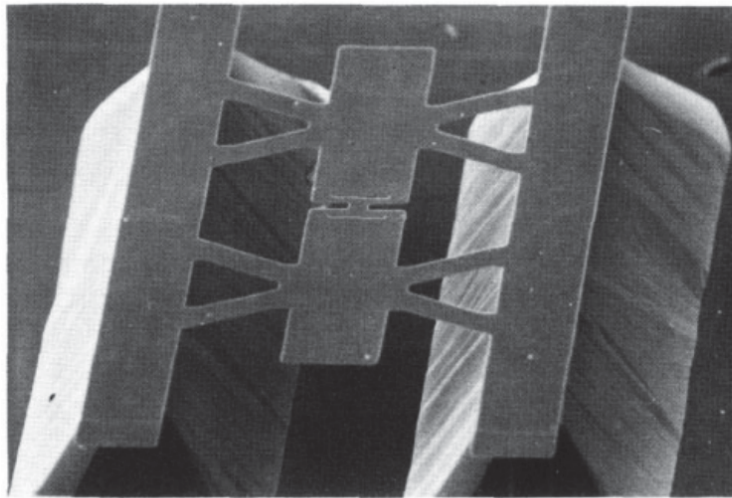

Figure 2.2.1: Two early implementation of free-standing MEMS structures. Top: Schematic of the resonant gate transistor fabricated by Nathanson *et al.* [31], and Bottom: the pressure sensor etched from a single silicon wafer by Greenwood [32]

Hence finding the Q of micro-cantilevers can be used for the sensitive measurement of viscosities of liquids.

2.2 MEMS Sensor Implementations

MEMS sensors provide such an attractive opportunity to create low-cost, highly accurate, miniature sensors that a substantial amount of work has been performed in this field. The first description of the use of a cantilever based chemical sensor was by Norton in a US patent named "Gas Analyzer" which was submitted in 1939, and accepted in 1943 [30]. In 1969, Shaver [28] refined this technique to demonstrate the detection of hydrogen at a sensitivity of 50 ppm by using large 100 mm long, 125 μm thick cantilevers.

At about the same time, in 1967, Nathanson *et al.* [31] presented the resonant gate transistor (shown in Figure 2.2.1(top)). This was a suspended gold microbridge which could be electrostatically actuated. It was not intended as a sensor, but rather a high Q frequency selection device, and it's sensitivity to temperature was seen to be an issue to be overcome, rather than a feature.

In 1969, Greenwood [33] noticed that certain of his silicon samples showed preferential etching in different regions when immersed in an ethylene diamine-catechol water mixture. Just over a decade later in 1983, even though the exact mechanism of this preferential etching was still undetermined [34], Greenwood used a similar etching technique to create a free-standing resonant pressure sensor from a silicon wafer (Figure 2.2.1(bottom)) [32]. As they were made from crystalline silicon, the resonators had *Q*s of approximately ten thousand in vacuum. Electrostatic actuation was used to drive the resonator, and the change in resonant frequency as a function of air pressure was successfully demonstrated.

A couple of years later, in 1986, Howe and Muller demonstrated a resonant microbridge xylene vapor sensor by depositing a polymer film (in this case a negative photoresist) on a poly-silicon microbridge [35, 36].

The potential of these devices was starting to become apparent, one of the requirements of an effective MEMS dynamic mode sensor would be a high *Q* factor, and so in 1990, Buser and Rooij fabricated a very high *Q* resonator from monocrystalline silicon, measuring a *Q* factor of 600 000 in a vacuum [37]. They fabricated the device by etching the silicon in 40% KOH with a SiO_2 mask in a technique that was later to be named bulk micromachining.

Also in 1990, Hetrick [38] demonstrated a vibrating cantilever mass flow sensor. The proposed application was to create the ability to measure the mass flow of incoming air at the intake of a fuel-injected internal combustion engine in order to maintain the correct balance of air to fuel. The increasing mass flow had the effect of damping the blade and so by measuring the change in *Q*, a sensitive measure of mass flow could be made.

Over the years, MEMS-based vibration sensors [39], high frequency ultrasonic imaging [40] and high-resolution accelerometers [41] have also been demonstrated.

2.2.1 Heat Sensing

One of the first truly impressive results obtained by cantilever sensors was in the arena of heat sensing. It has long been known that the bending of the tip of a bilayer beam, *z*, can be predicted by [42]:

$$z = \frac{5}{4} \frac{(t_1 + t_2)\, l^3}{4\,(\lambda_1 t_1 + \lambda_2 t_2)\, w t_2^2} \cdot \frac{(\alpha_1 - \alpha_2)\,(dQ/dt)}{4\,(1 + t_1^2/t_2^2) + 1/t_1 t_2\,(6t_1^2 + E_1 t_2^2/E_2) + E_1 t_1^3/E_2 t_2^3} \tag{2.13}$$

where dQ/dt is the incident heat energy; l and w are the length and width of the beam, respectively; t_1 and t_2 are the thicknesses of the two layers; and λ_1, λ_2, α_1, α_2, and E_1, E_2 are the thermal conductivities, thermal expansion coefficients, and Young's moduli of elasticity of the two layers; respectively.

In 1994, Barnes *et al.* [43] used the bending of an aluminium and silicon nitride cantilever bilayer to demonstrate femtojoule heat sensitivity. This was a landmark result, as the device provided a power sensitivity two orders of magnitude better than that of the best technique of the time: photothermal deflection spectroscopy. Subsequently, Gimzewski *et al.* [44] then used

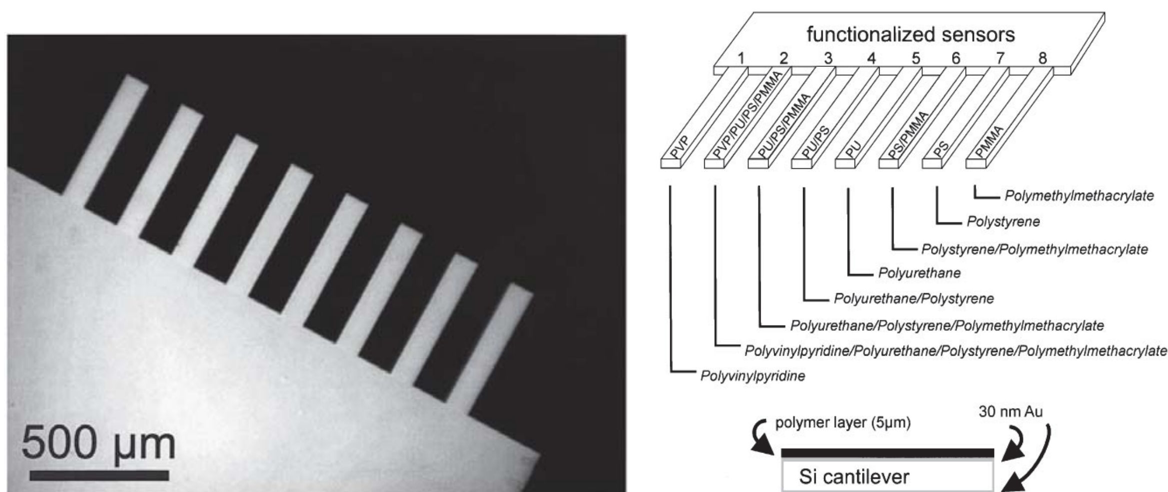

Figure 2.2.2: An early implementation of a cantilever sensor array. Left: SEM image of the microcantilever sensor array prior to the deposition of sensor coatings [45], and Right: schematic view of the polymer coatings used for the eight cantilevers [46]

this technique to observe the catalytic conversion of hydrogen and oxygen to water over a thin platinum catalyst.

2.2.2 Chemical and Biological Sensing

The proven sensitivity of these devices triggered a large research effort into other sensing applications. The addition of a chemistry specific functionalization layer turned micro-cantilevers into effective chemical and biological sensors for any number of species. Before long, several groups had demonstrated the sensing of simple chemicals, and then moved towards applying this technique to more complex biological samples.

Thundat *et al.* performed work demonstrating the detection of relative humidity [27], mercury vapour [16], toulene and mercaptans [26]. Once again, these approaches showed incredibly sensitive results. The frequency response of the mercury vapour cantilever sensor was shown to be 11 pg/Hz, and even in an unoptimized experimental setup, the minimum detection level of the mercaptans was 50 parts per billion (ppb).

Due to the ease of mass fabrication of MEMS devices, arrays of cantilever beams on chips were soon implemented. Many cantilevers were desired in order to give better detection statistics, the ability for simultaneous multianalyte sensing, and the provision of reference cantilevers which were not functionalized to provide a measure of thermal drift. At the turn of the millenium, several research groups demonstrated such arrays with up to eight cantilever sensors on a single device [45–47]. An example of such an array is shown in Figure 2.2.2.

The range of chemicals these devices could sense is only limited by the ability of chemists to find specific functionalization layers [29, 48]. Therefore, soon MEMS sensors were demonstrated to be able to detect many different types of chemicals, ranging from explosives such as TNT and RDX [49], or pesticides such as DDT [50]. MEMS sensors were also shown to be able to perform medical tasks such as the rapid detection of bacterial resistance to

antibiotics [51], diagnosing head and neck cancer through the analysis of breath [52] or detecting skin cancer melanomas [53]. It is predicted that this last technique can be applied to other cancers such as gastrointestinal stromal tumours and lung cancer [54].

Gas sensing was not the only considered application. Substantial work was also performed analysing the behaviour of micro-cantilever beams in viscous fluids [55], and Nieradka *et al.* [56] have demonstrated micro-cantilever sensors operating immersed in a liquid cell. Burg [57] demonstrated the weighing of biomolecules, single cells and single nanoparticles in fluid flowing through a micro-channel embedded in a MEMS cantilever beam. This ability has given rise to a strong, new field, dubbed *nanomicrobiology* [58].

2.3 Read-out methods

Critical to the operation of this type of sensor is the method of detecting the height change (for static mode) or motion (for dynamic mode) of the MEMS beam to determine whether a detection event has occurred. Less critical, but still eminently desirable is the ability to address large numbers of MEMS beams, giving the aforementioned benefits.

A large number of MEMS sensor read-out techniques have been demonstrated over the past twenty years. These can be classed as either optical or electronic techniques. Generally speaking, optical techniques have far higher resolution than electronic techniques, yet electronic techniques are capable of addressing far larger numbers of cantilevers than optical techniques. Optical techniques have the additional benefit of being able to operate in fluidic environments. This section will discuss these read-out techniques, and cover the exceptions to these generalizations.

2.3.1 Optical Techniques

In 1986, Binning, Quate, and Gerber [17] announced the invention of the atomic force microscope (AFM), a feat for which they were awarded a Nobel Prize. This device is essentially a micro-cantilever with a sharp point on the tip, which builds up the profile of a surface by moving the cantilever over the scanned surface in relation to each other, and watching the way in which the tip of the micro-cantilever responds to the surface. Thus it is unsurprising that when read-out techniques were required for micro-cantilever sensors, the first techniques examined were those that had previously been invented for the AFM.

Several optical techniques have been designed for use with MEMS sensors. Some are adaptations of AFM-like read-out techniques, whereas some have been designed with the integrated addressing of large arrays of sensors in mind.

Optical Beam Deflection

In 1988, Meyer and Amer [59] demonstrated the use of light being reflected from the cantilever tip to a distant position sensitive detector (PSD) as a read-out technique for AFM. It was this

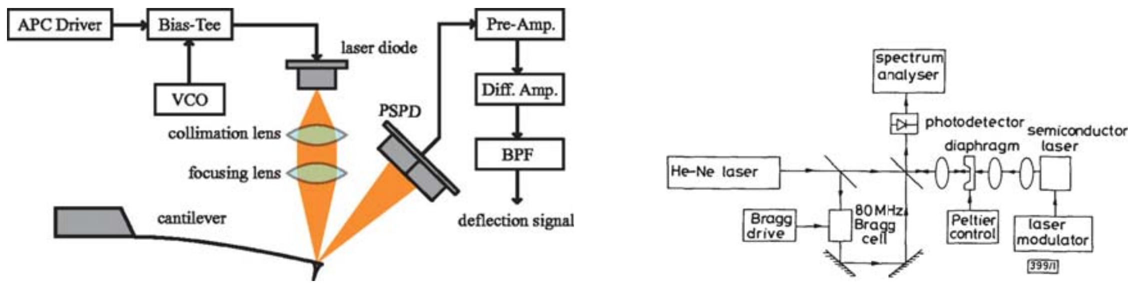

Figure 2.3.1: Schematics of external optical read-out techniques. Left: Fukuma's position sensitive detector technique [63], and Right: Thornton's external optical interferometer technique [64]

technique that was then used as an incredibly sensitive read-out for much of the early work in MEMS sensing [16, 26, 27, 43].

Subsequently, this technique was extended to a small linear array of eight cantilevers [60]. The cantilevers were spaced at a pitch of 250 μm. These cantilevers were aligned to a fiber-optic ribbon of eight multimode fibers (also at a pitch of 250 μm) which shone 644 nm light onto the tips of each individual cantilever in the array. This light is then reflected onto a single PSD, to infer the bending of the cantilever. A quasi-simultaneous read-out can be obtained by time multiplexing: i.e. switching the individual light sources on and off for each cantilever.

Alvarez *et al.* [61] presented a modification of the above PSD technique, rather than using several light sources, only one scanning laser source was used, and moved the laser beam sequentially over the tips of five micro-cantilevers to again provide a quasi-simultaneous time-multiplexed cantilever position measurement. This technique provided sub-angstrom resolution, and was used to demonstrate the detection of single-stranded DNA.

In an attempt to remove the time-multiplexing requirement, and hence increase the time resolution of PSD read-outs of micro-cantilever arrays for sensing, Nieradka *et al.* [62] demonstrated a truly simultaneous array read-out method using an expanded beam deflection method (EBD). This involves using lenses to expand a beam to become wide enough to encompass the cantilever beams to be read, and then reading the reflections simultaneously. This was demonstrated for arrays of up to four cantilevers. The authors demonstrated that in the case of the two cantilever array the sensitivity was limited only by the thermal noise of the 500 μm long, 100 μm wide cantilever beams.

In a drive to achieve the highest possible position resolution, Fukuma *et al.* paid particular attention to the removal of noise at each step of the measurement system, and were able to reduce noise to the point where they achieved a deflection noise density (DND) of 16.7 fm/$\sqrt{\text{Hz}}$ [63]. As this technique was designed for AFM, the experimental set-up used only one micro-cantilever. A schematic of this design is shown in Figure 2.3.1 (left).

External Optical Interferometry

To improve the sensitivity of the read-out to the ultimate optical limits possible, interferometric techniques were applied to the problem. As early as 1986, Thornton *et al.* [64] measured the

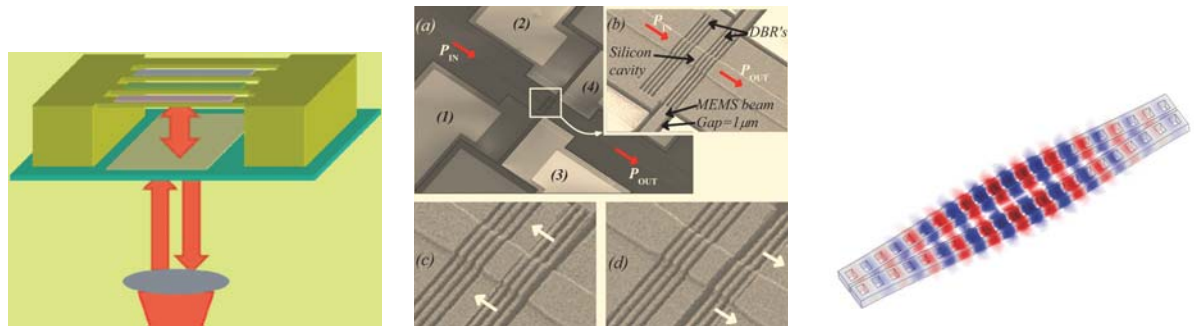

Figure 2.3.2: Various integrated micro-cavity read-out techniques. Left: Schematic of microharp technique. Optical power is fed to the differently functionalized microbridges, and an optical micro-cavity is formed between the substrate and the reflective microbridge [69]. Center: SEM of the Preussner *et al.* in plane micro-cavity. Light is fed along a silicon waveguide, and the etched DBR grating can be actuated to the left (c) or right (d) either shortening or lengthening the cavity [70]. Right: Eichenfield *et al.* zipper cavity. Mechanical motion of the zipper cavity nanobeams changes the transmitted optical intensity through the phase modulation of the internal cavity field [71]

vibrations of thin silicon diaphragms using a He-Ne laser as a light source for a free space optical heterodyne interferometer (Figure 2.3.1(right)).

In the following year, 1987, Andres *et al.* [65] improved on this method, making it potentially more practical for the field by using a fibre interferometer to remove the free space optical components. This technique was used to successfully measure the vibration of suspended silicon structures, and study the feasibility of using such a device as an accelerometer [66].

In 2005, Helm *et al.* [67] used a white light phase shifting interferometric technique map micro-cantilever deflection over it's length to within 2 nm resolution, with a lateral resolution of 2 μm. The interference pattern this generates along the length of the micro-cantilever can be useful for applications that require an extremely accurate measurement of the radius of curvature, rather than just the height movement of the tip.

Schonenberger and Alvarado [68] implemented a differential interferometer read-out system for a micro-cantilever which achieved a DND of 6 fm/$\sqrt{\text{Hz}}$. To date, this remains the highest sensitivity attained using an external optical technique.

Integrated Micro-cavities

Whilst external interferometers can provide extremely high sensitivity, they are extremely difficult to align to the MEMS devices being tested, and as such, are not conducive to the addressing of large arrays of MEMS sensors. There is a strong desire to keep the high sensitivity that optically resonant techniques such as interferometry provide, while adding the ability to address multiple devices. To this end, several research groups have attempted to integrate optical micro-cavities into the sensor design, and so gain these capabilities.

A strong attempt in this direction was performed by Stievater *et al.* [72, 73] using a microcavity interferometric technique. This technique involves fabricating a reflective microbridge over a reflective substrate, forming a hi-Q optical microcavity, then aligning a fibre

optic light source directly above the microbridge. The amount of light that reflects back from the microcavity into the fibre optic is strongly related to the height of the microbridge above the substrate. This technique has the added advantage of being able to use a second laser, fed by the same fibre, to excite the microbridge into movement photothermally.

The group extended the technique to create a photonic microharp array [69]. Here, multiple microbridges of varying lengths (and hence resonant frequencies) are arranged so that they all receive light from the same fibre. If the resonant frequencies of each microbridge are spaced sufficiently far apart, then they all can be interrogated with the same laser. As this technique is all-optical, i.e. both actuation and measurement of the beams are performed optically, it is proposed that the technique could be used with multiple-quantum-well retroreflectors designed for free-space data links to create wireless line-of-site sensors operated from up to 1 km away [74, 75].

An alternative to the concept of an out-of-plane optical microcavity such as that described above is an in-plane optical microcavity. Pruessner *et al.* [70] created one implementation of this by etching a distributed Bragg reflector (DBR) into a silicon waveguide running to a MEMS beam. A Fabry-Pérot microcavity was created within a silicon waveguide by etching two DBRs consisting of suspended Si and air gaps in-plane with the optical waveguide. When the MEMS beam is actuated laterally, the movement of the DBR either lengthens or shortens the Fabry-Pérot microcavity, and provides a method for the sensitive measurement of the movement of the MEMS beam. This technique was shown to have a DND better than 10 fm/$\sqrt{\text{Hz}}$.

A second in-plane microcavity technique is that of Eichenfield *et al.* [71]. Here a zipper optical cavity was formed from side by side mechanical beams fabricated from silicon nitride. A high-efficiency optical-fibre-taper coupler is run alongside these beams to couple light into and back out of the beams to perform optical measurements of their position. This technique was able to measure nanometre-scale movements of the beams, and was used to measure mass changes of a picogram.

Microdisk Resonators

Whispering-gallery modes [79] are a phenomenon where waves travel repetitively around a concave surface. The recent ability to fabricate microdisks that support resonance of optical wavelengths has led to a large amount of research in this field. As might be expected, microdisks have been used in several schemes to detect the movement of MEMS beams, with a view towards sensing. These schemes rely on the MEMS beam interacting with the evanescent optical field emanating from the microdisk. Microdisk schemes are integrated on-chip and so can generally be expanded to measure large arrays of beams with extremely good sensitivity.

In 2011, Srinivasan *et al.* [76] presented an integrated silicon cantilever probe using a microdisk resonator fed by fibre taper waveguides as the read-out (Figure 2.3.3(i)). This technique requires the cantilever be separated from the microdisk by a nanoscale gap (less than 250 nm), and has been used to measure thermally driven vibrations of the cantilever which

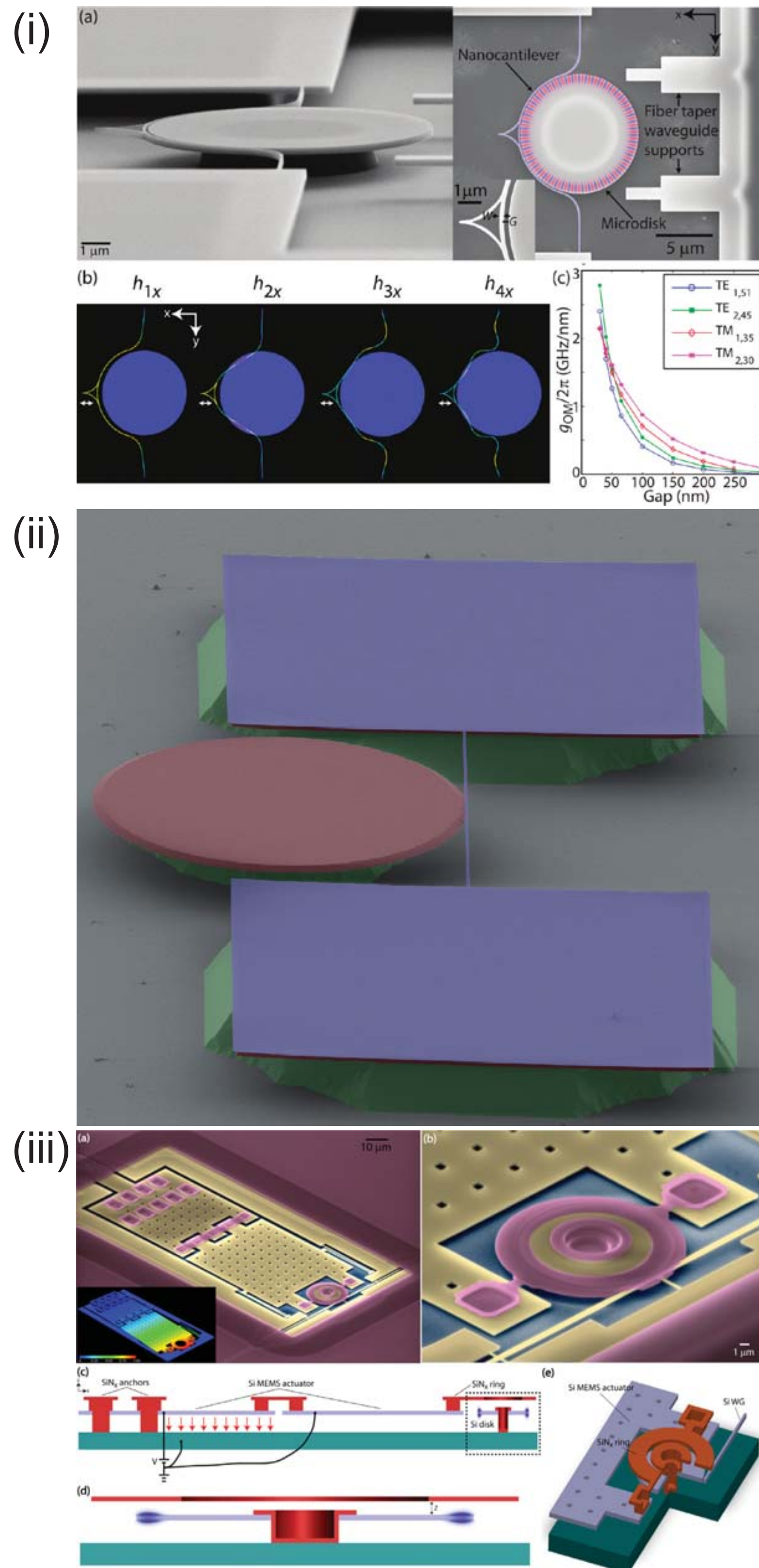

Figure 2.3.3: Various integrated micro-disk read-out techniques. (i) Srinivasan *et al.* microdisk coupled to a nanocantilever [76]. (ii) Colourized SEM of the microdisk system fabricated by Gavartin *et al.* This system consists of a doubly clamped, high-stress Si_3N_4 nanomechanical beam (blue) coupled via the near-field to a silica microdisk resonator (red). Both the resonator and the pads holding the beam rest on silicon pedestals (green) [77]. (iii) Micro-disk technique demonstrated by Miao *et al.* [78].

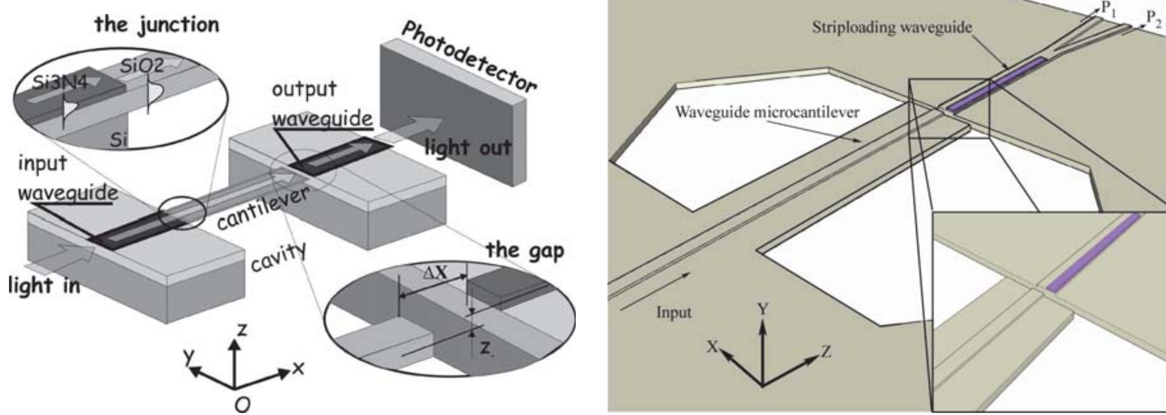

Figure 2.3.4: Schematics of two cantilever as waveguide techniques. Left: Zinoviev *et al.* system [80]. Right: Noh *et al.* differential output system [81].

showed that the read-out had a DND sensitivity of 440 am/$\sqrt{\text{Hz}}$.

In the following year, 2012, Gavartin *et al.* [77] used a silica microdisk coupled to silicon nitride beam to demonstrate a force sensitivity of 74 aN/$\sqrt{\text{Hz}}$ at room temperature (Figure 2.3.3(ii)). By cooling the chip using dissipative opto-mechanical feedback, they were able to improve this technique to measure forces with a sensitivity of 15 aN/$\sqrt{\text{Hz}}$, which is 25 times less than the thermal noise that would otherwise be present in the beam.

In the same year, Miao *et al.* [78] fully integrated a high-*Q* cavity optomechanical position sensor into an electrostatically actuated MEMS device (Figure 2.3.3(iii)). They demonstrated a DND sensitivity of 4.6 fm/$\sqrt{\text{Hz}}$, corresponding to a force sensitivity of 53 aN/$\sqrt{\text{Hz}}$ while using only 250 nW optical power.

Cantilever as a Waveguide

A concept that has gained a fair amount of traction as a read-out system is that of using a cantilever as a waveguide. These read-out techniques provide high sensitivity, and because they are integrated into the cantilever, and can be implemented in such a way to address large arrays of microcantilevers. The cantilever as a waveguide system consists of an input waveguide leading into the microcantilever on the anchor end, and having an output waveguide aligned to the free end of the microcantilever. As the cantilever is actuated up and down, the amount of light coupled into the output waveguide changes. This technique requires extremely good control of fabrication stresses, as otherwise the cantilever may not be aligned with the output waveguide upon release.

Zinoviev *et al.* [80] demonstrated an array of 20 waveguide/cantilever channels using silicon nitride and silicon dioxide, and was able to measure displacement with a DND of 18 fm/$\sqrt{\text{Hz}}$ (Figure 2.3.4(left)). This is very close to the sensitivity of external optical systems, while demonstrating simultaneous displacement measurements of twice as many cantilevers that had previously been demonstrated using PSD techniques [46]. Silicon nitride was used as the input/output waveguide material as the thermally grown silicon dioxide did not make a good

total internal reflection waveguide when layered on a silicon substrate. Due to stress issues when attempting to fabricate a silicon nitride cantilever, silicon dioxide was used as the cantilever material (the silicon dioxide was a good waveguide when completely surrounded by air). The cantilevers were 500 nm thick, and the end displacement was measured over a range of 350 nm.

A similar system was demonstrated by Nordstrom *et al.* [82]. The cantilever and the input waveguides were fabricated using the polymer SU-8, successfully allowing a single material to be used for both. By making the cantilever 4.5 μm thick, the group was able to increase the dynamic range to 9 μm.

Koev *et al.* [83] took the cantilever as a waveguide technique, and immersed it in a liquid sample in order to show the detection of enzymatically produced homocysteine. Until this point, the cantilever as a waveguide technique had only been demonstrated in air. The proof of the ability for this technique to operate in aqueous solutions was extremely important for many chemical and biological sensing applications. The minimum detectable displacement (MDD) in this system was 5 nm.

In order to attempt to improve the sensitivity of this system further, Noh *et al.* made the output waveguide an asymmetrical multimode waveguide which terminated in a Y-branch [81]. They then used these Y-branch outputs to form a differential signal for measuring the micro-cantilever deflection (Figure 2.3.4(right)). They measured an MDD of 350 pm, but believe that improving the detectors and electronics to reach the shot noise limit would improve the MDD to 54 pm.

Other Optical Techniques

There are a number of other notable optical techniques which have been considered in the past few years. These will be discussed here.

In 2005, Kocabas and Aydinli also designed a cantilever with an integrated waveguide, but introduced a Bragg grating to act as a photo-elastic strain sensor at the point where the cantilever is expected to flex to the greatest degree [87]. The light reflected back from the end of the waveguide can then be measured to determine cantilever displacement. To the best of my knowledge, they did not publish a demonstration of this technique, however, in 2010, Carpenter *et al.* fabricated an extremely similar device, demonstrating a four-cantilever array made from glass microcantilevers containing Bragg gratings [88]. In 2012, this group enhanced the technique by adding a second Bragg grating to the waveguide feeding the cantilever (Figure 2.3.5(top)), forming a Fabry-Pérot interferometer [84]. This cavity technique improved the sensitivity of the read-out by an order of magnitude, making the smallest resolvable force 264 nN.

Iannuzzi *et al.* demonstrated hydrogen detection using a fiber-top cantilever [85]. A microcantilever was etched into the end of a optic fiber, then coated with a palladium functionalization layer (Figure 2.3.5(bottom left)). Laser light was launched into the optic fiber, and the reflection back was measured. Accordingly, sub-nanometre displacements of the

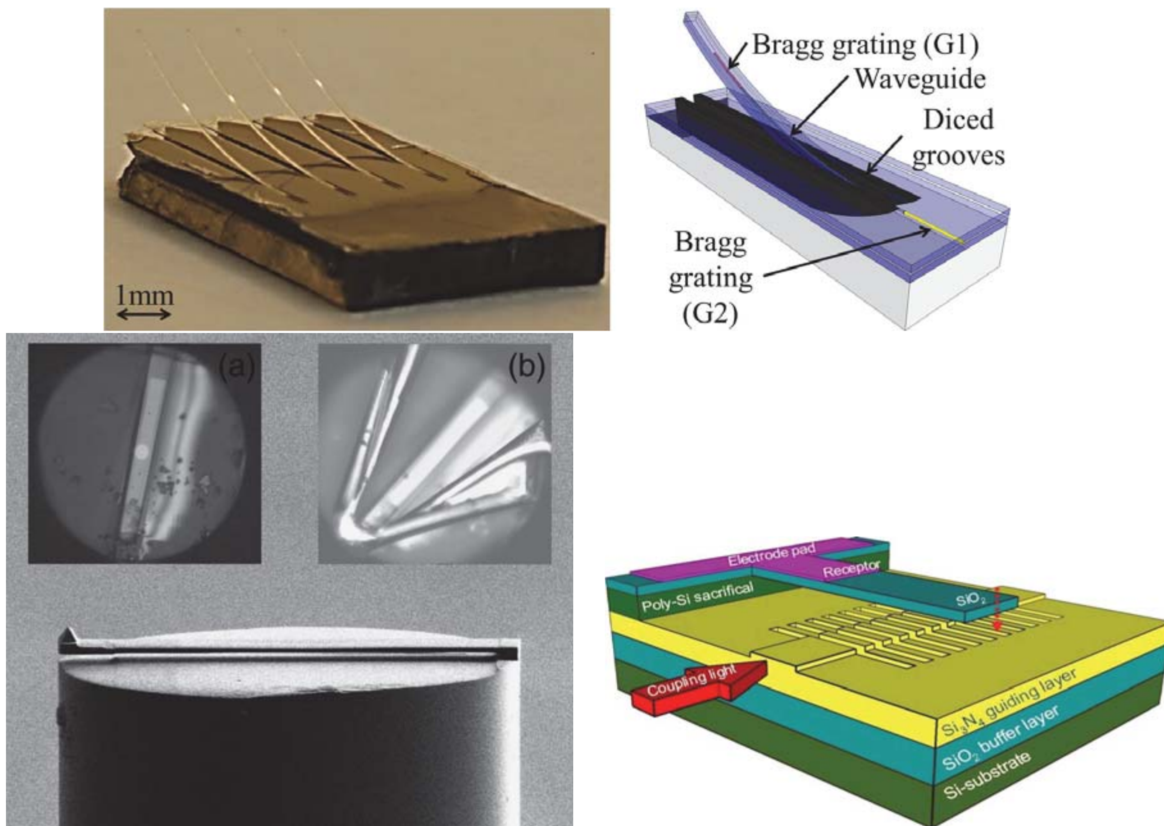

Figure 2.3.5: Implementation of miscellaneous optical readout techniques. Top: Photo and schematic of Carpenter *et al.* double Bragg grating technique [84]. Bottom Left: Iannuzzi fiber top cantilever [85]. Bottom Right: Schematic of Pham *et al.* grated waveguide evanescent field technique [86].

cantilever can be measured using this technique.

Pham *et al.* [86, 89] demonstrated an evanescent field technique. By etching gratings into a slab waveguide, the evanescent field travelling along the waveguide was extended enough such that a dielectric cantilever could interact with the field (Figure 2.3.5(bottom right)). It was demonstrated that movement of the cantilever over a range of 400 nm above the grated waveguide would effect the output optical transmission spectra.

Graphene has outstanding mechanical, electrical and optical properties, and multilayer graphene containing several tens of atomic layers of carbon is sufficiently stiff to produce freestanding cantilevers [90]. Reserbat-Plantey *et al.* [91] took advantage of these properties to create multilayer graphene cantilevers which acted as multilayer mirrors, and allowed them to implement a read-out technique combining Fizeau interferometry and Raman spectroscopy. The strength of the coupling between the Raman peak shift and the cantilever displacement had a maximum sensitivity of 1×10^{17} Hz m^{-1}, which, in terms of resolution, makes it very close to the quantum limit [92].

2.3.2 Electronic Techniques

Although optical techniques are able to determine sensitivity with extremely high precision, to date, they have been limited in the number of MEMS devices they can address simultaneously. Chips containing up to one thousand cantilevers have been fabricated [93], and multiple applications can benefit from the ability to address this many cantilevers on a single chip, even if the positional resolution is lower than that achievable by optical methods. In addition, electronic interrogation is cost effective and well established, however, it cannot be used in areas of strong EM fields or in hazardous environments where there are ignition risks [84]. In aqueous/electrolyte environments, ions in the solution tend to cause parasitic currents that can overwhelm the electric signal [94]. The work performed in this area of electronic interrogation is discussed further in this section.

Piezoresistive Techniques

Perhaps the most widely used and hence successful electronic readout technique for MEMS cantilever based chemical sensing is that utilizing piezoresistance [95], that is, a resistance change in the deflecting MEMS structure due to an applied mechanical load (Figure 2.3.6(top left)).

In 1990, Boustra demonstrated a mass flow controller based on a resonating microbridge built from a polysilicon film doped with phosphorus. Changes in the atomic spacing caused when actuation deforms the structure effects the bandgap and therefore modifies the conductivity/resistivity of the polysilicon microbridge [98].

Using gold films 30 nm in thickness deposited onto silicon carbide cantilevers, Li *et al.* [99] were able to obtain a piezoelectric effect based on the change in geometry of the metal caused by mechanical movement. Using this technique, the group was able to obtain a DND sensitivity of

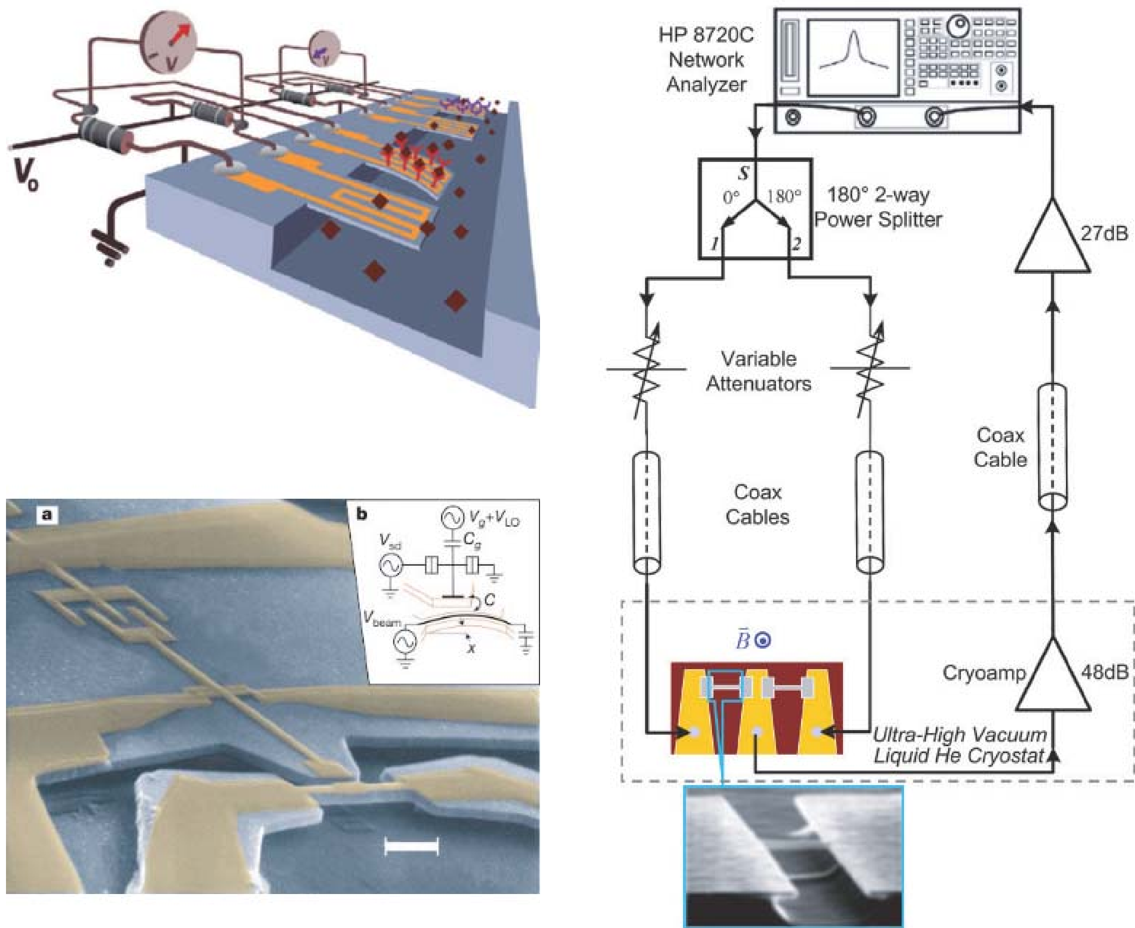

Figure 2.3.6: Various electronic read-out systems: Top Left: Schematic of piezoresistance array technique [95]. Right: Schematic and SEM of Huang *et al.* magnetomotive technique [96]. Bottom Left: Knobel *et al.* single electron transistor [97]. The scale bar represents 1 μm

39 fm/$\sqrt{\text{Hz}}$, which gave them a sub-attogram mass resolution for chemical sensing measurements in air at room temperature.

Arrays of piezoresistive cantilevers are now commercially available, and in 2008, Loui *et al.* [100] took four-cantilever chips manufactured by Cantion A/S, functionalized them, and used them to perform measurements of a wide range of chemicals, including the chemical warfare agents VX and sulfur mustard.

Piezoelectric Techniques

Piezoelectric materials such as zinc oxide will generate transient charge currents when their structure is deformed. In 1996, Lee and White [101] demonstrated a piezoelectric cantilever device formed from a zinc oxide piezoelectric thin film sandwiched between two aluminium layers on a supporting layer of silicon nitride. They were able to demonstrate its use as a highly sensitive microphone.

A major disadvantage of the piezoelectric technique is that to obtain large output signals, the thickness of the piezoelectric film must be well above the thickness that is desired for flexible cantilevers, and so application of piezoelectric readouts to MEMS sensors is somewhat limited [94]. Additionally, since the transient currents are only generated when the beam is moving, this technique is unsuitable for static mode sensors.

Capacitative Techniques

An alternative electronic technique is to measure the capacitance between the MEMS beam and the substrate of the chip. Since the capacitance of two metal plates is inversely proportional to the distance between them, this should theoretically have the advantage over piezoelectric methods in that it can be used to provide absolute displacement and so be a simple method for measuring the movement of MEMS.

In practice, the large parasitic capacitance of the devices make it difficult to perform energy-efficient, real-time readouts without the use of complex FPGA circuitry [102]. The capacitance technique is not suited to measure large displacements, and does not work well in electrolyte solutions because of the Faradaic currents that exist between the capacitor plates [103].

Other Electronic Techniques

Some of the other notable electronic techniques are described here.

A 20 zeptogram (zg) real time noise floor was demonstrated by Yang *et al.* [21]. The best mass resolution they achieved was 7 zg - the equivalent of 30 xenon atoms. The read-out technique used was to create a magnetic field and place the microbridges such that they were laid out perpendicular to the field lines (Figure 2.3.6(right)) [96]. The movement of the beams can then be measured by means of magnetomotive transduction. Venstra and Zant [104] later extended this magnetomotive technique to be able to discriminate individual resonators in a six device, 2D array.

Knobel and Cleland [97] demonstrated perhaps the most sensitive electronic read-out system to date, achieving a DND sensitivity of 2 fm/$\sqrt{\text{Hz}}$ by using a single-electron transistor (Figure 2.3.6(bottom left)). This is an ultrasensitive, potentially quantum-limited displacement sensor. This result was obtained by operating the device at a temperature of 30 mK and in an 8 Tesla magnetic field.

2.4 Chapter Conclusions and Thesis Objectives

MEMS chemical and biological sensing systems show a huge potential for applications requiring the detection of trace amounts of specific substances. To a very real extent, the efficacy of the technology has been proven, but currently there is a gap in the ability to read the state of a large array of MEMS sensors. There has been a great amount of research into technologies for performing the measurements of the microscopic mechanical sensor movement. These technologies include the use of a large range of both optical and electronic techniques. The optical techniques developed for atomic force microscopy are incredibly sensitive, however can only be adapted to test small numbers of cantilevers. Electronic techniques based on effects such as piezoresistance or capacitance can easily address many hundreds of devices, but do not have the sensitivity of the optical techniques, and can have issues in various non-standard environments. The most sensitive electronic techniques available rely on the use of large magnetic fields, and can not be expanded to address large arrays.

For multiplexed and massively parallel detection of analytes, the MEMS sensing technique requires signal-detection approaches that are compatible with parallel and efficient signal detection and amplification [54]. Therefore, next generation read-out techniques are being researched to provide this capability. Some of the next generation optical techniques being studied by groups around the world include the use of cantilevers as waveguides, and optical microdisks. These techniques come closer to the requirements desired for effective MEMS sensors.

An additional ability desirable for MEMS cantilever sensors operating in static mode is the ability to quickly determine the cantilever shape. Techniques which rely on measuring the tip of the cantilever suffer from the disadvantage of needing to wait for the cantilever to arrive at a steady state after an adsorption event before a measurement can be taken. A technique which could measure the deformation in the cantilever the instant the adsorption event occurs would have the benefit of providing a much faster sensing turnaround.

In this thesis, I will present and analyze a novel read-out technique applicable to both MEMS cantilevers and microbridges. This technique will have extremely high sensitivity, a large measurement range, the ability to address large arrays of cantilevers, should operate in various environmental conditions, be relatively easy to fabricate using silicon and CMOS compatible technologies, can measure sensors operation in either the static or dynamic mode, and will be tolerant to the variations in MEMS properties that can arise due to the issues caused by MEMS processing drift.

Lasers... a solution looking for a problem.

Irnee D'Haenens

3
Theory of Operation

When boiled down to essentials, the solution proposed to the problems described in the previous chapter is a novel technique for measuring the distance between two surfaces with very high accuracy. This chapter analyses this technique using MEMS beams, however, in theory, the technique can be used on any two suitable surfaces. The technique to read-out the height position of the micromachined beams is based on forming an optical cavity between the underside of the micromachined beam, and an optical waveguide incorporating a diffraction grating underneath the beam. The diffraction grating couples light out of the waveguide and light reflected from the micromachined beam back into the waveguide. This chapter describes the technique, uses simulations to validate the suitability of the technique for the problem at hand, and discusses the physical design parameters of the device.

3.1 Physical Description of Device

Figure 3.1.1 shows an isometric view of the microsystem. In sensing applications, the doubly clamped beam or cantilever (shown) would change it's height or mechanical resonance frequency in response to an absorbed analyte. To sense such changes, an optically resonant cavity is created when a micromachined beam with a reflective undersurface is suspended above a diffraction grating etched into a waveguide. The diffraction grating will be designed to be efficient for light in the mid-infrared. Very effective waveguides for 1550 nm light can be fabricated using SOI wafer, and lasers at the wavelength are cheaply available due to their ubiquitous use in optical telecommunications. When infra-red light travels through the silicon waveguide, the grating will diffract some of the light out of the waveguide towards the

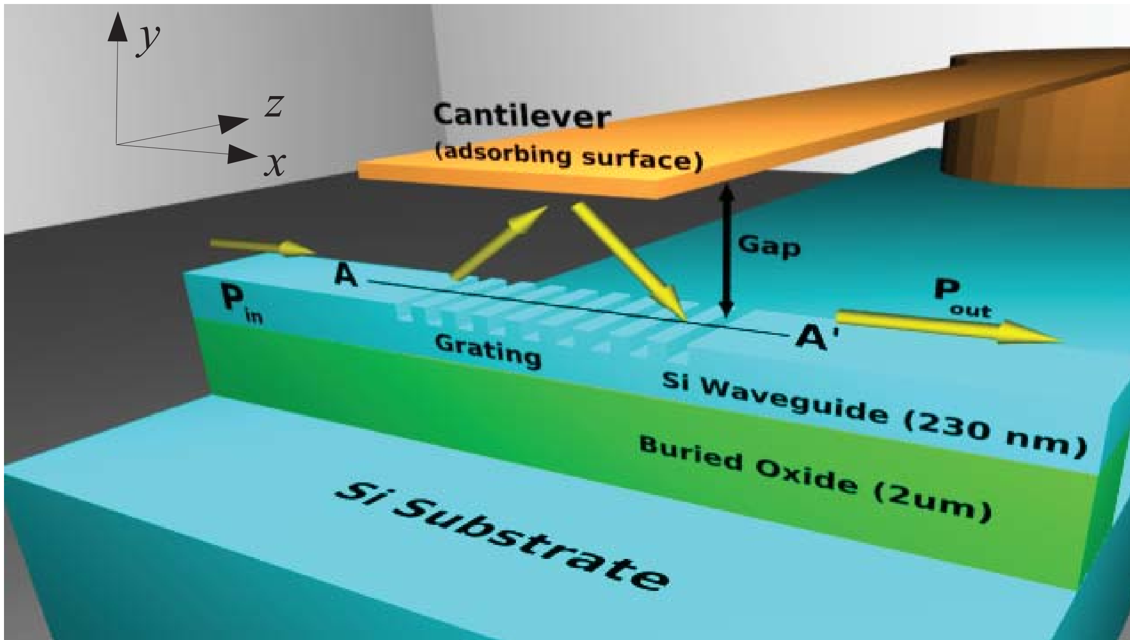

Figure 3.1.1: Isometric view of the proposed interrogating grating structure (not to scale).

micromachined beam. The mirror on the micromachined beam will reflect the light back towards the grating. The recombination of the remaining light in the waveguide with the reflected light leads to constructive and destructive interference in the light out of the waveguide, creating an interferometer. As a result, the intensity of the light travelling through the waveguide is amplitude modulated by movement of the micromachined beam (due to interferometer path length change).

Superficially, the grating and cantilever arrangement used in this technique appears similar to the technique of Pham *et al.* [86], however, the technique of Pham *et al.* relies on a dielectric cantilever interacting with the evanescent optical field leaking from the grating, while it will be seen that the technique discussed in this work uses a reflective cantilever over a directional grating coupler to form a optically resonant microcavity. Among other things, this means that the technique which is the subject of this work can operate over substantially larger ranges than is possible in a technique which relies on near-field optics.

The entire opto-mechanical interaction occurs over the volume defined by the waveguide and cantilever, assuming 50 μm long, 10 μm wide cantilevers that are a height of 2 μm above the substrate, this is a volume of 1000 μm^3. Over a sensor area of 1 cm^2, and assuming a fill factor of 50%, this technique can readily be extended to the interrogation of 10^5 micro-cantilever sensors. Subsequently, wavelength, time or spatial multiplexing of these signals could allow them to be coupled into a single output optical fiber, allowing the signals to be transmitted over exceptionally long distances [105], although arrays are outside of the scope of this work.

Figure 3.1.2 shows a cross-section of the full device through the line A'A indicated in Figure 3.1.1. Light is launched into the silicon waveguide via an input grating coupler (not shown in Figure 3.1.1). The grating couplers were designed to be broadband and have optimized coupling efficiency for light at a wavelength of 1550 nm. They were built to the same dimensions and

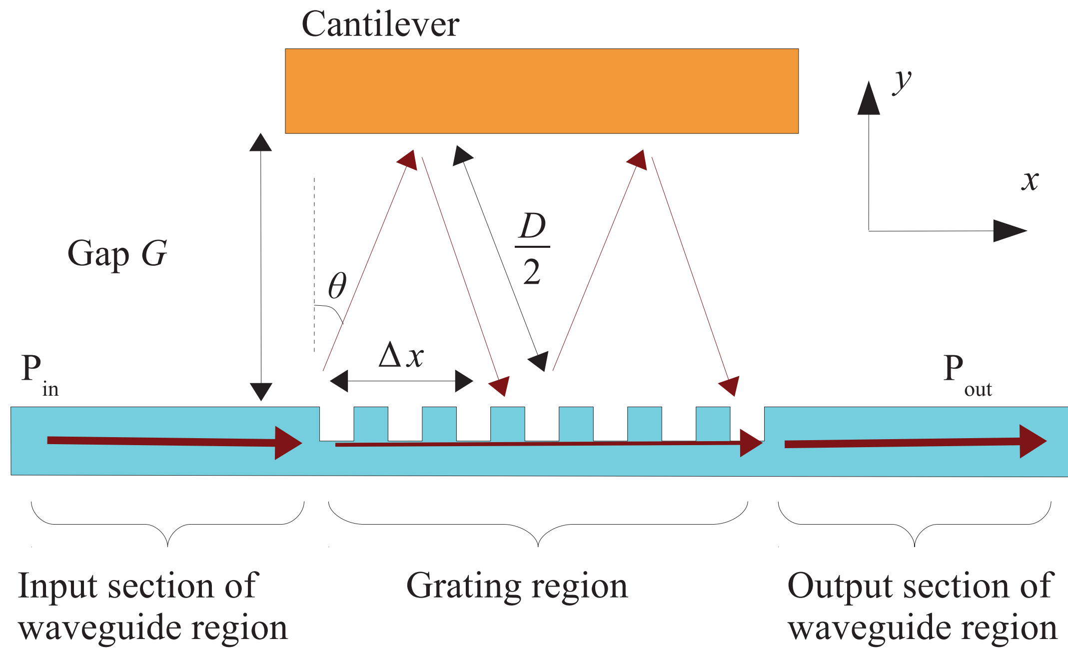

Figure 3.1.2: Cross-section of the full device through A'A from Figure 3.1.1

specifications as the grating in silicon-on-insulator (SOI) with oxide top cladding analysed by Taillaert *et al.* [106]. The light modulated by the interferometer is coupled out by an output grating coupler. By detecting the optical power, a sensitive measure of the beam deflection can be obtained.

In this chapter, the transmission of an optical signal through the waveguide is analyzed to understand how modulation of the transmitted optical power is induced by a deflecting micro-cantilever. In Chapter 6, these results will be used to estimate the theoretical noise inherent to this technique when applied to measurement of the deflection of a micro-cantilever.

In the approach illustrated in Figure 3.1.1, some of the optical power (P_{in}) of the waveguided input signal is coupled out of the waveguide by a diffraction grating positioned directly below a micro-cantilever. The reflective underside of the cantilever and the air-silicon waveguide grating form a resonant optical cavity in which the cantilever acts as a moveable high reflectivity mirror, while the grating acts as an angle and wavelength dependent mirror creating a structure similar to an angled Fabry-Pérot cavity. As a result of the resonance effects in the cavity, the amount of input light (P_{in}) coupled into the output section(P_{out}) of the waveguide is a sensitive function of the separation between the grating and the cantilever. Just how sensitive is the subject of this chapter's theoretical study.

3.2 Modeling methodology

Project feasibility initially required an understanding of whether the resonant effect would be strong enough to fabricate a usable device, and secondly, what design constraints and

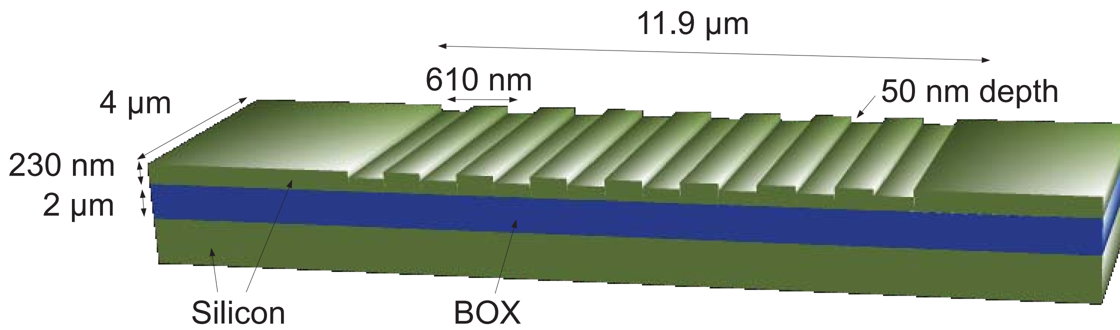

Figure 3.2.1: Isometric diagram of the modeled diffraction grating implemented in SOI wafer (not to scale). The SOI wafer is made up of a 230 nm thick epitaxial silicon layer, 2 μm thick BOX layer, and silicon handle layer. It is proposed that the grating is etched into the epitaxial silicon and has a pitch of 610 nm, depth 50 nm, length 11.9 μm, and width 4μm.

parameters would effect device design. To this end, the optical considerations of the design were analysed by undertaking two and three dimensional electromagnetic modeling of the structure using the Meep finite difference time domain (FDTD) package [107]. The model was based on a SOI platform for the optical waveguide/grating structure, which consisted of a 230 nm epitaxial silicon layer for the waveguide, 2000 nm thick buried oxide (BOX) for the bottom cladding layer, and a silicon handle wafer as the base. The waveguides are designed to be single mode in the *y*-direction perpendicular to the plane of the substrate and multimode in the *z*-direction (*x*, *y*, and *z* directions are defined in Figure 3.1.1). SOI photonic structures have the advantage of being a relatively well developed technology. Further, silicon provides very strong optical guiding so that minimal evanescent field coupling will occur, reducing crosstalk and leakage where the approach is utilized with large sensor arrays where waveguides need to be closely spaced. The grating utilized is a square-wave grating of 610 nm pitch, 50 nm depth and 11.9 μm length, and, in the absence of the cantilever structure, is an efficient waveguide output coupler [106]. This reference grating is shown in Figure 3.2.1. Some modifications to this basic grating design will also be discussed. The bottom surface of the suspended cantilever is assumed to be a perfect reflector at the wavelength of interest (1550 nm), and extend 1 μm beyond the interrogating grating on all sides. Further discussion of cantilever fabrication is found in Chapter 4.

In the FDTD model, a transverse electric (TE) polarized Gaussian beam was launched into the waveguide. The diffraction grating was placed a sufficient distance away (8 μm) from the source so that a stable propagating optical mode was incident on the grating section of the waveguide. The cross-section used to determine the optical power only contains the waveguide, so that substrate modes and small evanescent field contributions are not included in the power calculations.

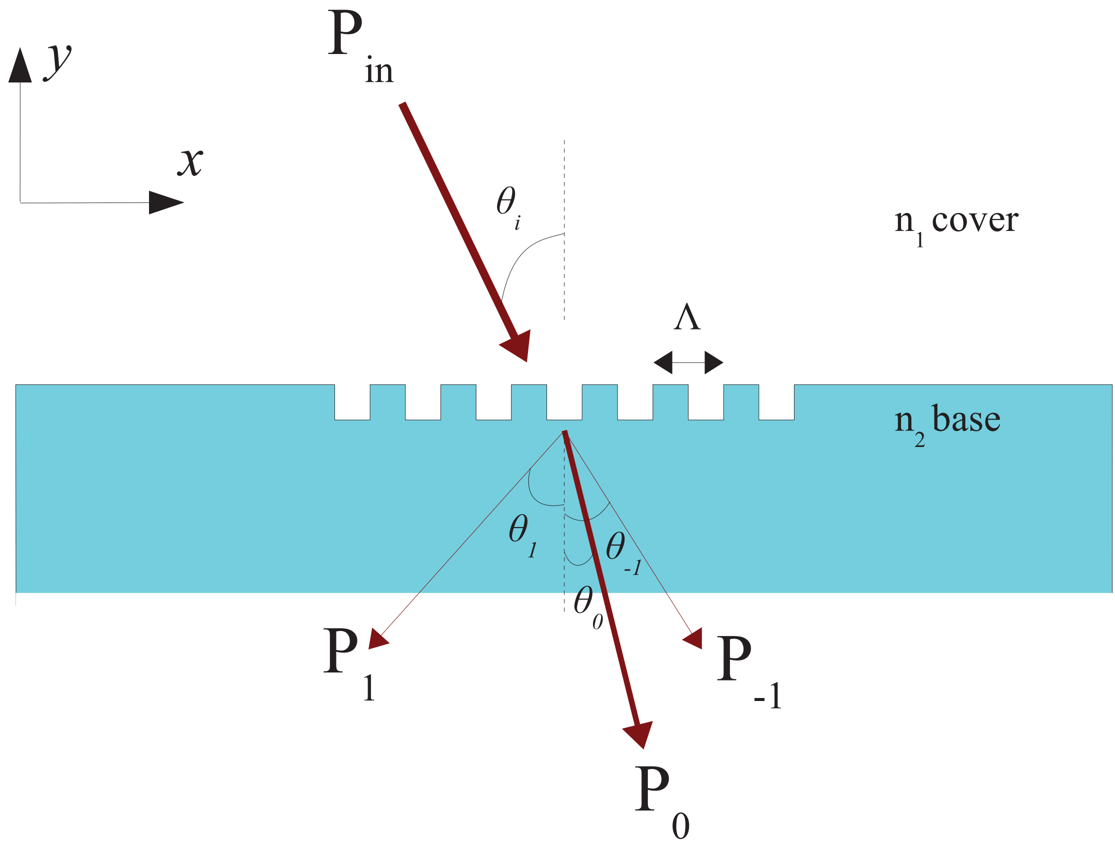

Figure 3.3.1: Ray diagram of light travelling at an angle of incidence, θ_i from the normal, passing from one medium (with refractive index n_1) through a grating with pitch Λ into an second medium (refractive index n_2). The light is diffracted at the grating and the rays of power P_m radiating at angles θ_m for the orders $m = -1, 0, 1$ of diffraction are shown.

3.3 Diffraction Grating Couplers - Background Theory

The use of dielectric "wires" as a tool for the conduction of electromagnetic waves was first discussed by Hondros and Dubye in 1910 [108]. However, thin film waveguides were not exhaustively studied until the field of integrated optics arose in the 1970's [109]. The Smart-Cut process patented in the late 1990's by Srikrishnan [110] provides a technique of manufacturing high quality SOI wafer, the epitaxial silicon layer of this wafer is an excellent medium for the conduction of electromagnetic waves to use for integrated optics.

Coupling light into waveguides made of a thin film is a problem that has achieved much attention. Schemes based on prism couplers [111], end-fire coupling [112], and diffraction grating couplers [113] have all been studied comprehensively. For the purposes of this work, diffraction gratings were chosen as the technique to couple light into the waveguides. The two main reasons for this were that (a) the input/output diffraction grating couplers could be fabricated at the same time using the same process as the interrogating grating, and (b) grating couplers are substantially easier to align and couple light into than end-fire couplers.

Grimaldi first recorded accurate observations of diffraction in 1665, and coined the latin term

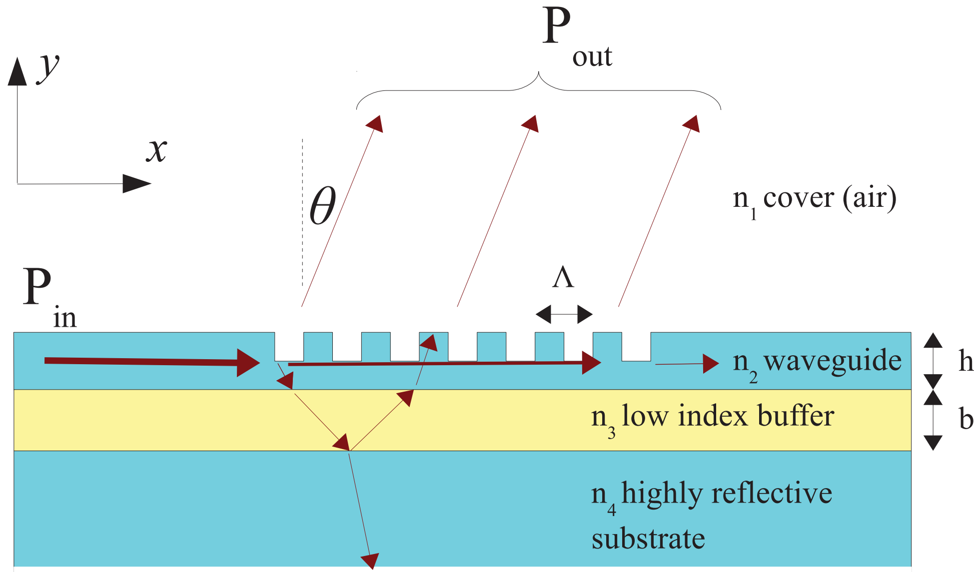

Figure 3.3.2: Slab waveguide grating structure on top of a high reflectivity substrate [117]. Light travelling in the waveguide in a guided mode (P_{in}) is coupled by the grating towards both the cover and the substrate. The light travelling towards the substrate passes through a low refractive index buffer which forms a highly reflective interface with the substrate. When this structure is well designed, the majority of light will reflect back from the substrate to join the light leaving the grating (P_{out}). Some light will be lost through the substrate, and, depending on the efficiency of the grating, a portion of light will continue to travel through the substrate. θ is the angle that the light leaves the grating. n_1, n_2, n_3, and n_4 are the refractive indices of the cover region, waveguide, low index buffer, and substrate respectively. Λ is the pitch of the grating, h is the thickness of the waveguide layer, and b is the thickness of the low index buffer layer.

"diffractionem" for the phenomena [114]. 120 years later Rittenhouse created the first man-made diffraction grating by stringing hairs between two screws [115].

If a plane wave of wavelength λ is incident on a diffraction grating of pitch Λ an angle of θ_i, diffracted light will have maxima at angles θ_m which can be estimated by the grating equation [116]:

$$n_1 \sin \theta_i + n_2 \sin \theta_m = \frac{m\lambda}{\Lambda} \tag{3.1}$$

where n_1 is the refractive index of the medium the light is arriving from, n_2 is the refractive index of the medium the light is travelling into, and m is the propagation-mode of interest. A ray diagram demonstrating the diffraction predicted by this equation is shown in Figure 3.3.2.

Dakss *et al.* initially proposed a diffraction grating coupler in 1970, designed to use the ability of gratings to bend light in order to couple light into a slab waveguide [113]. Over the years, the efficiency of this coupler has been improved by the addition of a third, reflective substrate layer [118], and through the tuning of various parameters to enhance performance [119]. An example of the three layer style of diffraction grating used in this study is shown in Figure 3.3.2. In this image, the case of light leaving the waveguide is shown. Such a grating is very easy to implement in silicon-based integrated optics [120]. The performance of this style of grating structure can be calculated numerically using the rigorous coupled-wave analysis (RCWA)

technique first presented by Moharam and Gaylord [121], via FDTD simulations of Maxwell's equations [107], or a number of other techniques [122].

3.4 Calculation of maxima and minima

Two optical paths are considered in the analysis of the proposed structure shown in Figure 3.1.2. The first optical path is that of the light which is diffracted out of the waveguide, travels through the medium of the gap, is reflected off the cantilever, and diffracted back into the waveguide.

The optical length of this path, L_d, can be expressed as a function of the cantilever-grating separation G by:

$$L_d = n_{gap} D = \frac{2 n_{gap} G}{\cos\theta} \tag{3.2}$$

where θ is the angle at which light is launched from the diffraction grating, and n_{gap} is the refractive index of the gap medium. The parameter D is the physical length of the path the light follows. In this approximation the small grating depth is ignored.

The second optical path is that of the light which remains in the waveguide up until the point that the light following the first path returns to the grating. This path length, L_r, can be expressed as a function of G by:

$$L_r = n_{eff} \Delta x = 2 n_{eff} G \tan\theta \tag{3.3}$$

where n_{eff} is the effective refractive index of the waveguide grating, and Δx is the physical length that the light remaining in the grating travels between the points where the diffracted light leaves and re-enters the grating.

The amount of light in the waveguide downstream of the grating will be a function of the difference in the optical lengths of these two paths. When the optical path difference is a multiple of $\lambda/2$, then either maximum or minimum transmission of light will occur. Within the grating, this condition occurs when:

$$\frac{m\lambda}{2 n_{eff}} = L_d - L_r = \frac{2 n_{gap} G}{\cos\theta} - 2 n_{eff} G \tan\theta \tag{3.4}$$

where λ is wavelength, and m is an integer counting instances of $\lambda/2$ difference.

Rearranging Equation 3.4 for the grating-cantilever separation G gives:

$$G = \frac{m\lambda}{4 n_{eff} \left(n_{gap} \sec\theta - n_{eff} \tan\theta \right)} \tag{3.5}$$

The angle θ for the described diffraction grating structure used in the modeling here is 13.6° in air. The effective refractive index of the grating section for the fundamental TE mode of waveguide is 2.83 [106]. The effective refractive index is only 1.89 for the fundamental transverse magnetic (TM) mode, making the coupler strongly polarization selective [106]. Therefore, we will not consider the TM case in this work. Assuming an air gap, and using these

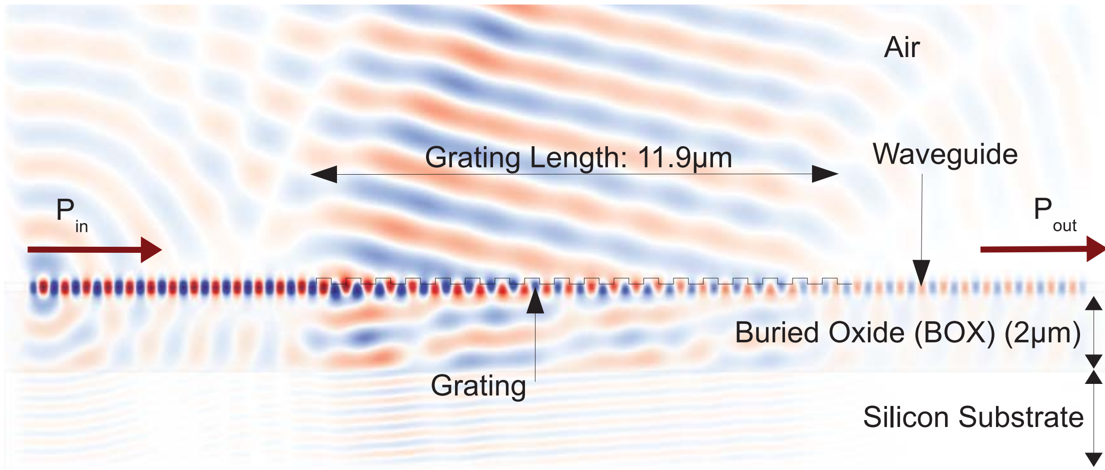

Figure 3.5.1: Modeled results at $\lambda = 1550$ nm for a SOI waveguide 230 nm thick with a grating of pitch 610 nm, depth 50 nm, and length 11.9 μm. Calculated TE field distributions through section A'A in Figure 3.1.1 for the case where there is no cantilever. Blue represents positive intensity, red represents negative.

structure parameters, maximal and minimal power transmission will occur at intervals of $\Delta G = 0.26\lambda$, which at a wavelength of 1550 nm, corresponds to gap changes of 400 nm.

3.5 FDTD simulations

3.5.1 Transverse Electric Field Distributions

The FDTD simulations performed to understand the transmission characteristics of the light as the cantilever deflects are described here. Figure 3.5.1 shows the optical TE field distribution arising from a 1550 nm input laser of a cross- section of the proposed device in the *x*-*y* plane of Figure 3.1.1, when the cantilever does not exist. It can be seen that at the end of the grating, most of the light that was travelling in the waveguide has been coupled out of the waveguide plane. Numerical values from this simulation predict that the flux through the waveguide at the output of a 11.9 μm grating is only 8.18% of the flux through the input waveguide.

The loss parameter α of a diffraction grating is defined as [123]:

$$\frac{dE(x)}{dx} = -\alpha E(x) \tag{3.6}$$

This is related to the power in the waveguide after length L along the grating by:

$$P(L) = P_0 e^{-2\alpha L} \tag{3.7}$$

Using this equation, the loss parameter α for an 11.9 μm long grating at 1550 nm can be calculated to be 0.11 μm^{-1}. Figure 3.5.2 shows the values of this parameter for the wavelength range from 1340 to 1830 nm. This grating design is quite broadband around 1500 nm. For example, over the range for a typical Erbium doped fibre amplifier, wavelength varies only from

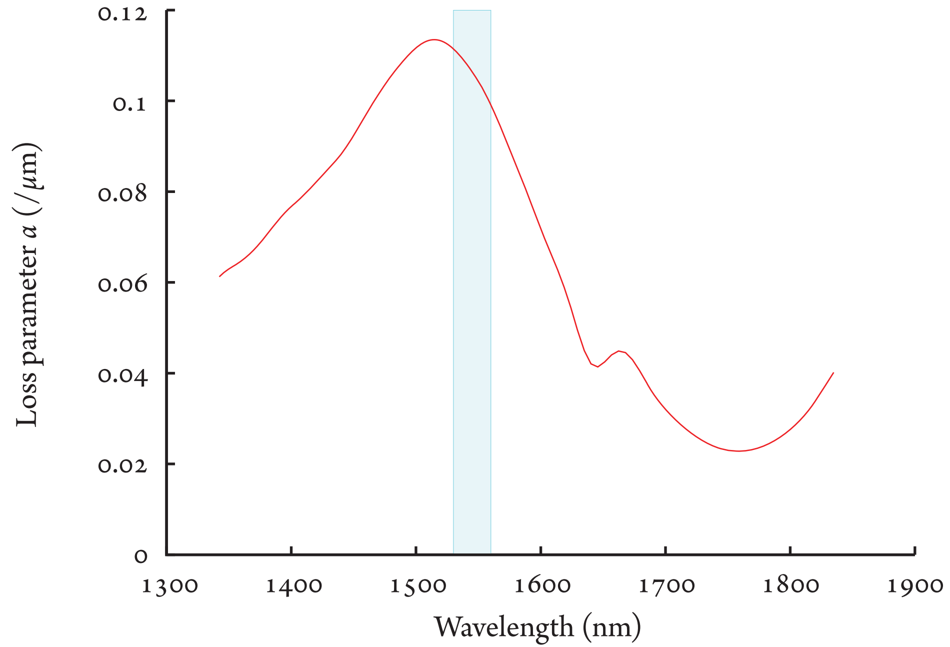

Figure 3.5.2: Modeled results of the loss parameter α for the wavelength range 1340-1830 nm. Shaded area represents the wavelength range of an erbium doped fiber amplifier.

1530-1560 nm.

Figure 3.5.3 shows the optical TE field distribution of a cross-section of the proposed device in the x-y plane of Figure 3.1.1, when the cantilever arm is at the height required to create constructive interference for the input wavelength of λ = 1550 nm ($m = 2$). It can be seen that most of the optical power stays within the waveguide, and that a large amount of power is diffracted into the cavity between the cantilever and grating. The code to generate this simulation using the Meep package is supplied in Appendix D.

Figure 3.5.4 shows the TE distribution when the cantilever arm is at the height required for destructive interference ($m = 3$). When compared to Figure 3.5.3, it can be seen that for the case of Figure 3.5.4, most of the light dissipates into the substrate, so that by the end of the grating, there is very little light left travelling through the waveguide. While not discussed here, the light transmitted into the substrate may provide an alternate detection method for this structure using a buried detector, substrate detector, or another grating waveguide structure.

3.5.2 Optical Power simulations

The amplitude modulated optical power leaving the output waveguide can be used to determine the height position of the cantilever. Here the FDTD simulated output power for various scenarios are presented in order to determine whether this technique will be at least theoretically possible. Figure 3.5.5 shows the calculated transmitted power as a function of the cantilever-grating separation for a grating 11.9 μm long, and 4 μm in width. As predicted by Equation 3.5, the transmitted light is modulated with a period of Λ = 800 nm. The extinction is defined as the difference between the maximum and minimum transmitted optical power. It can

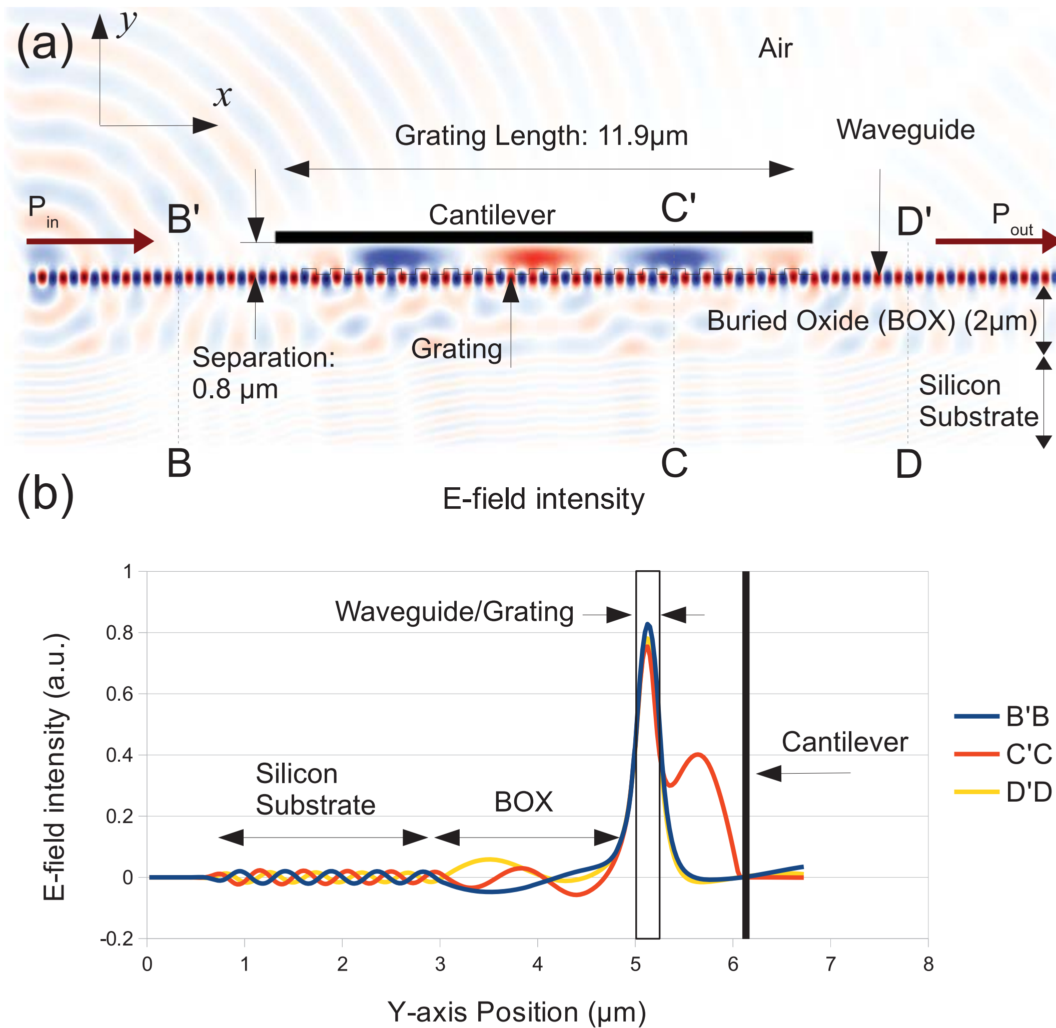

Figure 3.5.3: Modeled results at $\lambda = 1550$ nm for a cantilever with a perfect reflector over a SOI waveguide 230 nm thick. The grating has pitch 630 nm and is 11.9 μm long. Calculated TE field distributions through section A'A in Figure 3.1.1 with a separation of 0.8 μm. This separation gives maximum transmitted power. (a) The TE field strength overlain over the structure. (b) Plot of the TE field intensity through sections B'B, C'C, and D'D, which represent points of interest before the grating, along the grating and after the grating respectively.

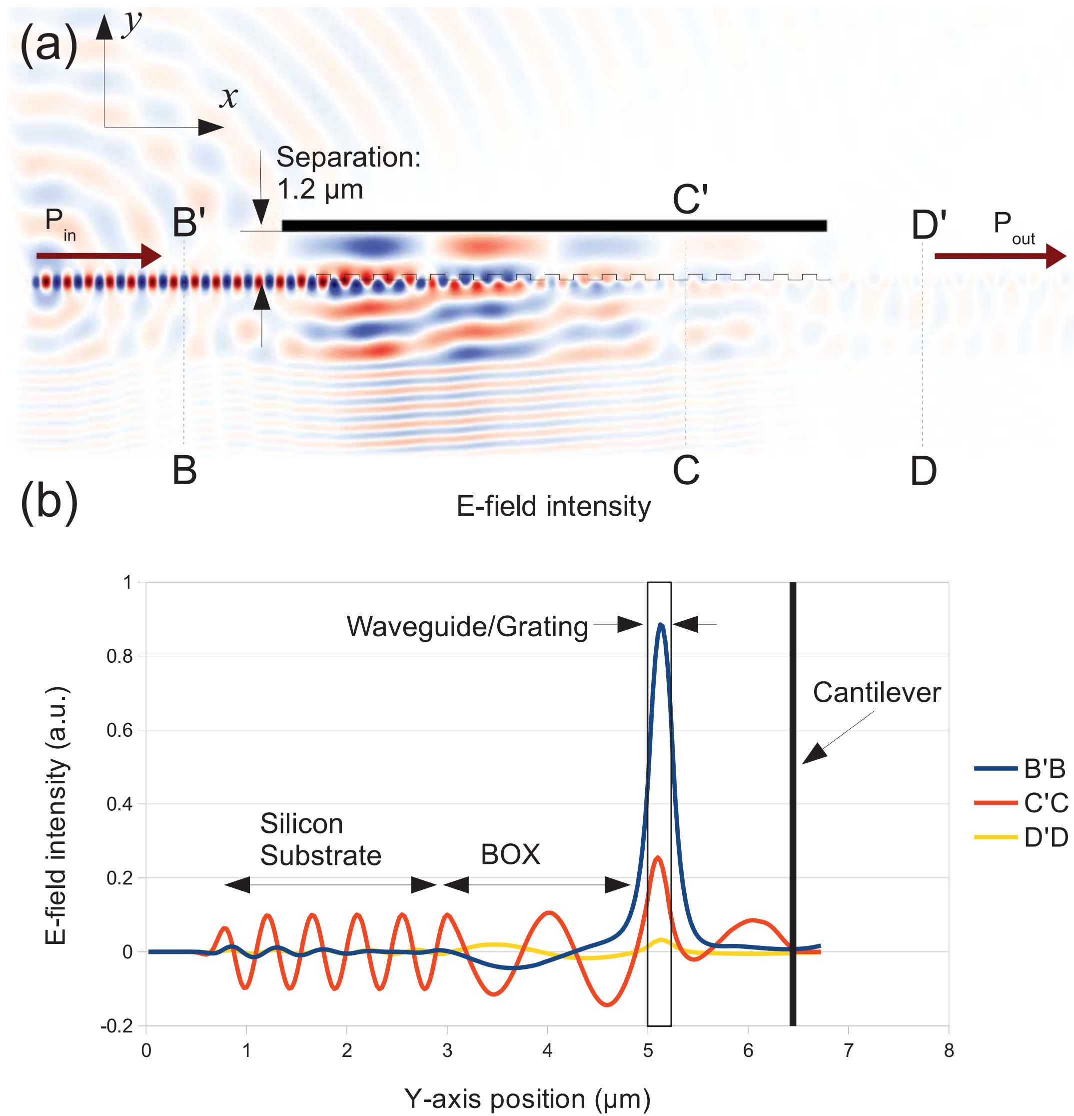

Figure 3.5.4: Modeled results at $\lambda = 1550$ nm for a cantilever with a perfect reflector over a SOI waveguide 230 nm thick. The grating has pitch 630 nm and is 11.9 μm long. TE field distribution with a separation 1.2 μm (minimum in transmitted power). (a) The TE field strength overlain over the structure. A significant portion of the energy is coupled into the substrate rather than the output waveguide. (b) Plot of the TE field intensity through sections B'B, C'C, and D'D, which represent points of interest before the grating, along the grating and after the grating respectively.

be seen in Figure 3.5.5 that a 10-12 dB extinction is achieved as the cantilever arm deflects under either static or dynamic mode. As the width of the grating is increased, the total extinction increases, due to fringing effects becoming less important. Nevertheless, the comparison indicates that a 4 μm wide grating achieves almost the same performance from 0-10 dB as an infinite grating. In most instances, the grating will be operated at the peak or at the 3 dB point, suggesting that a 4 μm wide grating is adequate and achieves optimum performance. The simulation for a theoretical infinitely wide grating shows that the extinction will be over 30 dB. The greater the magnitude of the extinction, the greater the range over which the sensor can operate. This will be investigated in greater detail in Chapter 6.

In order for the device to create a strong interference pattern, and achieve such large extinction ranges, it is important that the grating be effective at coupling light in and out at the operating wavelength. As mentioned in Section 3.5.1 earlier, the grating was modeled to have an loss parameter, α of 0.11 μm^{-1}, resulting in only 8% transmission for an 11 μm grating length when no cantilever was present. Interferometric techniques based on optical path length change have a repeating pattern dependent on the path length. Figure 3.5.5 indicates that measuring only the static optical power using a single waveguide structure under the cantilever will only provide unambiguous transmission values for deflections over a range less than 400 nm. To achieve larger deflection range for static operation and high sensitivities for dynamic operation, multiple waveguides can be placed under a single cantilever at different distances from the cantilever anchor, allowing the shape of the deflected cantilever to be determined. An example of a scheme which might implement this is shown in Figure 7.2.3. Due to the repeating spectral characteristics, the transmission spectra of the resonant structure allows operation over a wide range of gaps. Such operation is not possible in previously reported evanescent coupled waveguides [89], as these devices do not have a repetitive transmission output dependent on the gap.

Multiple Wavelengths

Figure 3.5.6 displays the optical power transmitted through the cavity for various wavelengths and grating-cantilever separations. It can be seen that for different wavelengths, the periodicity and phase of the power fluctuations change. This is due to two wavelength parameters from Equation 3.5:

1. explicit wavelength dependence which alters the effect of the gap, and
2. implicit wavelength dependence of the grating launch angle θ.

Figure 3.5.6 implies that the technique will work even for quite long wavelengths (up to 1702 nm and beyond) and will be ultimately limited by grating performance (see Figure 3.5.2). This is particularly interesting because the large wavelength operational range means that wavelength division multiplexing techniques (WDM) can be exploited to couple to multiple

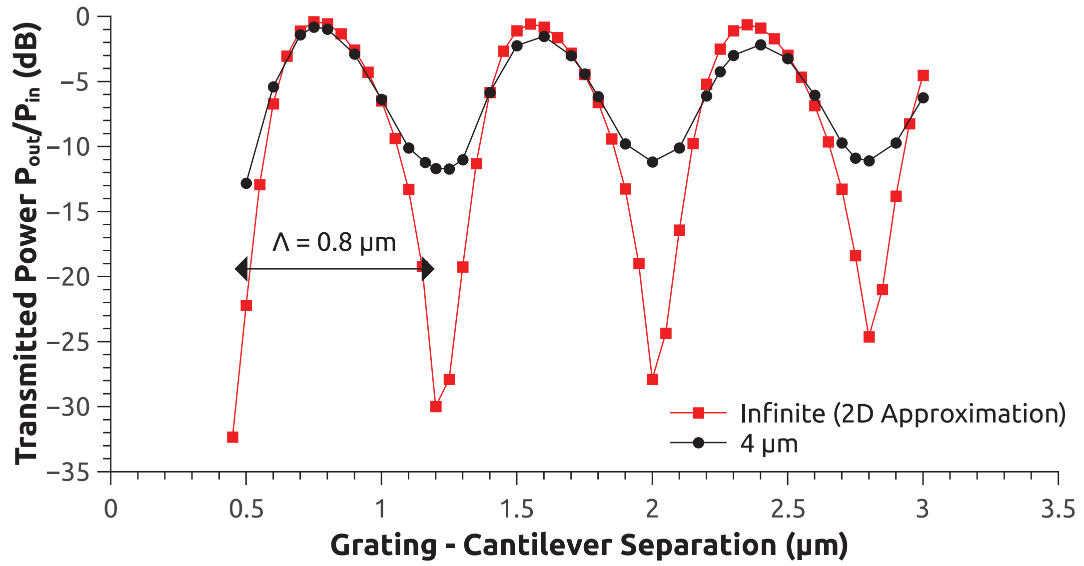

Figure 3.5.5: Modeled results at $\lambda = 1550$ nm for a cantilever with a perfect reflector over a SOI waveguide 230 nm thick. Power transmitted as a function of cantilever-grating separation for a diffraction grating of both 4 μm width and an infinite width (2D) approximation.

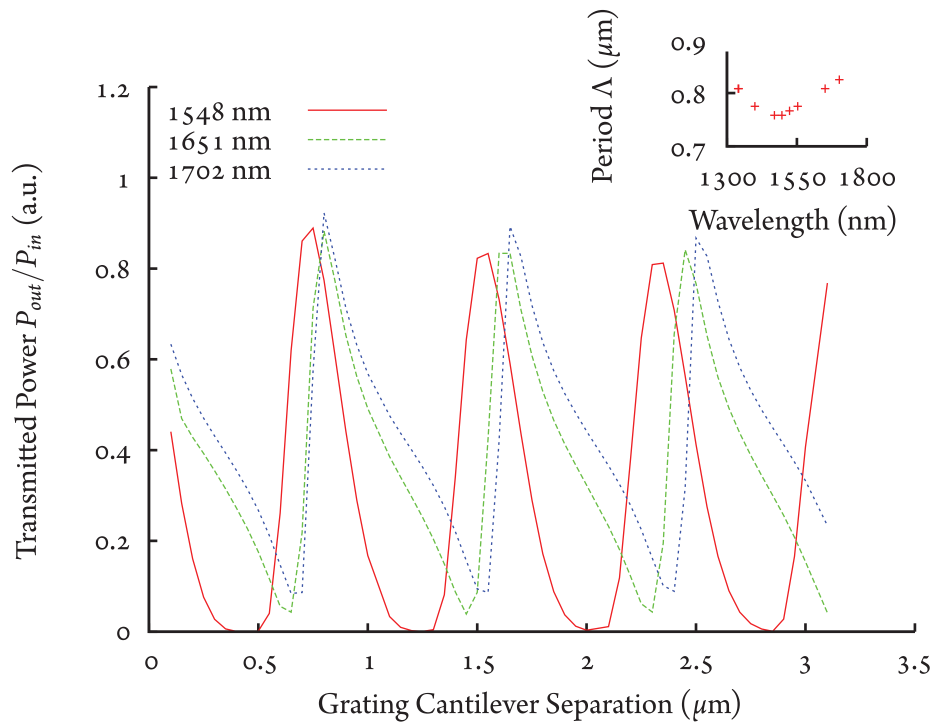

Figure 3.5.6: 2D FDTD modeled results at $\lambda = 1548$, 1651, and 1702 nm for a cantilever with a perfect reflector over a SOI waveguide 230 nm thick. Power transmitted as a function of cantilever-grating separation for the various wavelengths. Inset shows the peak-to-peak period (Λ) for various wavelengths in the range 1300-1800 nm.

waveguides and create large sensor arrays. Figure 3.5.7 provides a schematic of what such a WDM system might look like. By coupling a set of waveguides to the output of an on-chip wavelength division demultiplexer and using a broadband or WDM source, each waveguide containing a microbridge could be interrogated using a separate wavelength. The output of all waveguides could be detected by separate detectors or combined in a second wavelength multiplexer and coupled to an output fiber for subsequent off-chip photonic processing. This technique is suitable for both static and dynamic mode of microbridges or micro-cantilevers. Frequency division multiplexing can be simultaneously utilized by arranging several microbridges of different length along the same waveguide with each microbridge above it's own grating. The resonant frequency of each microbridge modulates the light, and could be separately detected to track analyte adsorption on each microbridge. Alternatively, electrostatic actuation of each microbridge allows time division multiplexing to be used by selectively resonating each sensor one at a time in succession. A combination of these techniques could be used to further increase cantilever density and build potentially massive arrays.

Note that the linear region of the power output is also enhanced at longer wavelengths - at the longest permissible wavelength of 1702 nm the linear region is almost 1 μm. Used correctly, this linear region can provide the ability to operate in either a higher sensitivity, lower dynamic range mode, or a lower sensitivity, higher dynamic range mode. This result is particularly surprising, as the grating is designed for 1550 nm light, and as can be seen in Figure 3.5.2 has a loss parameter of less that 0.04 /μm for wavelengths above 1700 nm (low coupling from the grating). The broad range of effective optical wavelengths can be attributed to the fact that the optical cavity is resonant, so that the multiple reflections in the cavity, can provide sufficient coherent interference to allow a useful measure of the cantilever-grating separation, even for wavelengths where the grating is not particularly efficient.

Grating Length

A particularly important parameter to investigate is the grating length. In the design of this device, the grating cannot be longer than the width of the MEMS beam from which the light is reflected or else significant light would be lost. In all simulations, the cantilever width extends 1 μm beyond each side of the grating. At the other extreme, where the grating is very long, losses through both the cantilever and grating would reduce the optical power. Therefore simulations were undertaken to investigate gratings of length 4, 8, 12, and 16μm. Since these gratings are identical in all parameters but length, power simulations show that the value of the loss parameter α remains at 0.11 μm^{-1} for all four gratings. Figure 3.5.8 shows the power transmitted through the gratings for various cantilever-grating separation distances.

Note that the value of peak optical power transmission remains the same for all grating lengths. The optical power extinction becomes greater as the grating length increases. This is because the finesse of the cavity increases by length due to simple geometry. As mentioned earlier, sensitivity of this device is related to the maximum power extinction, so a longer grating

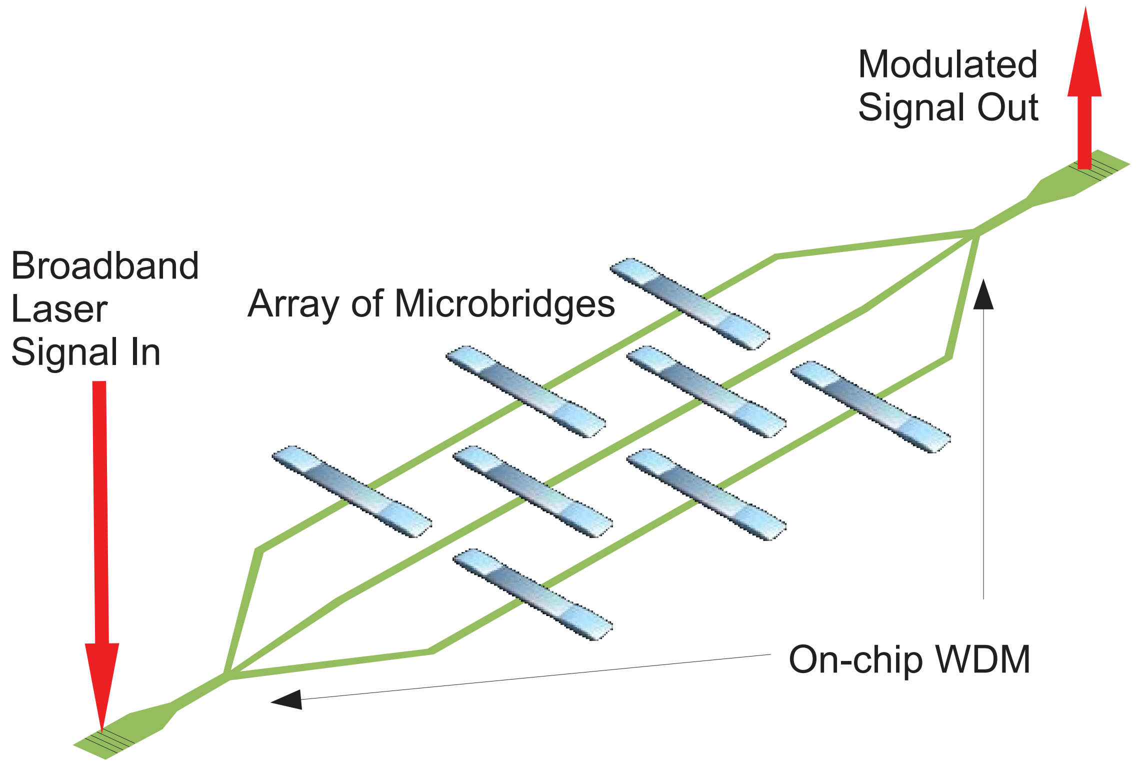

Figure 3.5.7: Schematic of a proposed system to address large arrays of microbridges.

will create a higher resolution system. If spatial design constraints are more important than sensitivity, 10 dB extinction is still predicted for gratings as short as 4 μm.

Reflectivity

All the simulations so far in this chapter have made the assumption that the mirror built into the MEMS structure at the top of the optical cavity was a perfect metal with perfect reflectivity ($R = 1$). Due to practical material and fabrications constraints, this may not always be the case. Therefore, the simulations in Figure 3.5.9 consider the situation where the cantilever is a lossless dielectric with a relative permittivity ε_r of either 3.45, 9, 16, or 36. The relative permeability, μ_r was set to 1. The optical refractive index of a material is given as [124]:

$$n = \sqrt{\frac{\varepsilon_r}{\mu_r}} \tag{3.8}$$

By assuming the dielectric is infinitely thick, a reasonable first order approximation of the reflectivity of the bottom surface of the MEMS structure can be given by:

$$R = \left| \frac{n_1 - n_2}{n_1 + n_2} \right|^2 \tag{3.9}$$

Where n_1 is the refractive index of the MEMS material, and n_2 is the refractive index of the surrounding medium. If the surrounding medium is set to have a refractive index of 1, then, considering the single sided reflectivity only, the reflectivity of the three MEMS structures in

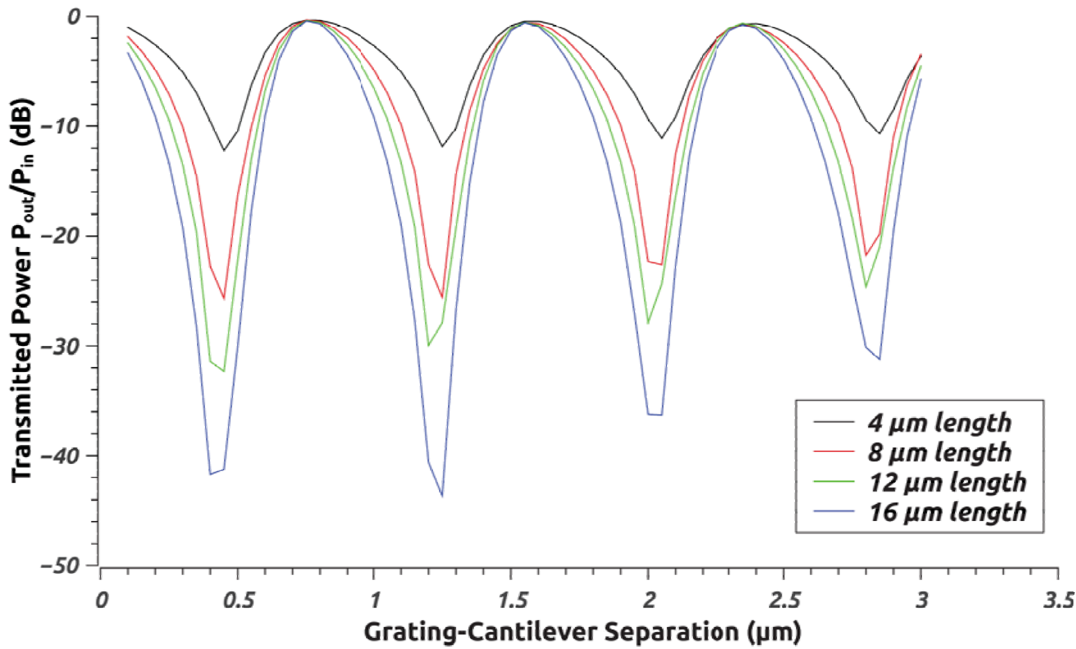

Figure 3.5.8: 2D FDTD modeled results at $\lambda = 1550$ nm for a cantilever with a perfect reflector over a SOI waveguide 230 nm thick. Power transmitted as a function of cantilever-grating separation for a diffraction grating of 4, 8, 12 and 16 μm length.

the simulations will be 9%, 25%, 36%, and 51%. The results in Figure 3.5.9 show that even when the reflectivity is only 36%, the effect of the resonant cavity is very strong. When the reflectivity is as low as 9%, the peak transmission through the structure finally drops to -5 dB, however the extinction is almost 15 dB. These simulations suggest that it will still be possible to use a device with such low reflectivity. The refractive index of crystalline silicon at infrared wavelengths is between 3.42 and 3.50 - implying that a pure silicon MEMS structure would have a reflectivity of between 30 and 31% at these wavelengths, making standard MEMS materials such as crystalline, amorphous, or polysilicon substances without any metal layers suitable from a microbeam material. The refractive index of silicon nitride at 1550 nm is 1.9, giving a reflectivity of 9.6%, meaning a pure silicon nitride MEMS structure should also operate well at mid-infrared wavelengths - although there will be an optical loss of 5 dB through the structure.

As the reflectivity changes, it can be seen that the grating-cantilever separation points for maximum and minimum transmission in Figure 3.5.9 shift. This is due to the phase change due to the dielectric mirror. This is not particularly relevant here as the purpose of these simulations is to examine the effect of reflectivity on the magnitude of the change in transmitted power. Optimising the dielectric thickness may provide additional control over the loss, extinction and shape of the transmitted power with separation, but will not be investigated further in this work.

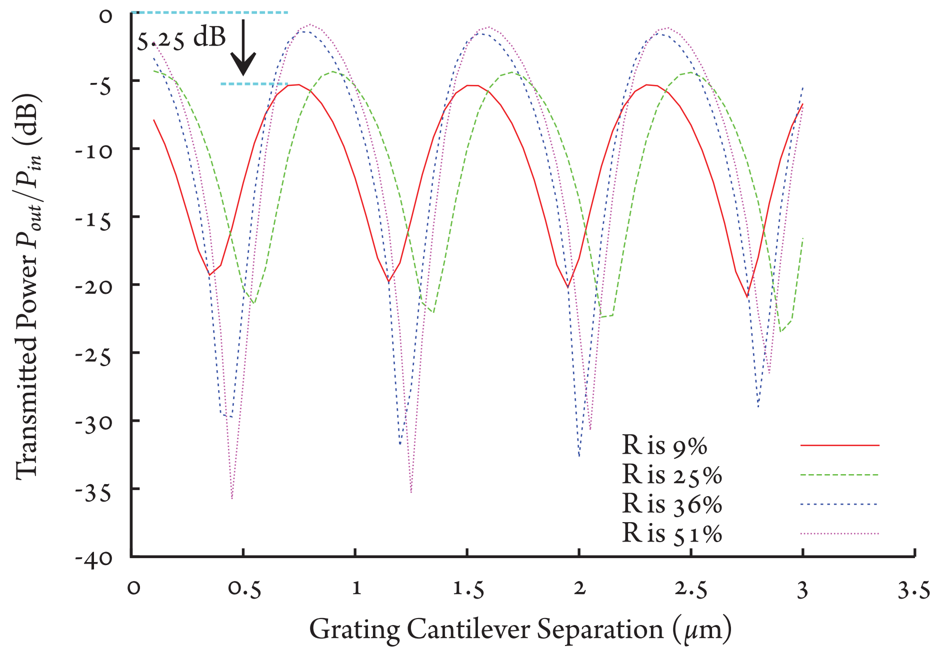

Figure 3.5.9: Modeled results at $\lambda = 1550$ nm for a cantilever with a dielectric mirror over a SOI waveguide 230 nm thick and 4 μm wide with a grating of pitch 610 nm, depth 50 nm, and length 11.9 μm. The mirrors simulated have a bottom surface reflectivity of 9%, 25%, 36%, and 51%. Power transmitted as a function of cantilever-grating separation is displayed.

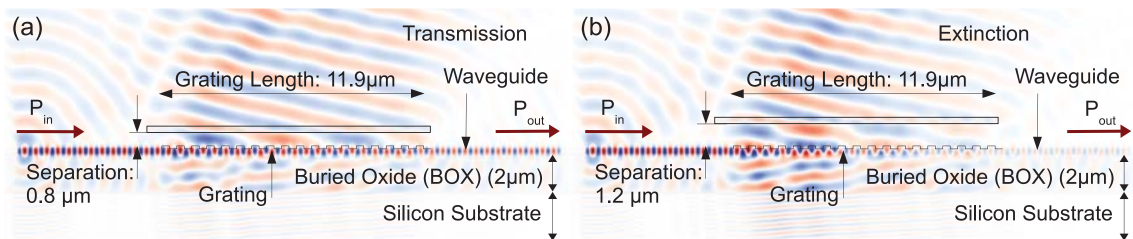

Figure 3.5.10: Modeled results at $\lambda = 1550$ nm for a SOI waveguide 230 nm thick and 4 μm wide with a grating of pitch 610 nm, depth 50 nm, and length 11.9μm. Calculated TE field distributions through section A'A in Figure 3.1.1 for the case of a dielectric cantilever with $\varepsilon_r = 3.45$ (Corresponding to a reflectivity of 9% at each surface). (a) TE field when the grating-cantilever separation is 0.8 μm. This separation gives maximum transmitted power. (b) TE field when the grating-cantilever separation is 1.2 μm (minimum transmitted power). Note that in both cases, substantial optical power (around 5 dB) is lost through the cantilever due to its low reflectivity.

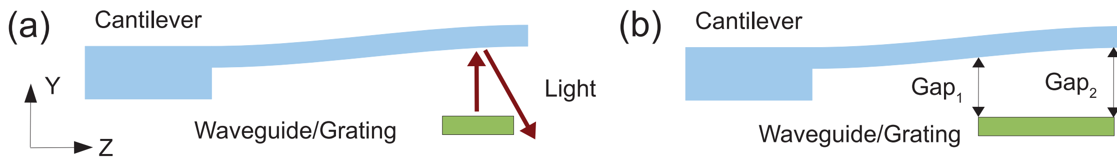

Figure 3.5.11: Schematic illustration of the cantilever/grating from Figure 3.1.1 in YZ cross-sectional view. a: Grating is too narrow – when the micro-cantilever is deflected, some light is not coupled back into the grating. b: Grating is too wide – when Gap1 » Gap2, multiple cavity resonances exist, broadening spectral width (axis is consistent with Figure 3.1.1).

Tilt

The results of Figure 3.5.5 imply that a wider grating width is preferable in device design. However, the simulations assumed that the MEMS mirror was parallel to the diffraction grating. Whilst this is true for a MEMS doubly clampled beam, for the case of a micro-cantilever, the mirror may be deflected by an angle of 1-2° (assuming a 100 μm long cantilever and an end displacement of 1.75 - 3.5 μm). This deflection will cause two additional optical losses that reduce the dynamic range that the previous FTDT (meep) simulations do not take into account:

1. For narrow width gratings: light is reflected away from the diffraction grating (shown in Figure 3.5.11a). This loss increases as the diffraction grating width decreases.

2. For wide gratings: the difference in grating-to-cantilever separation from one side of the cantilever to another (Figure 3.5.11b). This loss increases as the diffraction grating width increases. For the case of a 4-μm wide grating, and a 1° deflection, the change in separation is 70 nm. For a 10-μm wide grating, the change in separation for the same deflection will be 175 nm. This much variation will result in the peaks and troughs of the power transmitted being effectively flattened.

To estimate the loss from tilt and grating width, additional 3D FDTD simulations were undertaken at gap sizes corresponding to the maximum and minimum transmission of light for both 4-μm and 10-μm wide gratings. These simulations focused on the extreme case of a cantilever deflection of 5.7° (0.1 rad), corresponding to a 100 μm cantilever deflecting by 10 μm. Additionally, for the 10-μm wide grating, a cantilever deflection of 2.29° (0.04 rad - and a 100 μm cantilever deflecting 4 μm) was simulated. This additional calculation was performed as the change in separation over the length of a 10-μm wide grating compares to a similar change in separation for the 4-μm wide, 0.1 rad case, which gives an interesting point of comparison. Table 3.5.1 shows the results for these simulations.

Table 3.5.1 shows that as the tilt angle is increased, the signal dynamic range decreases. Increasing the width of the grating makes the device far more sensitive to loss: with a dynamic range of 9.48 dB, a 0.1 rad deflection still achieves a suitable dynamic range for a 4-μm wide grating, whereas the same angle deflection for a 10-μm grating is unusable with a dynamic range of 0.97 dB. However the 10-μm wide grating still has 10 dB dynamic range when deflected by 0.04 rad, providing an upper limit to the tilt allowable during either fabrication or operation.

The devices with high dynamic ranges in Table 3.5.1 show that these devices are highly tolerant to cantilever tilt. Machining a perfectly flat cantilever is not necessary for the device to operate successfully, significantly reducing fabrication constraints. Further, the diffraction grating width represents an optimisable design parameter of a particular cantilever deflection, ultimately limited by the need to maintain a single mode of propagation.

An alternative structure is obtained by aligning the cantilever parallel to the diffraction grating. This structure will have different properties with respect to how tilt and bowing of the cantilever effect the light transmission. In this structure, light that is reflected away from the grating by cantilever tilt, would instead be reflected back into the grating. The grating width could then be optimized with respect to the second source of loss. However designing the cantilevers over the waveguide requires methods to reduce optical losses from the cantilever anchors.

	4 μm width		10 μm width		
Gap (μm)	Flat (dB)	0.1 rad (dB)	Flat (dB)	0.04 rad (dB)	0.1 rad (dB)
0.75	-0.82	-1.51	-0.54	-1.8	-5.17
1.20	-11.68	-10.83	-14.86	-11.8	-4.38
1.25	-11.71	-10.99	-13.97	-10.05	-4.2
Signal Range (dB)	**10.89**	**9.48**	**14.32**	**10**	**0.97**

Table 3.5.1: Power transmitted for various cantilever deflections and grating widths

Aqueous Environments

As discussed in Chapter 2, one of the important benefits of MEMS sensors is their ability to be used in both aqueous and gaseous environments. One of the issues with electronic read-out techniques is the need to isolate the electrical and aqueous environments to avoid electrical leakage or degradation of biological samples. The following simulations investigate the feasibility of using this read-out system in an aqueous solution.

The medium in the FDTD simulation was given a refractive index of 1.33 in order to match that of a biological electrolyte [125]. This will have two effects on the operation of the diffraction grating. Firstly, because the refractive index difference between the grating material (Si, $n = 3.42$) and the aqueous medium ($n = 1.33$), is less than the previous studies (of $n = 1$), the grating will be less efficient at coupling light out of the waveguide. Secondly, again because of the higher refractive index of the aqueous medium, the angle at which light is coupled out of the grating will be steeper.

Figure 3.5.12: Modeled results of the loss parameter α for the wavelength range 1340-1830 nm in both air and water.

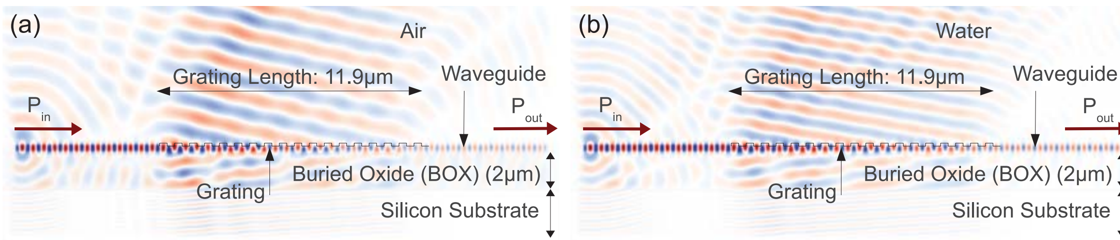

Figure 3.5.13: Modeled results at $\lambda = 1550$ nm for a SOI waveguide 230 nm thick and 4 μm wide with a grating of pitch 610 nm, depth 50 nm, and length 11.9 μm. Calculated TE field distributions through section A'A in Figure 3.1.1 for the case without a cantilever. (a) TE field when the medium above the grating is air. (b) TE field when the medium above the grating is water.

From the simulation results and Equation 3.7, the loss parameter was calculated to be $\alpha = 0.078\ \mu m^{-1}$ for a wavelength of 1550 nm in an aqueous solution. Figure 3.5.12 shows the value of α over the wavelength range from 1340-1830 nm for operation in both air and water. As expected, the grating efficiency is lower in an aqueous environment for all wavelengths analysed.

Figure 3.5.13 shows simulations of the TE field distribution around the grating for both air ($n = 1$) and water ($n = 1.33$). The three main points to note from this figure are:

1. Due to the higher refractive index of water, the angle of the optical wave-front leaving the grating is steeper than that of the case of air.

2. Due to the lower value of α for the grating in water, the out-of-plane coupling of the grating is less efficient in water than in air, so there is more light in the output waveguide.

3. Due to the higher refractive index of water, the positive and negative peaks of the TE field are closer together than in the case of air.

From effects 1 and 3 above, it is expected that the periodicity of the interferometric effect will be shorter than in air. This is shown from simulations presented in Figure 3.5.14. It can be seen that the periodicity (Λ) reduces from 800 nm in air to 500 nm in water. Interestingly, the extinction is still extremely strong in water, even though the grating is less efficient in water than in air.

This simulation only takes into account the effect of the difference in refractive index between liquid and air, and does not consider the effects of optical absorption of the liquid, or potential scattering due to particles in the liquid. No experiments involving liquid environments were performed over the course of this work. Therefore, there is an excellent opportunity for future work in performing in-depth study of the theory and operation of this read-out technique in liquid environments.

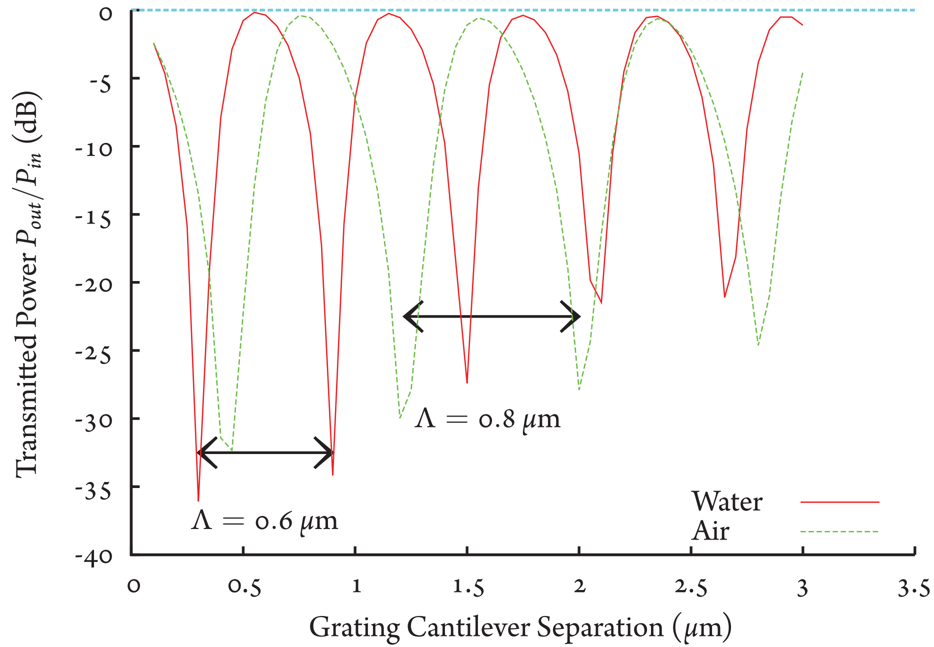

Figure 3.5.14: Modeled results at $\lambda = 1550$ nm for a cantilever in air and water over a SOI waveguide 230 nm thick with an embedded grating. Power transmitted as a function of cantilever-grating separation is displayed.

3.6 Theory and Simulation Conclusions

This chapter presented a novel optical technique for determining the effect of the gap between a moving mirror and a waveguide containing an embedded diffraction grating. Simulations were undertaken on a grating based on silicon on insulator (SOI) substrates, and out of plane coupling of 1550-nm light. The simulations show that the interferometric effect that extinguishes the light is very strong, and is more than adequate for applications where the grating is short as 4 μm. Excellent performance was predicted in both gaseous ($n = 1$) and aqueous ($n = 1.33$) environments. The periodicity of the interference decreases in the aqueous environments which reduces the useful (1-period) range by 75%. Multiple wavelengths were simulated, and broad-band performance predicted. This is particularly useful for sensing applications requiring massive arrays as they can be addressed using combinations of WDM, FDM, and TDM techniques.

If the beam being measured is a micro-cantilever, simulations of tilt show that for deflections of up to 5.7° a 4-μm wide grating will still provide almost 10 dB extinction of the input light. Note that microbridges will actuate symmetrically over the grating, and so will not suffer degradation due to tilt effects. The technique is also tolerant to mirrors with low reflectivity - the 2D simulations show 14 dB extinction for the case of a dielectric mirror of only 9% reflectivity.

The following chapters will investigate the fabrication and testing of this device.

The man who moves a mountain begins by carrying away small stones.

Confucius

4 Device Design and Fabrication

In order to demonstrate the position readout technique described in the previous chapter, it is necessary to build a silicon photonic circuit containing interrogating gratings, then build MEMS microbridges and micro-cantilevers above the gratings. This chapter discusses the design of the devices used for demonstration, presents an introductory analysis of the MEMS structures, and describes the fabrication techniques used to build them. Readers familiar with photolithography, MEMS and silicon photonics design and fabrication concepts may wish to skip forward to the next chapters, where results from the structure will be presented and discussed.

4.1 Photonic circuit

The core of the device is the silicon photonic circuit that will be used to interrogate the suspended MEMS structures. It is desirable to decouple the fabrication of this optical component from the fabrication of the MEMS structures which will be added later, so that the MEMS structures can be separately optimised. To this end, the waveguides and diffraction gratings were fabricated using a silicon on insulator (SOI) wafer by the Laboratoire d'électronique et de technologie de l'information (LETI) standard passive process using the ePIXfab silicon photonics platform [126]. Appendix C contains a listing of the supported capabilities of the LETI process. The high resolution required to create features capable of diffraction effects in the near infra-red (NIR) is reached by using 193 nm deep ultra-violet (DUV) photolithography. The SOI wafer used has a buried oxide (BOX) layer of 2 µm thick, and an epitaxial silicon layer of 220 nm thick. The pertinent steps in this process are an initial

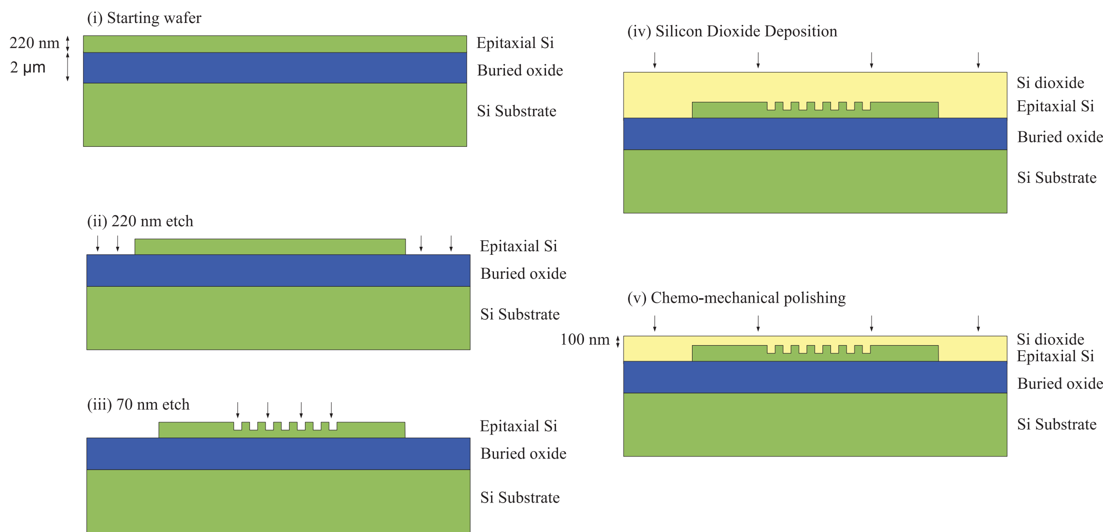

Figure 4.1.1: LETI process flow. (i) Starting with an SOI wafer chosen with an epitaxial silicon thickness able to operate as a waveguide for infra-red light (220 nm), and a SiO_2 thickness (2 μm) chosen to support the operation of the Si waveguide and grating couplers, (ii) a 220 nm silicon etch is performed to remove the parts of the epitaxial silicon which are not going to be needed for the photonic circuit. This forms the waveguides and adiabatic tapers. (iii) Subsequently, a 70 nm silicon etch is performed to define the diffraction gratings. (iv) A layer of SiO_2 is deposited, and (v) is chemo-mechanically polished down to a height of 100 nm above the top of the epitaxial silicon. This step provides a flat planarized surface for the fabrication of the overlying MEMS structures.

70 nm deep etch into the epitaxial silicon to form grating pits, a 220 nm etch of the epitaxial silicon, followed by a deposition of SiO_2 which is chemo-mechanically polished to create a 100 nm flat layer above the epitaxial silicon. This process is shown in Figure 4.1.1. With correctly designed photolithograthy masks, these process steps can be used to create the diffraction gratings and waveguides that the photonic circuit will need to operate. These features will be discussed in this section.

Figure 4.1.2 presents a top down view of a typical photonic circuit used. Laser light from an optic fiber is launched into the input grating. Adiabatic tapers are used to confine or expand the light to the widths of the various waveguides used. The interrogating grating will sit beneath a suspended MEMS beam. The output coupler will launch light into an output optic fiber. The modulated optical power received at the output will be measured, and is expected to be modulated according to the movement of the MEMS beam. The length from the start of the input grating to the end of the output grating, L_t, on the chips is 4.6 mm. There are several waveguides on the chip for testing, and the length from the start of the input grating to the start of the interrogation grating, L_i, varies from 770 μm to 3.9 mm. Each component in the photonic circuit is discussed below.

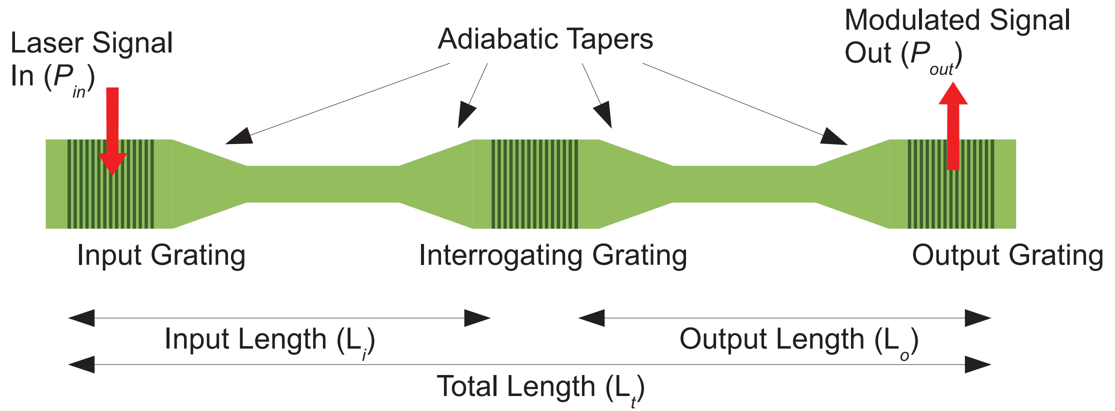

Figure 4.1.2: Top schematic view of the photonic circuit used. When a suspended MEMS beam with a reflective under-surface (not shown) is fabricated above the interrogating grating, an optical microcavity will form, and the input laser signal, P_{in} will be modulated based on the movement of the MEMS beam, creating the output signal P_{out}.

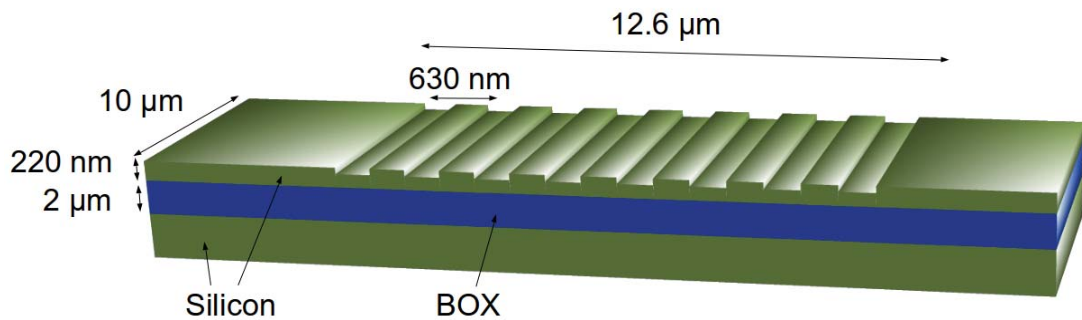

Figure 4.1.3: Isometric diagram of the diffraction grating (not to scale). The grating is 12.6 μm long, 10 μm wide, with a thickness of 220 nm, and a pitch of 630 nm. The grating is a square wave grating, and so its ridges and grooves are both 315 nm. The grating depth is 70 nm.

4.1.1 Input and Output Gratings

The input/output gratings are designed to be broadband around 1550 nm (FWHM is 65 nm) [127]. These components are used to couple light to and from single mode SMF-28 optical fiber with a core diameter of 10 μm. These gratings are etched into the epitaxial silicon layer using the process described in Figure 4.1.1 and their geometric details are given in the isometric diagram shown in Figure 4.1.3. The input/output gratings were designed to have a fiber-to-waveguide coupling loss of 6 dB at a wavelength of 1550 nm [127, 128]. The nominal loss for a silicon photonic waveguide connecting the input and output is 2 dB/cm [129]. As the total distance between the input and output gratings is 4.6 mm, the expected insertion loss was 13 dB.

4.1.2 Adiabatic Tapers

The input/output gratings are 10 μm wide in order to match the core diameter of the optical fiber. As the distance between the input and output gratings is almost half a centimetre, it is

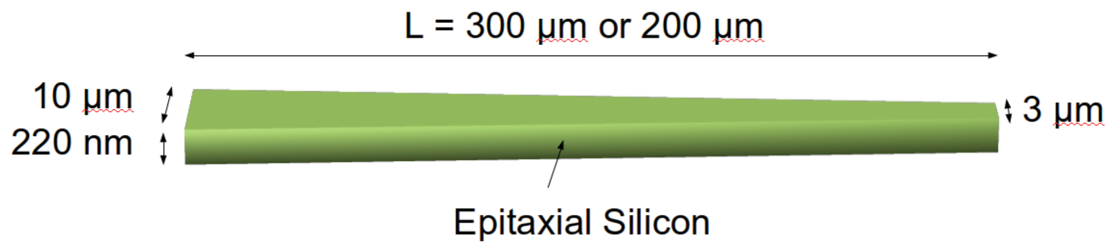

Figure 4.1.4: Isometric diagram of an adiabatic taper (not to scale). This component 220 nm thick, starts with a width of 10 μm and shrinks to a width of 3 μm over a length of either 300 or 200 μm.

important to decrease the width of the silicon waveguide for the majority of the propagation distance in order to avoid mode scrambling issues along the waveguide [130]. To this end, adiabatic tapers were introduced in order to confine the light from a 10 μm wide grating waveguide, to a waveguide that is 3 μm wide. Adiabatic tapers 350 μm long are placed directly after the input gratings, and directly before the output gratings. Adiabatic tapers 200 μm long are placed on either side of the interrogating gratings. An isometric diagram of the adiabatic taper is shown in Figure 4.1.4.

4.1.3 Interrogating Grating

The interrogating grating is the core of the interferometric system that is used to determine the height of the suspended beam. For testing purposes, interrogating gratings in 12 different sizes of 4-, 7-, and 10-μm width combined with lengths of 6.30, 12.60, 15.75, and 18.90 μm were fabricated. The geometric details of the interrogating gratings are similar to the input/output gratings (see Figure 4.1.3).

4.1.4 50-50 Optical Splitter

For the purposes of calibrating the effect of the interrogating grating, some waveguides were integrated with a 50-50 on-chip optical splitter. The top arm of the output of the splitter led to an interrogating grating and then to an output grating coupler. The bottom arm of the output of the splitter led directly to an output grating coupler. The splitter was etched into the epitaxial silicon with the design shown in Figure 4.1.5.

4.2 MEMS Structures

The design and fabrication of the MEMS structures was almost entirely decoupled from that of the photonic circuit. The fabrication of the photonic circuit was performed by LETI in France, and the fabrication of the MEMS structures were performed in the laboratories of the University of Western Australia in Australia. The only constraints linking the two together were:

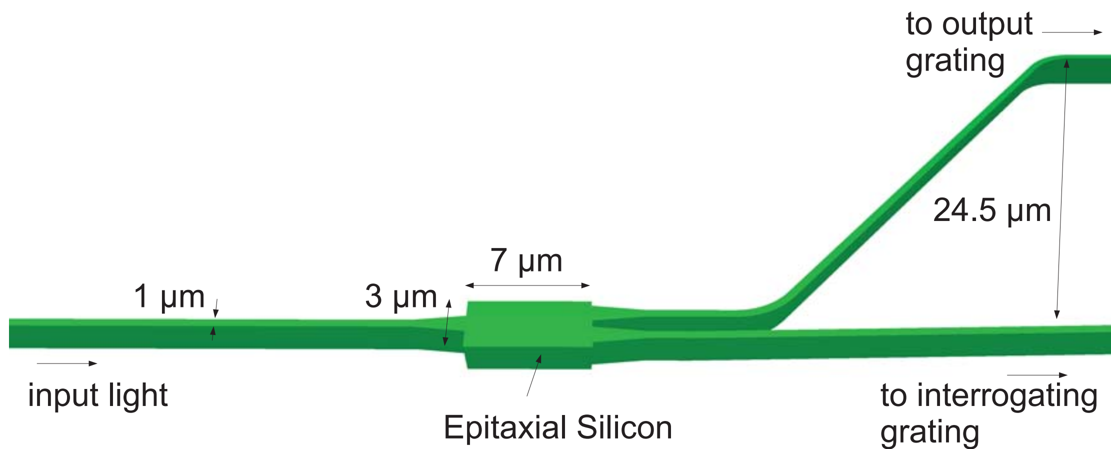

Figure 4.1.5: Isometric diagram of the 50-50 optical splitter (not to scale)

- the design requirement of needing to ensure that the MEMS structures are suspended directly above the interrogating gratings in the photonic circuit, and
- the requirement that electrostatic actuation traces were not deposited above the waveguide structures.

For this investigation, three main MEMS structures were fabricated: cantilevers, microbridges (sometimes referred to as either doubly-clamped beams or Euler columns), and Guckel rings [131]. Only cantilevers and microbridges were used as the suspended structures above the interrogating grating. The deflection profiles of released cantilevers microbridges, and Guckel rings were used to diagnose the residual stress in the structural thin film layers [131, 132].

4.2.1 Design of MEMS

There are two main requirements that the MEMS structures must have in order to function correctly in this device. These requirements are:

1. the structures must have an efficient reflector at a wavelength of 1550 nm on the underside of the deflecting beam, and
2. The structures must have a low enough level of residual stress such that they are flat enough to form a high-Q resonant cavity with the interrogating grating.

For the chosen optical wavelength of 1550 nm, there are many materials that can be used to create an efficient reflector. As can be seen in Figure 4.2.1, the reflectance of aluminium, silver and gold are each well over 95% at 1550 nm [133, 134]. Alternatively, using thin film layer deposition technologies, dielectric mirrors of very close to 100% (>99.999%) reflectivity can be created for 1550 nm light [135].

To keep the fabrication process simple, reduce the layer thickness and remove multilayer stress balancing issues, the use of dielectric mirrors was not considered, and a thin layer of gold

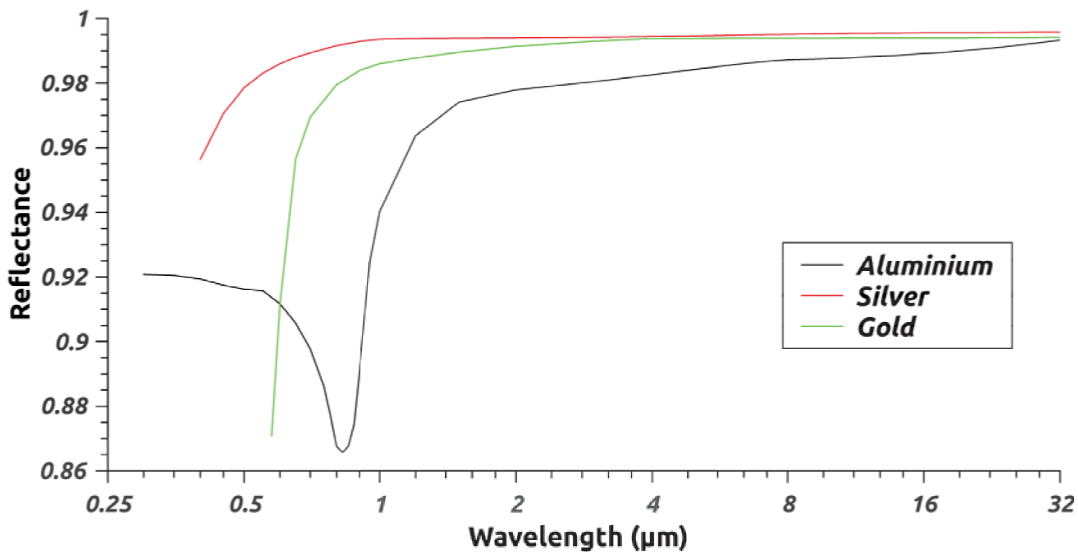

Figure 4.2.1: Reflectance of Aluminium, Silver and Gold evaporated in ultrahigh vacuum [133, 134]

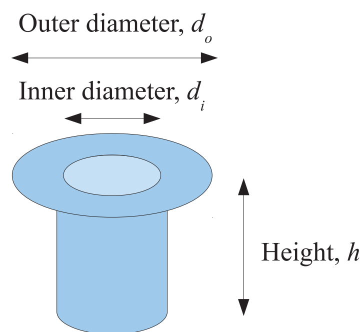

Figure 4.2.2: Typical top hat anchor structure.

was chosen to be the mirror. Gold is a particularly strong reflector of infra-red radiation, giving 98%-99% reflectivity through the infra-red, and so a layer of 50 nm was considered sufficient to provide good reflectivity at 1550 nm.

The structural layer for the MEMS structures was chosen to be non-stoichometric silicon nitride (SiN_x). SiN_x is a relatively chemically inert, extremely mechanically strong material with a Young's Modulus typically between 120-315 GPa. SiN_x can be deposited using plasma enhanced chemical vapour deposition (PECVD) technique by combining silane and ammonia to form the SiN_x layer [136]. The deposition rate can be well controlled - the recipe used had a deposition rate of 28 nm/s, and the PECVD instrument used PC control to time the process to per second accuracy.

An inverted top hat style anchor was chosen to support the suspended structures. An example of a circular top hat anchor is shown in Figure 4.2.2. This structure has very good mechanical support when formed from SiN_x, and lends itself very well to surface micro-machining techniques.

4.2.2 Stress Considerations

Thin film stress is important to consider when designing surface micro-machined devices. Generally speaking, all films are in a state of either compressive or tensile residual internal stress. The total stress of a film is given by [137]:

$$\sigma = \sigma_{extrinsic} + \sigma_{residual} \tag{4.1}$$

where

$$\sigma_{extrinsic} = \sigma_{\Delta CTE} + \sigma_{external} \tag{4.2}$$

and

$$\sigma_{residual} = \sigma_{thermal} + \sigma_{intrinsic} \tag{4.3}$$

$\sigma_{\Delta CTE}$ is the thermal stress caused by the difference in the coefficients of thermal expansion between film/film or film/substrate layers, $\sigma_{external}$ is the stress due to factors such as packaging or stresses from other films or sources, $\sigma_{thermal}$ is the stress resulting from deposition temperature conditions, and $\sigma_{intrinsic}$ is the stress developed during film formation due to lattice mismatch, too rapid film growth, phase transformations or incorporation of impurities into the film.

Stress Considerations - microbridges

Controlling stress is important for all free-standing MEMS structures. For microbridges, compressive stress can bow the device, and too much tensile stress can strain the microbridge too much, causing the beam to break. Stress in microbridges will also change the mechanical resonant frequency of the microbridge. The fundamental resonant frequency of a microbridge under tension can be given by [138]:

$$f = 1.03\sqrt{\frac{Et^2}{\rho L^4} + \frac{T}{3.4mL}} \tag{4.4}$$

where T is the tension, E is the Young's modulus, ρ is the density, m is the effective mass, t is the thickness and L is the length of the beam.

The stress in the beam is given by:

$$\sigma = \frac{T}{tw} \tag{4.5}$$

where w is the width of the beam, therefore the fundamental resonant frequency in terms of stress is:

$$f = 1.03\sqrt{\frac{Et^2}{\rho L^4} + \frac{\sigma tw}{3.4mL}} \tag{4.6}$$

Microbridges in this work were manufactured for two purposes - first to act as diagnostic structures for compressive stress, and second to serve as suspended vibrating mirrors above the diffraction gratings to form the optical cavity for the testing of this displacement measurement technique. The diagnostic microbridges were built with a width of 10 μm, and lengths ranging from 110 μm to 230 μm, varying in increments of 20 μm in length. The mirror microbridges

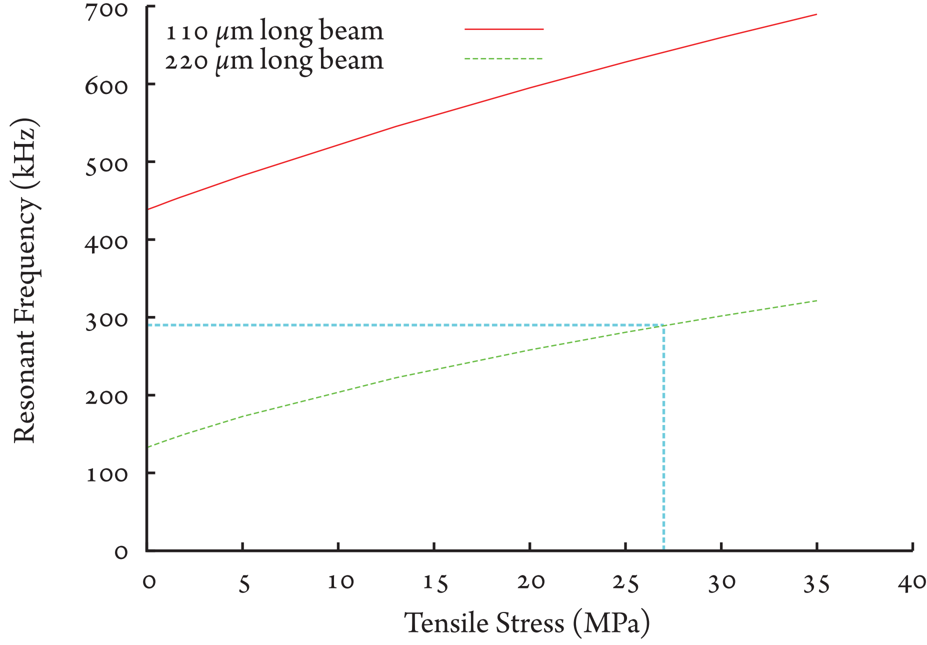

Figure 4.2.3: Impact of tensile stress on the theoretical resonant frequency of microbridges made from PECVD SiN_x with a thickness of 750 nm, and a length (width) of either 220 μm (20 μm) or 110 μm (10 μm). The resonant frequency and tensile stress of the beam fabricated in Section 4.3.1 is indicated by the dashed blue line. For this calculation a Young's modulus, E, of 150 GPa and a density, ρ, of 3184 kg/m^3 were assumed for the silicon nitride.

were either 10 μm wide and 110 μm long; or 20 μm wide and 220 μm long. The predicted resonant frequency of the 110- and 220 μm long microbridges as a function of tensile stress are shown in Figure 4.2.3.

Stress Considerations - MEMS Cantilever

MEMS cantilevers were manufactured to serve as suspended mirrors above the diffraction gratings, and were either 10 μm wide and 110 μm long; or 20 μm wide and 220 μm long.

The micro-cantilevers fabricated are a bimorph made from two materials - a gold mirror underlayer and silicon nitride structural layer - and the stress mismatch between the two layers can cause the cantilever to curve up- or downwards if that stress is not balanced. The residual strain in the gold film layer, ε_f, of the cantilever can be measured from the radius of curvature R of the bi-layer beam by [139]:

$$\frac{t_b}{R} = \frac{2c_1}{1 + c_2} \tag{4.7}$$

where

$$c_1 = \frac{E_r t_r \varepsilon_f - c_2 \left(E_r t_r + 1\right)}{E_r t_r^2 - 1} \tag{4.8}$$

$$c_2 = \frac{E_r^2 t_r^4 \varepsilon_f + 3E_r t_r^2 \varepsilon_f + 4E_r t_r \varepsilon_f + \varepsilon_1 \left(E_r t^2 - 1\right)}{3\left(E_r t_r^2 - 1\right) - 4\left(E_r t_r + 1\right)\left(E_r t_r^3 + 1\right)} \tag{4.9}$$

$E_r = E_f / E_b$, where E_f and E_b are the Young's moduli of the gold film layer and the silicon nitride

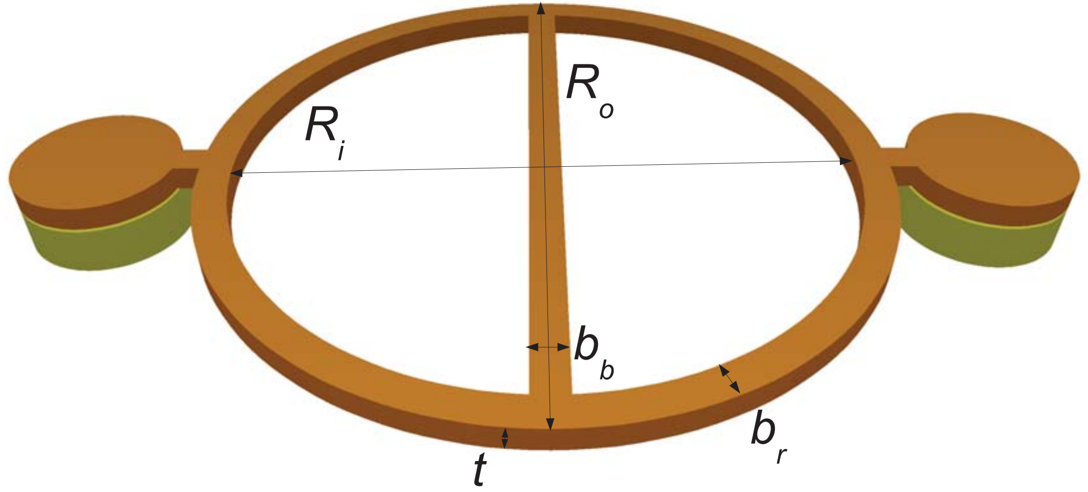

Figure 4.2.4: Isometric image of a Guckel Ring.

base structural layer, respectively. $t_r = t_f/t_b$, where t_f and t_b are the thicknesses of the gold film layer and the silicon nitride base structural layer, respectively. ε_1 is the gradient residual strain in the silicon nitride layer. *epsilon*$_1$ can be determined by fabricating separate, single layer silicon nitride micro-cantilevers on the same chip and in the same processing run (without the gold film layer), and using the relation [139]:

$$\varepsilon_1 = \frac{t_b}{2r} \tag{4.10}$$

where r is the radius of curvature of the single layer silicon nitride beam (not to be confused with R, which is the bi-layer radius of curvature).

Stress Considerations - Guckel Rings

Guckel rings are a diagnostic microstructure useful for measuring tensile stress in a processed chip [131]. A Guckel ring is a suspended ring with a crossbar through the middle. An isometric view of such a structure is shown in Figure 4.2.4. By making several of these structures with varying radii, critical strain values can be measured by observing the smallest ring for which the crossbar buckles. Specifically, if R^- represents the largest unbuckled radius, and R^+ the smallest buckled radius, the tensile strain values lies between [131]:

$$\frac{(kR)^2(t/R^+)^2}{12g(R^+)} \leq \varepsilon_0 \leq \frac{(kR)^2(t/R^-)^2}{12g(R^-)} \tag{4.11}$$

where t is the thickness of the deposited film, R is the average of the the outer and inner radii of the Guckel ring, calculated by $R = \frac{R_o+R_i}{2}$. The ratio of the conversion efficiency of tensile strain into compressive strain of the Guckel ring is $g(R)$, given by [131]:

$$g(R) = -\frac{2b_r f_2}{2b_r f_1 + b_b f_1^2 - b_b f_2^2} \tag{4.12}$$

where, referring to Figure 4.2.4, b_r is the width of the ring of the Guckel structure, b_b is the width of the crossbar, and

$$f_1 = \frac{R}{e}\left(\frac{\pi}{4} - \frac{2}{\pi}\right) - \frac{2e}{\pi R} + \frac{4}{\pi} - \frac{\pi}{4} + \pi k_f \frac{1+\nu}{2} \tag{4.13}$$

$$f_2 = \frac{R}{e}\left(\frac{1}{2} - \frac{2}{\pi}\right) - \frac{2e}{\pi R} - \frac{1}{2} + \frac{4}{\pi} - k_f(1+\nu) \tag{4.14}$$

k_f is a form factor and e is the eccentricity:

$$e = R - \frac{b_r}{ln(R_o + R_i)} \tag{4.15}$$

The variable k from Equation 4.11 is defined by $k^2 = P_{cr}/EI_b$, where I_b is the area moment of inertia of the crossbeam. For the case of out of plane buckling (when $b_b > t$), $I_b = b_b t^3/12$. $P_{cr} = \varepsilon_{cr} E b_b t$ is the beam-bucking force, where ε_{cr} is the strain needed to buckle the beam. The Guckel ring buckling criteria can be found by solving the following equation for kR [131]:

$$\frac{kEI_b}{a} + \tan(kR) = 0 \tag{4.16}$$

For out of plane buckling of the cross beam, a is defined by [131]:

$$a = \frac{4c_r E b_r t^3}{\pi R(6c_r + 1 + \nu)\left(1 - \frac{4(1+\nu-6c_r)^2}{\pi^2(1+\nu+6c_r)^2}\right)} \tag{4.17}$$

where ν is Poisson's ratio for the beam material, and c_r is the torsion coeffient for rectangular areas, $\frac{1}{3}$. Poisson's ratio for this material has been previously measured as being 0.25 [140], therefore,

$$a = \frac{0.1335 E b_r t^3}{R} \tag{4.18}$$

Combining Equations 4.16, 4.18, and the expression for moment of inertia I_b:

$$\frac{kRI_b}{0.1335 b_r t^3} + \tan(kR) = \frac{kRb_b}{12 * 0.1335 b_r} + \tan(kR) = 0 \tag{4.19}$$

so

$$\tan(kR) = -\frac{kRb_b}{1.602 b_r} \tag{4.20}$$

An array of Guckel rings were manufactured to act as diagnostic structures for tensile stress. The width of both the rings ($R_o - R_i$) and crossbar was 10 μm. Knowing this, Equation 4.20 can be solved numerically to find $kR = 2.2$. The radius of the rings (R_o) fabricated ranged from 90 μm to 210 μm, varying with increments of 20 μm. Table 4.2.1 shows the predicted buckling strain calculated using Equation 4.11 for each of the Guckel rings in the array assuming the thickness of the film is 750 nm, and also the buckling stress that this would correspond to assuming that the Young's modulus of the silicon nitride used to make the rings is 150 GPa. This

array of Guckel rings can be used as diagnostic structures to measure stress between 2.15 and 12.39 MPa.

Outer Radius R_o (μm)	Buckling Strain ε_{cr} ($\times 10^{-5}$)	Buckling Stress (MPa)
90	8.28	12.39
110	5.43	8.14
130	3.84	5.75
150	2.85	4.28
170	2.21	3.31
190	1.76	2.64
210	1.43	2.15

Table 4.2.1: Values of buckling stresses and strains for the fabricated Guckel rings

4.2.3 Electrostatic Actuation

Wiring for electrostatic actuation was deposited on some of the samples. To understand how the MEMS structures will move in this situation, the forces involved will be modeled by considering two charged plates; one fixed, and one movable on a spring with spring constant k. This is schematically depicted in Figure 4.2.5. When modeled like this, the force balance equation is $F_e = F_r$ where F_r is the restoring spring force, and F_e is the electrostatic force. Assuming that the plate area A is much greater than the separation x between the plates, the electrostatic force between two parallel plates can be given by [141]:

$$F_e = \frac{A\varepsilon V^2}{2x^2} \tag{4.21}$$

where V is the applied voltage, and ε is the permittivity of the medium between the plates. For air, the permittivity is very close to $\varepsilon_0 = 8.85 \times 10^{-12}$ F/m[142].

The restoring spring force can be written as:

$$F_r = k\Delta x = kd - kx \tag{4.22}$$

where d is the initial starting separation between the plates, k is the spring constant, and x is the current separation between the plates. As can be seen from these equations, the electrostatic force F_e scales in relation to the inverse square of x, while the spring restoring force F_r only scales directly in relation to x. Therefore, as the voltage is increased and the plates near each other (i.e. x becomes smaller) there will be a point where F_e overwhelms F_r. If this occurs the top plate will

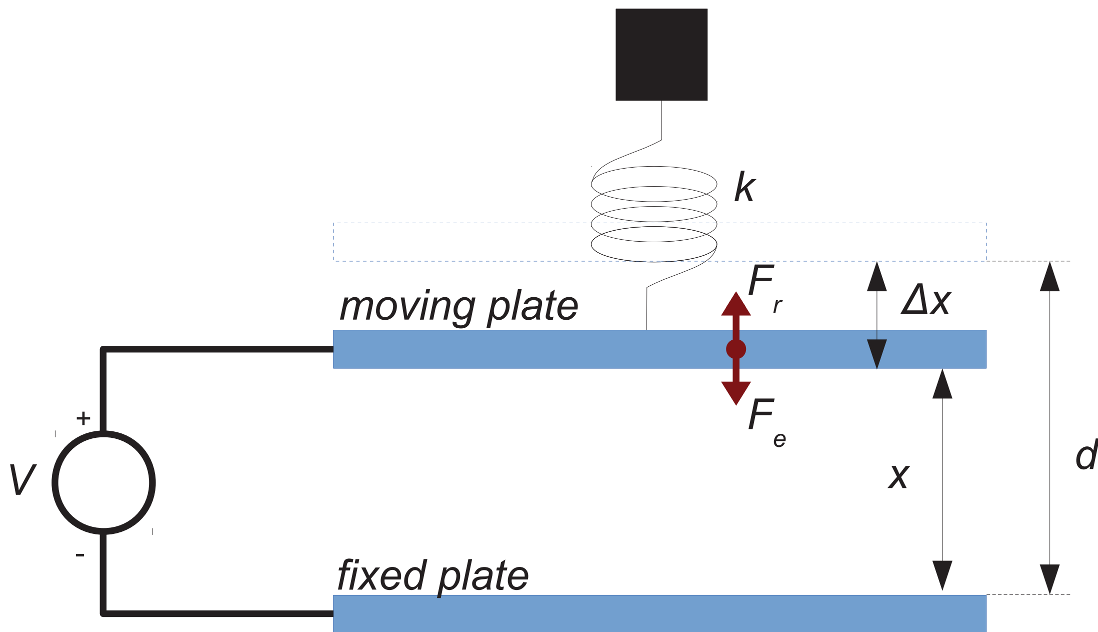

Figure 4.2.5: Electrostatic actuation of a cantilever modeled as two charged plates, one of which is movable on simple spring. At rest, the two plates are separated by distance d. When a voltage V is applied, the generated electrostatic force, F_e, draws the movable plate a distance Δx towards the fixed plate until F_e is balanced by the spring restoring force, F_r. If F_e large enough that it can overwhelm F_r, then snap down occurs.

snap down, and make contact with the bottom plate. In the case of surface micro-machined MEMS, the two deposited plates will be extremely flat, meaning that when the plates make contact, van der Waals intermolecular forces will become dominant, bonding the two plates together [143]. This phenomenon is called stiction, and can cause failure of the MEMS device.

It can be shown that if the spring constant k is indeed constant, then the beam can be deflected by up to one third of the initial plate separation (i.e. $\frac{d}{3}$) before snap down will occur. This is generally true for micro-cantilevers, however, due to effects such as strain stiffening, k is not constant, and it has been observed that doubly clamped beams can be deflected by up to one half of the initial plate separation ($\frac{d}{2}$).

4.3 Fabricated Devices

This section describes the properties of notable devices which were fabricated while refining the MEMS process. The micromachining process used to created these devices is given in Appendix E. A combination of optical microscopy, optical profilometry, and scanning electron microscopy was used to examine the devices.

4.3.1 MEMS Doubly-Clamped Beam

From the onset of the process development the total stress in the deposited beams was found to be tensile to varying degrees, as the diagnostic doubly-clamped beams did not bow in the manner demonstrating compressive stress. The effect of tensile stress on the doubly-clamped beams was to leave them very straight and flat after release. A surface optical profilometry image

of a beam of length of 220 μm is displayed in Figure 4.3.1. The beam is flat to less than 10 nm over the length of the beam. The methodology of the optical profilometry measurements in this thesis are discussed in Appendix F.

This degree of flatness served as excellent, flat mirrors above the diffraction gratings, forming an optical cavity suitable for the height measurement technique. The performance of this height measurement technique will be discussed further in Chapter 5. Vibrometer measurements of these microbridges give a resonant frequency of an average of 290 kHz. From Figure 4.2.3, this corresponds to a tensile stress of 27 MPa. The experimental methodology of the vibrometer measurements is discussed in Appendix F.

4.3.2 MEMS Cantilever

The allowable stress tolerance in machining flat micro-cantilevers is far less than that for doubly-clamped beams. In particular, stress mismatches can cause cantilevers to curve to such an extent that this effect has been used as a feature to lift other MEMS components above the substrate to heights that would not normally be possible using standard surface micro-machining. This effect has been demonstrated in the past with beam-steering micromirrors by depositing a high stress metal layer on polysilicon cantilever beams and using the resulting curvature of the beams to lift the micromirror up to 70 μm above the substrate [144].

The simulations in Section 3.5.2 predict that this technique is tolerant to MEMS beam tilt (up to 5.7° for 4 μm wide diffraction gratings), however, the highest sensitivity of the device occurs when the beam is flat. Therefore the cantilevers should be fabricated such that they are as flat as possible. One source of bending to be eliminated is caused by the differential stresses between the gold mirror underlayer and the SiN_x structural layer. Given the constraints that the gold mirror layer must be a minimum of 50 nm thick to allow high reflectivity in the infra-red, and that the metal evaporation process used for depositing this gold has no parameters available to control deposition stress, some of the options to balance the stress that were available are:

1. Modifying the thickness of the SiN_x structural layer.

2. Modifying parameters in the PECVD technique. Parameters available to change the stress of the deposited SiN_x are:

    - Relative mixture percentages of the silane and ammonia gases.
    - Deposition temperature.
    - Deposition Pressure.
    - RF power used.

3. Depositing a second gold layer above the SiN_x structural layer in order to balance the stresses from gold underlayer.

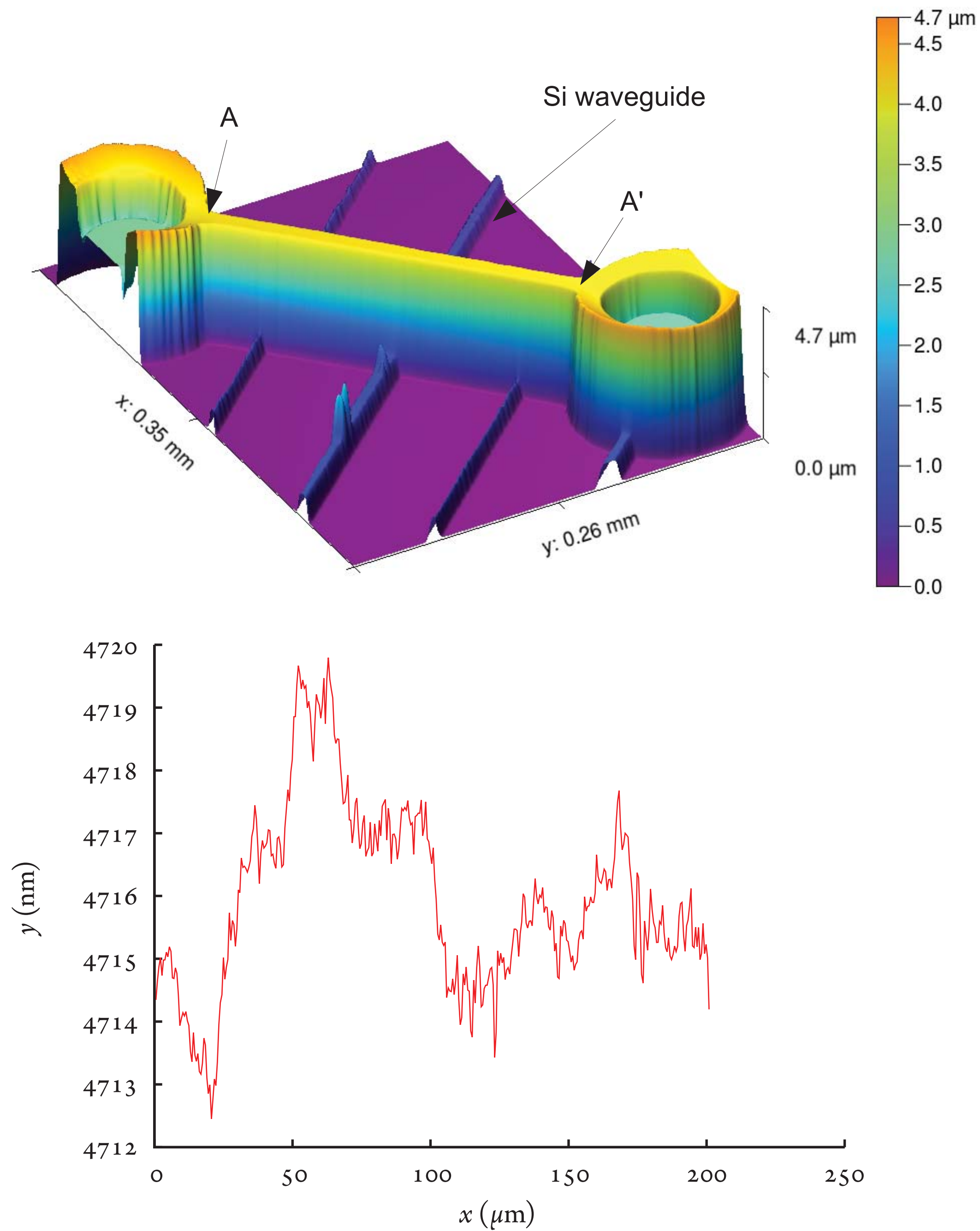

Figure 4.3.1: Sample doubly clamped beam fabricated over a photonic circuit. (top) Colourized 3D optical profilometry image. (bottom) Plot of the measured beam profile of cross-section AA'.

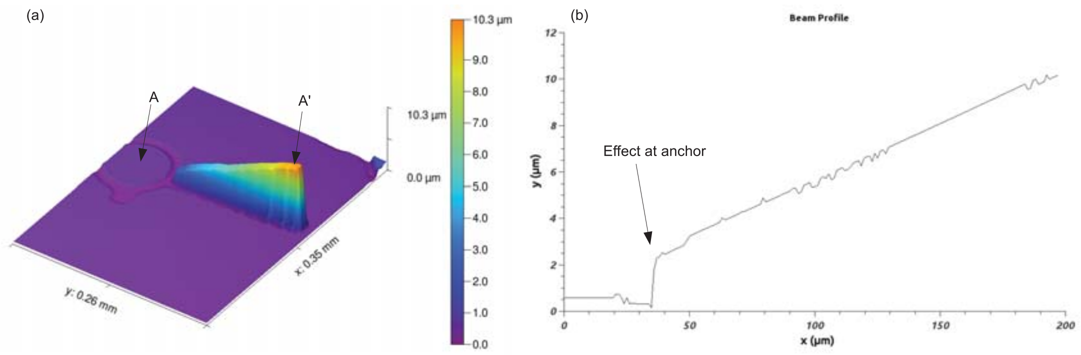

Figure 4.3.2: Sample cantilever fabricated without actuation pads. (a) Colourized 3D optical profilometry image of cantilever, (b) Plot of the measured beam profile of cross-section AA'. Note that the anchor shows only as a shadow in the profilometry image as there is no metal on that part of the device, and the SiN_x does not provide enough of a reflection for the profilometer to map an image.

4. Pre-stressing the substrate.
5. Post deposition stress modification (such as annealing).

Since the thickness of the SiN_x layer is a free parameter in the design, it was decided to modify this thickness to balance the stresses. To avoid additional changes due to anchor effect, initial experimentation was performed by depositing gold underneath the cantilever beam only, and not on the anchor. A sample cantilever fabricated in this manner is shown in Figure 4.3.2. It was found that a ratio of 50 nm of gold to 750 nm of SiN_x eliminates the undesirable curvature of the cantilever. This can be seen in Figure 4.3.2(b). An anchor effect remains, which is responsible for the angle at which the beam rises from the substrate. This angle could be further reduced by the use of an argon plasma treatment processing step, such as that demonstrated by Jiang *et al.* [145].

Structural Effect of Electrostatic Pads

Even though the polyimide used was spun on, it was found to cover the surface conformally. This became noticeable in the devices after deposition of the metallisation for the actuation pads on the substrate. Dektak stylus profilometry was performed on a 200 μm long micro-cantilever which had been processed up to the final release step. This measurement is shown in Figure 4.3.3(b), where the humps arising from the polyimide flowing over the actuation pads are clearly visible. Stylus profilometry cannot be performed on released devices, as even with very fine-grained control of the downward force of the stylus, the stylus will bend the cantilever, giving inaccurate measurements along the length of the device. Therefore optical profilometry was performed on the released device. The 3D plot is shown in Figure 4.3.3(a), and the beam profile is shown in Figure 4.3.3(c). After release, the impression left by the actuation pads is still discernible, as the SiN_x has kept the shape of the underlying structure.

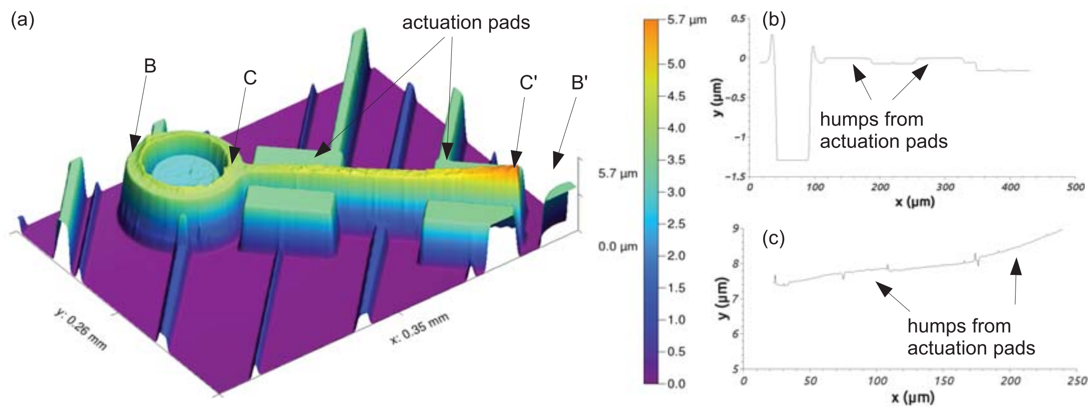

Figure 4.3.3: Sample released cantilever fabricated over a photonic circuit with actuation pads. (a) Colourized 3D Zygo optical profilometry image of cantilever, (b) Plot of the Dektak stylus profilometry measured beam profile of cross-section BB' for the unreleased device. (c) Plot of optical profilometry measured beam profile of cross-section CC' for the released device.

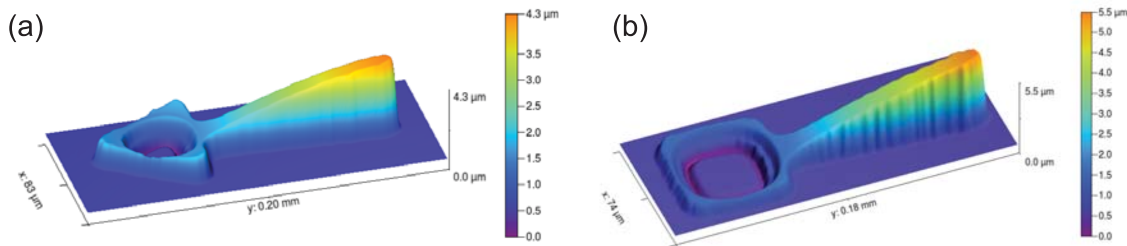

Figure 4.3.4: Anchor effect measurements. 3D Optical profilometry of released cantilever beam profiles for devices with (a) a triangular, and (b) a square top hat style anchor.

Anchor Effects

Due to the anchor effect observed in Figure 4.3.2(b), a number of alternate anchor geometries were fabricated in an attempt to lower the angle at which the beam leaves the anchor. Triangular, square and circular anchor geometries were fabricated on the same chip during the process run and compared. Figure 4.3.4 shows 3D optical profilometry images of two sample devices that were fabricated. The cantilever beams all had a length of 100 μm, width of 10 μm and thickness of 750 nm. Figure 4.3.5(a) is an optically measured profile from these devices, and shows that the beams for the cantilevers with square and circular anchors rise at a much steeper angle than the beam with a triangular shaped anchor.

The chip carrying these MEMS devices was attached to a piezo stack to induce external mechanical excitation, driving all the cantilevers into resonance. Since the cantilever beams in these devices all have the same length, thickness and width, their resonant frequencies are very close. Vibrometer measurements were made of their actuation velocities for different frequencies and are shown in Figure 4.3.5(b). From this figure, it may be seen that when the chip is subjected to vibration, a microcantilever with a circular anchor moves at a greater velocity than a microcantilever with a triangular anchor. From this it may be concluded that the same structural strength in the triangular anchor which helps decrease the upward bending of

the cantilever beam in relation to the cantilever with a circular anchor, also limits the motion of the triangular anchor cantilever beam at it's resonant frequency.

For the purposes of testing the optical cavity it is of interest to move the cantilever beam over as large a range as possible. Since the tilt upwards of the circular anchor cantilever is within the acceptable tolerances calculated in Section 3.5.2, this style of cantilever will be used rather than the triangular anchor style, since it has a larger movement range. However, future work where devices are made for sensing purposes may benefit from using triangular style anchors, due to the fact that the movement of flatter devices is more sensitively measured by the grating readout technique.

4.3.3 Guckel Rings

As mentioned earlier, Guckel rings were used as a diagnostic microstructure to test for tensile stress. The smallest rings of outer radius 90 μm buckled as seen in the example in Figure 4.3.6. From Table 4.2.1, this means that the stress is tensile, and has a value greater than 12.4 MPa. This is in agreement with the value for tensile stress obtained from measuring the resonant frequency of the microbridge in Section 4.3.1.

4.3.4 Mirror Roughness

At a wavelength of 1550 nm, films deposited must have a roughness less than $\lambda/20$ (<78 nm) for them to act as good quality optical mirrors in the infrared. To determine the roughness of the underlayer mirror, a sample chip was prepared with a coating of polyimide, followed by an evaporated coating of chromium and gold. The resulting surface was then measured using a Zygo Optical profilometer over a length of 1.25 mm. This profilometer has a vertical resolution of < 0.1 nm. The profile measured is shown in Figure 4.3.7. The root mean square (RMS) roughness was found to be less than 1 nm, and the maximum roughness height to be 3 nm. This roughness is not large enough to materially effect the reflections of infra-red light at wavelengths around 1550 nm, allowing this process to be used to produce mirrors for the experiment. Low frequency waviness and bowing of the beams will have a substantially greater effect on mirror performance than the roughness of the surfaces that have been deposited.

4.4 Device Design and Fabrication Conclusions

This chapter presented the design and fabrication process for the test devices. The design of the main optical components - diffraction gratings, and waveguides were presented. The fabrication process of the MEMS structures was detailed. The tensile stress in the devices resulting from the process was estimated from measurements to be 27 MPa, which produces both micro-cantilever and microbridge devices which are within the design constraints acceptable for the purposes.

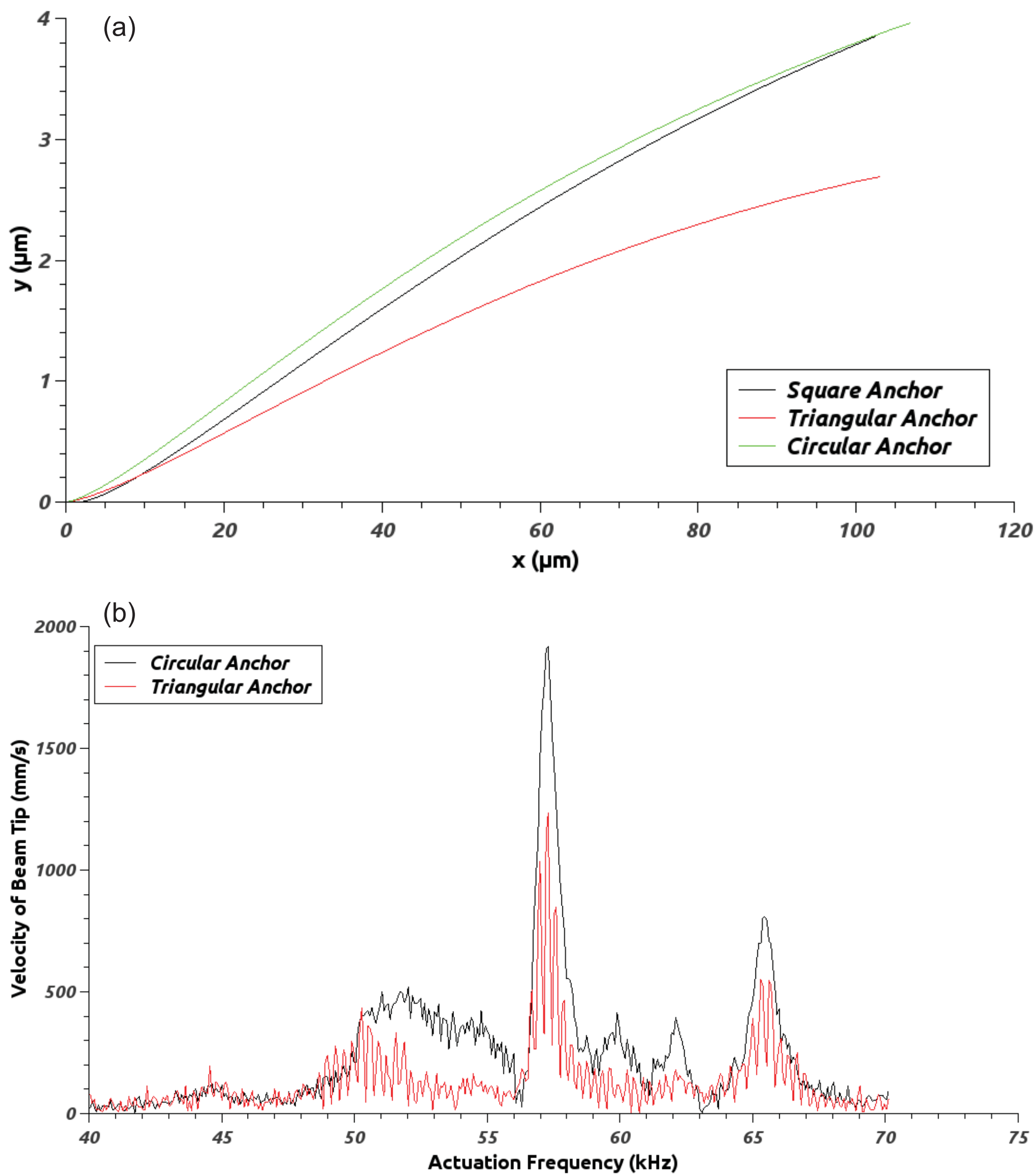

Figure 4.3.5: Anchor effect measurements. (a) Optical profilometry of released cantilever beam profiles for devices with a square, triangular and circular anchor (b) Vibrometer speed measurements for cantilevers with a triangular and circular anchor.

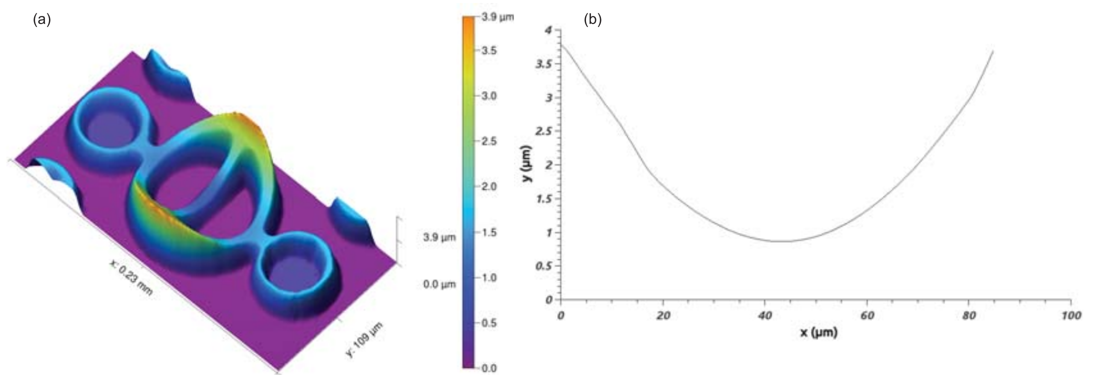

Figure 4.3.6: Guckel ring measurements. A buckled Guckel ring with initial pre-released outer radius of 90 μm (a)3D Optical profilometry of the ring (a) Profile of the middle cross-bar.

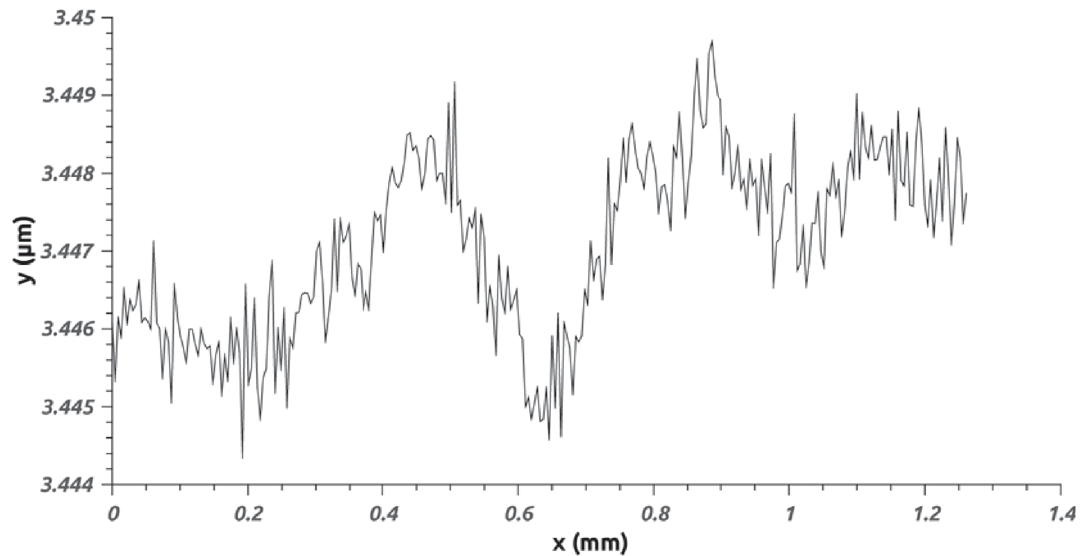

Figure 4.3.7: Optical profilometry of a film of polyimide and gold deposited on a silicon substrate.

The RMS roughness of the mirror layer when unreleased was measured to be less than 1 nm, which is suitable for operation at the wavelengths that will be used with the device.

The next chapters will test these devices, allowing comparison between the modelled expectations and experimental observations.

The whole is greater than the sum of its parts.

Aristotle

5

Demonstration of Readout Technique

Once suitable devices are fabricated, the position readout technique can now be demonstrated. This chapter details the experimental setup used to analyse the MEMS devices and test the optical cavity. The capability of the grating system to accurately detect heights is demonstrated and shown to be effective for both microbridge and microcantilever structures. The wide bandwidth of grating in the infrared is demonstrated and leveraged to demonstrate a technique to remove positional ambiguity arising from the inteferometric nature of the readout system.

5.1 Reference Measurements

To calibrate the change in optical output from the device resulting from the motion of the MEMS, it is necessary to perform reference measurements so that it is understood how the MEMS devices move relative to the grating under actuation conditions. An optical profilometer was used to measure the position of the MEMS device at rest. A laser doppler vibrometer was used to measure the motion of the MEMS when excited both electrically and through external mechanical forces (piezo-transducer). These static and dynamic characteristics were compared to the optical outputs of the devices when the MEMS components were subjected to the same actuation conditions. Further details about the reference measurements are supplied in Appendix F.

5.1.1 Reference Measurements - Optical Profilometer

The optical profilometer used was a Zygo NewView 7300 system. This is a non-contact surface profile measurement system based on white light interferometry capable of a vertical resolution of less than 0.1 nm, and a lateral resolution of between 0.36 and 9.50 μm, depending on the lens objective used. This instrument gives an extremely accurate measure of the surface profile of the MEMS structures. As this instrument measures the surface profile only, 3D visualizations created with data from this system (such as Figure 5.5.2) will show a solid "curtain" effect for regions beneath suspended structures, even though those regions may be empty.

5.1.2 Reference Measurements - Vibrometer

The vibrometric system used was comprised of a Polytec OFV-5000 laser doppler vibrometer controller with a DD-500 displacement decoder, and an OFV-552 differential fiber sensor head. This system was used to monitor the MEMS devices when they were in motion in order to measure their mechanical resonance frequency and quality factor, and to calibrate the extent of their motion under various stimuli.

5.2 Experimental Setup - Optical alignment and Coupling

Optical power is coupled into and out of the device through the use of two flat-cleaved, bare end SMF-28 single mode optical fibers. The input laser has a FC/PC output, and is coupled into an optical isolator to avoid back-reflection from the device. The isolator is then connected to a three-paddle polarization controller. As mentioned in Section 3.4, the input diffraction grating couplers integrated onto the microchip samples are extremely polarization sensitive and couple most light into the waveguide when the light is TE polarized, so this polarization controller is used to adjust the input light to this polarization and couple maximum power into the chip.

The polarization controller is then connected to the cleaved fiber. The cleaved fiber is held in place by a fiber chuck, and clamped into a goniometer with two degrees of freedom. The goniometer is attached to a translation stage, which has three degrees of freedom. This stage is used to adjust the position of the fiber. This bare fiber end is suspended above the input grating of the microchip. A bright white light source was used to illuminate this region. A microscope objective was connected to a CCD camera and focused on the grating. Through this camera, the image of the fiber, and the image of the shadow of the fiber cast by the illumination source were used to coarsely align the fiber with the input grating. A typical image from the CCD camera is shown in Figure 5.2.1.

The CCD camera is mounted on a rail which runs parallel to the direction of the photonic waveguides on the microchip sample. As a result, the camera can be slid along the rail to image the photonic waveguide from the input to the output without disturbing the microchip or the coupling fibers. With the camera pointed at the output grating, the same coarse alignment technique using the CCD camera, and rotational/translational stages can be used to align the

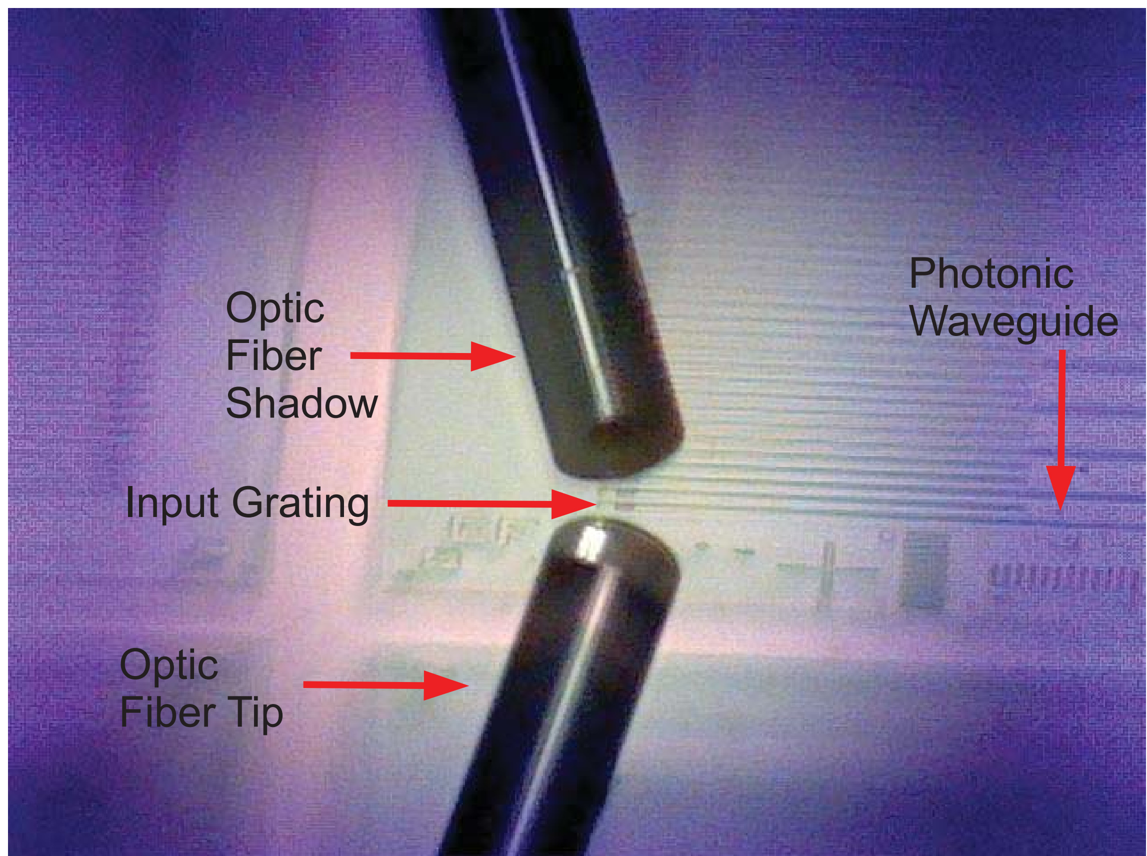

Figure 5.2.1: Typical CCD camera image used for the alignment of input/output fiber tips to diffraction input/output gratings on the microchip.

cleaved fiber output to the output grating. The output fiber was connected to an InGaAs photodiode, which was connected in turn to a transimpedance amplifier. The photodiode output voltage was measured using a Rigol DS1204B digital oscilloscope. Once a small voltage increase was detected, the translation stage positions were adjusted to improve the fiber/grating couplings such that the power transmitted through the microchip was at maximum.

In addition, the microchip samples were mounted on two translation stages, giving the ability to move the chip independently of the optics fibers. A single microchip contained multiple devices demonstrating the microcavity technique. Once fine alignment was achieved a specific device, this microchip translation capability was useful for moving the chip to a coarse alignment position for a different device.

5.2.1 Lasers and light sources

As mentioned previously, the gratings and photonic waveguides were designed for the near infra-red region of the electromagnetic spectrum, and optimised for a wavelength of 1550 nm (see Section 4.1). Lasers at a wavelength of 1470, 1550, 1585, and 1610 nm were used as device input light sources. The available powers ranged from 1 mW to 18.8 mW.

The 1550 nm laser used was an Amonics ADFB-1550-20B optical light source. This laser can provide power in the of 1 to 18.8 mW. The 1585 nm laser used was a LDLS-02 light source Fabry-Pérot laser diode with a power range of 0 to 1.5 mW. The 1470- and 1610-nm light sources

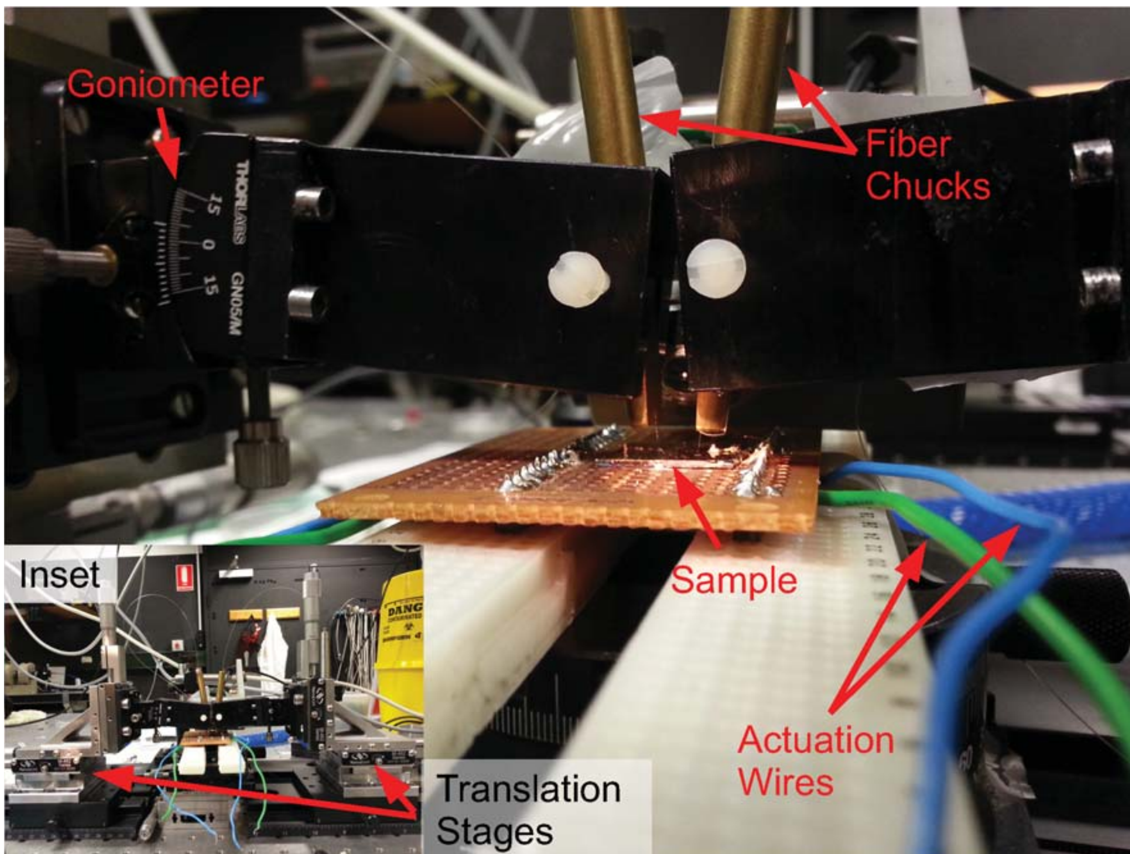

Figure 5.2.2: Photo of the laboratory experimental setup. Main image is a close up of an electrically actuated sample sitting on a chip carrier and fed light via optic fibers suspended in brass fibre chucks. The inset shows an image of the optical station which includes the translation stages used to align the fiber optics to the sample.

were laser diodes powered by a custom built laser diode driver. The 1470 nm laser had a power of 2.33 mW, and the 1610 nm laser had a power of 5.99 mW. A supercontinuum light source was used to measure the performance of the gratings at wavelengths from 900 to 1700 nm.

The light sources were calibrated using a HP 86142A optical spectrum analyzer.

5.2.2 Optical Attenuation

The main source of optical power loss in the experimental setup was from the coupling of light from the optical fibers into and out of the microchip sample via the input and output diffraction gratings. By launching light into an input diffraction grating of a waveguide with no interrogation grating, and measuring the output from a diffraction grating at the end of that waveguide, the minimum total loss for the 1585 nm laser was measured to be 15.5 dB. Assuming a typical SOI slab waveguide loss of 2 dB/cm [129], over the 1.5 cm length of the waveguide, the insertion loss fiber-to-waveguide (through the grating) to be 6.25 dB at each end. This closely matches the 6 dB previously demonstrated for this coupling technique [127], indicating excellent coupling into and out of the waveguides.

5.3 Grating Characterisation

To characterise the wavelength dependent loss of the gratings and determine whether they were fabricated correctly, a supercontinuum light source was used to launch light into the gratings and waveguides over an optical wavelength range from 1100 to 1700 nm. The photonic circuit on the microchip used to perform this characterisation did not contain an interrogation grating or cantilever, but was simply an input grating, into a waveguide, which led to an output grating. The output power of this light source is constant to within 10 dBm for the wavelength range from 1100 to 1600 nm. Figure 5.3.1 shows the calculated transmission (wavelength dependent loss) through a waveguide only device (no interrogation grating), obtained by normalizing the measured power from the output coupler using the supercontinuum spectrum. It can be seen that the setup is fairly efficient in light transmission in the ranges of 1200-1300 nm and 1500-1600 nm. It is clear that higher order coupling occurs around 1200 nm, and it is most likely these waveguides become multimode below this wavelength. The peak in transmission is measured to be at 1590 nm. Another low loss transmission window appears above 1700 nm (possibly due to coupling into the cladding layer), unfortunately, the optical spectrum analyser available did not reach that far into the infrared, and so this wavelength region was not investigated further.

5.4 Microbridge

The first ever demonstration of the position sensing technology at the core of this thesis was performed using a MEMS microbridge suspended over a grating interrogator [146]. As detailed in Chapter 4, the microbridges were fabricated using a surface micro-machining process. These

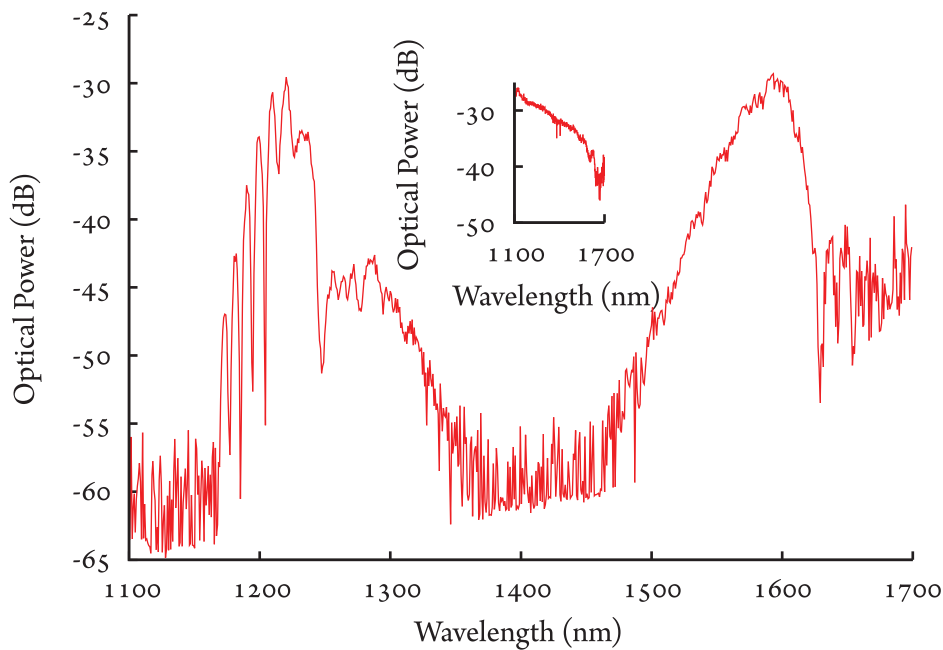

Figure 5.3.1: Optical spectrum of the normalised output from a sample chip when using the supercontinuum light source as an input. Inset shows the output of the supercontinuum light source.

microbridges were fabricated without electrostatic actuation pads, and were also made slightly tensile in order to produce a flat mirror over the interrogating grating. The microbridges were actuated piezoelectrically by connecting a piezoelectric stack to the underside of the substrate of the chip. A colourized SEM image of one of the fabricated microbridge devices tested using external piezo driven mechanical actuation is shown in Figure 5.4.1.

Microbridges under tensile stress have a much higher resonant frequency than microcantilevers of the same length (see Chapter 4) and so are an excellent structure for operating in dynamic mode. This is because the sensitivity of the MEMS device is improved at high frequencies [147]. However, operating at higher order resonant modes makes detection schemes more complex and the associated smaller displacements of microbridges over cantilevers are more difficult to measure using non-optical techniques [148], which has led to most MEMS chemical sensing work being focusing on cantilevers rather than microbridges. In this section it will be shown that the detection scheme is capable of high resolution position detection of microbridges.

5.4.1 Microbridge Piezoelectric Actuation

The piezoelectric actuator used to externally mechanically excite the microbridges was a NEC Corporation AE0203D04F piezoelectric stack, and was controlled by an Agilent 33220A arbitrary waveform generator. The actuator was bonded to the microchip using a temporary, water soluble mounting wax (Crystalbond 555). This piezo actuator was used to drive the various beams on the chip at their resonant frequency. At the microbridge resonance, the typical movement range of the microbridges was measured to be 250 nm.

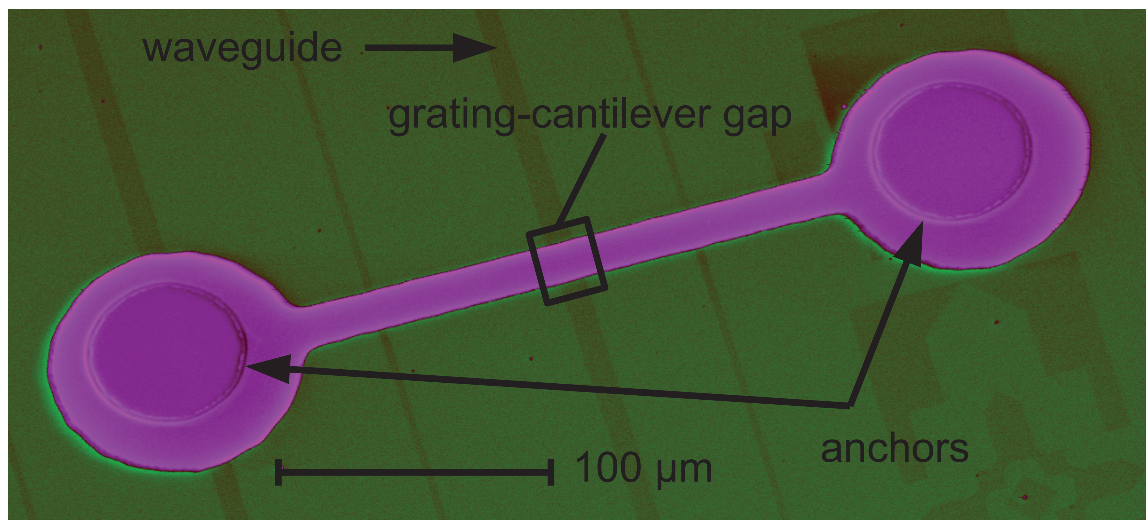

Figure 5.4.1: Colourized SEM image of the fabricated microbridge.

5.4.2 Microbridge Characterization

A specific beam was chosen to be extensively characterized and tested. The beam flatness was measured using the optical profilometer, and the resonant frequency of the beam was measured with the laser Doppler vibrometer. The surface profile of the examined beam was shown in Figure 4.3.1, where it is evident that the microbridges are flat in the region above the grating. At rest, the beam was found to be suspended 1.6 *um* above the surface of the chip.

For resonant frequency measurement a waveform generator was used to drive the piezo with a sine wave variable frequency sweep. The relative motion between the microbridge and the substrate was measured using the differential vibrometer. This is achieved by focusing the reference laser from the vibrometer onto the substrate, and focusing the measurement laser from the vibrometer onto the microbridge. The actuation frequency which causes greatest motion of the beam is the resonant frequency. The resonant frequency of this beam was measured to be 291 kHz.

5.4.3 Microbridge Optics Measurements

The microbridge was actuated by driving the piezo at the microbridge resonant frequency of 291 kHz while the transmitted 1585 nm optical power from the chip was monitored. Figure 5.4.2 presents the optical power output as well as the separation between the microbridge and the interrogating grating as a function of time. As can be seen from Figure 5.4.2, the optical power is modulated as the distance between the underside reflector on the microbridge and the grating changes. The power output is not completely monotonic over the range that the microbridge is actuated. This is due to the interferometric nature of the technique, and is expected.

The measured transmitted optical power is shown in Figure 5.4.3 as a function of the gap, alongside the optical FDTD simulation first presented in Chapter 3, which gives the ratio of optical output power to input power. Excellent agreement between the theoretical and

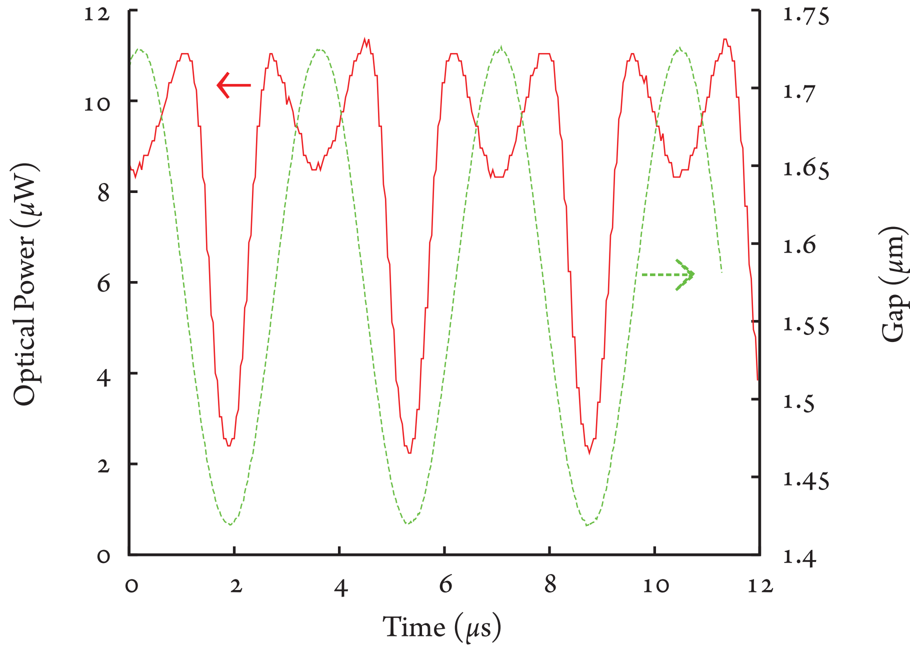

Figure 5.4.2: Measured 1585 nm laser optical power and displacement for the actuated microbridge with respect to time.

experimental results is evident. Slight discrepancies between the model and the experimental results are due to the assumed perfect reflector in the model, and the use of a 2D model which did not include optical fringing effects or mechanical dynamics at resonance.

The experiment was repeated at wavelengths of 1550 nm and 1610 nm. The normalized optical power through the sensor from all three lasers are shown in Figure 5.4.4 with each measurement normalized to it's peak power. The transmission maxima are shifted to occur at different microbridge gaps from the waveguide due to the changing wavelength of the lasers. This effect is useful for extending the gap range for applications which require a larger range of operation. These results demonstrate that the device operates in a systematic manner over a wide range of wavelengths, enabling wave division multiplexing (WDM) techniques to be utilised towards addressing large numbers of MEMS beams on a single chip array in a scheme such as that shown in Figure 3.5.7.

An actuation sweep was performed for frequencies around the resonant frequency of the microbridge by driving the piezo at a fixed sine wave amplitude voltage for various frequencies. The optical power transmitted through the device is shown in Figure 5.4.5.

An estimate of the quality factor, Q, of the beam can be made using [149]:

$$Q = \frac{f_o}{\Delta f} \tag{5.1}$$

where f_o is the resonant frequency of 291 kHz, and Δf is the 3 dB bandwidth. From the data in Figure 5.4.5 a Q of 153 can be calculated.

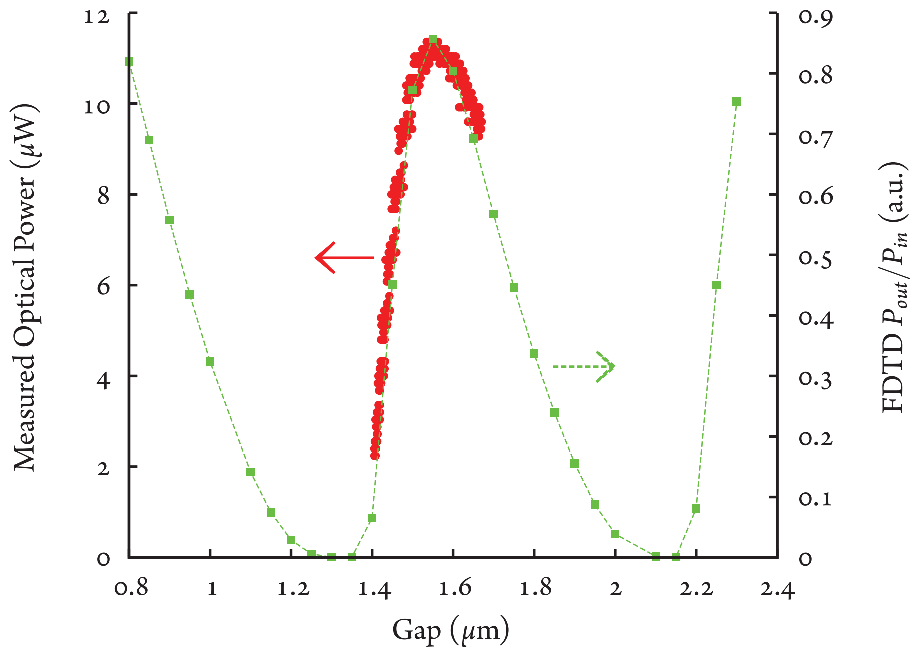

Figure 5.4.3: Measured 1585 nm optical power transmitted through the device for several vibration cycles of the suspended microbridge compared to 2-D FDTD simulation results as a function of the gap.

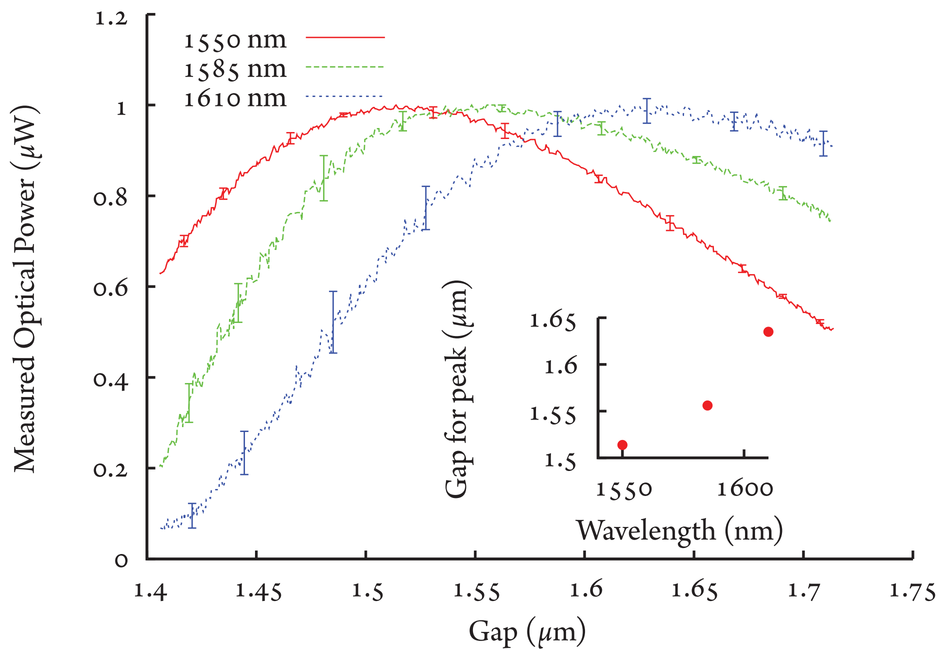

Figure 5.4.4: Measured 1550- 1585-, and 1610 nm optical power transmitted through the device for several vibration cycles of the suspended microbridge. Error bars show the extent of measured variation. The inset shows the gap for peak optical transmission shifting as a function of laser wavelength.

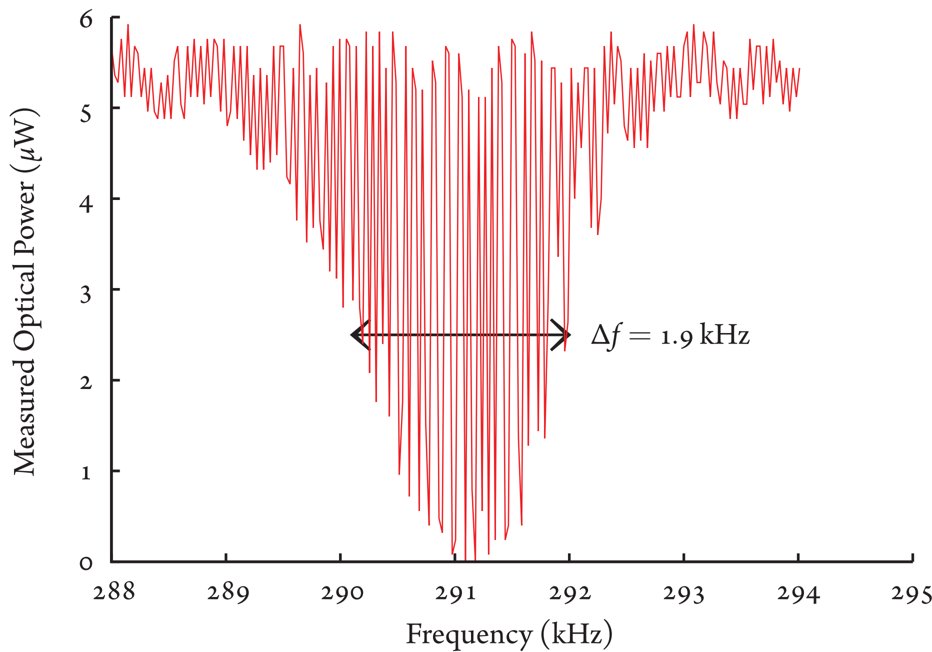

Figure 5.4.5: Measured optical power transmitted through the device for an actuation frequency sweep from 288-294 kHz.

5.5 Microcantilever

Microcantilevers are an essential component required in the fabrication of atomic force microscopes. They are also the core component of static mode MEMS biological and chemical sensors. Both these applications require a technology capable of accurate measurements of the deflection of the cantilever beam. This section demonstrates the applicability of the technique towards this goal via measurement of cantilever suspension height. The microcantilever was fabricated using a similar surface-micromachining technique as the microbridge above that was presented in Section 5.4.

5.5.1 Electrostatic Actuation

Electrostatic actuation pads were evaporated onto the sample substrate beneath the cantilever beam as a bottom electrode. The gold undercoat layer of the cantilever served as both the reflective mirror and the top electrode for electrostatic actuation of the cantilever. A silver epoxy was used to bond thin gold wire from the chip to a break out board. The Agilent 33220A arbitrary waveform generator (voltage range 0-10V) was used to drive the microcantilever directly for small (less than tens of nm) movements, for large (μm range) movements cantilevers were driven by a Tegam Model 2350 dual channel high voltage precision power supply having a 50x gain and capable of output voltages up to 400 V_{pp}.

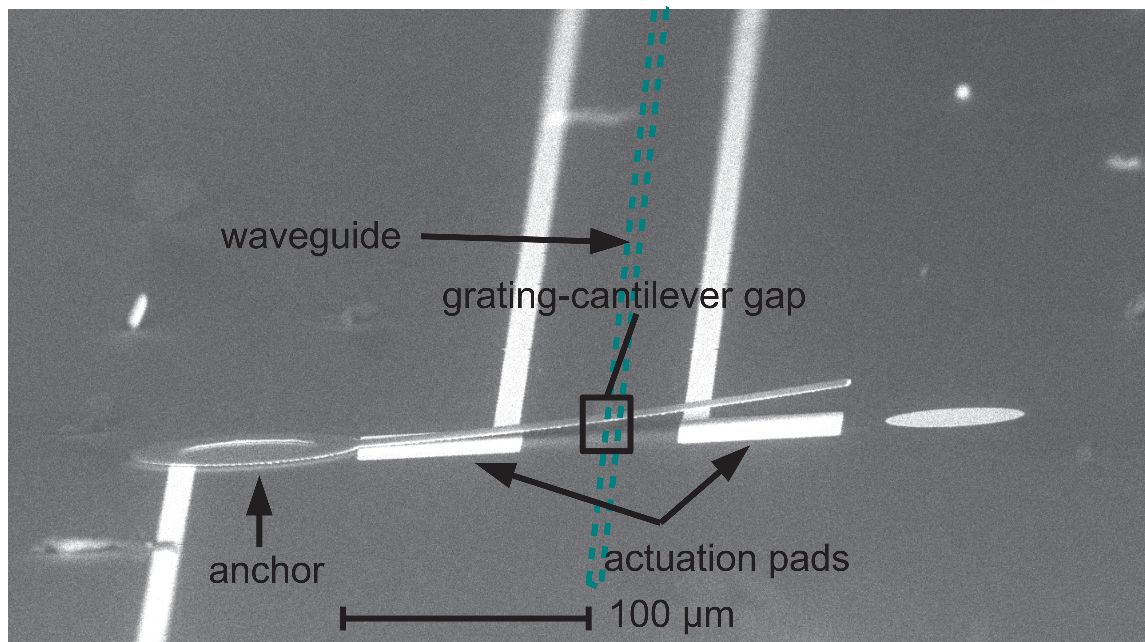

Figure 5.5.1: SEM image of a microcantilever. Note that the optical waveguide does not appear in an SEM image as it is below the SiO_2 planarization layer. The dashed line is drawn on the image to indicate the position of the optical waveguide.

5.5.2 Cantilever Characterization

A specific cantilever was chosen for characterization and testing. An optical profilometry image of the cantilever is shown in Figure 5.5.2. This cantilever is not perfectly flat, but is rather deflected upwards from the anchor to the tip due to relief of residual stresses. When the cantilever is at rest, the tip of the cantilever beam is 11.5 μm higher than the region of the beam near the anchor. The resonant frequency of the cantilever was measured using the vibrometer to be 13.2 kHz (significantly lower than the microbridges).

For investigated cantilever (shown in Figure 5.5.2), the grating is placed underneath the mid point of the cantilever beam (rather than underneath the tip). Therefore, all cantilever position and movement measurements from this point on will refer to the region above the grating unless otherwise specified. When actuated at its resonant frequency, the gap between the grating and the reflective underside was measured to range from 4.3 to 6.5 μm using the vibrometer. Figure 5.5.3 shows the cantilever response to actuation at its resonant frequency as a function of actuation voltage.

5.5.3 Cantilever Optical Response

The cantilever was electrostatically actuated at its resonant frequency of 13.2 kHz. The measured transmitted optical power output as a function of time is shown in Figure 5.5.4. At the smallest amplitude actuation (5 V), the optical output follows a sine wave similar to the motion of the cantilever. As the movement of the cantilever becomes larger due to increasing actuation voltage, the output becomes increasingly more non-linear. The output goes through a series of

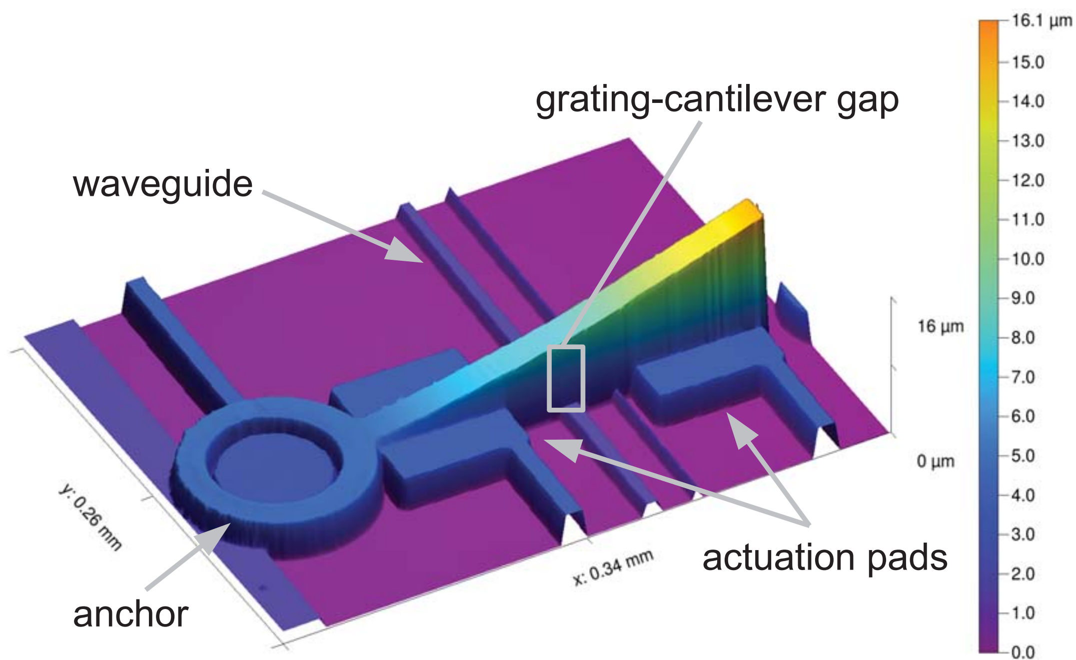

Figure 5.5.2: Optical surface profile of the microcantilever to be analysed.

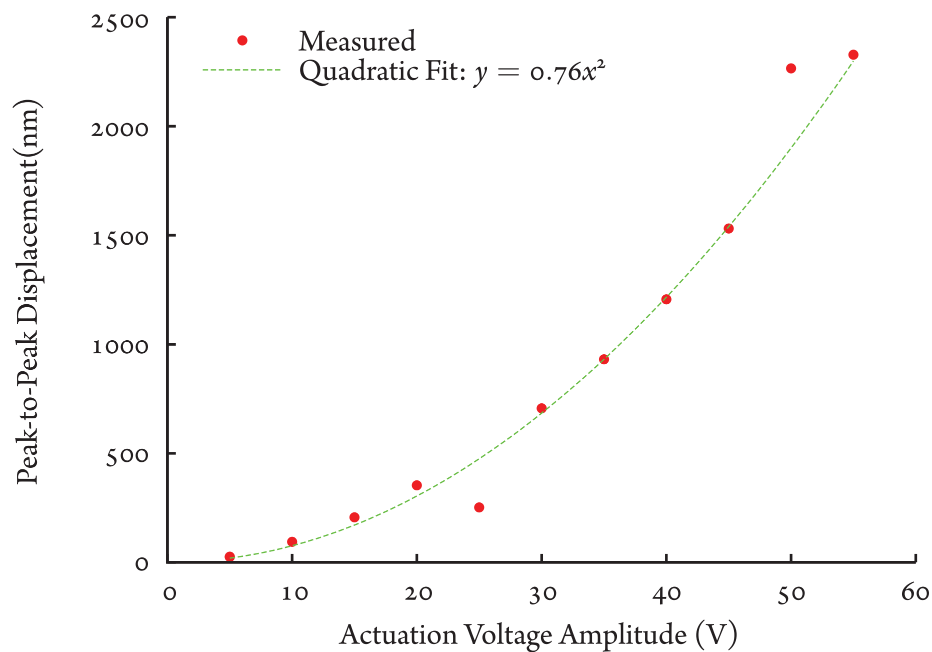

Figure 5.5.3: Measured cantilever peak-to-peak displacement amplitude as a function of sinusoidal wave actuation voltage at the microcantilever's resonant frequency.

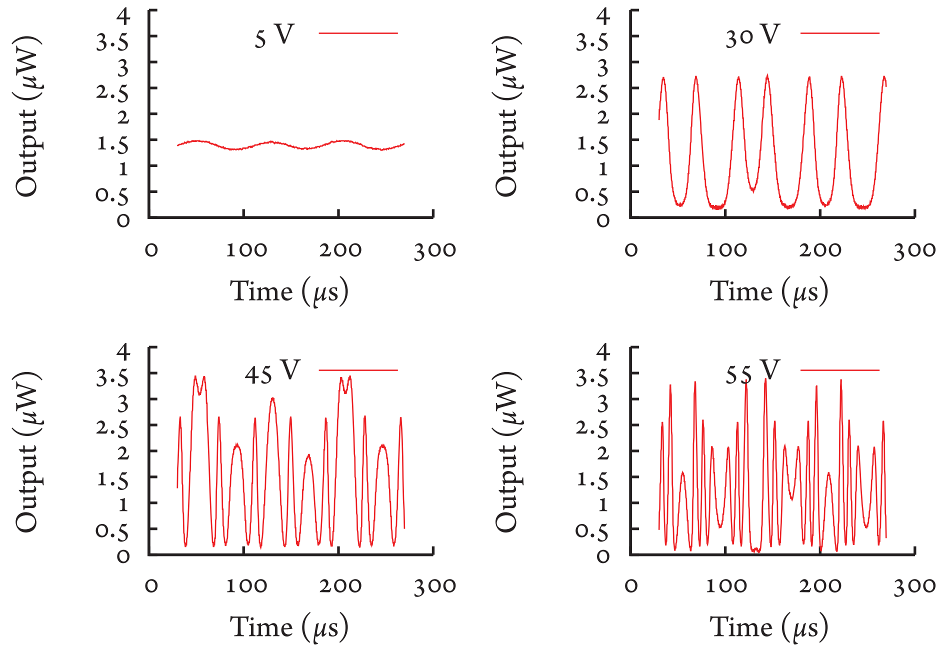

Figure 5.5.4: Transmitted optical power from grating ($\lambda = 1585$ nm) when the microcantilever is actuated with a sinusoidal signal of various voltage amplitudes at the microcantilever's resonant frequency.

optical maxima and minima defined by the interferometric effect of the optical microcavity between the grating and the cantilever, as detailed in Section 3.5.2.

The measured transmitted optical power at a wavelength of 1550 nm is shown in Figure 5.5.5 as a function of cantilever-grating gap. A very strong amplitude modulation due to gap change is evident. As the modulation effect is inteferometric in nature, the amplitude does not monotonically increase, but rather can be seen to be periodic with respect to the gap distance with maxima and minima separated by 400 nm as predicted by Equation 3.5. Figure 5.5.5 includes an overlay of a 2-D FDTD simulation of the expected outputs of the structure.

The measured results show good agreement with the simulated results, however, it can be seen in Figure 5.5.5 that the peak amplitude of each cycle in the measured results decreases by a greater margin than the simulation predicts. The most significant factor causing this can be attributed to the fact that the 2-D simulations do not take into account the deflection angle of the cantilever as it moves, and so do not consider light lost by reflection away from the grating. Other less significant factors that could be related to this discrepancy between the modeled and experimental results could be associated with effects such as optical fringing and the mechanical dynamics of the beam at resonance.

The experiment was repeated using 1585, and 1610 nm wavelength lasers and the corresponding results are shown in Figure 5.5.6. The technique is seen to be quite broadband, which will be of use for both applications wishing to address multiple cantilevers via the WDM scheme proposed in Figure 3.5.7, or as a Vernier technique to more explicitly determine

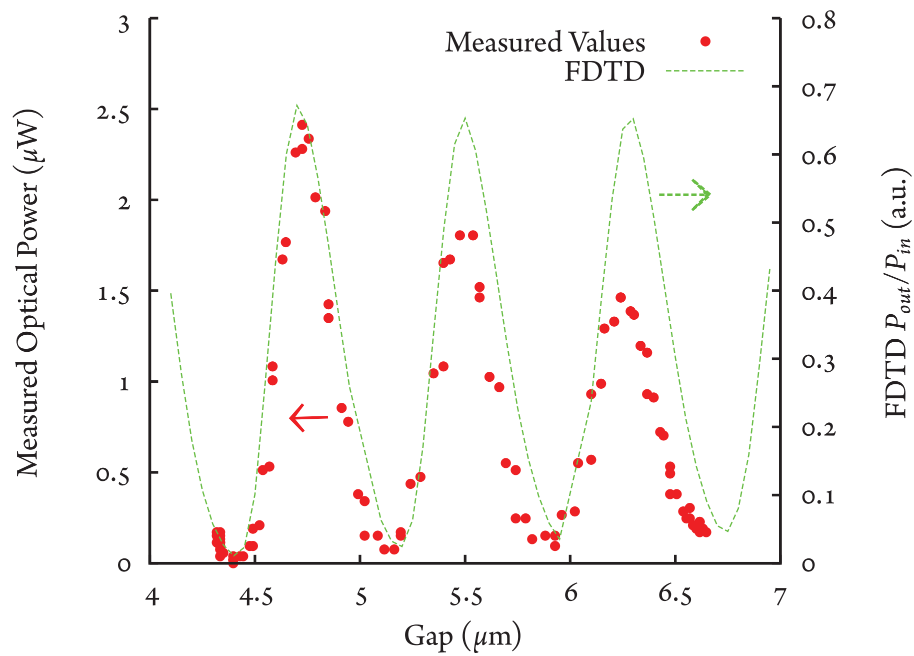

Figure 5.5.5: Measured and FDTD simulated optical output of the device for a 1550 nm laser vs cantilever-grating gap.

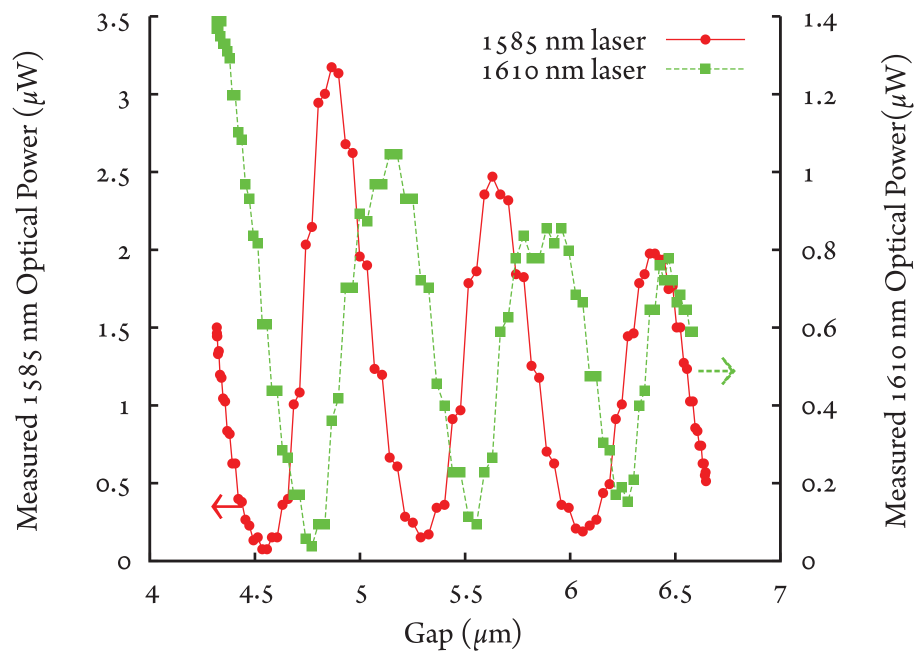

Figure 5.5.6: Measured optical output of the device vs cantilever-grating gap for 1585 and 1610 nm light. Differing y-axis scales are used here due to the experimental setup having different coupling efficiencies for the various laser wavelengths tested.

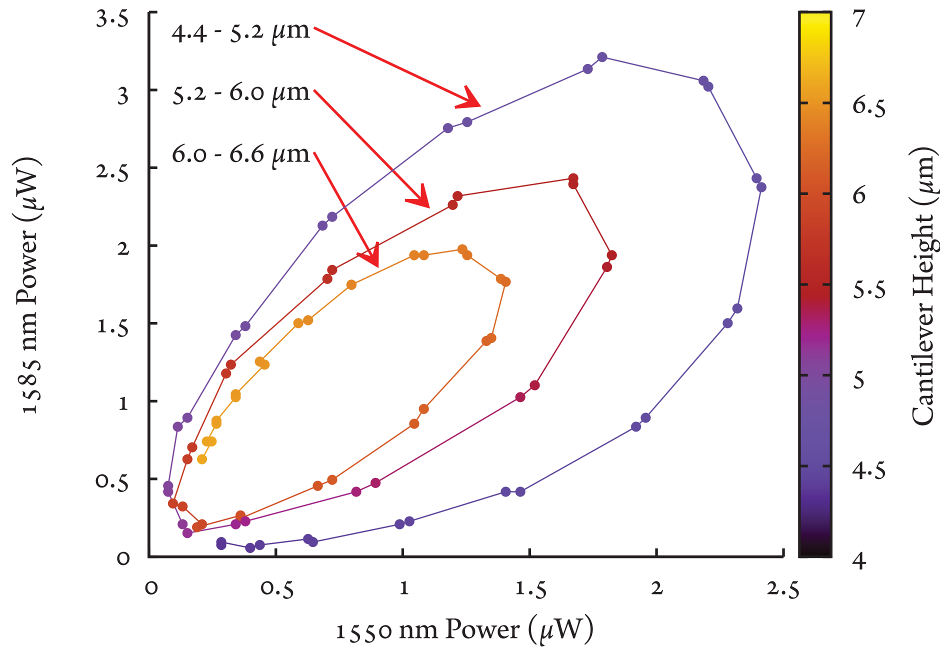

Figure 5.5.7: Locus of points obtained by comparing measured 1550- and 1585 nm wavelength output power for matching cantilever positions as the cantilever beam travels from through its movement range. Each arm of the spiral represents approximately an 800 nm segment of the distance the cantilever oscillates through (indicated by both arrows and colour shading).

position for a single cantilever (proposed in Figure 5.5.7).

As optical interferometric techniques are not monotonic, the cantilever position readout can be ambiguous if the range of movement of the MEMS being measured is greater than the periodicity of the interferometer (seen in Figure 5.5.6). This ambiguity would cause problems for sensors requiring position measurements over a large dynamic range. To demonstrate that this problem can be mitigated, Figure 5.5.7 shows the locus of points obtained when the 1550 and 1585 nm wavelength output signals for the same cantilever positions are plotted against each other. This figure shows that the locus follows a spiral, and so the positional ambiguity can be resolved for most positions between 4.4 and 6.6 μm as indicated by the colour scale. The amplitude decay noted in Figure 5.5.5 assists this effect - the arms of the spiral would not be so widely separated if the amplitude roll-off did not occur.

The position of the cantilever for the low optical powers in the bottom left corner of Figure 5.5.7 may be difficult to discern, this could be solved by either improving the signal to noise ratio through the use of higher powered input lasers (or more efficient input/output coupling), by choosing laser wavelengths that do not approach power throughput local minima at cantilever-grating gap positions which are near each other, or by adding a third laser wavelength.

5.5.4 Cantilever Frequency Sweep

Towards the experimental investigation of the sensitivity, the optical output of the device was connected to a Stanford Research Systems SR830 lock-in amplifier, and the cantilever was

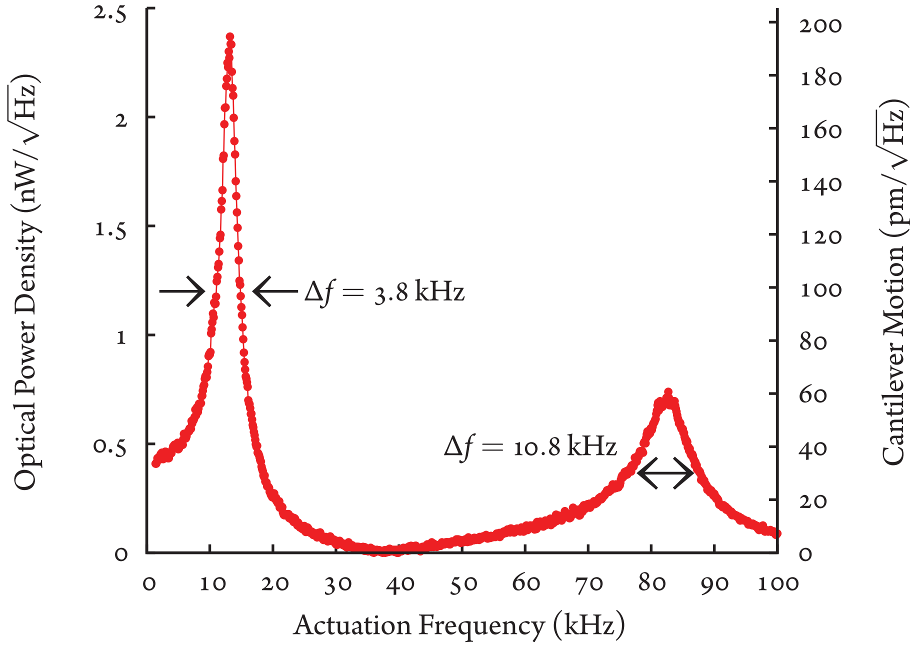

Figure 5.5.8: Measured optical response of the readout technique when the microcantilever is subjected to a frequency sweep from 1 to 100 kHz using sine wave actuation with a peak to peak voltage of 10 mV.

electrostatically actuated with a sinusoidal signal having a peak-to-peak voltage of 10 mV for frequencies between 1 kHz and 100 kHz. The time constant of the lock-in amplifier was set to 100 ms, and the lock-in filter slope was set to 12 dB/oct. Figure 5.5.8 shows the transmitted optical power density ($\mu W/\sqrt{Hz}$) and the corresponding cantilever motion ($pm/\sqrt{Hz}$) as a function of actuation frequency. These measurements show a resonant frequency peak at 13.2 kHz, matching the measurements made using the commercial vibrometer. A second peak is seen at 82.7 kHz and corresponds to the first harmonic frequency. The ratio between the peak magnitudes of the resonance frequency of 13.2 kHz and the first harmonic frequency of 82.7 kHz is 6.267.

The harmonic frequencies of a cantilever are found from the solutions to the frequency equation for a cantilever beam [150]:

$$\cos(k_n L)\cosh(k_n L) = -1 \tag{5.2}$$

where L is the length of the beam, and k_n is defined by:

$$k_n^4 = \frac{4\pi^2 f_n^2 \lambda_m}{EI} \tag{5.3}$$

where f_n are the natural frequencies of the beam, λ_m is the linear mass density of the beam, E is the Young's modulus and I is the area moment of inertia. The first two solutions of Equation 5.2 for $k_n L$ are 1.875 and 4.694. Therefore from Equation 5.3, it is found that the ratio f_2/f_1 to equal k_2^2/k_1^2 or 6.267. This matches the measurement of frequency ratios from the lock-in amplifier extremely well, confirming that the cantilever beam is resonating in near perfect agreement with

theory, and that the technique is accurately sensing the motion of the microcantilever.

An estimate of the quality factor, Q, of the beam can be made using Equation 5.1, where f_0 is the resonant frequency of 13.2 kHz. From the data in Figure 5.5.8 it is seen that at FWHM $\Delta f = 3.8$ kHz. The estimate of Equation 5.1 is only mathematically accurate for high values of Q. For the cantilever being examined, this calculation gives a Q of 3.5. The quality factor of the beam when vibrating at the second mechanical mode can be calculated by the same technique to be $82.7/10.8 = 7.7$.

5.5.5 Cantilever Step Response

The resonant frequency of the cantilever can also be obtained by applying a small step voltage to the beam, and then measuring the mechanical or vibrational response. This capability is especially useful for dynamic mode MEMS gas sensors where a simple test for resonance frequency of the cantilever is required. This response for the device is shown in Figure 5.5.9, where a typical underdamped second order step response for the beam is observed, with oscillations near the resonant frequency and an exponential decrease in oscillation magnitude due to damping. The logarithmic decrement technique can be used to find the damping ratio, ζ, of an underdamped system in the time domain. First the logarithmic decrement, δ, is found by [150]:

$$\delta = \frac{1}{n} \ln \frac{x(t)}{x(t+nT)} \tag{5.4}$$

where $x(t)$ is the amplitude of a peak at time t, and $x(t+nT)$ is the amplitude of the peak n periods away, where n is any integer number of successive, positive peaks. T is the time between peaks. The damping ratio, ζ, is then found by [150]:

$$\zeta = \frac{1}{\sqrt{1 + \left(\frac{2\pi}{\delta}\right)^2}} \tag{5.5}$$

Using this technique, ζ is found to be 0.07. From this damping ratio, the quality factor, Q, of the beam is calculated using [151]:

$$Q = \frac{1}{2\zeta} \tag{5.6}$$

which in this case is 7.2. This is a more accurate measure of quality factor than that found using the method of Equation 5.1, as the method of Equation 5.1 is only mathematically accurate for high values of Q, and so the value of 7.2 is the value that will be used in the calculations found in Chapter 6.

The natural frequency f_0 of the cantilever can be calculated by [150]:

$$f_0 = \frac{1}{T\sqrt{(1-\zeta^2)}} \tag{5.7}$$

From this, f_0 is found to be 13.2 kHz - again matching the previous resonant frequency measurements. The measured step response results presented in Figure 5.5.9 can be fit to an

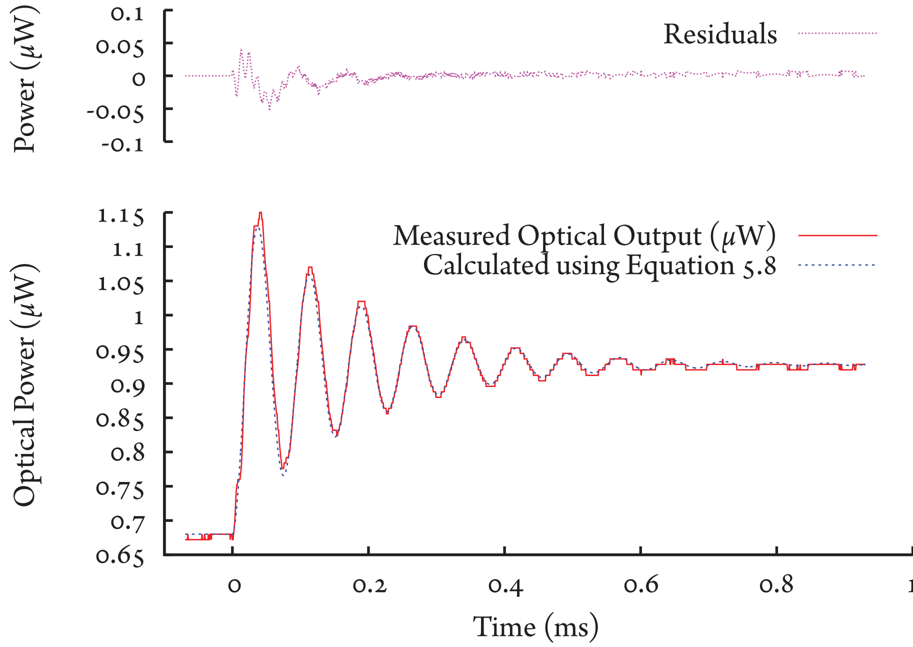

Figure 5.5.9: Measured optical response when a 200 μm microcantilever is actuated by a 5 V step at time $t = 0$

equation representing the second order step response of an underdamped system, $z(t)$ [150]:

$$z(t) = A\left[1 - \frac{1}{\sqrt{1-\zeta^2}} e^{-\zeta 2\pi f_0 t} \cos\left(2\pi f_0 \sqrt{1-\zeta^2 t}\right)\right] + C \tag{5.8}$$

where A is a scaling constant representing the optical response to the mechanical response of the cantilever induced by the electrostatic step voltage, and C is the final settling amplitude. Equation 5.8 is plotted in Figure 5.5.9 and shows an extremely close match to measurement as indicated by the residuals which were kept below 5%.

5.6 Conclusion

This chapter presented the laboratory setup used to optically characterise the MEMS devices. The integrated input/output gratings and silicon photonics waveguides were tested independently of any MEMS devices, and found to be operating within expectations. Fabricated MEMS devices were tested in this setup, and the efficacy of the proposed read-out scheme was demonstrated. A microbridge was actuated piezoelectrically over a range of 250 nm, and a microcantilever was actuated over a range of 2.2 μm. The optical outputs from these microchips were found to be modulated in response to the movement of the MEMS beams in the manner which was predicted by the simulations from Chapter 3. The optical readout technique was found to be sensitive enough to determine mechanical parameters (such as resonant frequency, damping ratio and quality factor) of the beams being measured. Even though the optical readout technique is interferometric in nature, a Vernier technique was

demonstrated to precisely identify the position of a cantilever beam over an extended range.

The next chapter will explore the sensitivity of the device, perform a noise analysis, and find the ultimate limits of detection for this measurement technique.

You can never know everything, and part of what you do know will always be wrong. Perhaps even the most important part. A portion of wisdom lies in knowing this.

Robert Jordan

6
Sensitivity, Noise Analysis and Brownian Motion

To push towards the ultimate detection limts, we must discover the threshold between what can be detected, and what limits the performance. This chapter performs a mathematically rigorous estimate of the ultimate sensitivity that could be expected to be attained by our approach, based on the modeling data from Chapter 3. The noise components which contribute to this ultimate limit are defined. Experiments are then performed to demonstrate how close the experimental setup can come to achieving this theoretical sensitivity. We find that the grating based optical microcavity can discern the first two modes of cantilever vibration due to thermo-mechanical noise. Suggestions for improving the experimental set-up to achieve the ultimate sensitivity are proposed.

6.1 Theoretical Sensitivity and Noise Analysis

In this section, the transmission of the optical signal through the waveguide is analyzed to study the modulation of the transmitted optical power induced by the deflecting micro-cantilever. The results will be used to estimate the theoretical noise inherent to this technique when applied to measurement of the deflection of a micro-cantilever.

The thermal, electrical and optical noise components will now be calculated in order to determine the deflection noise density (DND) and minimum detectable deflection (MDD) for this readout method. The existing expressions for typical micro-cantilever behaviour are used to calculate the thermal noise components, and new expressions tailored to this readout technique are derived to calculate the electrical and optical noise components.

The transmission efficiency through the device from input to output waveguide, η, is first

defined as a function of cantilever height, z, as:

$$\eta(z) = \frac{P_{out}(z)}{P_{in}} \tag{6.1}$$

where $P_{out}(z)$ is the power in the output waveguide as a function of the cantilever-grating separation, z, and P_{in} is the power in the input waveguide entering the interrogating grating underneath the cantilever.

A measure of sensitivity, S, in units m^{-1} can then be defined as [152]:

$$S = \frac{\delta\eta}{\delta z} = \frac{1}{P_{in}}\frac{\delta P_{out}}{\delta z} \tag{6.2}$$

Figure 6.1.1 shows the 3-D FDTD modeled transmitted power as a function of the cantilever-grating separation for a grating of 4 μm in width. Greatest sensitivity will occur when operating in the regions of greatest slope of the curve in this figure. One of these operating points is at a cantilever-grating separation of $z = 1$ μm (being the mid-point between the first maximum and minimum). When operating around this height, sensitivity can be numerically calculated from the simulation data to be $S = 3.0$ μm^{-1}. Factors that affect the slope include:

1. losses in the gratings-cantilever resonance (tilt, mirror losses),
2. wavelength,
3. grating order.

The MDD will be limited by the shot noise of the photodetector, Johnson noise of the load resistor, noise in the measurement system, cantilever vibration due to thermal noise, and the noise from the laser source. With the exception of the case for mechanical thermal noise, all DND components will be calculated independently of the micro-cantilever properties. All MDD components, and the DND component for mechanical thermal noise will be calculated based on the properties of a reference 50 μm long, 10 μm wide, 1 μm thick silicon nitride micro-cantilever.

For a given signal to noise ratio (SNR), MDD is calculated by [152]:

$$MDD = \frac{1}{\sqrt{SNR}} \tag{6.3}$$

and DND is generally calculated by [80]:

$$DND = \frac{MDD}{\sqrt{\Delta f}} \tag{6.4}$$

where Δf is the measurement bandwidth.

Optical feed forward techniques such as the scheme discussed next chapter in Section 7.2.3 can significantly reduce laser relative intensity noise (RIN) [153], and measurement system noise can be filtered or compensated using synchronous detection techniques, so are not included in this analysis.

6.1.1 Thermo-mechanical Noise

Cantilever thermal noise is independent of the read-out method, as it varies depending on the dimensions and material properties of the cantilever. For the purpose of this analysis it is assumed that a silicon nitride cantilever beam has been fabricated using the surface micromachining techniques described in Chapter 4. The thermo-mechanical limited MDD due to Brownian motion, MDD_{br}, of such a cantilever can be estimated by [87]:

$$MDD_{br} = \sqrt{\frac{2k_b T \Delta f}{\pi Q k f_o}} \tag{6.5}$$

where k_b is Boltzman's constant, T is temperature, Δf is the electrical bandwidth in Hz, Q is the quality factor of the cantilever, k is the spring constant of the cantilever, and f_o is the resonance frequency of the cantilever. The DND for thermal mechanical noise, DND_{br}, is then defined by:

$$DND_{br} = \frac{MDD_{br}}{\sqrt{\Delta f}} = \sqrt{\frac{2k_b T}{\pi Q k f_o}} \tag{6.6}$$

For a surface micro-machined cantilever of length of 50 μm, width 10 μm, and a thickness of 1 μm, fabricated from typical PECVD silicon nitride with a Young's modulus of 120 GPa [136] and density of 3184 kg/m^3 [154], Equation 2.5 can be used to estimate a spring constant $k = 2.3$ N/m, and a resonant frequency f_o = 400 kHz.

For the purposes of this analysis, a quality factor, Q, of 100 is chosen for the cantilever, as this is a typical room pressure limited value for microcantilevers [155]. Assuming an ambient room temperature of 293 K gives a DND_{br} of 5.2 fm/$\sqrt{\text{Hz}}$. For the cantilever, if an electrical bandwidth matched to the mechanical bandwidth such that $\Delta f = 2\frac{f_o}{Q} \approx 8$ kHz is used, then the thermo-mechanical MDD component, MDD_{br}, will be 460 fm. It is worth noting that increasing the length of the cantilever will also increase this DND component, while increasing the width and thickness will decrease the DND. Modifying the deposition conditions of the silicon nitride to achieve ultra flat cantilevers will effect the material density and Young's modulus, which although slightly modifies the spring constant and resonance frequency of the beam will change the final MDD_{br} component by less than 10%.

6.1.2 Shot Noise

The RMS shot noise current is defined by [80]:

$$\langle i_{sn} \rangle = \sqrt{2eP_{out}\gamma \Delta f} \tag{6.7}$$

where $e = 1.6 \times 10^{-19}$ C is the electron charge. Since $P_{out} = \eta P_{in}$, then shot noise current, $\langle i_{sn} \rangle$ is :

$$\langle i_{sn} \rangle = \sqrt{2e\eta P_{in}\gamma \Delta f} \tag{6.8}$$

The output current, i_{out} from the photodiode is directly related to the power impinging on the photodiode scaled by the photodiode's responsivity, γ. Knowing this and Equation 6.1, the output current can be given by:

$$i_{out}(z) = \gamma P_{out}(z) = \gamma P_{in} \eta(z) \tag{6.9}$$

It is necessary to know how the current changes as the cantilever-gap separation, z, changes, and so a partial differentiation with respect to z gives:

$$\frac{\delta i_{out}}{\delta z} = \gamma P_{in} \frac{\delta \eta}{\delta z} \tag{6.10}$$

Recalling the definition of sensitivity, S, from Equation 6.2 and substituting it here gives us:

$$\frac{\delta i_{out}}{\delta z} = S P_{in} \gamma \tag{6.11}$$

The signal to shot noise ratio, SNR_{sn}, is:

$$SNR_{sn} = \frac{(\delta i_{out}/\delta z)^2}{\langle i_{sn}^2 \rangle} \tag{6.12}$$

This, Equation 6.8, and Equation 6.11 give an expression for the shot noise SNR:

$$SNR_{sn} = \frac{(\delta i_{out}/\delta z)^2}{\langle i_{sn}^2 \rangle} = \frac{(S P_{in} \gamma)^2}{2e\eta P_{in} \gamma \Delta f} = \frac{S^2 P_{in} \gamma}{2e\eta \Delta f} \tag{6.13}$$

The shot noise limited MDD, MDD_{sn}, is defined by:

$$MDD_{sn} = \frac{1}{\sqrt{SNR_{sn}}} = \sqrt{\frac{2e\eta \Delta f}{S^2 P_{in} \gamma}} \tag{6.14}$$

This leads to a shot noise limited DND, DND_{sn}, given by:

$$DND_{sn} = \frac{MDD_{sn}}{\sqrt{\Delta f}} = \sqrt{\frac{2e\eta}{S^2 P_{in} \gamma}} \tag{6.15}$$

At optimum sensitivity based on the FDTD simulations, if an input power $P_{in} = 1$ mW at $\lambda = 1550$ nm into the input waveguide is assumed, then using an InGaAs PIN detector with a photodetector responsivity γ of 1 A/W, the optimal shot noise limited DND for the cantilever is 4.1 fm/$\sqrt{\text{Hz}}$. For the same bandwidth, Δf of 8 kHz, the shot noise limited MDD will be 370 fm. Note that since η, and correspondingly, S, are defined to be independent of P_{in}, both MDD_{sn} and DND_{sn} scale in relation to $1/\sqrt{P_{in}}$.

In these experiments, the output of the photodiode is fed to a transimpedance amplifier which amplifies the photodiode current signal by a factor of A V/A. The voltage output measured from the transimpedance amplifier, V_{out}, is related to the output optical power, P_{out},

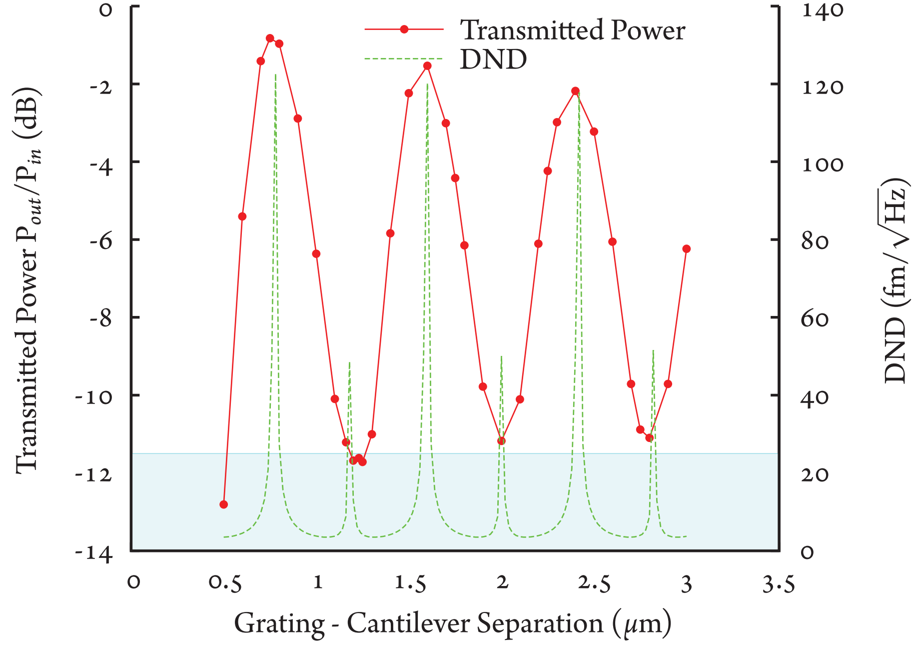

Figure 6.1.1: 3-D FDTD simulation of power transmitted as a function of cantilever grating separation for a diffraction grating 4 μm in width. The shot noise limited DND, DND_{sn}, calculated from Equation 6.15 over this separation range is also shown. The region where DND values are less than 25 fm/$\sqrt{\text{Hz}}$ is shaded, showing the operating ranges where DND can be kept below this level.

by:

$$V_{out} = AI_{out} = A\gamma P_{out} \tag{6.16}$$

and, assuming that the responses of both the transimpedance amplifier and the photodiode are linear, $\delta V_{out}/\delta z$ is:

$$\frac{\delta V_{out}}{\delta z} = A\frac{\delta I_{out}}{\delta z} = A\gamma\frac{\delta P_{out}}{\delta z} \tag{6.17}$$

Using Equations 6.1, 6.2, 6.16 and 6.17; MDD_{sn} and DND_{sn} can be rewritten in a form more useful to experimental observations as:

$$MDD_{sn} = \sqrt{\frac{2eP_{out}\Delta f}{\left(\frac{\delta P_{out}}{\delta z}\right)^2\gamma}} = \sqrt{\frac{2eAV_{out}\Delta f}{\left(\frac{\delta V_{out}}{\delta z}\right)^2}} \tag{6.18}$$

and:

$$DND_{sn} = \sqrt{\frac{2eP_{out}}{\left(\frac{\delta P_{out}}{\delta z}\right)^2\gamma}} = \sqrt{\frac{2eAV_{out}}{\left(\frac{\delta V_{out}}{\delta z}\right)^2}} \tag{6.19}$$

Figure 6.1.1 presents the shot noise limited DND over as a function of cantilever-gap separation for this approach. For a cantilever positioned anywhere within ±0.18 μm of the optimal height for the read-out system (i.e. away from max and min output power), the shot noise limited DND stays below 25 fm/$\sqrt{\text{Hz}}$, giving low noise operation over 90% of the unambiguous (half period) deflection range. Achieving this low DND over such a large gap

range could potentially allow relaxation of other requirements in system development that are generally very stringent such as wider process variation during fabrication, potentially allowing for elimination of the need for electrostatic biasing.

6.1.3 Johnson Noise

Johnson noise current is the thermal current in the load resistor of the photodetector, i_{jn}, and is defined by [156]:

$$i_{jn} = \sqrt{\frac{4k_bT\Delta f}{R}} \tag{6.20}$$

where R is the load resistance. Equation 6.11 from the shot noise derivation above gives the partial derivative of the output current with respect to z, and so using this, the signal to Johnson noise ratio, SNR_{jn} is:

$$SNR_{jn} = \frac{(\delta i_{out}/\delta z)^2}{i_{jn}^2} = \frac{R\,(SP_{in}\gamma)^2}{4k_bT\Delta f} \tag{6.21}$$

The Johnson noise limited MDD, MDD_{jn}, is then defined as:

$$MDD_{jn} = \frac{1}{\sqrt{SNR_{jn}}} = \sqrt{\frac{4k_bT\Delta f}{RS^2P_{in}^2\gamma^2}} \tag{6.22}$$

and the Johnson noise limited DND, DND_{jn}, will be:

$$DND_{jn} = \frac{MDD_{jn}}{\sqrt{\Delta f}} = \sqrt{\frac{4k_bT}{RS^2P_{in}^2\gamma^2}} \tag{6.23}$$

At optimum sensitivity, using the same InGaAs PIN detector and power as for the shot noise analysis above, with a photodetector responsivity γ of 1 A/W, and a load resistance of 1 kΩ , at room temperature the Johnson noise limited DND will be 1.3 fm/$\sqrt{\text{Hz}}$. For the same bandwith, of $\Delta f = 8$ kHz as used above, the Johnson noise limited MDD will be 120 fm.

6.1.4 Total Noise

The total noise is the square root of the sum of the squares of all noise contributions, that is:

$$MDD = \sqrt{MDD_{br}^2 + MDD_{sn}^2 + MDD_{jn}^2} \tag{6.24}$$

and

$$DND = \sqrt{DND_{br}^2 + DND_{sn}^2 + DND_{jn}^2} \tag{6.25}$$

and so when taking the MDD components from shot noise, Johnson noise, and thermal mechanical noise, the final MDD is 600 fm. The total DND is similarly calculated to be 6.8 fm/$\sqrt{\text{Hz}}$.

Figure 6.1.2 provides the DND components as a function of the laser power in the input

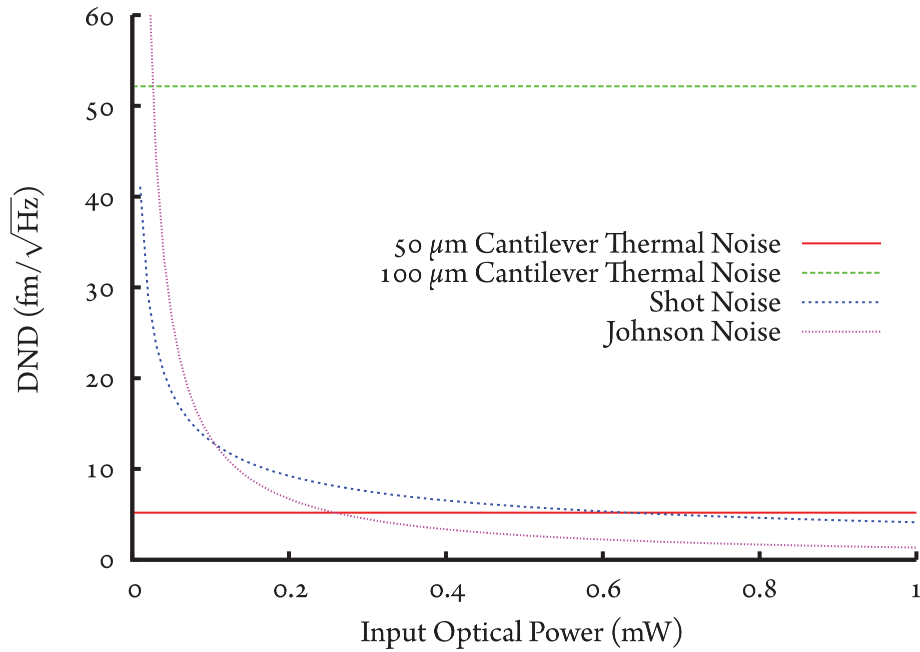

Figure 6.1.2: Calculation of DND components as a function of input laser power, P_{in}. For a 100 μm long cantilever, thermal-mechanical noise dominates for input optical powers above 50 μW. For a 50 μm long cantilever thermal-mechanical noise dominates for input optical powers above 0.6 mW.

waveguide leading to the interrogating grating. It can be seen that for a 100 μm long, 10 *mu*m wide, 1 μm thick silicon nitride cantilever, the dominant noise will arise from thermo-mechanical motion when the input laser power is in the hundreds of μW range. This makes the thermo-mechanical noise inherent to the cantilever itself the practical noise floor of this read-out technique.

Table 6.1.1 provides a comparison of MDD and DND for various optical techniques relevant to this approach. The numerical values provided for MDD and DND for the Putrino *et al.* column are a summary of the theoretical calculations performed in throughout this section. For the purposes of comparing optical read-out technologies monitoring the deflections of micro-cantilevers, it is illuminating to directly compare the shot noise limited DND, since the thermal noise from cantilevers is independent of the read-out technique. The shot-noise limited DND of 4.1 fm/$\sqrt{\text{Hz}}$ measured here is comparable to the best reported shot-noise limited DND of 6.0 fm/$\sqrt{\text{Hz}}$ achieved using significantly more elaborate external interferometers [68]. Note that for multiplexed operation, significantly lower powers would be incident on each grating.

6.2 Experimental Limits of Detection

In this section, the equations derived in Section 6.1 will be applied to the optical measurements presented in Chapter 5 to determine the achieved sensitivity, DND and MDD for both the microbridge and the cantilever structures that where experimentally examined.

		Putrino *et al.* [157]	Schonenberg *et al.* [68]	Noh *et al.* [81]	Pham *et al.* [89]	Stievater *et al.* [69]	Zinoviev *et al.* [80]
Thermal	DND (fm/$\sqrt{\text{Hz}}$)	5.2	8	-	-	tens*	-
	MDD (pm)	0.46	-	-	-	-	-
Johnson	DND (fm/$\sqrt{\text{Hz}}$)	1.3	-	-	-	-	-
	MDD (pm)	0.12	-	-	-	-	-
Shot	DND (fm/$\sqrt{\text{Hz}}$)	4.1	6	-	-	-	18-80
	MDD (pm)	0.37	-	54	170	-	-
Total (rss)†	DND (fm/$\sqrt{\text{Hz}}$)	6.8	10	-	-	tens*	18-80
	MDD (pm)	0.60	-	54	170	-	-

* Estimated by Steivater *et al.* based on microbridge structures similar to those used in the microharp [69]
† Total is the root sum square (rss) of all noise components.

Table 6.1.1: Comparison of Deflection Noise Density (DND) and Minimum Detectable Deflection (MDD) for various optical read-out techniques

6.2.1 Measured Microbridge Sensitivity

The microbridge that was presented in Section 5.4 had a resonant frequency, $f_o = 291$ kHz, and a quality factor at this frequency, $Q \approx 153$. Therefore a bandwidth of $\Delta f = 2f_o/Q = 3.8$ kHz can be chosen. The greatest slope, $\delta P_{out}/\delta z$, observed experimentally for this microbridge was 106 nW/nm, which occurred at a gap of 1450 nm as shown in Figure 6.2.1, and is very linear over a range of ± 40 nm. Given this value and an output power of $P_{out} \approx 6.9\ \mu$W (see Figure 6.2.1), the shot-noise limited MDD_{sn} and DND_{sn} can be calculated from Equations 6.14 and 6.15 to be 860 fm and 14 fm/$\sqrt{\text{Hz}}$ respectively.

With a higher power laser and/or more efficient coupling into and out of the waveguide, it should be possible to increase P_{out} to 1 mW. Assuming that all optical effects in the device scale linearly at this power density, $\delta P_{out}/\delta z$ would be 15,300 nW/nm, and so the MDD_{sn} would be 72 fm, and the DND_{sn} would be 1.2 fm/$\sqrt{\text{Hz}}$.

6.2.2 Measured Cantilever Sensitivity

The cantilever that was presented in Section 5.5 had a resonant frequency, $f_o = 13.2$ kHz, and a quality factor at this frequency, $Q = 7.2$. The experimental measurement data of the transmitted

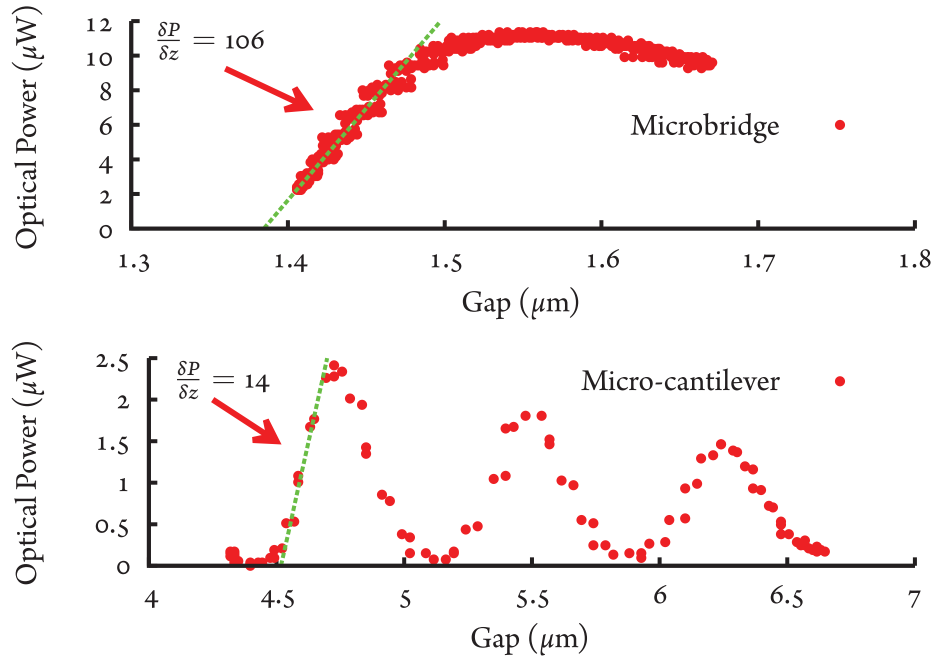

Figure 6.2.1: Measured power transmitted through (top) the microbridge and (bottom) the microcantilever. The slope used as $\delta P_{out}/\delta z$ in the MDD and DND calculations is indicated (106 nW/nm for the microbridge, 14 nW/nm for the micocantilever). (Replotted data was first presented in Figures 5.4.3 and 5.5.5)

optical power as a function of the cantilever-grating gap that is replotted in Figure 6.2.1 show that in the linear region over the cantilever-grating separation gap range from 4.5-4.7 μm, that $\delta P_{out}/\delta z = 14$ nW/nm. Taking the midpoint of this range, where the gap is 4.6μm, and the output power is 1.1 μW, then the DND_{sn} is calculated to be 46 fm/$\sqrt{\text{Hz}}$. Based on the resonant frequency and quality factor of this cantilever, if an electrical bandwidth of 3.7 kHz is chosen, the MDD_{sn} will be 2.8 pm. These limits of detection values are slightly less impressive than that of the microbridge in the previous section. This is mainly due to the height of the cantilever being further above the substrate, and the angle of the cantilever reflecting light away such that it is not coupled back into the grating, resulting in a smaller value for $\delta P_{out}/\delta z$, whereas the microbridge is extremely flat, less than 2 μm above the grating, making the optical microcavity significantly more effective.

Microcantilever Brownian Motion

The shot noise limit of this technology is low enough that the measurement system should be able to detect the thermo-mechanical motion of the cantilever beam (induced from room temperature and pressure variations). In this section the theoretical Brownian noise density of the cantilever will be calculated, and compared to values measured by the system when the cantilever actuation signal is grounded.

A finite element method (FEM) model is adopted, and the Coventorware software package is used to calculate the beam profiles for the first two longitudinal vibration modes of the cantilever. These are shown in Figure 6.2.2. The region above the grating is highlighted in this

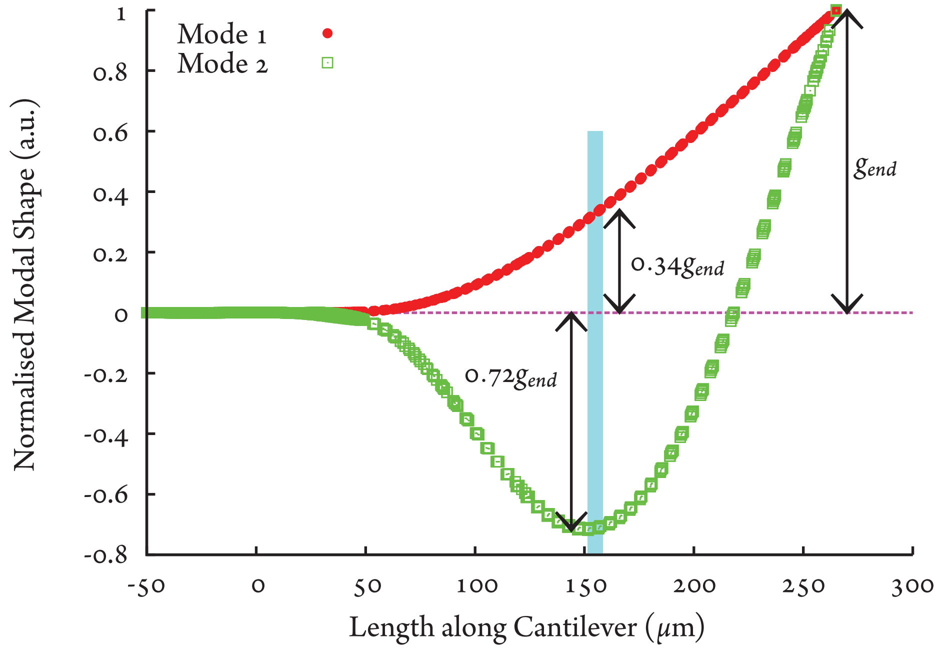

Figure 6.2.2: Modeled normalized modal shapes of the cantilever for the first two vibration modes (Normalization is to the end deflection for each mode). The highlighted area represents the region of the cantilever that the diffraction grating is measuring. The outer circumference of the top hat anchor starts at -50 μm and ends at +50 μm along the x-axis, which is the starting point of the suspended beam of the cantilever.

figure. This modeling predicts that when the cantilever is excited at its resonance frequency (Mode 1), the region measured by the grating will move by 34% of the distance the cantilever tip moves, whereas when excited at its first harmonic frequency (Mode 2), the region measured by the grating will move by 72% of the distance the tip moves. The Brownian motion measured will be from this region of the micro-cantilever.

Due to interest in characterizing MEMS cantilevers for use in AFMs, substantial work in the literature has been performed on the topic of predicting Brownian motion for a MEMS cantilever. The z-direction component of the Brownian noise density, $n_{zb}(f)$, in units of $m/\sqrt{Hz}$, of a MEMS cantilever around its resonant frequency (mode 1) can be predicted by [63]:

$$n_{zb}(f) = \sqrt{\frac{2k_b T}{\pi Q k f_o} \frac{1}{\left(1 - [\left(\frac{f}{f_o}\right)^2 + \frac{f}{f_o Q}]^2\right)}} \tag{6.26}$$

where k_b is Boltzmann's constant, T is Temperature (K), Q is the quality factor of the cantilever, k is the spring constant of the cantilever, f_o is the resonant mechanical frequency of the cantilever, and f is the frequency of interest. Note that this equation does not model Brownian motion around higher mechanical modes of the cantilever. The values, $T = 293$ K, $Q = 7.2$ and $f_o = 13.2$ kHz are adopted for the cantilever.

An accurate spring constant k for the cantilever, that takes into account the medium that it is

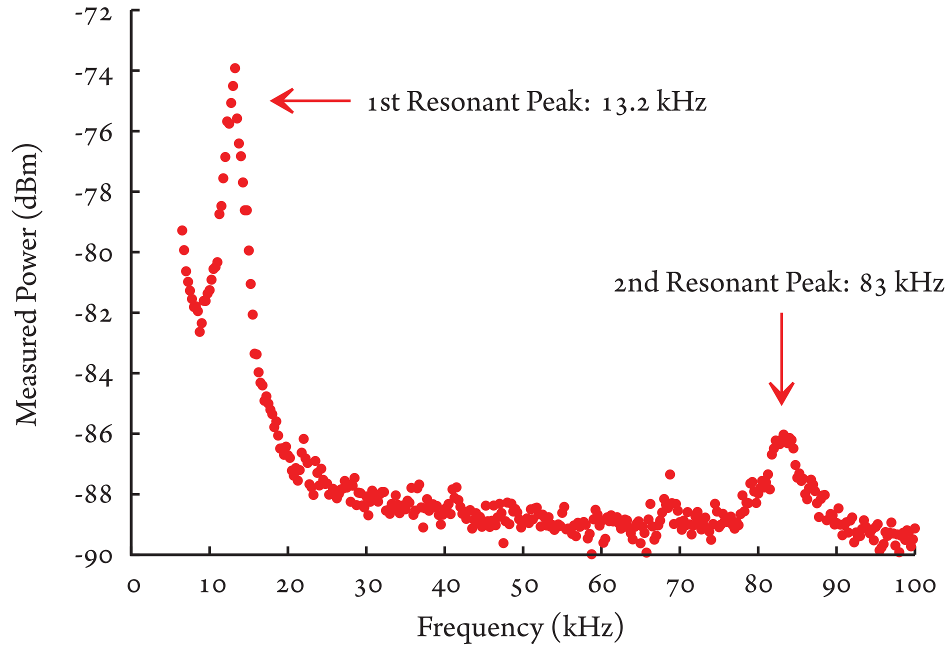

Figure 6.2.3: Transmitted power through a grating beneath a thermo-mechanically excited cantilever and measured by the spectrum analyzer using a reserve bandwidth of 1 kHz.

moving in can be calculated using the Sader method [158]:

$$k = 0.1906 \rho w^2 l Q_f \omega_f^2 \Gamma_i^f \left(\omega_f\right) \tag{6.27}$$

where w is the width of the cantilever, l is the length of the cantilever, ρ is the density of the medium the cantilever is moving through, ω_f and Q_f are the radial resonant angular frequency ($\omega_f = 2\pi f_o$) and quality factor of the fundamental resonance peak, respectively, and Γ_i^f is the imaginary part of the hydrodynamic function given by Equation (20) in the work of Sader [55]. For the micro-cantilever in air, the spring constant, k, can be calculated by this method to be 6.06 mN/m.

From Figure 6.2.2, it can be seen that at frequencies near the fundamental resonance frequency, the region measured by the grating will only move 34% the distance that the tip moves, so the Brownian noise deflection density at the midpoint above the interrogating grating, $n_{zbm}(f)$, can be estimated by:

$$n_{zbm}(f) = 0.34 n_{zb}(f) \tag{6.28}$$

Measurements for the Brownian motion were conducted by connecting the grating optical output to the transimpedance amplifier, and the output of the amplifier to an Agilent ESA-E Series model E4402B spectrum analyzer. As the measurements were performed in an open laboratory environment, it is plausible to expect some additional acoustic noise from this environment to also affect the cantilever. Figure 6.2.3 presents Brownian noise density that was obtained via the measured power transmitted through the device as a function of frequency for

thermally stimulated cantilever motion. Two peaks can be seen in the measured spectrum, one at the fundamental resonant frequency of the cantilever at 13.2 kHz, and one at the first harmonic frequency of 83 kHz.

To calculate the root mean square voltage, V_{rms}, from the power measured by the spectrum analyzer in dBm, S_{out}, the equation used is:

$$V_{rms} = \sqrt{\frac{Z \times 10^{\frac{S_{out}}{10}}}{1000}} \tag{6.29}$$

where Z is the input resistance of the spectrum analyser, for this equipment, $Z = 50\Omega$. The power measurements were made using a resolution bandwidth (RBW) of 1 kHz. Therefore the power spectral density in dBm/Hz, PSD, referenced to 1 Hz is:

$$PSD = P_{out} - 10 \log \frac{RBW}{1} = S_{out} - 30 \tag{6.30}$$

For the motion of the cantilever, the value of interest is the peak-to-peak voltage, V_{p-p}, rather than V_{rms}. This is obtained by $V_{p-p} = 2\sqrt{2}V_{rms}$. To convert this voltage value to distance units, it is necessary to divide the voltage by $\delta V_{out}/\delta z$. Therefore the brownian noise deflection density measured by the grating technique, in units of $\mathrm{m}/\sqrt{\mathrm{Hz}}$, is:

$$n_g = \frac{2\sqrt{2}}{\delta V_{out}/\delta z} \sqrt{\frac{Z \times 10^{\frac{S_{out}-30}{10}}}{1000}} \tag{6.31}$$

Since the purpose of these calculations is to measure the Brownian motion of the beam, it is undesirable to use voltage actuation to move the beam closer to the substrate to reach the point of highest sensitivity at the gap of 4.6 μm mentioned earlier in this section, as this will add extra motion due to noise from the actuation voltage source. Therefore, for this measurement, the cantilever is left at its rest point at the gap height of 5.9 μm. At this gap height, the calibrated measurements from Figure 6.2.1 can be used to get $\delta P_{out}/\delta z_{|z=5.9\ \mu\mathrm{m}} = 0.685$ nW/nm. As the micro-cantilever movements are relatively small (proportionally 10^{-5} of the interferometric period), the assumption that this value will be constant over the range to be examined can be made.

A measurement of the laser power transmitted through a silicon photonic waveguide without an overlying cantilever on the sample chip was also made, and is provided in Figure 6.2.4. This provides a combined measurement of the noise arising from relative intensity noise (RIN) and shot noise.

The thermo-mechanical noise values predicted for the cantilever by Equation 6.28 are shown by the solid line in Figure 6.2.4. It can be seen that around the resonance frequency the measured values strongly follow the envelope predicted by Equation 6.26, showing excellent agreement, and that this read-out technique is sensitive enough to detect Brownian motion at the mid-point of the cantilever beam. Furthermore, detection of the Brownian motion at the second mechanical mode at the expected frequency of 83 kHz is also clearly seen. The

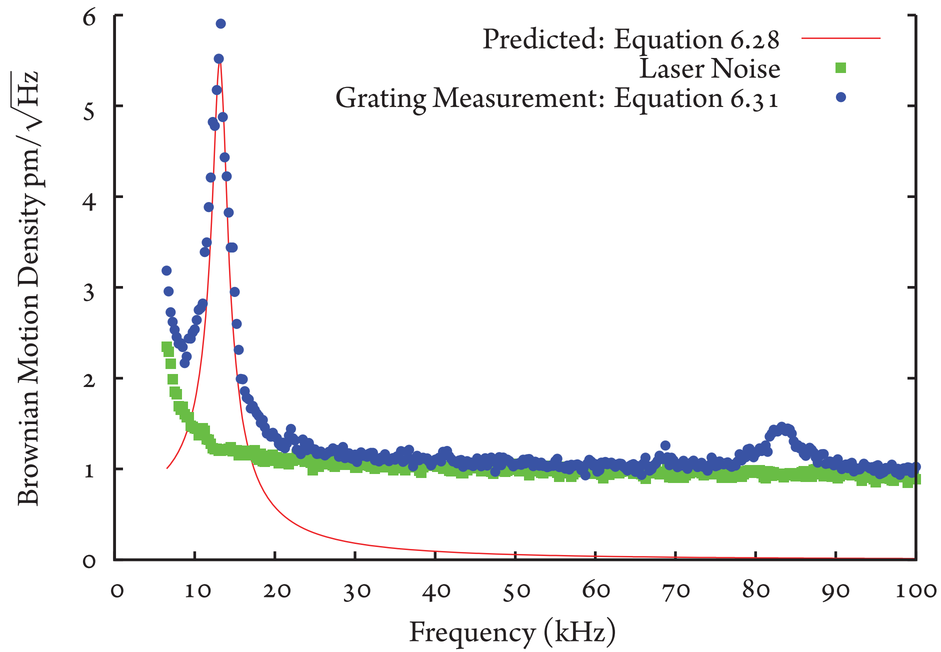

Figure 6.2.4: Predicted Brownian noise envelope compared to measured optical power modulation from read-out device. A measurement of the noise of the laser when coupled through the chip is also presented.

magnitude of the noise density measured at the fundamental resonant frequency peak is slightly greater than the theoretically predicted Brownian noise density - this is likely because of the additional acoustic noise present in the laboratory environment adding additional excitations to the cantilever. The noise floor when using this laser can be seen from Figure 6.2.4 to be around 1 pm/$\sqrt{\text{Hz}}$. Most of the noise in the system will also be due to relative intensity noise (RIN). This could be reduced by the use of a low RIN laser, or via other RIN compensation techniques [153]. Shot noise can be decreased through the use of either a higher power laser, or better coupling into- and out of- the chip.

The ability to use an integrated, interrogating diffraction grating to determine the position of a MEMS cantilever with this level of sensitivity is an excellent result. Groups such as Nieradka *et al.*[56] have recently performed work using an external optics based real-time Brownian noise extraction technique to measure the movement of microcantilever biosensors in environments where the external excitation of vibrations is undesirable. The integrated optical technique described in this thesis is sensitive enough to also be capable of this feat, and since this technique can be fiber-fed, it eliminates the need for alignment of large external optics.

6.3 Conclusion

This chapter presented a sensitivity analysis of this read-out technique. Expressions for the limits of detection of the read-out technique were derived, and applied to the optical response of a 3-D FDTD simulation of the cantilever-grating device. It was predicted that for most cases, the noise floor of the device would be the room temperature thermal motion of the cantilever. The

model predicted that the optical limits of the grating read-out technique itself could have a DND of 4.1 fm/$\sqrt{\text{Hz}}$ if shot-noise limited performance can be achieved. This has the benefit of being very similar to results obtained using external optical interferometers, without the need for external alignment to the micro-cantilever to be measured. Further, the technique can maintain a DND of below 25 fm/$\sqrt{\text{Hz}}$ when the beam is situated in 90% of the possible static beam positions.

The expressions for the limits of detection were applied to the experimental optical measurements of these devices. Although sub-picometer resolution had been predicted mathematically, the experimental set-up was unable to reach the shot noise limit, and thus the noise floor reached using a 200μm long micro-cantilever was 1 pm/$\sqrt{\text{Hz}}$. Even so, the technique was sensitive enough to be used to observe the thermal mechanical motion of a micro-cantilever around its first two vibrational modes. To get closer to the theoretical shot noise limit of this device will require more laser power via either better coupling or higher powered lasers, and lower RIN, possbly achieved by using RIN compensation techniques.

The next chapter will present the final conclusions of this thesis, and set out important opportunities for future investigations which have arisen from the significant contributions of this thesis.

A designer knows he has achieved perfection not when there is nothing left to add, but when there is nothing left to take away.

Antoine de Saint-Exupry

7
Conclusions and Future Work

The objective of this thesis was to design and test a novel technology capable of measuring ultra-small out-of-plane movements of MEMS devices. It was desirable that the technology have the ability to address large arrays of devices, while maintaining sub-nanometre position resolution.

7.1 Conclusions

7.1.1 Design and Modelling

A novel optical technique was decided upon: to form an optical microcavity between surface-micromachined MEMS devices and diffraction gratings embedded into a silicon photonic waveguide running along the substrate. The concept was based on a resonant cavity, through which an optical interferometer would modulate the light. By combining a deformable MEMS structure into the path, displacement of the MEMS is strongly linked to the optical modulation. This concept was designed to (a) operate at commonly available, 1550 nm laser wavelengths, and (b) allow easy fabrication using SOI wafers. The novelty arose through the blend of the best characteristics of optical waveguides and MEMS technologies, and a desired to exploit the optical multiplexing and large scale integration to enable vast arrays of sensors to be created.

Extensive FDTD modeling was performed on the optical properties of the structure. The simulations showed that the interferometric effect existed, was very strong ($>$ 10 dB extinction), and continues to be effective even in gratings as short as 4 μm. The simulations predicted that

the technique would be effective in both aqueous and gaseous environments. Operation in liquid and gaseous environments was through design, by the choice of a high index silicon waveguide and grating, as the refractive index of water is far closer to that of air than that of silicon, so the optical phenomenon in the resonant microcavity was expected to be very similar.

A large range of wavelengths were included in the simulation, and it was found that even for wavelengths where the diffraction grating is not particularly efficient (high loss), the interferometric effect resulted in significant signal modulation, providing a sensitive indication of the position of the MEMS across a broad wavelength band. This ability to operate over large wavelength ranges will allow WDM addressing of large arrays of MEMS, and/or allow Vernier techniques to be utilized to determine the position of individual MEMS components over a large deflection range, larger than the periodicity of the interferometric effect would otherwise allow.

Micro-cantilevers are of particular interest, being a crucial component in both AFMs and many types of MEMS chemical sensors[16, 46, 57, 80], so simulations of tilt were performed. These showed the sensors were largely insensitive to tilt, with deflections up to 5.7°, able to modulate the output light sufficiently. For a 50 μm long cantilever, this corresponds to a deflection of 5 μm, which is far greater than the deflections occurring during normal operation of a surface-micromachined cantilever for chemical sensing operations. This tolerance of cantilever tilt can allow less stringent fabrication tolerances - the cantilever need not be perfectly flat in relation to the substrate.

MEMS with varying degrees of reflectivity were also simulated - it was found that even a mirror with 25% reflectivity (equivalent to a refractive index > 3 in air) could potentially provide 15 dB extinction of the light travelling through the device.

7.1.2 Fabrication of Devices

The fabrication processes of the device were designed to decouple the photonic circuit fabrication and MEMS construction. The photonic circuit was fabricated using an SOI wafer utilizing standard DUV photolithography. Since the sub-micron features required for the diffraction grating could not be realized with the photolithography equipment of the laboratory, the photonic circuit manufacture was outsourced to LETI. Once the wafers containing the photonic circuits were produced and supplied, the MEMS devices were fabricated by the author using surface-micromachining processes available in the research group's cleanroom at UWA.

Fabrication residual stresses in micromachined structures were initially a problem in the manufacture of the MEMS, causing any number of micro-cantilevers and micro-bridges to fail at the release stage of the fabrication process. Tuning of various steps of the fabrication process was performed, and a reproducible fabrication process was developed, which was able to provide MEMS with the desired properties.

7.1.3 Optical Measurements

A free-space optical system was put together to supply optical power to the chip, and measure the optical power being returned. The fiber to fiber insertion loss of this system was measured to be 12 dB, and was responsible for the majority of optical power loss in the system. MEMS microbridges and micro-cantilevers were tested in this setup, and when actuated, the optical output power was found to modulate in a manner consistent with the previously performed FDTD simulations that had been performed. More specifically, the technique was found to work with a wide range of optical wavelengths (1550-1610 nm), and the periodicity of the maxima and minima of the power output as a function of gap distance matched the simulation predictions. Through the use of two of these wavelengths, a Vernier technique was demonstrated which gave the ability to accurately position the cantilever over ranges exceeding the interferometric periodicity of any individual laser wavelength.

7.1.4 Limits of Detection

The limits of detection of this device were investigated. Expressions were derived for the MDD and DND figures of merit and related to the rate of change of output optical power with respect to the gap between the cantilever and the grating ($\delta P_{out}/\delta x$). When these expressions were applied to the 3-D FDTD optical model of a 4 μm wide, 12 μm long grating, a shot noise DND limit of 4.1 fm/$\sqrt{\text{Hz}}$ was predicted. As the output power did not vary monotonically with the gap above the grating, the points at the maximum and minimum output power regions were found to have high DND values. However, the technique can maintain a shot-noise limited DND of below 25 fm/$\sqrt{\text{Hz}}$ for 90% of the deflection of the MEMS beam.

Optical transmissive measurements were made through a microbridge suspended 1.5 μm above a 7 μm wide, 19 μm long grating. The measured values of $\delta P_{out}/\delta x$ implied that a shot-noise limited implementation of this system could achieve a DND as low as 14 fm/$\sqrt{\text{Hz}}$. Increasing the optical output of the system to 1 mW should theoretically lower the shot-noise limited DND to 1.2 fm/$\sqrt{\text{Hz}}$. This is slightly lower than the FDTD modeled values above due to the wider grating (7 vs 4 μm) reducing fringing effects, and the increased length of the grating (19 vs 12 μm) improving the finesse of the microcavity. These noise limits are comparable to state-of-the-art AFM systems based on external interferometers.

Similar measurements were made of a microcantilever. Here, the measured values of $\delta P_{out}/\delta x$ suggest a shot-noise limited DND of 46 fm/$\sqrt{\text{Hz}}$ could be achieved when the output power is 1.1 μW. The experimental set-up was not shot noise limited, so the actual noise floor reached was considerably greater at 1 pm/$\sqrt{\text{Hz}}$. Nevertheless, this level of resolution will be sufficient for most gas sensing applications, and was high enough to demonstrate a measurement of the first two modes of the thermo-mechanical motion of a suspended micro-cantilever. This thermo-mechanical motion is the dominant noise in this system - allowing optical detection of the beam resonance independent of any external actuation, which in turn will allow the system to be used in all-optical, remote operations.

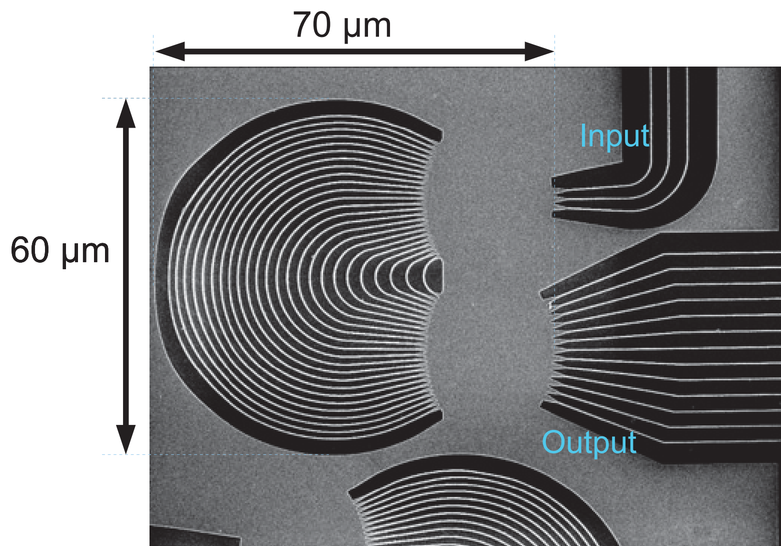

Figure 7.2.1: Scanning electron micrograph of a fabricated, compact $70 \times 60\ \mu m^2$ WDM based on arrayed waveguide grating technology [160].

7.2 Future Work

This research has created a position sensing element with extremely high accuracy, and opens significant opportunity which would have impact in AFM and biosensing applications. A wide range of applications would benefit from the technique described in this thesis, due to it's optical nature and high accuracy.

This section will detail some additional research directions and applications which would have significant impact but were outside the scope of this thesis.

7.2.1 Wavelength Division Multiplexing

A key feature of this technology is the ability to use WDM techniques to address large arrays of MEMS sensors. An example of how such a WDM scheme might work was proposed in Figure 3.5.7. On-chip silicon photonics features capable of wave division multiplexing and demultiplexing have been used for many years in fibre optic telecommunications applications [159].

Figure 7.2.1 shows an SEM image of an implementation of such an integrated multiplexing feature [160]. By splitting a broadband input light source (shown in Figure 7.2.1) into various component wavelengths, the various wavelengths can be fed via different waveguides to different MEMS devices. This spectral slicing technique has be proposed for low cost optical access networks. A similar on-chip technique could recombine the wavelengths back to a single output from the chip. This would lower loss, increase the number of sensors, and decrease the physical footprint.

This technique is particularly useful where no active components (laser diodes and photodiodes) can be used on chip. An example of this might be biological sensors for use in an aqueous environment where an all-optical device without electronic components is necessary.

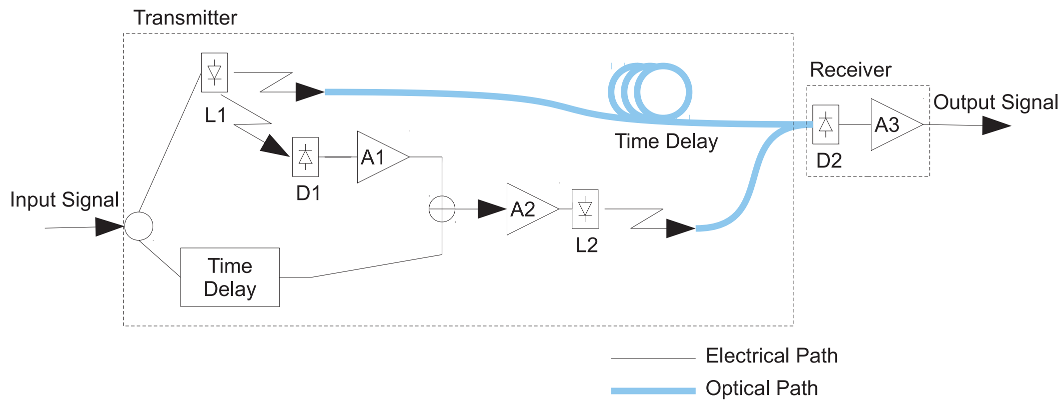

Figure 7.2.2: Schematic diagram of an optical feedforward compensation system shown to lower RIN to -160 dB/Hz [153].

A demonstration of on-chip WDM addressing of micro-cantilevers would provide confirmation of the ability to address large arrays of devices. Issues to resolve here include total launch power into the waveguides, on-chip losses, crosstalk and back reflection which could affect sensing operation.

7.2.2 Liquid Environments

Some MEMS sensor applications must operate in liquid environments [56, 58, 94]. The readout technique is purely optical, and FDTD simulations predict that it will work effectively when immersed.

While dynamic mode MEMS sensors are difficult to implement due to the damping effect of the liquid environment, static mode MEMS sensors are still effective. This results from the same bending of the cantilever whether the sensor is in air or liquid.

Characterising the operation of this readout technique in an aqueous environment is desirable to verify that the simulations are correct. Such a demonstration would be extremely attractive to a wide field of bio-chemical aqueous sensing.

Issues to resolve here include the damage that can result from surface tension and snapdown during liquid evaporation. Technologies to overcome this include anti-stiction bumps, robust supports and controllable on-chip evaporation control (heaters). For these reasons, aqueous tests were not performed in this work.

7.2.3 Attaining the Shot Noise limit

If this readout technique can be demonstrated close to- or at the shot noise limit, it will provide unprecedented resolution in the measurement of the position of suspended MEMS devices. While an extremely low noise level of 1 pm/$\sqrt{\text{Hz}}$ was achieved, sub-picometre measurement accuracy was not achieved with the chips. This was partially because the experimental equipment was unable to couple large enough amounts of light into the chip, and partially because of the RIN in the lasers used.

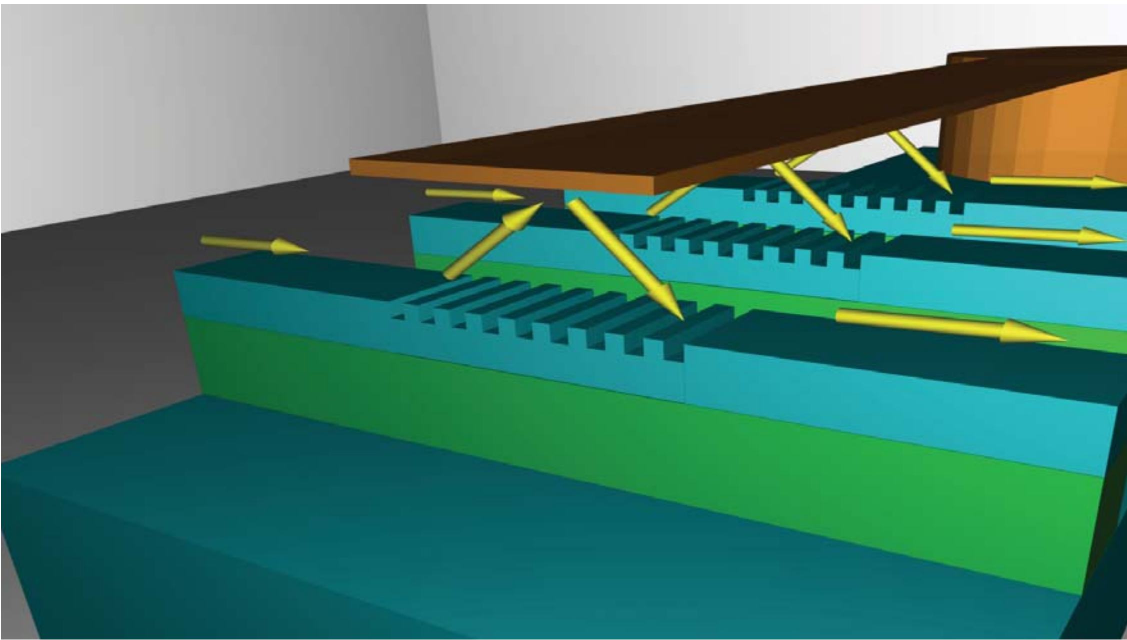

Figure 7.2.3: Isometric view of a proposed multiple interrogating grating structure.

Lasers with extremely low RIN are available [161], alternatively, optical feed forward techniques have been designed which can compensate for RIN. A schematic design of a typical feed-forward system is shown in Figure 7.2.2 [153].

Due to the desire to use silicon photonics technology, there has been significant work on coupling light into on-chip waveguides [111–113, 118]. CMOS compatible gratings with a coupling loss of 1.5 dB have been designed recently [162]. Use of these in conjunction with the readout system described in this thesis, rather than the coupling efficiency of 6 dB that was obtained, would provide greater optical power into the waveguide and move closer to the shot noise limit.

7.2.4 Multiple Gratings Beneath a Micro-cantilever

Functionalised static mode micro-cantilever sensors deflect due to surface stresses when a chemical binds to the functionalization layer. Currently, most static mode MEMS sensors measure the movement of the tip of the micro-cantilever beam to determine whether a detection event has occurred. The readout technique can improve upon this through the use of multiple gratings beneath a single micro-cantilever. An isometric view of such a structure is shown in Figure 7.2.3. Multiple gratings will give the ability to measure the overall shape of a micro-cantilever, both before and after a detection event, providing more information about the species detected than could be discerned by measuring the movement of the micro-cantilever tip alone.

As the optical measurement technique has a substantially faster response time in comparison to the mechanical action of the micro-cantilever, interesting information could also be obtained from the time-domain micro-cantilever shape response to a detection event.

This will require modeling and design to ensure that there is no optical cross-talk between

adjacent gratings. A new design of the photonic circuit based on this concept to allow multiple waveguides that are close enough together to fabricate a micro-cantilever over is required for such an investigation.

7.2.5 Optical Actuation Effects

When the optical power in the optical micro-cavity between the micro-cantilever and the grating is large, it is extremely likely that either heating or optical pressure [163] will induce motion in a micro-cantilever. For WDM systems where high launch powers may be required, or all-optical remotely operated sensors which require high powers to transmit across long distances, investigation of the effects of high optical power on the sensors performance are essential.

7.2.6 Alternate Material Systems

This research looked at the implementation of the photonic circuit component of this technology in silicon (SOI wafer), as this is a material system compatible with CMOS technologies and is widely used for any number of microelectronics devices throughout the world. However, this readout technique is not limited to SOI and can be built in other material systems, and indeed, there may be benefits to doing so.

As an example, InGaAs wafers would provide the opportunity to build a completely integrated system, as infra-red laser diodes and photodiodes can be directly fabricated with InGaAs and so embedded on-chip along with all other components. This would make coupling of light into and out of the waveguides feeding the interrogating grating far more efficient, and eliminate the packaging problems that arise when feeding external optical signals into microchips.

A second potential material system that is worth investigation is the silicon nitride CMOS-compatible photonics platform such as that presented by Romero-García *et al.* [164]. Their work demonstrated waveguide bends, grating couplers and multimode interference couplers for light at a wavelength of 660 nm, fabricated on silicon wafers in a standard CMOS pilot line. Reducing the laser wavelength from 1550 nm to 660 nm will more than double the sensitivity of the read-out technique, while still using standard fabrication techniques.

7.2.7 Applications

Application of this readout technique to various existing technologies offers significant opportunity for advancement over state of the art as will be discussed in this section.

Chemical/Biological Sensors

An overview of MEMS chemical and biological sensors was provided in Chapter 2. The read-out technique is excellent for use in these types of applications for several reasons:

- Picometer-scale position resolution

- Ability to operate in hazardous environments (explosive gas, remote pipes and mines)

- Ability to address large arrays

- Ability to operate in aqueous environments

The ability to address large arrays is of particular importance for sensing applications, as the sensing accuracy improves statistically with a greater number of active sensing components. Large arrays provide the ability to leave a small number of micro-cantilevers unfunctionalized - acting as references for thermal drift. Large numbers of micro-cantilevers on chip also provide the opportunity to functionalize different cantilevers for different chemicals - enabling multiple chemical sensing using a single chip.

Various functionalizations for MEMS devices already exist, and have been demonstrated [53, 54, 165]. A simple sensing demonstration could be provided by thermally evaporating platinum onto the top surface of the micro-cantilevers. Platinum is an extremely efficient absorber of hydrogen gas, and as calculated in Section 2.1.1, a micro-cantilever sensor would bend by enough to accurately detect even the trace amounts of hydrogen in air. Modelling, simulation, and experimentation would need to be performed to design a fabrication process that would be able to create flat micro-cantilevers with the additional stresses added by the presence of palladium. Additionally, a chemical test chamber capable of supplying trace elements of the gases to be sensed needs to be built and calibrated. Such a facility does not exist in the research group's laboratory, and would perhaps be better pursued as a collaboration effort with a research group more familiar with chemical testing.

Atomic Force Microscopy

Figure 7.2.4 shows a visualization of a possible AFM implementation. By adding fabrication steps to grow and sharpen a pointed tip at the end of the cantilever, an AFM device could be made. The AFM sample can be placed on a micro-positioning plate and run under the cantilever chip allowing measurements to be taken. As the cantilever deflects due to the sample's surface profile, an accurate image of the sample surface can be recorded.

One of the greatest disadvantages in the use of atomic force microscopes has been the need to align the external optical measurement system to the sensing micro-cantilever head before measurements can begin to be made. Since the readout technique is integrated onto the same chip as the sensing micro-cantilever, these alignment issues do not occur.

The integrated nature of this read-out technique should also allow the miniaturization of an AFM system, as the external optics will no longer be required. Additionally, the readout technique should potentially be able to match the precision of any available commercial AFM, making further investigation in this direction compelling.

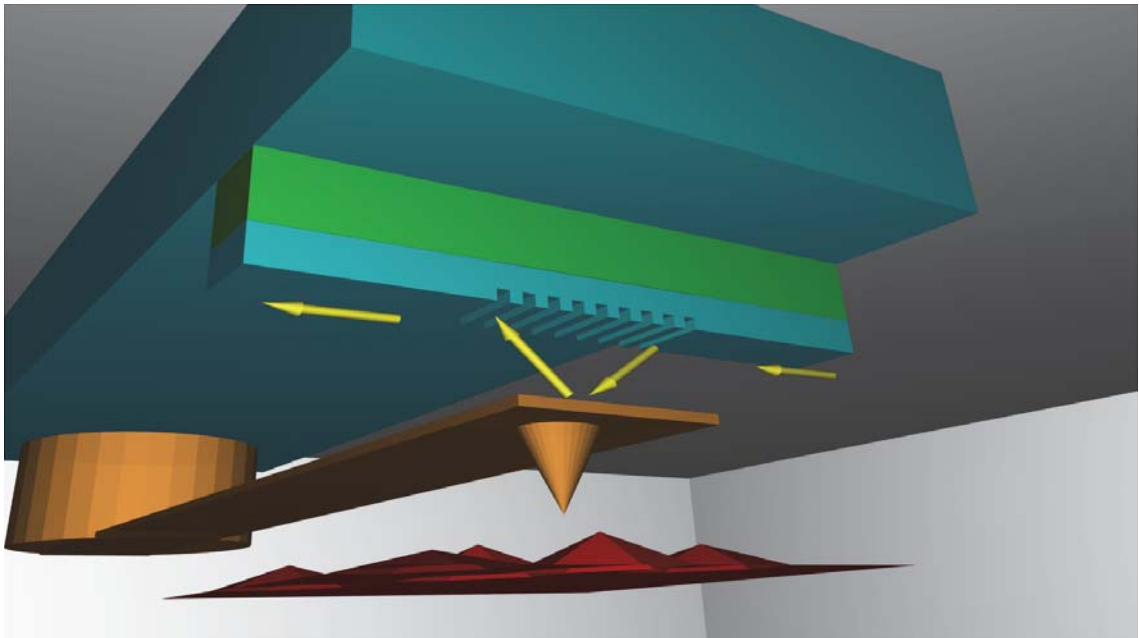

Figure 7.2.4: Isometric view of a possible AFM implementation.

Other applications

Although initially designed for sensors and sensing, there are many other applications in the fields of mining, aerospace, telecommunications and research that this technique can contribute to.

The high optical extinction achieved in this grating-cantilever technique means that it may be of use as a very efficient optical switch. High optical extinction coupled with the electrostatic control of the micro-cantilever also allows this device to be used as a variable optical attenuator (VOA). The scanning speed for commercial VOAs based on variable neutral density filters such as the JDSU mVOA-A2 can be as fast as 25 dB/s, whereas the scanning speed over the full attenuation range of a MEMS VOA based on the cantilever-grating cavity would be around 5-6 orders of magnitude faster than this. Such a capability would likely be of particular interest to the telecommunications industry, as running test sequences using current VOAs are typically extremely time consuming. More interesting would be an on-chip integration of such VOAs within an optical WDM multiplexer/demultiplexer. This would allow any optical channel to be set to the desired optical power level. As an add/drop multiplexer, by using a substrate detector, channels could be suppressed at the output, while still being monitored by the substrate detector. This is possible because, as shown in Section 3.5.1, at extinction the optical power is redirected to the substrate.

MEMS biological and chemical sensors are not the only MEMS devices that rely on precision measurements of out-of-plane movements of the device. MEMS microphones, microseismic sensors, and accelerometers are all devices that may find benefits in the ability to measure the movements of the MEMS components with the accuracy that a technique based on optical interferometry can provide.

As the technique has the potential to be implemented in a completely optical manner, there

are inherent benefits of its use compared to devices that use electronics. Aircraft environments prefer their equipment to have RF emissions as low as possible. Mining applications require sensors for flammable gases in environments where a spark from an electronic device could be disastrous. The purely optical nature of this sensor means that there is potential to place these sensors at desired locations, and have the optical power fed to them using fibre optic cables. This opens up the opportunity to create sensor networks containing various optical-only sensors, such as micro-cantilever sensors and Bragg grating sensors, spreading them over large distances and feeding/receiving optical power to/from them using fibre optic cables. The entire network could be controlled using optical cross-connect switches, and so provide comprehensive information about the surveyed environment.

A particularly interesting research topic that has arisen in recent years is that of cavity optomechanics and optical back-action. A study of the optomechanical dynamics of cavity systems can be useful in many applications from gravitational wave detectors to scanning probe microscopy [163]. The grating-cantilever technique is a novel method of creating a micro-cavity beneath a mechanical beam, and may be of use to such experiments.

7.2.8 Final Comments

A low power, extremely high precision optical technique for measuring the position of suspended MEMS components has been demonstrated. Using WDM, or even standard optical power splitting techniques (such as MMI couplers) with integrated photodiodes at the output, this technique has the potential to be used to address very large arrays of devices.

There are many applications for this technique, and it is hoped that the work demonstrated here will be of assistance in the implementation of future MOEMS-based sensors.

Appendices

Publications Arising From The PhD Program

A.1 Refereed Journal Articles

The author's journal publications arising from this thesis were:

1. **Putrino G.**, Keating, A., Martyniuk, M., Faraone L., Dell, J., Model and Analysis of a High Sensitivity Resonant Optical Read-Out Approach Suitable for Cantilever Sensor Arrays, Journal of Lightwave Technology, 30, 12, pp 1863-1868 (2012)

2. **Putrino, G.**, Keating, A., Martyniuk, M., Faraone, L., Dell, J., Integrated, Resonant Optical Readout Applicable to Large Arrays of MEMS Beams, IEEE Photonics Technology Letters, 24, 24, pp. 2243-2246 (15 Dec 2012)

3. **Putrino, G.**, Keating, A., Martyniuk, M., Faraone, L., Dell, J., Demonstration of a Brownian Motion Limited, Integrated Optical Read-out Approach for MEMS Cantilevers, In Progress

A.2 Patents

Patent applications arising from this work that the author is named in are below. All patents were registered at both the Australian Patent Office (APO) and the United States Patent and Trademark Office (USPTO).

1. Dell, J.M., Martyniuk, M., Keating, A.J., **Putrino, G.M.**, Faraone, L., Optical cantilever based analyte detection I: US Patent No: 20120218556, Issue Date: 08/30/2012, Australian Patent No: AU2011200816

2. Dell, J.M., Martyniuk, M., Keating, A.J., **Putrino, G.M.**, Faraone, L., Optical cantilever based analyte detection II: US Patent No: 20120218559, Issue Date: 08/30/2012, Australian Patent No: AU2011200816

3. Dell, J.M., Martyniuk, M., Keating, A.J., **Putrino, G.M.**, Faraone, L., A system and method of performing atomic force measurements: US Patent No: 20130205455, Issue Date: 08/08/2013, Australian Patent No: AU2012900444

A.3 Refereed Conference Papers

The Author's peer reviewed conference papers arising from this thesis were:

1. **Putrino, G.**, Keating, A. Martyniuk, M., Dell, J.M., A novel multiplexed optical read-out technology for micromachined cantilever sensor arrays using diffraction gratings, Oral presentation (CSM13) at APCOT 2010, UWA, Perth, WA, Australia, 6-9 July 2010

2. **Putrino, G.**, Keating, A., Martyniuk, M., Dell, J.M., Comparison of dynamic and static operation of a novel optical read-out technology for micromachined cantilever sensors, Oral presentation at COMMAD 2010, 12-15 Dec 2010, Canberra, ACT, Australia, IEEE Proceedings (ISBN 978-1-4244-8332-8), pp 21-22 (2010)

3. **Putrino, G.**, Keating, A., Martyniuk, M., Faraone, L., Dell, J.M., A Novel Optical Read-out Technology for Large Arrays of Micromachined Cantilever Sensors, Poster presentation at CLEO Pacific Rim, Sydney, NSW, Australia, 28 Aug-1 Sept 2011

4. **Putrino, G.**, Martyniuk, M., Keating, A., Dell, J., Faraone, L., Integrated optical readout of a MEMS biological sensor, Oral presentation at ICONN 2012, Perth, WA, Australia, 5-9 February 2012

5. **Putrino, G.**, Keating, A., Martyniuk, M., Faraone, L., Dell, J.M, Demonstration of a Method for Detecting MEMS Suspended Beam Height, Poster presentation at Optical MEMS & Nanophotonics Conference, Banff, Alberta, Canada, 6-9 Aug 2012

6. **Putrino, G.**, Martyniuk, M., Keating, A., Dell, J., Faraone, L., A WDM Capable Integrated Optical Readout of a MEMS Sensor, Oral presentation at The 26th EUROSENSORS Conference, Krakow, Poland, 9-12 Sept-12

7. **Putrino, G.**, Keating, A., Martyniuk, M., Faraone, L., Dell, J.M, An optically resonant, grating-based technique for the sensitive detection of MEMS cantilever beam height, Accepted for Oral presentation at COMMAD 2012, Melbourne, Victoria, Australia, 12—14 December 2012

8. **Putrino, G.**, Martyniuk, M., Keating, A., Dell, J., Faraone, L., A high resolution, large range, position sensing technique for MEMS cantilevers, Oral presentation at SPIE Micro+Nano Materials, Devices, and Applications 2013, Melbourne, Victoria, Australia, 8-11 December 2013.

Awards Won During The PhD Program

The list of awards won by the author over the course of this work are as follows:

1. Poster presentation award at the Nanophotonics Workshop, Mclaren Vale, SA, 2011. Award: Bottle of wine.
2. Best oral presentation at the Postgraduate Electrical Engineering and Computing Symposium (PEECS) 2012. Award: Cash Prize.
3. Oral presentation award at the Conference on Optoelectronic and Microelectronic Materials and Devices (COMMAD) 2012. Award: Cash Prize.
4. Two Minute Thesis finalist for PhD Comics. Award: Two minute animation drawn and coloured by Jorge Cham. Animation available at either http://www.youtube.com/watch?v=2thPLCpyyBo or http://www.phdcomics.com/tv/#032.

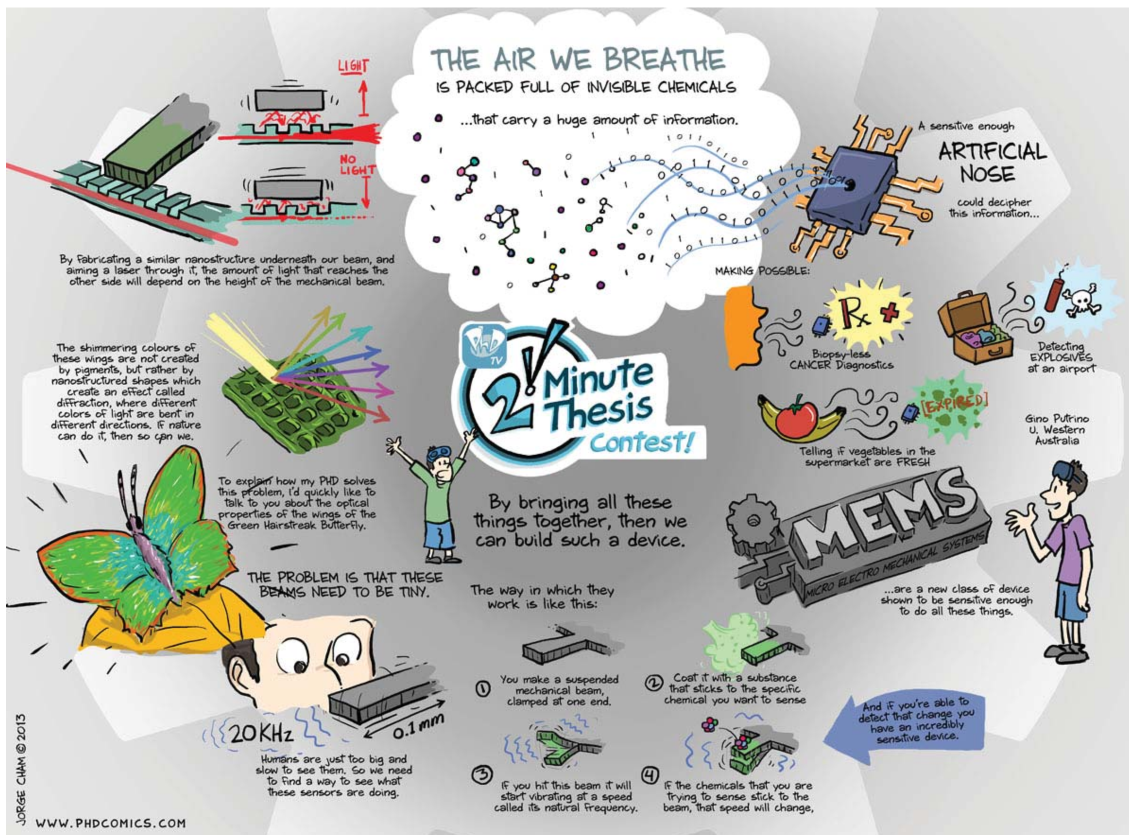

Figure B.0.1: Splash screen of two minute thesis animation.

LETI Standard Process Capabilities

C.1 ePIXfab

ePIXfab is an european silicon photonics platform made up of a consortium of 7 partners. The mission of ePIXfab is to build a future for silicon photonics in Europe through the development of a fabless model for the fabrication of silicon photonic circuits based on existing CMOS labs and commercial foundries relying on European know-how.

This should be done by involving all interested parties, from academia, industy and policy-making bodies.

C.2 LETI

LETI provide two process technologies to the ePIXfab platform: the LETI Standard Process, and the LETI Photodetector Technology. To fabricate our photonic circuit, we used the LETI Standard Process.

C.2.1 LETI Standard Process

The key aspects of the LETI Standard Process are as follows:

1. 200 mm silicon-on-insulator wafers, 220 nm crystalline Si on 2 μm BOX
2. 193 nm deep UV lithography
3. WG module: 220 nm full etch for waveguides, photonic crystals, etc.
4. FC module: 70 nm partial etch for grating couplers, splitters, etc.

5. Heater module: 600 nm of top oxide Ti/TiN heaters
6. Minimum linewidth: 120 nm
7. Minimum pitch: 280 nm
8. Choice from fixed design sizes
9. Delivery of at least 50 dies

D

Sample FDTD Code

Below is a sample listing of MEEP code used to generate the FDTD simulation results shown in Figure 3.5.3. The code of the other simulations performed in this thesis is available upon request.

```
;
; PERFECT METAL CANTILEVER - SEPARATION 0.80UM
;
; define helper function to print out calculated values
;
(define (myprinter message value)
    (begin
        (display message)
        (display value)
        (newline)
    )
)
;
; define geometry parameters
;
(define-param sxmax 64) ; maximum sx
(define-param symax 32) ; maximum sy
(define-param pad 4) ; padding distance between waveguide and cell edge
(define-param pml-thick 1) ; pml layer thickness
;
; substrate parameters
;
(define-param sub-thick 3) ; substrate thickness - note that 1 pml
    thickness is subtracted from this
(define-param subeps 12) ; substrate permittivity
;
; waveguide parameters
;
(define-param w 0.23) ; width of waveguide
(define-param wgeps 12) ; waveguide material permittivity
```

```
30 (define-param wg-len 8) ; launch/receive waveguide length
31 ;
32 ; grating parameters - need to define dimensions even if grating? is
     false so that
33 ; normalisation volume to same for the straight waveguide and those
     with the grating
34 ;
35 (define-param grating? true) ; is this going to model the grating?
36 (define-param myperiod 0.610) ; myperiod of grating
37 (define-param msratio 0.5) ; mark space ratio
38 (define-param num-periods 19.5) ; number of myperiods
39 (define-param depth 0.05) ; depth of the grating
40 ;
41 ; cantilever parameters - need to define dimensions even if cantilever?
      is false so that
42 ; normalisation volume to same for the straight waveguide and those
     with the cantilever
43 ;
44 (define-param cantilever? true) ; is this going to model the cantilever
     ?
45 (define-param max-cant-sep 5) ; maximum separation of the cantilever
     from the grating
46 (define-param cant-sep 0.80) ; separation of the cantilever from the
     grating
47 (define-param cant-ohang 1 ) ; extension of cantilever over either end
     of the grating
48 (define-param cant-thick 0.3) ; cantilever thickness
49 (define-param canteps 12) ; cantilever material permittivity
50 ;
51 ; BOX parameters
52 ;
53 (define-param box-thick 2) ; thickness of BOX
54 (define-param boxeps 2) ; BOX permitivity
55 ;
56 ; calculate grating parameters
57 ;
58 (define grating-len (* myperiod num-periods)) ; define length of
     grating
59 (define grating-thick (- w depth)) ; define grating thickness
60 ;
61 ; calculate geometry parameters and define geometry
62 ; if geometry too large STOP (will have to comment out stop statements
     to run)
63 ;
64 (define sx (+ grating-len (* 2 wg-len))) ; x dimension of geometry
65 (if (> sx sxmax)
66     (begin
67         (display "sx = ")
68         (display sx)
69         (display " > sxmax = ")
70         (display sxmax)
71         (newline)
72         (exit))
73     (begin
74         (display "sx = ")
75         (display sx)
76         (newline)))
77 (define sy (+ sub-thick box-thick w max-cant-sep cant-thick pad)) ; y
     demension of geometry
78 (if (> sy symax)
```

```
79      (begin
80          (display "sy = ")
81          (display sy)
82          (display " > symax = ")
83          (display symax)
84          (newline)
85          (exit))
86      (begin
87          (display "sy = ")
88          (display sy)
89          (newline)))
90  (set! geometry-lattice (make lattice (size sx sy no-size))) ; set up
        geometry
91  ;
92  ; calculate substrate parameters
93  ;
94  (define sub-xcen 0) ; x centre of substrate
95  (define sub-ycen (* -0.5 (- sy sub-thick))) ; y centre of substrate
96  ;
97  ; calculate BOX parameters
98  ;
99  (define box-xcen 0) ; x centre of BOX
100 (define box-ycen (+ sub-thick (* -0.5 (- sy box-thick)))) ; y centre of
        BOX
101 ;
102 ; calculate waveguide parameters
103 ;
104 (define launch-xcen (* -0.25 (+ sx grating-len))) ; x centre of
        launching guide
105 (define receive-xcen (* 0.25 (+ sx grating-len))) ; x centre of
        receiving guide
106 (define wg-ycen (+ sub-thick box-thick (* -0.5 (- sy w)))) ; y centre
        of launching/receiving guides
107 (define grating-xcen 0) ; x centre of grating guide
108 (define grating-ycen (+ wg-ycen (* -0.5 depth))) ; y centre of grating
        guide
109 (define gblock-ycen (+ wg-ycen (* 0.5 (- w depth)))) ; ycentre of
        grating blocks
110 ;
111 ; calculate cantilever parameters
112 ;
113 (define cant-len (+ grating-len (* 2 cant-ohang))) ; cantilever length
114 (define cant-xcen 0) ; x centre of cantilever
115 (define cant-ycen (+ wg-ycen cant-sep (* 0.5 (+ w cant-thick)))) ; y
        centre of cantilever
116 ;
117 ; define substrate, BOX, guides and cantilever
118 ;
119 (set! geometry (list
120     (make block (center launch-xcen wg-ycen) (size wg-len w infinity)
121         (material (make dielectric (epsilon wgeps))))
122     (make block (center receive-xcen wg-ycen) (size wg-len w infinity)
123         (material (make dielectric (epsilon wgeps))))
124     (make block (center grating-xcen grating-ycen) (size grating-len
            grating-thick infinity)
125         (material (make dielectric (epsilon wgeps))))
126     (make block (center box-xcen box-ycen) (size sx box-thick infinity)
127         (material (make dielectric (epsilon boxeps))))
128     (make block (center sub-xcen sub-ycen) (size sx sub-thick infinity)
129         (material (make dielectric (epsilon subeps))))))
```

```
130
131 (if cantilever?
132     (begin
133     (display "cantilever will be included")
134     (newline)
135     (set! geometry (append geometry (list (make block (center cant-xcen
          cant-ycen) (size cant-len cant-thick infinity)
136             (material (make perfect-metal))))))))
137 ;             (material (make dielectric (epsilon canteps))))))))
138     (if grating?
139         (begin
140         (display "grating being made")
141         (newline)
142             (do ((iterator 1 (+ iterator 1))) ((> iterator num-periods)
                )
143                 (begin
144                     (set! geometry (append geometry (list
145                         (make block (center (- (* iterator myperiod) (*
                            0.5 grating-len) (* 0.5 msratio myperiod))
                            gblock-ycen)
146                             (size (* msratio myperiod) depth infinity)
147                                 (material (make dielectric (epsilon
                                    wgeps)))))))
148                     (display "centre is ")
149                     (display (- (* iterator myperiod) (* 0.5 grating-
                        len) (* 0.5 msratio myperiod)))
150                     (newline)))))
151
152 ;
153 ; define source
154 ;
155 (define-param src-freq 0.645)
156 (set! sources (list
157     (make source
158         (src (make continuous-src (frequency src-freq)))
159         (component Ez)
160         (center (+ 1 (* -0.5 sx)) wg-ycen))))
161 ;
162 ; matched boundaries and resolution
163 ;
164 (set! pml-layers (list (make pml (thickness 1.0))))
165 (set-param! resolution 40)
166 ;
167 ; generate geometry and field plots
168 ;
169 (define-param final-time 500) ; time to run in order to get to steady
    state
170 (run-until final-time
171             (at-beginning output-epsilon)
172             (at-end output-efield-z))
```

E

Microfabrication Process Used To Create MEMS

E.1 Fabrication of MEMS

The MEMS structures were fabricated using a multi-step surface micro-machining process, which will be described in detail in this section. A fabrication process was designed to create MEMS free-standing structures which contained an under-coating of metal to be used as an infra-red mirror. The process involves deposition and patterning of several thin films to create the structure. Matching the stress in subsequent films is important to create devices that will remain in the desired shape after release occurs.

The first step is to deposit the wiring and pads which will be used for electrostatic actuation of the MEMS structures. This step is only performed for devices which require electrostatic actuation, and not for the devices that are externally acoustically actuated. The second step is to deposit a sacrificial layer of a thickness that will become the height of the suspended MEMS device. Next, holes are etched into the sacrificial layer - these holes will become the supporting legs of the MEMS devices. Following this, the mirror material is deposited, and patterned to create mirrors in locations which will become the bottom of the MEMS beams. The structural layer is then deposited, patterned to the same geometry of the mirror material, and finally the release process is performed. This process flow is shown in Figure E.1.1. Each step in the process is discussed in further detail in the sections below.

E.1.1 Wafer Cleaning

To prepare the surface of the wafer for processing, the wafer was cleaned using the following steps:

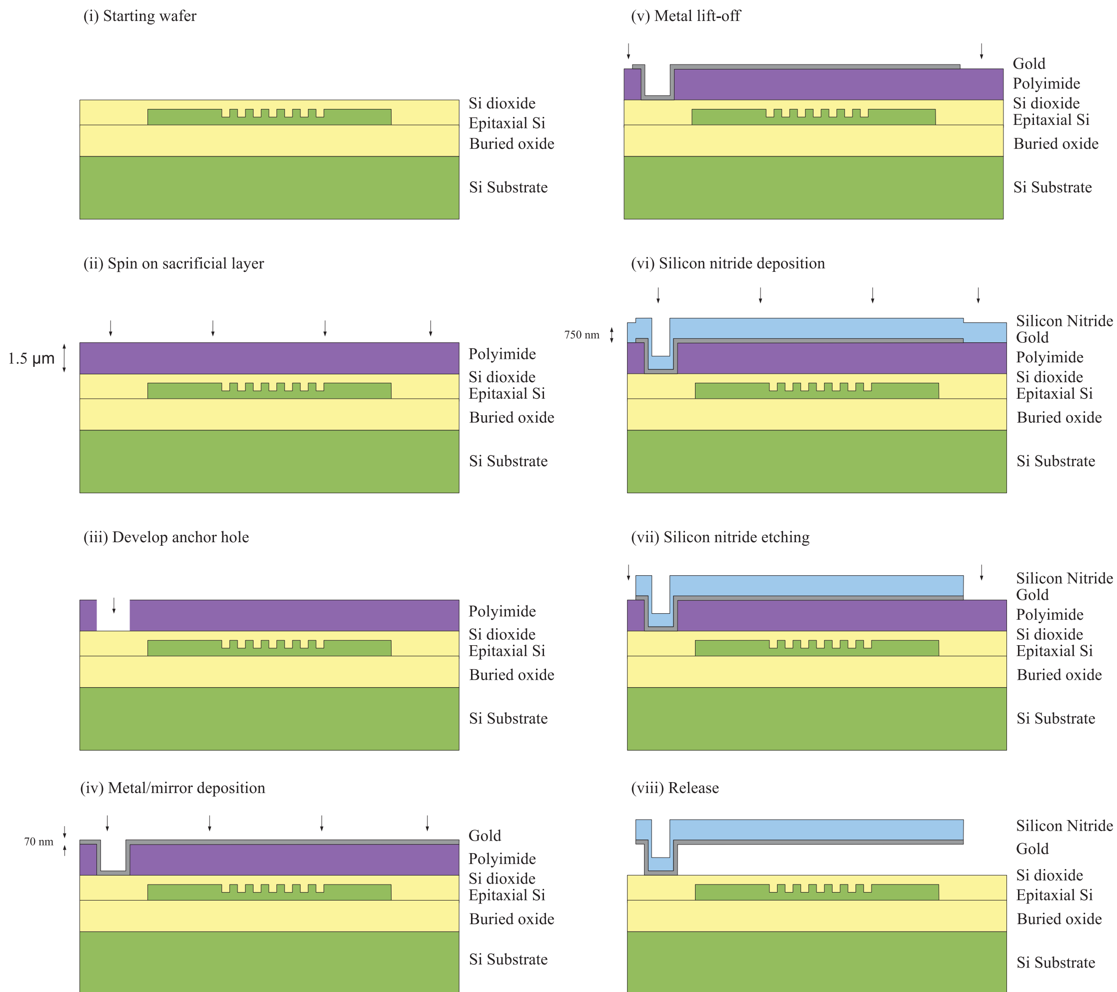

Figure E.1.1: MEMS process flow. A MEMS cantilever is built by depositing and patterning several layers of various thin films. This figure does not include the step for the deposition of the electrostatic pads and wiring.

1. Immerse wafer in 75 ml of trichloroethylene heated to 60○C for 5 minutes, followed by one minute of ultrasonic vibration

2. Immerse wafer in 75 ml of acetone heated to 60○C for 5 minutes, followed by one minute of ultrasonic vibration

3. Immerse wafer in 75 ml of methanol heated to 60○C for 5 minutes, followed by one minute of ultrasonic vibration

4. Rinse wafer in isopropanol, then dry using a nitrogen gas gun.

E.1.2 Wiring and Actuation Pads

The wiring and actuation pads are necessary for the individual electrostatic actuation of MEMS beams. The actuation pads must not occlude the diffraction grating of the optical circuit. This step was only performed for devices where electrostatic actuation is desired, and skipped for chips where this was not. The wiring and pads were created by using photolithography to first pattern the wafer. A metal thermal evaporator is then used to deposit a stiction layer of 3 nm of chromium, then a 100 nm gold wiring layer. A lift-off process is then performed to leave the gold and chromium wiring in the correct pattern.

The photoresist used for this step is AZ 2035 negative photoresist. The recipe used to apply this photoresist is as follows:

1. Preheat the wafer at 100°C for 1 minute to remove any moisture from the surface by dehydration

2. Apply the photoresist to the wafer and spin at 5000 rpm for 45 seconds in order to evenly distribute the photoresist over the wafer surface

3. Prebake the wafer for 1 minute at 113°C (also know as a softbake) This step removes some of the solvent in the photoresist by evaporation. This step is necessary in order to:

   - avoid mask contamination or sticking to the mask for the case of contact lithography,
   - prevent bubbling or foaming from nitrogen during exposure,
   - minimize dark erosion during development
   - prevent bubbling during subsequent thermal processes

4. UV i-line (365 nm) exposure. The exposure time for an appropriate dose for this photoresist using the available mask aligner was approximately 3 s. This exposure time could become variable and can increase as the UV lamp bulb ages and decreases in intensity.

5. Post exposure bake (PEB) at 113° for 90 seconds. This step is necessary to assist the reactions initiated during exposure to run to completion [3].

6. Leave wafer at room temperature for 2-3 minutes for photoresist reactions to complete and the wafer to cool down, then develop using either AZ 826 or AZ 326 developer for 80 seconds. This will pattern the photoresist by removing the unexposed photoresist (in this case the area that will become wires and pads), and leaving the exposed photoresist

7. Rinse in de-ionised (DI) water, then dry with a nitrogen gun.

Thermal evaporation is a technique where a heated material is either evaporated or sublimated onto a substrate in a vacuum. [3]. Resistive heating is used in the thermal evaporator that was available, and so the metal was evaporated by running a current through a tungsten boat containing the metal to be evaporated. By controlling the current, the rate of deposition can be controlled. Both the Cr and Au layers were deposited at a rate of 0.5 Å/s in a vacuum of 10^{-6} Torr. A chromium layer 30 Å thick was deposited as the stiction layer, and 1000 Å of gold was deposited to provide the wiring layer. Minor contamination from the material of the boat can occur using this type of resistive heating, however, this effect did not notably effect the conductivity of the wiring for the low current and low frequency actuation purposes required, or the reflectivity of the gold (discussed in Chapter 4).

After the metal deposition, the lift-off process is performed. This process involves immersing the sample in heated acetone. The acetone will attack and dissolve the photoresist that is beneath the unwanted metal, lifting off that unwanted metal, and leaving the metal desired in the circuit attached to the sample. The acetone was heated to 50°C, and the sample was immersed for periods of 5 minutes, following which the sample was ultrasonically vibrated for another minute. This process was repeated until all unwanted metal had been removed. The sample was then dipped in isopropanol, and dried with a nitrogen gas gun.

E.1.3 Sacrificial Layer

In MEMS processing, a sacrificial layer is a layer made of a material which will be patterned to provide a support (similar to a scaffold) to allow structures to be built up out of the plane (in the y-direction as defined in Figure 3.1.1). At the end of processing, the sacrificial material will be completely removed. For the purposes of this device, the sacrificial layer will be etched to create holes which the inverted top hats of the structural layer will be later built into.

After some experimentation with alternatives, DuPont Polyimide 2610 was chosen as the sacrificial layer. The 2600 series of polyimides are low stress and allow a 2-stage curing process, so that anchor holes can be etched into this layer after the first stage of curing, and then the final cure can be performed to harden this layer prior to depositing later films. At the end of processing, this polyimide can be removed using oxygen ashing, leaving the rest of the structures of the device in place. Polyimide 2610 was specifically chosen because its viscosity is such that the target thickness of 1.5 μm can be easily achieved.

This polyimide can be deposited with a uniform thickness using a spin coating technique. The process used to do this is as follows:

1. Dehydrate the wafer by heating for 1 minute at 100°C.

2. Apply the polyimide and spin at 5000 rpm for 45 seconds.

3. Heat the polyimide for 2 minutes at 100°C then ramp the temperature to 125°C for a further 10 minutes.

The polyimide is now partially cured and ready for the next step which will etch the anchor holes. After this step the wafer looks like the image in Figure E.1.1(ii).

E.1.4 Anchor Holes

The anchor holes are developed by using a basic photolithography process. AZ 2035 photoresist is used once again with an anchor hole mask, following the same recipe photoresist development process described previously. Once that recipe is complete, holes will have been etched in both the photoresist and the underlying sacrificial layer. The wafer is then immersed in acetone which has been heated to 60°C for 5 minutes. This step removes the undeveloped photoresist, but leaves the partially cured polyimide sacrificial layer intact. After rinsing the wafer in DI water and drying with nitrogen, the polyimide undergoes it's final cure by being baked for 20 minutes at 325°C. The state of the wafer after this step is seen in Figure E.1.1(iii).

E.1.5 MEMS Mirror

The mirror layer is created by using photolithography to first pattern the photoresist which will be used for liftoff. A thermal evaporator is then used to deposit a stiction layer of 3 nm of chromium, the 70 nm gold mirror layer, followed by a second 3 nm layer of chromium for stiction. The photoresist used here is AZ 2035, and the process used is the same as when depositing the actuation wiring and pads. Note that this type of deposition is conformal, so the metal follows the contours of the sacrificial layer as seen in Figure E.1.1(iv). After this, the same acetone lift-off process is performed to remove the unwanted gold and chromium, leading to the final state shown in Figure E.1.1(v).

E.1.6 Structural Layer Deposition

As mentioned earlier, the material chosen for the structural layer was silicon nitride. This was deposited using a PECVD technique. Chemical vapour deposition (CVD) is a technique where reactive gasses are mixed to create the desired end products to deposit onto a substrate [3]. PECVD extends this technique to use plasma activation to create radicals which form the desired film. The more energetic ion bombardment made possible by the plasma leads to higher density films with good adhesion and improved mechanical properties.

The silicon nitride used was formed using a silane (SiH_4), ammonia (NH_3) and nitrogen (N_2) gas mix at a temperature of 200°C. Conditions were chosen to minimize stress. The flow rates for these gases were 6.8, 50, and 100 sccm respectively. The initial plasma strike is performed using an RF forward power of 50 W, and an inductively coupled plasma (ICP) forward power of 150 W. The SiN_x deposition is then performed using ICP forward power of 150 W. This process was found to give a deposition rate of 28 nm/s and so was run for 23 mins

to create a layer 750 nm thick. This deposition is also conformal, on completion of this step, the wafer cross-section will look like Figure E.1.1(vi).

E.1.7 Structural Layer Etching

The structural layer must now be patterned to form the final device structure. The technique chosen to perform this step was reactive ion etching (RIE). RIE uses a chemically reactive plasma in a vacuum to remove material deposited on wafers. A mix of tetrafluoromethane (CF_4) and oxygen (O_2) was used to remove the silicon nitride structural layer.

The photoresist used for this step is AZ6632 positive photoresist. This photoresist was chosen to provide a thick protective layer for the silicon nitride from the RIE. The recipe used to apply this photoresist is as follows:

1. Dehydrate the wafer by heating for 1 minute at 100°C.
2. Apply the photoresist to the wafer and spin at 4000 rpm for 40 seconds.
3. Prebake the wafer for 50 seconds at 110°C.
4. UV i-line exposure for 7 seconds using the available mask aligner.
5. No post exposure bake is required for this resist.
6. Develop in AZ 826 metal ion free (MIF) developer for 1 minute at room temperature.
7. Rinse in DI water then dry with a nitrogen gun.

An RIE etch on the SiN_x was then performed using a CF_4 and O_2 mix with a flow of 100 sccm CF_4 and 6 sccm O_2. The RF forward power was 100 W, and the ICP forward power was 150 W. Following this step, an O_2 descum was performed in the RIE chamber, using an O_2 flow of 20 sccm, an RF forward power of 50 W, and an ICP forward power of 100 W. After this process, the wafer is in the state represented by Figure E.1.1(vii).

E.1.8 Sacrificial Layer Release

The final step in creating the MEMS device is the sacrificial layer release. As the sacrificial layer used was a polyimide, oxygen plasma ashing can be used to remove it. A plasma was created using an RF power of 200 Watts, with a strong flow of oxygen at a pressure of 1 Torr. This plasma was then used to slowly remove the polyimide layer in three bursts of eight minutes each, with time in between each burst to allow the wafer to cool down. After this step the MEMS structure is released, and looks similar to the image in Figure E.1.1(viii).

F
Measurement methodology

This appendix details the measurement methodology used to calibrate the optical output of the grating measurement system, and contains a listing of equipment used.

Two MEMS characterization systems were used to perform this calibration task: a Zygo NewView 7300 optical profilometer, and a Polytec OFV-5000 laser doppler vibrometer. The optical profilometer was used to obtain the height of the MEMS structures when at rest. The vibrometer was subsequently used to characterize the movement of the MEMS structures under different actuation conditions.

F.1 Optical Profilometer

The Zygo Optical surface profilometer is a scanning white light interferometer which can perform fast non-contact measurements of topographical features. In order for this tool to provide accurate measurements, the reflectivity of the surfaces being profiled must be similar. Due to this feature of the equipment, the height difference between the substrate and the suspended MEMS beams cannot be measured directly, as the thin films that the MEMS structures are made from reflect differently to the surface of the chip substrate. This can be clearly seen in Figure F.1.1 where the embedded silicon waveguide appears to be *above* the substrate surface, even though the silicon waveguide is *below* a silicon dioxide planarization layer.

Fortunately, for our device designs, the anchors of the cantilevers are formed from the same silicon nitride and gold process steps that form the cantilever beams. The thickness and reflectivity of these layers are the same, and so the profilometer can be used to indirectly, yet accurately determine the height that the suspended beam is above the substrate by measuring the height difference between the top surface of the base of the MEMS anchor, and the top

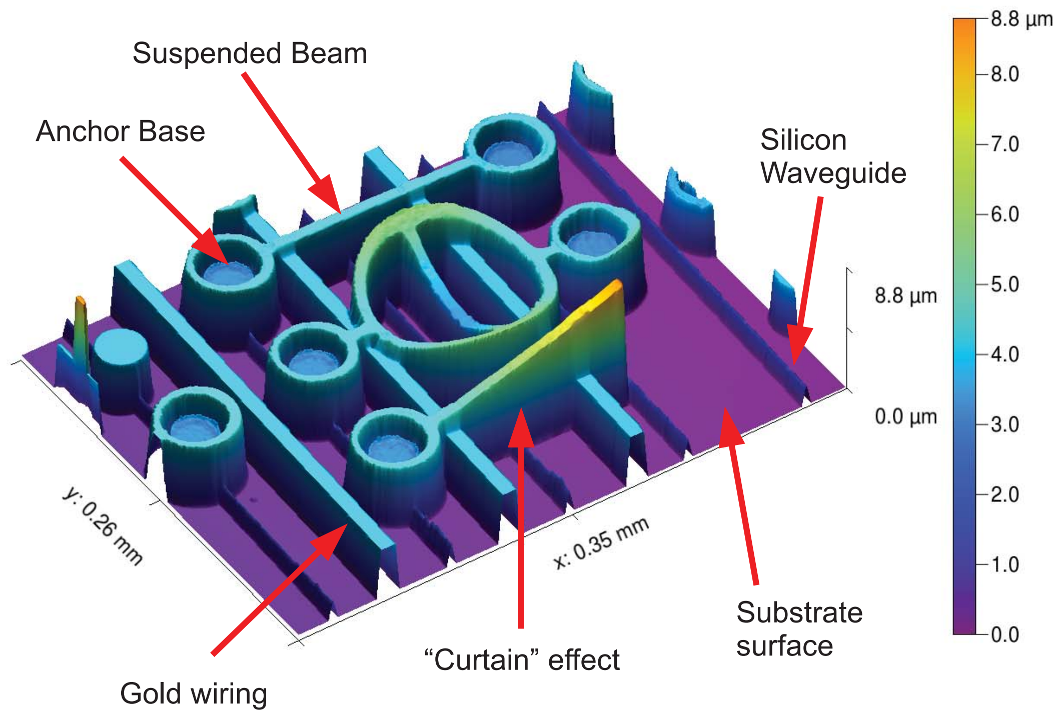

Figure F.1.1: 3D optical surface profilometry image of various MEMS devices. Idiosyncrasies of the measurement tool can be seen: the embedded Si waveguide appears to be above the substrate surface, and a "curtain" effect in the region beneath suspended structures is visible.

surface of the cantilever beam.

As mentioned in Chapter 5, because this tool takes top-down surface images, 3D visualizations from the measured data exhibit a "curtain" effect in the region shadowed by suspended structures. This effect can also be seen in Figure F.1.1.

F.2 Vibrometer

The vibrometer used to measure the motion of the MEMS structures was a differential laser doppler vibrometer. It is comprised of a Polytec OFV-5000 laser doppler vibrometer controller with a DD-500 displacement decoder, and an OFV-552 differential fiber sensor head. The output of this system was connected to either an oscilloscope (for time domain measurements), a lock-in amplifier (for sensitive narrowband measurements), or a spectrum analyser (for analysing the full spectra of the output signal). The DD-500 displacement decoder has a minimum resolution of 15 pm over the bandwidth from 0 to 350 kHz.

The differential fiber sensor head provides two laser beams - and the vibrometer calculates the difference in either the velocity or the displacement between two objects which the two laser beams are focussed upon. Measurements using the vibrometer where performed by focussing the reference laser beam to a reflective feature on the substrate (e.g. a gold electrostatic actuation pad), and then focussing the second, measurement laser beam upon the MEMS structure. This provided measurement of the displacement/velocity of the beam when

the MEMS structure was actuated by either electrostatics or a piezoelectric stack connected to the underside of the substrate of the chip.

F.3 Photodiodes

Two different InGaAs photodiodes were used in this experiment. The first was a Thorlabs DC400FC high speed photo detector and the second was a Hamamatsu G8376-03. Both photodiodes have a spectral response from 800-1700 nm, and a peak response of 0.95 A/W at 1550 nm. The Thorlabs photo detector has a FC/PC connector, and an internal 12 V bias battery, providing the ability to connect the photodiode directly to measurement equipment. The Thorlabs photo detector has a typical dark current of 0.7 nA, and a noise equivalent power (NEP) at 1550 nm of 1×10^{-15} W/$\sqrt{\text{Hz}}$. The Hamamatsu photodiode comes in a 3-pin TO-18 package. This photodiode was built into the low-noise custom transimpedance amplifier that was used in this work. The Hamamatsu photodiode has a typical dark current of 0.3 nA, and a NEP at 1550 nm of 4×10^{-15} W/$\sqrt{\text{Hz}}$

F.4 Transimpedance Amplifiers

Two transimpedance amplifiers were used for the measurements in this work. The first was a Stanford Research Systems SR570 low noise current preamplifier. This device had 1 pA/V maximum gain, but was generally operated at much lower gains to obtain increased measurement bandwidth. The Thorlabs photo detector used was plugged directly into this piece of equipment.

The second transimpendance amplifier was a custom 1 MΩ amplifier with 500 kHz bandwidth based on Texas Instruments OPA659 operational amplifiers. This is the amplifier that the Hamamatsu photodiode was built into. The circuit schematic for this amplifier is available on request.

F.5 Actuation

The signal to perform actuation of the MEMS was supplied by an Agilent 33220A arbitrary waveform generator. This tool can supply waveforms of amplitude up to 20 V peak to peak, and has a frequency range from 1 μHz to 20 MHz. It has USB and GPIB connections for remote control.

For measurements requiring voltage actuation higher than the Agilent was capable of, a Tegam Model 2350 dual channel high voltage precision power supply was used to amplify the Agilent signal.

F.6 Time Domain Measurements

Time domain measurements of the response of the device were performed by connecting either of the transimpedance amplifier outputs to a Rigol DS1204B digital oscilloscope. This scope has USB outputs that can be used to either allow the scope to be controlled via an external computer, or record data directly to a USB storage device.

F.7 Frequency Domain Measurements

Frequency domain measurements were made via either a Stanford Research Systems SR830 lock-in amplifier or an Agilent E4402B spectrum analyzer.

The SR830 lock-in amplifier has the option of an extremely sensitive current input, and so measurements involving this device were performed by connecting the Thorlabs photo detector directly to the input of the lock-in amplifier, without using either of the transimpedance amplifiers described above. When using the current input, the input impedance is 1 kΩ to a virtual ground, and has an input noise of 6 nV/$\sqrt{\text{Hz}}$ at 1 kHz. The lock-in amplifier has a frequency range from 1 mHz to 102 kHz. This lock-in amplifier was controlled externally via a GPIB connection. By using a computer to set the both the frequency of the Agilent 33220A waveform generator actuation signal, and the lock-in frequency of the lock-in amplifier, very accurate frequency sweep measurements were made.

The Agilent E4402B spectrum analyzer has a 50 Ω input, a frequency range of 9 kHz to 3.0 GHz, and an average noise level of -139 dBm in the frequency range below 10 MHz. When taking measurements with this tool, either of the transimpedance amplifiers was connected to the input, and frequency domain measurements were taken. A discussion of the method used to convert these measurements into distance measurements for the purposes of our experiments is given in Section 6.2.2.

References

[1] Frank Wanless. United states patent: 3356858, December 1967.

[2] M. Bohr. The new era of scaling in an SoC world. In *Solid-State Circuits Conference - Digest of Technical Papers, 2009. ISSCC 2009. IEEE International*, pages 23–28, 2009. doi: 10.1109/ISSCC.2009.4977293.

[3] Marc J. Madou. *Fundamentals of Microfabrication: The Science of Miniaturization, Second Edition*. CRC Press, 2 edition, March 2002. ISBN 0849308267.

[4] K. Kanda, I. Kanno, H. Kotera, and Kiyotaka Wasa. Simple fabrication of metal-based piezoelectric MEMS by direct deposition of thin films on titanium substrates. *Journal of Microelectromechanical Systems*, 18(3):610–615, 2009. ISSN 1057-7157. doi: 10.1109/JMEMS.2009.2015478.

[5] Shuhei Matsushita, Isaku Kanno, Kazuhiko Adachi, Ryuji Yokokawa, and Hidetoshi Kotera. Metal-based piezoelectric microelectromechanical systems scanner composed of pb(zr, Ti)O3 thin film on titanium substrate. *Microsystem Technologies*, 18(6):765–771, June 2012. ISSN 0946-7076, 1432-1858. doi: 10.1007/s00542-012-1462-8.

[6] P.F. van Kessel, L.J. Hornbeck, R.E. Meier, and M.R. Douglass. A MEMS-based projection display. *Proceedings of the IEEE*, 86(8):1687–1704, August 1998. ISSN 0018-9219. doi: 10.1109/5.704274.

[7] C.L. Goldsmith, D.I. Forehand, Z. Peng, J. Hwang, and J.L. Ebel. High-cycle life testing of RF MEMS switches. In *Microwave Symposium, 2007. IEEE/MTT-S International*, pages 1805–1808, 2007. doi: 10.1109/MWSYM.2007.380099.

[8] L.M. Roylance and J.B. Angell. A batch-fabricated silicon accelerometer. *IEEE Transactions on Electron Devices*, 26(12):1911–1917, 1979. ISSN 0018-9383. doi: 10.1109/T-ED.1979.19795.

[9] S.C. Terry, J.H. Jerman, and J.B. Angell. A gas chromatographic air analyzer fabricated on a silicon wafer. *IEEE Transactions on Electron Devices*, 26(12):1880–1886, 1979. ISSN 0018-9383. doi: 10.1109/T-ED.1979.19791.

[10] T. Ishihara, K. Suzuki, S. Suwazono, M. Hirata, and H. Tanigawa. CMOS integrated silicon pressure sensor. *IEEE Journal of Solid-State Circuits*, 22(2):151–156, 1987. ISSN 0018-9200. doi: 10.1109/JSSC.1987.1052696.

[11] J. Bryzek, R. Mayer, and P. Barth. Disposable blood pressure sensors with digital on-chop laser trimming. In *, IEEE Solid-State Sensor and Actuator Workshop, 1988. Technical Digest*, pages 121–122, 1988. doi: 10.1109/SOLSEN.1988.26455.

[12] A.D. Yalcinkaya, H. Urey, D. Brown, T. Montague, and R. Sprague. Two-axis electromagnetic microscanner for high resolution displays. *Journal of Microelectromechanical Systems*, 15(4):786–794, 2006. ISSN 1057-7157. doi: 10.1109/JMEMS.2006.879380.

[13] Jean-Christophe Eloy. MEMS pace picking up. *III-Vs Review*, 18(6):34–35, August 2005. ISSN 0961-1290. doi: 10.1016/S0961-1290(05)71230-8.

[14] P.W. Coteus, J.U. Knickerbocker, C.H. Lam, and Y.A. Vlasov. Technologies for exascale systems. *IBM Journal of Research and Development*, 55(5):14:1–14:12, 2011. ISSN 0018-8646. doi: 10.1147/JRD.2011.2163967.

[15] Y.A. Vlasov. Silicon CMOS-integrated nano-photonics for computer and data communications beyond 100G. *IEEE Communications Magazine*, 50(2):s67–s72, 2012. ISSN 0163-6804. doi: 10.1109/MCOM.2012.6146487.

[16] T. Thundat, E. A. Wachter, S. L. Sharp, and R. J. Warmack. Detection of mercury vapor using resonating microcantilevers. *Applied Physics Letters*, 66(13):1695, 1995. ISSN 00036951. doi: 10.1063/1.113896.

[17] G. Binnig, C. F. Quate, and Ch. Gerber. Atomic force microscope. *Physical Review Letters*, 56(9):930–933, March 1986. doi: 10.1103/PhysRevLett.56.930.

[18] John Marcel Dell, Mariusz Martyniuk, Adrian John Keating, Gino Michael Putrino, and Lorenzo Faraone. OPTICAL CANTILEVER BASED ANALYTE DETECTION, August 2012.

[19] John Marcel Dell, Mariusz Martyniuk, Adrian John Keating, Gino Michael Putrino, and Lorenzo Faraone. OPTICAL CANTILEVER BASED ANALYTE DETECTION, August 2012.

[20] John Marcel Dell, Mariusz Martyniuk, Adrian John Keating, Gino Michael Putrino, Lorenzo Faraone, and Dilusha Silva. SYSTEM AND METHOD OF PERFORMING ATOMIC FORCE MEASUREMENTS, August 2013.

[21] Y. T. Yang, C. Callegari, X. L. Feng, K. L. Ekinci, and M. L. Roukes. Zeptogram-scale nanomechanical mass sensing. *Nano Letters*, 6(4):583–586, April 2006. ISSN 1530-6984. doi: 10.1021/nl052134m.

[22] G. Gerald Stoney. The tension of metallic films deposited by electrolysis. *Proceedings of the Royal Society of London. Series A*, 82(553):172 –175, May 1909. doi: 10.1098/rspa.1909.0021.

[23] Sumio Okuyama, Yuichi Mitobe, Katsuro Okuyama, and Koichi Matsushita. Hydrogen gas sensing using a pd-coated cantilever. *Japanese Journal of Applied Physics*, 39(Part 1, No. 6A):3584–3590, 2000. doi: 10.1143/JJAP.39.3584.

[24] K. Salama and C. R. Ko. Effect of hydrogen on the temperature dependence of the elastic constants of palladium single crystals. *Journal of Applied Physics*, 51(12):6202–6209, December 1980. ISSN 00218979. doi: doi:10.1063/1.327603.

[25] Adolf Sieverts. Absorption of gases by metals. *Zeitschrift für Metallkunde*, 21:37–46, 1929.

[26] T. Thundat, P. I. Oden, and R. J. Warmack. Microcantilever sensors. *Microscale Thermophysical Engineering*, 1(3):185–199, July 1997. ISSN 10893954. doi: 10.1080/108939597200214.

[27] G. Y. Chen, T. Thundat, E. A. Wachter, and R. J. Warmack. Adsorption-induced surface stress and its effects on resonance frequency of microcantilevers. *Journal of Applied Physics*, 77(8):3618–3622, April 1995. ISSN 00218979. doi: doi:10.1063/1.359562.

[28] P. J. Shaver. Bimetal strip hydrogen gas detectors. *Review of Scientific Instruments*, 40(7): 901–905, 1969. ISSN 0034-6748. doi: 10.1063/1.1684100.

[29] Sviatlana Kalinina, Hartmut Gliemann, Mónica López-García, Andre Petershans, Jörg Auernheimer, Thomas Schimmel, Michael Bruns, Alexandra Schambony, Horst Kessler, and Doris Wedlich. Isothiocyanate-functionalized RGD peptides for tailoring cell-adhesive surface patterns. *Biomaterials*, 29(20):3004–3013, July 2008. ISSN 0142-9612. doi: 10.1016/j.biomaterials.2008.04.003.

[30] Francis J. Norton. Gas analyzer, January 1943. U.S. Classification: 73/31.05; 73/25.01.

[31] H.C. Nathanson, W.E. Newell, R.A. Wickstrom, and Jr. Davis, J.R. The resonant gate transistor. *IEEE Transactions on Electron Devices*, 14(3):117–133, 1967. ISSN 0018-9383. doi: 10.1109/T-ED.1967.15912.

[32] J. C. Greenwood. Etched silicon vibrating sensor. *Journal of Physics E: Scientific Instruments*, 17(8):650, August 1984. ISSN 0022-3735. doi: 10.1088/0022-3735/17/8/007.

[33] J. C. Greenwood. Ethylene Diamine-Catechol-Water mixture shows preferential etching of p-n junction. *Journal of The Electrochemical Society*, 116(9):1325–1326, September 1969. ISSN 0013-4651, 1945-7111. doi: 10.1149/1.2412316.

[34] E. D. Palik, J. W. Faust, H. F. Gray, and R. F. Greene. Study of the Etch-Stop mechanism in silicon. *Journal of The Electrochemical Society*, 129(9):2051–2059, September 1982. ISSN 0013-4651, 1945-7111. doi: 10.1149/1.2124367.

[35] R.T. Howe and R.S. Muller. Resonant-microbridge vapor sensor. *IEEE Transactions on Electron Devices*, 33(4):499 – 506, April 1986. ISSN 0018-9383. doi: 10.1109/T-ED.1986.22519.

[36] R. T. Howe. Polycrystalline silicon micromachining: A new technology for integrated sensors. *Annals of Biomedical Engineering*, 14(2):187–197, March 1986. ISSN 0090-6964, 1573-9686. doi: 10.1007/BF02584269.

[37] R.A. Buser and N.F. De Rooij. Very high q-factor resonators in monocrystalline silicon. *Sensors and Actuators A: Physical*, 21(1–3):323–327, February 1990. ISSN 0924-4247. doi: 10.1016/0924-4247(90)85064-B.

[38] Robert E. Hetrick. Vibrating cantilever mass flow sensor. *Sensors and Actuators A: Physical*, 21(1–3):373–376, February 1990. ISSN 0924-4247. doi: 10.1016/0924-4247(90)85074-E.

[39] Eric Ollier, Paul Philippe, Claude Chabrol, and Patrick Mottier. Micro-opto-mechanical vibration sensor integrated on silicon. *Journal of Lightwave Technology*, 17(1):26, January 1999.

[40] Shane Lani, Sarp Satir, Gokce Gurun, Karim G. Sabra, and F. Levent Degertekin. High frequency ultrasonic imaging using thermal mechanical noise recorded on capacitive micromachined transducer arrays. *Applied Physics Letters*, 99:224103, 2011. ISSN 00036951. doi: 10.1063/1.3664775.

[41] Alexander G. Krause, Martin Winger, Tim D. Blasius, Qiang Lin, and Oskar Painter. A high-resolution microchip optomechanical accelerometer. *Nature Photonics*, 2012.

[42] Raymond J. Roark (Raymond Jefferson). *Roark's formulas for stress and strain*. McGraw-Hill, New York, 8th ed. / warren c. young, richard g. budynas, ali m. sadegh.. edition, 2012. ISBN 0071742476.

[43] J. R. Barnes, R. J. Stephenson, M. E. Welland, Ch Gerber, and J. K. Gimzewski. Photothermal spectroscopy with femtojoule sensitivity using a micromechanical device. *Nature*, 372(6501):79–81, November 1994. doi: 10.1038/372079a0.

[44] J.K. Gimzewski, Ch. Gerber, E. Meyer, and R.R. Schlittler. Observation of a chemical reaction using a micromechanical sensor. *Chemical Physics Letters*, 217(5–6):589–594, January 1994. ISSN 0009-2614. doi: 10.1016/0009-2614(93)E1419-H.

[45] H. P. Lang, M. K. Baller, R. Berger, Ch. Gerber, J. K. Gimzewski, F. M. Battiston, P. Fornaro, J. P. Ramseyer, E. Meyer, and H. J. Güntherodt. An artificial nose based on a micromechanical cantilever array. *Analytica Chimica Acta*, 393(1-3):59–65, June 1999. ISSN 0003-2670. doi: 10.1016/S0003-2670(99)00283-4.

[46] M. K. Baller, H. P. Lang, J. Fritz, C. Gerber, J. K. Gimzewski, U. Drechsler, H. Rothuizen, M. Despont, P. Vettiger, F. M. Battiston, et al. A cantilever array-based artificial nose. *Ultramicroscopy*, 82(1-4):1–9, 2000.

[47] F. M. Battiston, J. P. Ramseyer, H. P. Lang, M. K. Baller, Ch. Gerber, J. K. Gimzewski, E. Meyer, and H. J. Güntherodt. A chemical sensor based on a microfabricated cantilever array with simultaneous resonance-frequency and bending readout. *Sensors and Actuators B: Chemical*, 77(1-2):122–131, June 2001. ISSN 0925-4005. doi: 16/S0925-4005(01)00683-9.

[48] Nickolay V. Lavrik, Christopher A. Tipple, Michael J. Sepaniak, and Panos G. Datskos. Gold nano-structures for transduction of biomolecular interactions into micrometer scale movements. *Biomedical Microdevices*, 3(1):35–44, 2001.

[49] D. Kong, T. Mei, Y. Tao, L. Ni, T. Zhang, W. Lu, Z. Zhang, and R. Wang. A MEMS sensor array for explosive particle detection. In *Information Acquisition, 2004. Proceedings. International Conference on*, page 278–281, 2004.

[50] Mar Alvarez, Ana Calle, Javier Tamayo, Laura M. Lechuga, Antonio Abad, and Angel Montoya. Development of nanomechanical biosensors for detection of the pesticide DDT. *Biosensors and Bioelectronics*, 18(5-6):649–653, May 2003. ISSN 0956-5663. doi: 10.1016/S0956-5663(03)00035-6.

[51] G. Longo, L. Alonso-Sarduy, L. Marques Rio, A. Bizzini, A. Trampuz, J. Notz, G. Dietler, and S. Kasas. Rapid detection of bacterial resistance to antibiotics using AFM cantilevers as nanomechanical sensors. *Nature Nanotechnology*, 8(7):522–526, July 2013. ISSN 1748-3387. doi: 10.1038/nnano.2013.120. 00009.

[52] F. Loizeau, H.P. Lang, T. Akiyama, S. Gautsch, P. Vettiger, A. Tonin, G. Yoshikawa, C. Gerber, and N. de Rooij. Piezoresistive membrane-type surface stress sensor arranged in arrays for cancer diagnosis through breath analysis. In *2013 IEEE 26th International Conference on Micro Electro Mechanical Systems (MEMS)*, pages 621–624, 2013. doi: 10.1109/MEMSYS.2013.6474318.

[53] F. Huber, H. P. Lang, N. Backmann, D. Rimoldi, and Ch Gerber. Direct detection of a BRAF mutation in total RNA from melanoma cells using cantilever arrays. *Nature Nanotechnology*, 8(2):125–129, February 2013. ISSN 1748-3387. doi: 10.1038/nnano.2012.263.

[54] Gajendra S. Shekhawat and Vinayak P. Dravid. Nanomechanical sensors: Bent on detecting cancer. *Nature Nanotechnology*, 8(2):77–78, February 2013. ISSN 1748-3387. doi: 10.1038/nnano.2013.10.

[55] John Elie Sader. Frequency response of cantilever beams immersed in viscous fluids with applications to the atomic force microscope. *Journal of Applied Physics*, 84(1):64–76, 1998. ISSN 0021-8979. doi: 10.1063/1.368002.

[56] Konrad Nieradka, Teodor Pawel Gotszalk, and Grzegorz Schroeder. A novel method for simultaneous readout of static bending and multimode resonance-frequency of microcantilever-based biochemical sensors. *Sensors and Actuators B: Chemical*, 2012.

[57] Thomas P. Burg, Michel Godin, Scott M. Knudsen, Wenjiang Shen, Greg Carlson, John S. Foster, Ken Babcock, and Scott R. Manalis. Weighing of biomolecules, single cells and single nanoparticles in fluid. *Nature*, 446(7139):1066–1069, 2007.

[58] Yves F. Dufrêne. Towards nanomicrobiology using atomic force microscopy. *Nature Reviews Microbiology*, 6(9):674–680, September 2008. ISSN 1740-1526. doi: 10.1038/nrmicro1948.

[59] Gerhard Meyer and Nabil M. Amer. Novel optical approach to atomic force microscopy. *Applied Physics Letters*, 53(12):1045–1047, September 1988. ISSN 00036951. doi: doi:10.1063/1.100061.

[60] H.P. Lang, R. Berger, F. Battiston, J.-P. Ramseyer, E. Meyer, C. Andreoli, J. Brugger, P. Vettiger, M. Despont, T. Mezzacasa, L. Scandella, H.-J. Güntherodt, C. Gerber, and J.K. Gimzewski. A chemical sensor based on a micromechanical cantilever array for the identification of gases and vapors. *Applied Physics A: Materials Science & Processing*, 66(7):S61–S64, March 1998. ISSN 0947-8396. doi: 10.1007/s003390051100.

[61] Mar Álvarez and Javier Tamayo. Optical sequential readout of microcantilever arrays for biological detection. *Sensors and Actuators B: Chemical*, 106(2):687–690, May 2005. ISSN 0925-4005. doi: 10.1016/j.snb.2004.09.016.

[62] K. Nieradka, G. Maloziec, D. Kopiec, P. Grabiec, P. Janus, A. Sierakowski, and T. Gotszalk. Expanded beam deflection method for simultaneous measurement of displacement and vibrations of multiple microcantilevers. *Review of Scientific Instruments*, 82(10):105112–105112, 2011.

[63] Takeshi Fukuma, Masayuki Kimura, Kei Kobayashi, Kazumi Matsushige, and Hirofumi Yamada. Development of low noise cantilever deflection sensor for multienvironment frequency-modulation atomic force microscopy. *Review of Scientific Instruments*, 76(5): 053704–053704–8, April 2005. ISSN 00346748. doi: doi:10.1063/1.1896938.

[64] K.E.B. Thornton, D. Uttamchandani, and B. Culshaw. Temperature dependence of resonant frequency in optically excited diaphragms. *Electronics Letters*, 22(23): 1232–1234, 1986. ISSN 0013-5194. doi: 10.1049/el:19860845.

[65] M.V. Andres, M. J. Tudor, and K. W H Foulds. Analysis of an interferometric optical fibre detection technique applied to silicon vibrating sensors. *Electronics Letters*, 23(15): 774–775, 1987. ISSN 0013-5194. doi: 10.1049/el:19870549.

[66] M. J. Tudor, M.V. Andres, K. W H Foulds, and J. M. Naden. Silicon resonator sensors: interrogation techniques and characteristics. *Control Theory and Applications, IEE Proceedings D*, 135(5):364–368, 1988. ISSN 0143-7054. doi: 10.1049/ip-d:19880055.

[67] M. Helm, J. J. Servant, F. Saurenbach, and R. Berger. Read-out of micromechanical cantilever sensors by phase shifting interferometry. *Applied Physics Letters*, 87(6): 064101, 2005. ISSN 00036951. doi: 10.1063/1.2008358.

[68] C. Schonenberger and S. F. Alvarado. A differential interferometer for force microscopy. *Review of Scientific Instruments*, 60(10):3131–3134, 1989.

[69] T. H. Stievater, W. S. Rabinovich, M. S. Ferraro, N. A. Papanicolaou, R. Bass, J. B. Boos, J. L. Stepnowski, and R. A. McGill. Photonic microharp chemical sensors. *Optics Express*, 16(4):2423–2430, February 2008. doi: 10.1364/OE.16.002423.

[70] Marcel W. Pruessner, Todd H. Stievater, and William S. Rabinovich. In-plane microelectromechanical resonator with integrated Fabry–Pérot cavity. *Applied Physics Letters*, 92(8):081101–081101, 2008.

[71] MattCamacho Eichenfield. A picogram- and nanometre-scale photonic-crystal optomechanical cavity. *Nature*, 459(7246):550–555, May 2009. ISSN 00280836. doi: 10.1038/nature08061.

[72] T.H. Stievater, W.S. Rabinovich, Harvey S. Newman, J.L. Ebel, R. Mahon, D.J. McGee, and P.G. Goetz. Microcavity interferometry for MEMS device characterization. *Journal of Microelectromechanical Systems*, 12(1):109–116, 2003. ISSN 1057-7157. doi: 10.1109/JMEMS.2002.807465.

[73] Todd H. Stievater, William S. Rabinovich, Mike S. Ferraro, J. Brad Boos, Nicolas A. Papanicolaou, Jennifer L. Stepnowski, and R. Andrew McGill. All-optical micromechanical chemical sensors. In *Proceedings of SPIE*, pages 64640D–64640D–10, San Jose, CA, USA, 2007. doi: 10.1117/12.700224.

[74] G. Charmaine Gilbreath, Mena Stell, Rita Mahon, Peter G. Goetz, Kerry Cochrell, Robert L. Lucke, Sharon Mozersky, Eun Oh, William S. Rabinovich, Timothy J. Meehan, John A. Vasquez, and Michael J. Vilcheck. Progress in development of multiple-quantum-well retromodulators for free-space data links. *Optical Engineering*, 42 (6):1611–1617, June 2003. ISSN 0091-3286. doi: 10.1117/1.1572155.

[75] T. H. Stievater, W. S. Rabinovich, M. S. Ferraro, N. A. Papanicolaou, J. B. Boos, R. A. McGill, J. L. Stepnowski, and E. J. Houser. All-optical micromechanical chemical sensors. *Applied Physics Letters*, 89(9):091125–091125–3, September 2006. ISSN 00036951. doi: doi:10.1063/1.2344936.

[76] Kartik Srinivasan, Houxun Miao, Matthew T. Rakher, Marcelo Davanço, and Vladimir Aksyuk. Optomechanical transduction of an integrated silicon cantilever probe using a microdisk resonator. *Nano Lett.*, 11(2):791–797, 2011. ISSN 1530-6984. doi: 10.1021/nl104018r.

[77] E. Gavartin, P. Verlot, and T. J. Kippenberg. A hybrid on-chip optomechanical transducer for ultrasensitive force measurements. *Nature Nanotechnology*, 7(8):509–514, 2012.

[78] Houxun Miao, Kartik Srinivasan, and Vladimir Aksyuk. A microelectromechanically controlled cavity optomechanical sensing system. *New Journal of Physics*, 14(7):075015, July 2012. ISSN 1367-2630. doi: 10.1088/1367-2630/14/7/075015.

[79] Baron John William Strutt Rayleigh. *The theory of sound*, volume 2. Macmillan, 1896.

[80] Kirill Zinoviev, Carlos Dominguez, Jose Antonio Plaza, Victor Javier Cadarso Busto, and Laura M. Lechuga. A novel optical waveguide microcantilever sensor for the detection of nanomechanical forces. *Journal of Lightwave Technology*, 24(5):2132, May 2006.

[81] Jong Wook Noh, Ryan Anderson, Seunghyun Kim, Jaime Cardenas, and Gregory P. Nordin. In-plane photonic transduction of silicon-on-insulator microcantilevers. *Optics Express*, 16(16):12114–12123, 2008. doi: 10.1364/OE.16.012114.

[82] Maria Nordstrom, Dan A. Zauner, Montserrat Calleja, Jorg Hubner, and Anja Boisen. Integrated optical readout for miniaturization of cantilever-based sensor system. *Applied Physics Letters*, 91(10):103512, 2007. ISSN 00036951. doi: 10.1063/1.2779851.

[83] S.T. Koev, R. Fernandes, W.E. Bentley, and R. Ghodssi. A cantilever sensor with an integrated optical readout for detection of enzymatically produced homocysteine. *Biomedical Circuits and Systems, IEEE Transactions on*, 3(6):415–423, 2009. ISSN 1932-4545. doi: 10.1109/TBCAS.2009.2026634.

[84] L.G. Carpenter, C. Holmes, B.D. Snow, J.C. Gates, and P. Smith. Photonic microcantilevers with interferometric bragg grating interrogation. *IEEE Photonics Journal*, 4(5):1387–1395, 2012. ISSN 1943-0655. doi: 10.1109/JPHOT.2012.2210396.

[85] D. Iannuzzi, M. Slaman, J.H. Rector, H. Schreuders, S. Deladi, and M.C. Elwenspoek. A fiber-top cantilever for hydrogen detection. *Sensors and Actuators B: Chemical*, 121(2): 706–708, February 2007. ISSN 0925-4005. doi: 10.1016/j.snb.2006.03.049.

[86] S. V Pham, L. J Kauppinen, M. Dijkstra, H. A.G.M Wolferen van, R. M Ridder de, and H. J.W.M Hoekstra. Cantilever deflection read-out with a grated waveguide optical cavity, 2010. We propose a novel and highly sensitive mechano-optical device for gas-sensing through nano-displacements, based on micro-cantilevers, supplied with a selective gas absorbing layer (Pd), suspended above a Si3N4 grated waveguide (GWG). We present the simulation and preliminary experimental results, which indicate the sensing of nano-displacements, an important intermediate step for the gas-sensing purpose.

[87] C. Kocabas and A. Aydinli. Design and analysis of an integrated optical sensor for scanning force microscopies. *IEEE Sensors Journal*, 5(3):411– 418, June 2005. ISSN 1530-437X. doi: 10.1109/JSEN.2005.846172.

[88] Lewis G. Carpenter, Christopher Holmes, Helen L. Rogers, Peter GR Smith, and James C. Gates. Integrated optic glass microcantilevers with bragg grating interrogation. *Optics express*, 18(22):23296–23301, 2010.

[89] S.V. Pham, L.J. Kauppinen, M. Dijkstra, H.A.G.M. van Wolferen, R.M. de Ridder, and H.J.W.M. Hoekstra. Read-out of cantilever bending with a grated waveguide optical cavity. *Photonics Technology Letters, IEEE*, 23(4):215–217, 2011. ISSN 1041-1135. doi: 10.1109/LPT.2010.2097246.

[90] Tim J. Booth, Peter Blake, Rahul R. Nair, Da Jiang, Ernie W. Hill, Ursel Bangert, Andrew Bleloch, Mhairi Gass, Kostya S. Novoselov, M. I. Katsnelson, and A. K. Geim. Macroscopic graphene membranes and their extraordinary stiffness. *Nano Letters*, 8(8): 2442–2446, August 2008. ISSN 1530-6984. doi: 10.1021/nl801412y.

[91] Antoine Reserbat-Plantey, Laëtitia Marty, Olivier Arcizet, Nedjma Bendiab, and Vincent Bouchiat. A local optical probe for measuring motion and stress in a nanoelectromechanical system. *Nature Nanotechnology*, 7(3):151–155, January 2012. ISSN 1748-3387. doi: 10.1038/nnano.2011.250.

[92] O. Arcizet, P.-F. Cohadon, T. Briant, M. Pinard, A. Heidmann, J.-M. Mackowski, C. Michel, L. Pinard, O. Français, and L. Rousseau. High-sensitivity optical monitoring of a micromechanical resonator with a quantum-limited optomechanical sensor. *Physical Review Letters*, 97(13):133601, September 2006. doi: 10.1103/PhysRevLett.97.133601.

[93] G. Binnig, M. Despont, U. Drechsler, W. Häberle, M. Lutwyche, P. Vettiger, H. J. Mamin, B. W. Chui, and T. W. Kenny. Ultrahigh-density atomic force microscopy data storage with erase capability. *Applied Physics Letters*, 74(9):1329–1331, March 1999. ISSN 00036951. doi: doi:10.1063/1.123540.

[94] Nickolay V. Lavrik, Michael J. Sepaniak, and Panos G. Datskos. Cantilever transducers as a platform for chemical and biological sensors. *Review of Scientific Instruments*, 75(7): 2229–2253, June 2004. ISSN 00346748. doi: doi:10.1063/1.1763252.

[95] Anja Boisen and Thomas Thundat. Design & fabrication of cantilever array biosensors. *Materials Today*, 12(9):32–38, September 2009. ISSN 1369-7021. doi: 10.1016/S1369-7021(09)70249-4.

[96] X. M. H. Huang, X. L. Feng, C. A. Zorman, M. Mehregany, and M. L. Roukes. VHF, UHF and microwave frequency nanomechanical resonators. *New Journal of Physics*, 7 (1):247, November 2005. ISSN 1367-2630. doi: 10.1088/1367-2630/7/1/247.

[97] Robert G. Knobel and Andrew N. Cleland. Nanometre-scale displacement sensing using a single electron transistor. *Nature*, 424(6946):291–293, July 2003. ISSN 0028-0836. doi: 10.1038/nature01773.

[98] Siebe Bouwstra, Rob Legtenberg, Harrie A.C. Tilmans, and Miko Elwenspoek. Resonating microbridge mass flow sensor. *Sensors and Actuators A: Physical*, 21(1–3): 332–335, February 1990. ISSN 0924-4247. doi: 10.1016/0924-4247(90)85066-D.

[99] Mo Li, H. X. Tang, and M. L. Roukes. Ultra-sensitive NEMS-based cantilevers for sensing, scanned probe and very high-frequency applications. *Nature Nanotechnology*, 2 (2):114–120, January 2007. ISSN 1748-3387. doi: 10.1038/nnano.2006.208.

[100] Albert Loui, Timothy V. Ratto, Thomas S. Wilson, Scott K. McCall, Erik V. Mukerjee, Adam H. Love, and Bradley R. Hart. Chemical vapor discrimination using a compact and low-power array of piezoresistive microcantilevers. *The Analyst*, 133(5):608, 2008. ISSN 0003-2654. doi: 10.1039/b713758c.

[101] Seung S. Lee and Richard M. White. Self-excited piezoelectric cantilever oscillators. *Sensors and Actuators A: Physical*, 52(1–3):41–45, March 1996. ISSN 0924-4247. doi: 10.1016/0924-4247(96)80123-3.

[102] Z. Zeng, M. A. P. Pertijs, and D. M. Karabacak. An energy-efficient readout circuit for resonant sensors based on ring-down measurement. *Review of Scientific Instruments*, 84 (2):025005–025005–8, February 2013. ISSN 00346748. doi: doi:10.1063/1.4792396.

[103] Chengyin Wang, Deyan Wang, Yindao Mao, and Xiaoya Hu. Ultrasensitive biochemical sensors based on microcantilevers of atomic force microscope. *Analytical Biochemistry*, 363(1):1–11, April 2007. ISSN 0003-2697. doi: 10.1016/j.ab.2006.12.010.

[104] W. J Venstra and H. S. J van der Zant. Efficient readout of micromechanical resonator arrays in ambient conditions. *Applied Physics Letters*, 93(23):234106–234106–3, December 2008. ISSN 00036951. doi: doi:10.1063/1.3042097.

[105] G. Putrino, M. Martyniuk, A. Keating, L. Faraone, and J.M. Dell. A WDM capable integrated optical readout of a MEMS sensor. *Procedia Engineering*, 47:386–389, 2012. ISSN 1877-7058. doi: 10.1016/j.proeng.2012.09.164.

[106] Dirk Taillaert, Frederik Van Laere, Melanie Ayre, Wim Bogaerts, Dries Van Thourhout, Peter Bienstman, and Roel Baets. Grating couplers for coupling between optical fibers and nanophotonic waveguides. *Japanese Journal of Applied Physics*, 45(No. 8A): 6071–6077, August 2006. ISSN 0021-4922. doi: 10.1143/JJAP.45.6071.

[107] Ardavan F. Oskooi, David Roundy, Mihai Ibanescu, Peter Bermel, J.D. Joannopoulos, and Steven G. Johnson. Meep: A flexible free-software package for electromagnetic simulations by the FDTD method☒. *Computer Physics Communications*, 181(3): 687–702, March 2010. ISSN 00104655. doi: 10.1016/j.cpc.2009.11.008.

[108] D. Hondros and P. Debye. Elektromagnetische wellen an dielektrischen drähten. *Annalen der Physik*, 337(8):465–476, 1910. ISSN 1521-3889. doi: 10.1002/andp.19103370802.

[109] P. K. Tien. Integrated optics and new wave phenomena in optical waveguides. *Reviews of Modern Physics*, 49(2):361–420, April 1977. doi: 10.1103/RevModPhys.49.361.

[110] Kris V. Srikrishnan. Smart-cut process for the production of thin semiconductor material films, March 1999. U.S. Classification: 438/458; 148/DIG.50; 257/E21.567; 257/E21.568; 438/406; 438/407; 438/455; 438/528; 438/977 International Classification: H01L 2130.

[111] P. K. Tien and R. Ulrich. Theory of prism-film coupler and thin-film light guides. *Journal of the Optical Society of America*, 60(10):1325–1337, October 1970. doi: 10.1364/JOSA.60.001325.

[112] P. K. Tien and R. J. Martin. EXPERIMENTS ON LIGHT WAVES IN a THIN TAPERED FILM AND a NEW LIGHT-WAVE COUPLER. *Applied Physics Letters*, 18 (9):398–401, May 1971. ISSN 00036951. doi: doi:10.1063/1.1653716.

[113] M. L. Dakss, L. Kuhn, P. F. Heidrich, and B. A. Scott. GRATING COUPLER FOR EFFICIENT EXCITATION OF OPTICAL GUIDED WAVES IN THIN FILMS. *Applied Physics Letters*, 16(12):523–525, June 1970. ISSN 00036951. doi: doi:10.1063/1.1653091.

[114] Francesco Maria Grimaldi. *Physico-mathesis de lumine, coloribus et iride.* ex typographia haeredis Victorii Benatii. Impensis Hieronymi Berniae, 1665.

[115] F. Hopkinson and David Rittenhouse. An optical problem, proposed by mr. hopkinson, and solved by mr. rittenhouse. *Transactions of the American Philosophical Society*, 2: 201–206, January 1786. ISSN 0065-9746. doi: 10.2307/1005186. ArticleType: research-article / Full publication date: 1786 /.

[116] Christopher A. Palmer, Erwin G. Loewen, and R. G. L. Thermo. *Diffraction grating handbook.* Newport Corporation Springfield, OH, 2005.

[117] Vladimir A. Sychugov. Optimization and control of grating coupling to or from a silicon-based optical waveguide. *Optical Engineering*, 35(11):3092, 1996. ISSN 00913286. doi: 10.1117/1.601048.

[118] I. A. Avrutsky, A. S. Svakhin, V. A. Sychugov, and O. Parriaux. High-efficiency single-order waveguide grating coupler. *Optics Letters*, 15(24):1446–1448, December 1990. doi: 10.1364/OL.15.001446.

[119] D. Taillaert, P. Bienstman, and R. Baets. Compact efficient broadband grating coupler for silicon-on-insulator waveguides. *Optics Letters*, 29(23):2749–2751, 2004. ISSN 0146-9592.

[120] S. Ura, T. Suhara, H. Nishihara, and J. Koyama. An integrated-optic disk pickup device. *Journal of Lightwave Technology*, 4(7):913–918, 1986. ISSN 0733-8724. doi: 10.1109/JLT.1986.1074821.

[121] M. G. Moharam and T. K. Gaylord. Rigorous coupled-wave analysis of planar-grating diffraction. *Journal of the Optical Society of America*, 71:811, July 1981. ISSN 0030-3941. doi: 10.1364/JOSA.71.000811.

[122] M. Nevière and E. Popov. Grating electromagnetic theory user guide. *Journal of Imaging Science and Technology*, 41(4):315–323, 1997.

[123] David Rosenblatt, A. Sharon, and A.A. Friesem. Resonant grating waveguide structures. *IEEE Journal of Quantum Electronics*, 33(11):2038–2059, 1997. ISSN 0018-9197. doi: 10.1109/3.641320.

[124] Bahaa E. A Saleh and Teich . *Fundamentals of photonics.* Wiley-Interscience, Hoboken, N.J., 2007. ISBN 0471358320 9780471358329.

[125] David B. Hand. The refractivity of protein solutions. *Journal of Biological Chemistry*, 108 (3):703–707, March 1935. ISSN 0021-9258, 1083-351X.

[126] P. Dumon, W. Bogaerts, R. Baets, J.-M. Fedeli, and L. Fulbert. Towards foundry approach for silicon photonics: silicon photonics platform ePIXfab. *Electronics Letters*, 45(12):581–582, June 2009. ISSN 00135194. doi: 10.1049/el.2009.1353.

[127] Dirk Taillaert, Wim Bogaerts, and Roel Baets. Efficient coupling between submicron SOI-waveguides and single-mode fibers. *IEEE/LEOS Benelux Chapter, Enscheda*, 2003.

[128] Dirk Taillaert, Wim Bogaerts, Peter Bienstman, Thomas F. Krauss, Peter Van Daele, Ingrid Moerman, Steven Verstuyft, Kurt De Mesel, and Roel Baets. An out-of-plane grating coupler for efficient butt-coupling between compact planar waveguides and single-mode fibers. *Quantum Electronics, IEEE Journal of*, 38(7):949–955, 2002.

[129] P. Dumon, W. Bogaerts, J. Van Campenhout, V. Wiaux, J. Wouters, S. Beckx, and R. Baets. Low-loss, single-mode photonic wires and ring resonators in silicon-on-insulator. In *The 16th Annual Meeting of the IEEE Lasers and Electro-Optics Society, 2003. LEOS 2003*, volume 1, pages 289–290 vol.1, 2003. doi: 10.1109/LEOS.2003.1251751.

[130] F. Ladouceur and P. Labeye. A new general approach to optical waveguide path design. *Journal of Lightwave Technology*, 13(3):481–492, 1995. ISSN 0733-8724. doi: 10.1109/50.372446.

[131] H Guckel, D Burns, C Rutigliano, E Lovell, and B Choi. Diagnostic microstructures for the measurement of intrinsic strain in thin films. *Journal of Micromechanics and Microengineering*, 2:86–95, June 1992. ISSN 0960-1317, 1361-6439. doi: 10.1088/0960-1317/2/2/004.

[132] H. Guckel, T. Randazzo, and D. W. Burns. A simple technique for the determination of mechanical strain in thin films with applications to polysilicon. *Journal of Applied Physics*, 57(5):1671–1675, March 1985. ISSN 00218979. doi: doi:10.1063/1.334435.

[133] H. E. Bennett, M. Silver, and E. J. Ashley. Infrared reflectance of aluminum evaporated in ultra-high vacuum. *Journal of the Optical Society of America*, 53(9):1089–1095, September 1963. doi: 10.1364/JOSA.53.001089.

[134] Jean M. Bennett and E. J. Ashley. Infrared reflectance and emittance of silver and gold evaporated in ultrahigh vacuum. *Applied Optics*, 4(2):221–224, February 1965. doi: 10.1364/AO.4.000221.

[135] R.S. Tucker, D.M. Baney, W.V. Sorin, and C.A. Flory. Thermal noise and radiation pressure in MEMS fabry-perot tunable filters and lasers. *IEEE Journal of Selected Topics in Quantum Electronics*, 8(1):88 –97, February 2002. ISSN 1077-260X. doi: 10.1109/2944.991403.

[136] H. Huang, K.J. Winchester, A. Suvorova, B.R. Lawn, Y. Liu, X.Z. Hu, J.M. Dell, and L. Faraone. Effect of deposition conditions on mechanical properties of low-temperature PECVD silicon nitride films. *Materials Science and Engineering: A*, 435–436:453–459, November 2006. ISSN 0921-5093. doi: 10.1016/j.msea.2006.07.015.

[137] Adrian Keating and John Dell. *MicroElectroMechanical Systems (MEMS)*. 2009.

[138] I. W. Frank, David M. Tanenbaum, A. M. Van der Zande, and Paul L. McEuen. Mechanical properties of suspended graphene sheets. *Journal of Vacuum Science & Technology B: Microelectronics and Nanometer Structures*, 25(6):2558–2561, 2007.

[139] W. Fang and J. A. Wickert. Comments on measuring thin-film stresses using bi-layer micromachined beams. *Journal of Micromechanics and Microengineering*, 5(4):276, December 1995. ISSN 0960-1317. doi: 10.1088/0960-1317/5/4/003.

[140] B.A. Walmsley, Yinong Liu, Xiao Zhi Hu, M.B. Bush, J.M. Dell, and L. Faraone. Poisson's ratio of low-temperature PECVD silicon nitride thin films. *Journal of Microelectromechanical Systems*, 16(3):622–627, 2007. ISSN 1057-7157. doi: 10.1109/JMEMS.2007.893518.

[141] I. Ladabaum, Xuecheng Jin, H.T. Soh, A. Atalar, and B.t. Khuri-Yakub. Surface micromachined capacitive ultrasonic transducers. *IEEE Transactions on Ultrasonics, Ferroelectrics and Frequency Control*, 45(3):678–690, 1998. ISSN 0885-3010. doi: 10.1109/58.677612.

[142] Peter J. Mohr, Barry N. Taylor, and David B. Newell. CODATA recommended values of the fundamental physical constants: 2010. *Reviews of Modern Physics*, 84(4):1527–1605, November 2012. doi: 10.1103/RevModPhys.84.1527.

[143] Niels Tas, Tonny Sonnenberg, Henri Jansen, Rob Legtenberg, and Miko Elwenspoek. Stiction in surface micromachining. *Journal of Micromechanics and Microengineering*, 6 (4):385, December 1996. ISSN 0960-1317. doi: 10.1088/0960-1317/6/4/005.

[144] V. A. Aksyuk, F. Pardo, D. Carr, D. Greywall, H. B. Chan, M. E. Simon, A. Gasparyan, H. Shea, V. Lifton, C. Bolle, S. Arney, R. Frahm, M. Paczkowski, M. Haueis, Ronald Ryf, David T. Neilson, J. Kim, C. Randy Giles, and D. Bishop. Beam-steering micromirrors for large optical cross-connects. *Journal of Lightwave Technology*, 21(3):634, March 2003.

[145] F. Jiang, A. Keating, M. Martyniuk, R. Pratap, L. Faraone, and J.M. Dell. Process control of cantilever deflection for sensor application based on optical waveguides. *Journal of Microelectromechanical Systems*, 22(3):569–579, 2013. ISSN 1057-7157. doi: 10.1109/JMEMS.2012.2231051.

[146] G. Putrino, A. Keating, M. Martyniuk, L. Faraone, and J. Dell. Integrated resonant optical readout applicable to large arrays of MEMS beams. *IEEE Photonics Technology Letters*, 24 (24):2243 –2246, December 2012. ISSN 1041-1135. doi: 10.1109/LPT.2012.2225611.

[147] Frédéric Lochon, Isabelle Dufour, and Dominique Rebière. An alternative solution to improve sensitivity of resonant microcantilever chemical sensors: comparison between using high-order modes and reducing dimensions. *Sensors and Actuators B: Chemical*, 108(1–2):979–985, July 2005. ISSN 0925-4005. doi: 10.1016/j.snb.2004.11.086.

[148] S. Morshed and B.C. Prorok. Tailoring beam mechanics towards enhancing detection of hazardous biological species. *Experimental Mechanics*, 47(3):405–415, 2007. ISSN 0014-4851. doi: 10.1007/s11340-006-9015-7.

[149] Mike Tooley and Michael H. Tooley. *Electronic Circuits: Fundamentals and Applications*. Elsevier, 2006. ISBN 9780750669238.

[150] W. Weaver Jr, S. P. Timoshenko, and D. H. Young. *Vibration Problems in Engineering*. John Wiley & Sons, February 1990. ISBN 9780471632283.

[151] William M. Siebert. *Circuits, Signals, and Systems (Paperback) by Siebert, William M. pulished by The MIT Press*. The MIT Press, September 1985.

[152] G. G. Yaralioglu, A. Atalar, S. R. Manalis, and C. F. Quate. Analysis and design of an interdigital cantilever as a displacement sensor. *Journal of Applied Physics*, 83(12): 7405–7415, June 1998. ISSN 00218979. doi: doi:10.1063/1.367984.

[153] L.S. Fock, A. Kwan, and RodneyS. Tucker. Reduction of semiconductor laser intensity noise by feedforward compensation: experiment and theory. *Journal of Lightwave Technology*, 10(12):1919–1925, 1992. ISSN 0733-8724. doi: 10.1109/50.202819.

[154] Frank L. Riley. Silicon nitride and related materials. *Journal of the American Ceramic Society*, 83(2):245–265, 2000. ISSN 1551-2916. doi: 10.1111/j.1151-2916.2000.tb01182.x.

[155] K.Y. Yasumura, T.D. Stowe, E.M. Chow, T. Pfafman, T.W. Kenny, B.C. Stipe, and D. Rugar. Quality factors in micron- and submicron-thick cantilevers. *Microelectromechanical Systems, Journal of*, 9(1):117–125, 2000. ISSN 1057-7157. doi: 10.1109/84.825786.

[156] Harry Nyquist. Thermal agitation of electric charge in conductors. *Physical review*, 32 (1):110–113, 1928.

[157] G. Putrino, A. Keating, M. Martyniuk, L. Faraone, and J. Dell. Model and analysis of a high sensitivity resonant optical read-out approach suitable for cantilever sensor arrays. *Lightwave Technology, Journal of*, 30(12):1863 –1868, June 2012. ISSN 0733-8724. doi: 10.1109/JLT.2012.2190973.

[158] John E. Sader, James W. M. Chon, and Paul Mulvaney. Calibration of rectangular atomic force microscope cantilevers. *Review of Scientific Instruments*, 70(10):3967–3969, October 1999. ISSN 00346748. doi: doi:10.1063/1.1150021.

[159] T. Rasmussen, J.K. Rasmussen, and J.H. Povlsen. Design and performance evaluation of 1-by-64 multimode interference power splitter for optical communications. *Journal of Lightwave Technology*, 13(10):2069–2074, 1995. ISSN 0733-8724. doi: 10.1109/50.469726.

[160] K. Sasaki, F. Ohno, A. Motegi, and T. Baba. Arrayed waveguide grating of 70$\times$ 60 μm< sup> 2</sup> size based on si photonic wire waveguides. *Electronics Letters*, 41 (14):801–802, 2005.

[161] F. Tan, R. Bambery, M. Feng, and N. Holonyak. Relative intensity noise of a quantum well transistor laser. *Applied Physics Letters*, 101(15):151118–151118–4, October 2012. ISSN 00036951. doi: doi:10.1063/1.4760225.

[162] Chao Li, Huijuan Zhang, Mingbin Yu, and G. Q. Lo. CMOS-compatible high efficiency double-etched apodized waveguide grating coupler. *Optics Express*, 21(7):7868–7874, April 2013. doi: 10.1364/OE.21.007868.

[163] T.J. Kippenberg and K.J. Vahala. Cavity optomechanics: Back-action at the mesoscale. *Science*, 321(5893):1172, 2008.

[164] Sebastian Romero-Garcia, Florian Merget, Frank Zhong, Hod Finkelstein, and Jeremy Witzens. Silicon nitride CMOS-compatible platform for integrated photonics applications at visible wavelengths. *Optics Express*, 21(12):14036–14046, June 2013. doi: 10.1364/OE.21.014036.

[165] Anna Salvati, Andrzej S. Pitek, Marco P. Monopoli, Kanlaya Prapainop, Francesca Baldelli Bombelli, Delyan R. Hristov, Philip M. Kelly, Christoffer Åberg, Eugene Mahon, and Kenneth A. Dawson. Transferrin-functionalized nanoparticles lose their targeting capabilities when a biomolecule corona adsorbs on the surface. *Nature Nanotechnology*, 8(2):137–143, February 2013. ISSN 1748-3387. doi: 10.1038/nnano.2012.237.

Colophon

This thesis was typeset using LaTeX, originally developed by Leslie Lamport and based on Donald Knuth's TeX. The body text is set in 11 point Arno Pro, designed by Robert Slimbach in the style of book types from the Aldine Press in Venice, and issued by Adobe in 2007. It was printed at UniPrint, at the office situated on The University of Western Australia Crawley campus. A template, which can be used to format a PhD thesis with this look and feel, has been released under the permissive MIT (X11) license, and can be found online at github.com/suchow/ or from suchow@post.harvard.edu.